

Freezing conditions in warm disks

snowlines and their effect on the chemical structure of
planet-forming disks

Proefschrift

ter verkrijging van
de graad van doctor aan de Universiteit Leiden,
op gezag van rector magnificus prof. dr. ir. H. Bijl,
volgens besluit van het college voor promoties
te verdedigen op woensdag 14 februari 2024
klokke 10:00 uur
door

Margot Leemker

geboren te Zwijndrecht, Nederland
in 1996

Promotores:

Prof. dr. E. F. van Dishoeck

Prof. dr. M. R. Hogerheijde Universiteit Leiden
Universiteit van Amsterdam

Co-promotor:

Dr. A. S. Booth Harvard & Smithsonian Center for Astrophysics

Promotiecommissie:

Prof. dr. I. A. G. Snellen

Prof. dr. H. V. J. Linnartz

Prof. dr. E. A. Bergin University of Michigan

Prof. dr. H. Nomura National Astronomical Observatory of Japan

Dr. V. V. Guzmán Pontificia Universidad Católica

ISBN:

Cover design: Marta Paula Tychoniec

The universe is made of stories, not of atoms.
- *Muriel Rukeyser*

Table of contents

1	Introduction	1
1.1	Star and planet formation	1
1.2	Protoplanetary disks	4
1.2.1	Evolution of disks	4
1.2.2	Dust evolution and planet formation	6
1.2.3	Observations of disks with ALMA	8
1.2.4	Disks are not smooth in dust	9
1.2.5	Disks are not smooth in gas	11
1.2.6	Dust traps are ice traps	12
1.2.7	Vertical structure in disks	13
1.3	Astrochemistry	13
1.3.1	Gas-phase chemistry	14
1.3.2	Grain surface chemistry	15
1.3.3	Inheritance or reset	15
1.3.4	Snowlines	17
1.3.4.1	Tracers of snowlines	18
1.4	Thermometers in disks	20
1.4.1	Brightness temperature	20
1.4.2	Line ratios	21
1.5	Modelling of protoplanetary disks using DALI	22
1.6	This thesis	24
1.6.1	Outlook	25
2	Chemically tracing the water snowline in protoplanetary disks with HCO⁺	27
2.1	Introduction	29
2.2	Protoplanetary disk model	31
2.2.1	Disk structure	31
2.2.2	Chemical models	34
2.2.3	Radiative transfer	35
2.3	Modelling results	37
2.3.1	Chemistry	37
2.3.1.1	Water versus electrons	38

2.3.1.2	Effect of the CO, H ₂ O abundance, and cosmic ray ionisation rate on the HCO ⁺ abundance	39
2.3.2	HCO ⁺ and H ¹³ CO ⁺ emission	40
2.3.2.1	Continuum optical depth	42
2.3.2.2	Molecular excitation	43
2.3.2.3	Chemistry	45
2.3.2.4	What causes HCO ⁺ rings?	45
2.3.3	Line profiles	45
2.4	Comparison with observations	46
2.4.1	H ¹³ CO ⁺ observations	48
2.4.2	HCO ⁺ observations	50
2.4.3	Model HCO ⁺ images: locating the snowline	50
2.5	Conclusions	53
	Appendices	54
2.A	Freeze-out and desorption coefficients	54
2.B	Chemical network	55
2.B.1	Analytical approximation for network NW	55
2.B.2	Initial conditions	56
2.C	HCO ⁺ and H ¹³ CO ⁺ $J = 1 - 0$, $J = 3 - 2$, and $J = 4 - 3$ transitions	57
2.D	V883 Ori	57
3	Resolving snow surfaces of water and methanol in the V883 Ori disk	63
3.1	Introduction	65
3.2	Methods	67
3.3	Results	68
3.4	Discussion	70
3.4.1	Layered or mixed ices on the grains	70
3.4.2	HDO and methanol snow surfaces in other disks	71
3.5	Conclusions	72
3.6	Acknowledgements	72
	Appendices	74
3.A	Channel maps	74
3.B	Optical depth	74
4	Gas temperature structure across transition disk cavities	77
4.1	Introduction	79
4.2	Observations	81
4.2.1	The sources	81
4.2.2	Data	84
4.3	Results	89
4.3.1	Dust	89
4.3.2	Gas	90
4.3.2.1	Radial profiles	90
4.3.2.2	Brightness temperatures	91
4.3.2.3	Spectra	93

4.4	Analysis	94
4.4.1	Temperature and column density determination	94
4.4.2	Results for LkCa15	96
4.4.3	Results for HD 169142	100
4.5	Thermochemical models	101
4.6	Discussion	103
4.6.1	Comparing models and observations	103
4.6.2	Comparison to other sources	105
4.6.3	Implications for the cause of the gas cavity	106
4.7	Conclusions	108
	Appendices	110
4.A	Observations	110
4.A.1	Channel maps $^{13}\text{CO } J = 6 - 5$	110
4.A.2	Azimuthally averaged radial profiles	110
4.A.3	Brightness temperature	110
4.A.4	Spectra	112
4.B	Line ratio analysis	114
4.B.1	Temperature and column density	114
4.B.2	Optical depth	114
4.C	DALI	116
4.C.1	Model setup	116
4.C.2	DALI models for other parameters	123
5	A major asymmetric ice trap in a planet-forming disk. IV. Nitric oxide gas and a lack of CN tracing sublimating ices and a C/O ratio <1	125
5.1	Introduction	127
5.2	Observations and methods	129
5.2.1	Data	129
5.2.2	Data analysis	132
5.2.3	Column densities	133
5.3	Observational results	135
5.3.1	Detected lines	135
5.3.2	NO column density	137
5.3.3	Upper limits on nitrogen-bearing molecules and C/O ratio	137
5.3.4	Upper limits on H_2O and OH	139
5.4	Models	140
5.4.1	Dust trap cools the disk midplane	143
5.4.2	Effect of sublimating ices: H_2O and NH_3	146
5.4.3	Effects of sublimating ices: Additional NO	149
5.4.4	Chemical composition of the non-dust trap side	150
5.5	Discussion	150
5.5.1	Possible parent molecules of NO	150
5.5.2	Comparison to other sources	152
5.6	Conclusions	154
5.7	Acknowledgements	154

Appendices	156
5.A Observations	156
5.B DALI	157
5.B.1 Model setup	157
5.B.1.1 Gas and dust density structure	157
5.B.1.2 Stellar spectrum	162
5.B.1.3 Chemical network	162
5.B.2 Model results	168
5.B.2.1 Initial distribution of nitrogen	168
5.B.2.2 Effect of evaporating ices on CN and C ₂ H	168
5.B.2.3 Chemical composition of the non-dust trap side	170
5.B.2.4 Time evolution	170
6 Chemistry across dust and gas gaps in protoplanetary disks: modelling the co-spatial molecular rings in the HD 100546 disk	179
6.1 Introduction	181
6.2 Methods	184
6.2.1 Source: HD 100546	184
6.2.2 ALMA data covering [C I]	185
6.2.3 DALI	185
6.2.3.1 Gas density structure	185
6.2.3.2 Dust density structure	186
6.2.4 Stellar spectrum	187
6.2.5 Chemistry	187
6.2.6 Raytracing	188
6.2.7 The fiducial model	188
6.3 Results	191
6.3.1 2D abundance maps	192
6.3.2 Integrated intensity maps	193
6.3.3 A deeper gas gap	195
6.3.3.1 Column densities	195
6.3.3.2 Emission maps	197
6.3.3.3 Molecular column densities and line ratios	197
6.3.4 Different C/O ratios	199
6.3.4.1 Column densities and emission profiles	199
6.3.4.2 Column density and emission line ratios	203
6.3.5 Background UV	203
6.3.6 Flaring	204
6.4 Discussion	205
6.4.1 Radial structures	205
6.4.1.1 CO isotopologues, HCO ⁺ , and HCN	205
6.4.1.2 CN, C ₂ H, and NO	206
6.4.2 Chemistry in the rings and gap	207
6.5 Conclusions	209
6.6 Acknowledgements	210
Appendices	211

6.A	Observed lines	211
6.B	DALI	212
6.B.1	Model setup	212
6.B.1.1	Radial and vertical structure	212
6.B.1.2	Initial conditions of the chemical networks	213
6.B.2	Model predictions	218
6.B.2.1	Emission profiles and emitting heights of CO isotopologues	218
6.B.2.2	Emission profiles and column densities of [C I], HCN, CN, C ₂ H, NO, and HCO ⁺ for different gas gaps	219
6.B.2.3	Column densities of [C I], HCN, CN, C ₂ H, NO, and HCO ⁺ for different C/O ratios	222
6.B.3	Molecular ratios	222
6.B.3.1	Column density ratios for different gap depths	222
6.B.3.2	Emission line ratios for different gap depths	224
6.B.3.3	Column density and line ratios for different C/O ratios	225
6.B.4	Background UV	226
6.B.5	Flaring	226
	Bibliography	226
	Nederlandse samenvatting	255
	Publications	263
	Curriculum Vitae	267
	Acknowledgements	269

Chapter 1

Introduction

Earth is the only inhabited planet that we know of to date. Over 5000 exoplanets have been discovered but whether any of them have life on them is unknown. Some exoplanets are extremely hot and life as we know it is impossible, but others are located just far enough from their host star to potentially have liquid water on their surface, a key ingredient for habitability. To understand if the Earth is truly unique in its ability to host complex life, we need to understand the process of star and planet formation and the changes in the chemistry during this process. Comparing the Earth and our Solar System to exoplanets and young, forming planets opens a window to look across the timeline of planet formation. This thesis focuses on the temperature and chemistry of the environment in which young planets are forming.

1.1 Star and planet formation

The cycle of star and planet formation starts with a molecular cloud, see the first panel of Fig. 1.1. As the name suggests, these clouds mainly consist of gas-phase molecular hydrogen (H_2) with trace amounts of CO (Frerking et al. 1982; Lacy et al. 1994). The very low temperatures of 10–20 K prevent molecules beyond H_2 , N_2 , and some CO to be in the gas phase at high abundances (Bergin et al. 2002; Caselli et al. 2002), though some clouds like TMC-1 are rich in long carbon chains and aromatic molecules at low abundances (e.g., McGuire et al. 2018; Cernicharo et al. 2023, and references therein). Typical gas-phase densities in these clouds range from $10^4 - 10^6$ particles per cm^3 (see Bergin & Tafalla 2007, for a review) and only 1 % of the mass of a cloud consists of (sub)micron sized dust particles (Draine 2003). Despite their low mass compared to the total gas mass, these dust particles are key to form water and complex organic molecules, the building blocks of life, see Section 1.3.2.

Molecular clouds range from relatively small, irregularly shaped ones of ~ 0.05 pc in size to filamentary giant clouds of 100 pc in diameter (Bok & Reilly

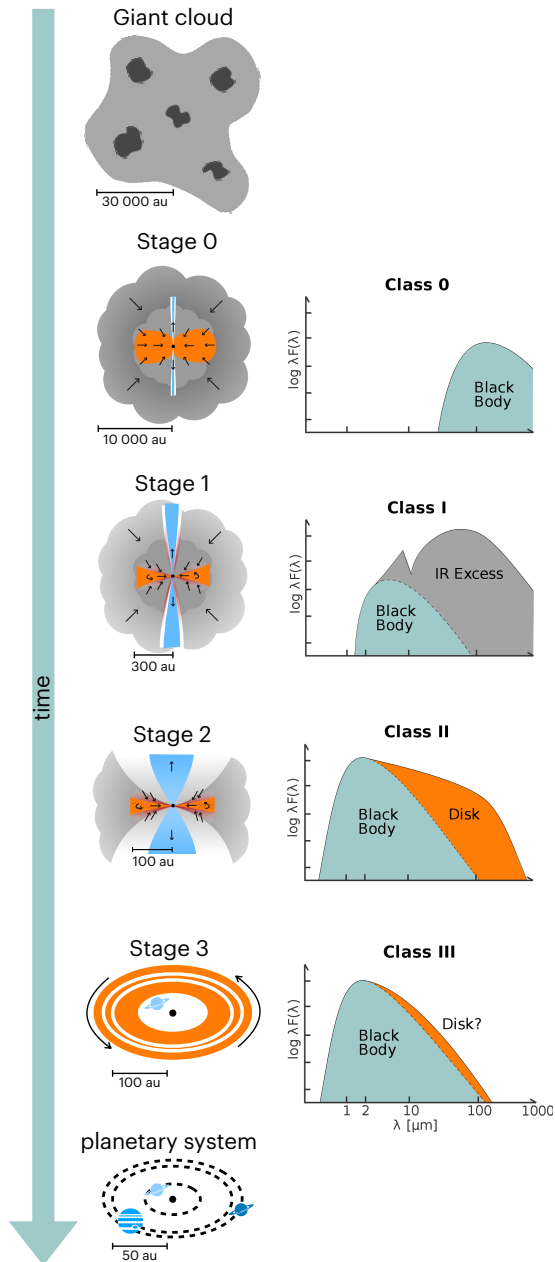


Figure 1.1: Cycle of star and planet formation. Left: theoretical stages from cloud to planetary system. Right: typical SEDs corresponding to the stages. Figure adapted from M. Persson.

1947; Lada & Lada 2003; Krumholz et al. 2014; André et al. 2010; Hacar et al. 2013, 2017). As the cloud evolves, these cloud cores become denser and colder to the point where their internal gas pressure, turbulent motions, and magnetic field cannot support the cloud cores from gravitational collapse. The mass at which a core becomes unstable is the Jeans mass and may be triggered by the slow evolution of the cloud or due to external factors (Jeans 1928). The cloud core then collapses from the inside out to form a protostellar core of $\sim 10^4$ au (second panel in Fig. 1.1) that then contracts to form one or multiple young protostars surrounded by a massive envelope (Shu 1977; Terebey et al. 1984; Galli & Shu 1993).

The subsequent evolution from the moment a protostar forms to the moment a debris disk is present around the star is characterized by four stages (Shu et al. 1987; Robitaille et al. 2006) that correspond to the same number of observational classes (Lada 1987; André et al. 1993). These classes are defined based on the bolometric temperature and luminosity, the sub-mm luminosity, and the slope of the spectral energy distribution in between 2 and 20 μm (α_{IR} Lada 1987; André et al. 1993; Greene et al. 1994). Even though the different stages show a close correspondence to the classes, the geometry of the source, e.g. an edge-on disk, may cause a misclassification of these objects (Crapsi et al. 2008).

The first stage, Stage 0 is characterized by a protostar surrounded by a massive, several 1000 au envelope, with a mass much larger than that of the star. As the initial core always has some small net angular momentum and because angular momentum is conserved, the gas and dust in the cloud cannot fall onto the star following a straight line. Instead, the material falls to the plane perpendicular to the rotation axis and then spirals inwards forming a pseudo-disk (Cassen & Moosman 1981; Terebey et al. 1984; Galli & Shu 1993). Material from this pseudo-disk is then accreted onto the star at a high rate of $\dot{M}_* > 10^{-6} M_{\odot} \text{ yr}^{-1}$. The angular momentum that is not stored in the disk or the envelope is removed by a collimated jet that emerges from the envelope. Observationally, these objects are classified through their low bolometric temperature of < 70 K, their bright sub-mm emission ($L_{\text{sub-mm}}/L_{\text{bol}} > 0.5$ %), and the lack of IR emission observed with telescopes before the advent of the JWST.

After $\sim 10^5$ yr, the star has accreted sufficient mass to outweigh its natal envelope and thus enters Stage 1 of star and planet formation, see the third panel in Fig. 1.1 (Kristensen & Dunham 2018). During this stage, the outflow becomes less collimated and the accretion disk surrounding the central star spreads due to the conservation of angular momentum, while the mass accretion rate onto the star remains high at $\dot{M}_* > 10^{-6} M_{\odot} \text{ yr}^{-1}$ up to ~ 0.5 Myr after the onset of star formation. Observations show that these Class I objects are characterized by a positive slope in the IR $\alpha_{\text{IR}} > 0$, a warmer bolometric temperature of 70 – 650 K, and a relatively low sub-mm luminosity compared to the bolometric luminosity.

Once the envelope has dissipated through accretion onto the disk and outflow of material, a pre-main sequence star surrounded by a ~ 100 au protoplanetary disk emerges (Stage 2, see the fourth panel in Fig. 1.1). During this phase, accretion onto the central star has slowed down to a rate $\dot{M}_* < 10^{-6} M_{\odot} \text{ yr}^{-1}$ (Manara et al. 2023, for a review). As planet formation likely starts in the Class 0 or Class I phase,

protoplanetary disks are also referred to as planet-forming disks (e.g., Segura-Cox et al. 2020; Tychoniec et al. 2020). Within the following 5 – 10 Myr, the planets continue to accrete disk material and the remaining gas and dust is cleared from the system through MHD disk winds and photoevaporation. As the emission from the central star is not attenuated as much by the surrounding envelope, these objects have an intermediate spectral index of $-1.5 < \alpha_{\text{IR}} < 0$ and a high bolometric temperature of 650 – 2800 K and are classified as Class II objects.

The third and final stage before a planetary system emerges is the debris disk stage (see the fifth panel in Fig. 1.1). In contrast to the gas-rich Stage 2 disk, the debris disks are gas-poor and the dust is likely of secondary origin due to collisions of planetesimals. The gas in many debris disks is consistent with a secondary origin though some may contain primordial gas from the protoplanetary disk phase (Kral et al. 2017; Hughes et al. 2018). Their spectral energy distribution only shows a small amount of excess emission in the (sub)-mm regime with a spectral index $\alpha_{\text{IR}} < -1.5$. After the disk has vanished, the star reaches the main sequence and is surrounded by a planetary system of exoplanets.

1.2 Protoplanetary disks

1.2.1 Evolution of disks

The direct detection of two young planets in the PDS 70 disk shows that planet formation is ongoing in disks. Disk formation is a natural outcome of the star formation process as disks are seen around many young stars (e.g., Ansdell et al. 2016; Manara et al. 2023). Both simulations and observations show that protoplanetary disks can form as early as in the Class 0 stage (Yorke et al. 1993; Tobin et al. 2012; Murillo et al. 2013). As the disk evolves its mass increases because the accretion rate of envelope material onto the disk is higher than the accretion rate of disk material onto the star (Hueso & Guillot 2005). Therefore, the disk mass increases over time till the system reaches a high disk-to-star mass ratio, possibly leading to a globally gravitationally unstable disk (Kratte & Lodato 2016; Xu & Kunz 2021a,b). Gravitational instability (GI) leads to spiral arms and clumps of material that can collapse to form a binary stellar companion or a young planet.

Another effect of a disk instability or an external trigger such as a flyby of a nearby star is the triggering of a protostellar outburst (see Kenyon & Hartmann 1987; Fischer et al. 2023, for a review). During an FU Orionis type outburst, the luminosity of the star increases by orders of magnitude and slowly decreases over a timescale of tens to over 100 yr before the luminosity approaches that before the outburst began. Additionally, stars accrete $10^{-3} - 10^{-2} M_{\odot}$ of material during this brief period due to the very high accretion rates that are observed (Audard et al. 2014).

As the disk further evolves the ratio of disk mass to stellar mass decreases to $10^{-1} - 10^{-4}$ due to accretion onto the central star, disk winds, and potentially by locking up material in newly formed planets (Manara et al. 2023). Even though the mass budget of a young star-disk system is dominated by the central star, the angular momentum is largely contained in the rotating disk. A consequence of the

conservation of angular momentum is that protoplanetary disk material cannot accrete onto the central star unless the angular momentum is redistributed across the disk.

The redistribution of angular momentum drives the evolution of the disk in time. Two leading hypotheses for the mechanism behind this are viscous evolution (Lynden-Bell & Pringle 1974; Pringle 1981) and magneto-hydrodynamic (MHD) disk winds (e.g., Lesur et al. 2013; Bai 2016). Both processes can be active at the same time in the disk but viscous evolution likely dominates the earlier phases while MHD driven disk winds dominate the later phases (e.g., Trapman et al. 2022).

The rotation velocity in a Keplerian disk is not constant but decreases with the square root of the distance from the star. Therefore, two adjacent annuli of gas experience a shearing force between them with the inner ring being slowed down and the outer one being sped up due to their velocity difference. This process transfers part of the angular momentum of the inner ring to the outer ring at an efficiency set by the disk viscosity (Shakura & Sunyaev 1973; Lynden-Bell & Pringle 1974; Pringle 1981; Hartmann et al. 1998). The driver of this viscosity is unknown but numerous processes have been suggested such as GI, vertical shear instability, and magneto-rotational instability, whereas the Brownian motion of gas-phase molecules is too low and thus excluded as the main driver of the viscosity (Lin & Pringle 1987; Balbus & Hawley 1991; Richard & Zahn 1999; Nelson et al. 2013; Stoll & Kley 2014; Armitage 2019). Recent observations of disks show that turbulence and thus the viscosity is low in most disks (e.g., Flaherty et al. 2015, 2017, 2018; Teague et al. 2018b; Trapman et al. 2020). Regardless of the source of the disk viscosity, the inner disk loses the angular momentum that the outer disk gains causing the material in the inner disk to accrete onto the star while the outer disk spreads outwards. The viscous spreading of the disk is one of the main observational discriminators between the viscous evolution model and the disk wind model.

MHD disk winds on the other hand, redistribute angular momentum by removing material from the disk surface layers along the magnetic field lines if the gas is sufficiently ionized to couple to the magnetic field (see Pascucci et al. 2023, for a review). Along with the removal of a small amount of gas mass, a large amount of angular momentum is removed. Detailed modelling of these disk winds shows that the removal of angular momentum is sufficient to drive accretion onto the central star (Ferreira et al. 2006; Béthune et al. 2017; Zhu & Stone 2018; Tabone et al. 2022a,b). In contrast to viscous evolution, MHD driven evolution predicts that the disk radius shrinks over time. Even though only a few spatially resolved disk winds or disk wind candidates have been observed with ALMA in Class II disks (Louvét et al. 2018; Booth et al. 2021a; Pascucci et al. 2023), distinguishing viscous evolution from MHD disk winds as the main driver of disk evolution remains an active topic in the field (Manara et al. 2023).

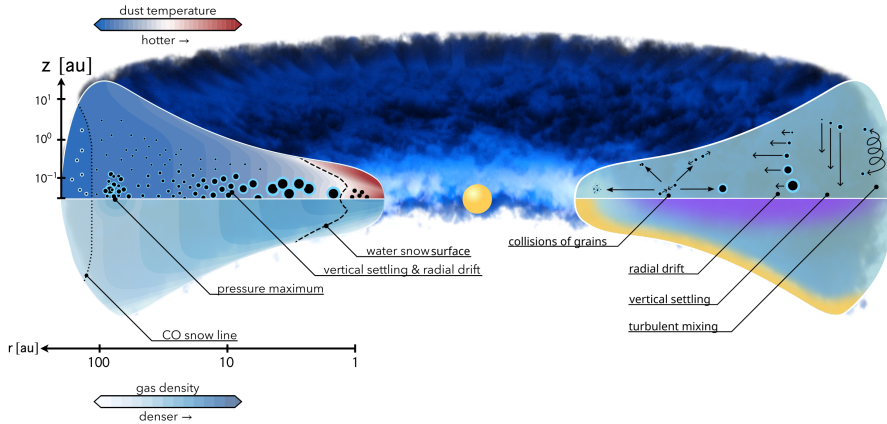


Figure 1.2: Schematic view of a protoplanetary disk. Left: temperature and density structure. Right: four main processes involving dust grains in a disk. Collisions between grains can result in four possible outcomes (counterclockwise): sticking, bouncing, mass transfer with some fragmentation, fragmentation. Figure adapted from Testi et al. (2014) and Miotello et al. (2023).

1.2.2 Dust evolution and planet formation

Another big question in the field is the formation of planets. Protoplanetary disks disperse on a timescale of a few million years (e.g., Haisch et al. 2001; Fedele et al. 2010), so planet formation must happen fast. The formation of planets starts with the micron-sized dust particles that a protoplanetary disk inherits from the molecular cloud. Frequent collisions between these dust particles and gas-phase molecules force the dust to follow the gas. Therefore, these small grains are seen in all disk layers, see Fig. 1.2. In addition to collisions with gas-phase molecules, the dust particles also collide with each other to form larger grains up to a few mm in size due to efficient sticking (e.g., Blum & Wurm 2008; Brauer et al. 2008; Wada et al. 2008; Birnstiel et al. 2010; Güttler et al. 2010; Birnstiel et al. 2012). Observations of Class 0 and I objects already show evidence for grain growth (Kwon et al. 2009; Harsono et al. 2018; Tychoniec et al. 2020).

During this process the larger dust grains decouple from the gas due to their increase in size and thus Stokes number. This causes these particles to settle towards the disk midplane due to a net gravitational force in this direction (see Fig. 1.2, Dubrulle et al. 1995; Villenave et al. 2020). In addition, the decoupling from the gas increases the relative velocities between the dust particles causing the particles to bounce or fragment instead of growing. As the fragmentation velocity of these particles is low at $1 - 10 \text{ m s}^{-1}$, dust growth beyond the fragmentation barrier seems impossible without invoking additional mechanisms to increase sticking or reduce fragmentation.

Even if cm-sized pebbles continue growing to boulders of ~ 1 m, retaining them in the disk to form planets is unlikely without anything to stop radial drift. The reason for this is that the gas rotates at a slightly sub-Keplerian velocity due to the gas pressure. The decoupled pebbles and boulders do not feel this gas pressure and thus rotate at the Keplerian velocity appropriate for their distance from the central star. The boulders thus feel a head wind from the gas in the disk, transferring their angular momentum to the gas and causing the boulders to drift towards the central star on a timescale of only 100 yr at a distance of 1 au from the star (Whipple 1972; Weidenschilling 1977). For mm size dust grains, the timescale is ~ 1 Myr at a distance of 100 au in the outer disk, respectively. An example of this process in a protoplanetary disk is provided by the CX Tau disk where the dust has drifted inwards to a radius five times smaller than that of the gas disk (Facchini et al. 2019).

Radial drift can be slowed down or even stopped in the pressure traps in a disk. A maximum in the gas pressure causes the particles to drift towards this location instead of drifting to the inner regions of the disk (e.g., Pinilla et al. 2012b,a). Many different mechanisms have been proposed to create these traps such as the outer edge of a gap carved by a massive planet, but also processes that do not require a planet to be present like GI, zonal flows, vortices, magneto-rotational instability, and the inner edge of dead zones (a disk region with low ionization suppressing the magneto-rotational instability; see Pinilla et al. 2017; Bae et al. 2023, for reviews). These pressure bumps provide a favourable location to grow pebbles and boulders into km-sized planetesimals due to the slower radial drift and smaller velocity differences between bodies reducing the chance of fragmentation upon a collision. GI not only creates spiral arms that act as pressure traps; the collapse of disk material can also directly form planets or stellar companions in the outer disk that could create new pressure traps (Boss 1997; Boley 2009; Kratter et al. 2010).

In addition, snowlines, i.e., the midplane radii where one of the major volatiles in the disk freezes-out onto the dust grains, may be a location where planet formation is enhanced. Especially the water snowline may be a good candidate as water is the first major volatile to freeze out. The diffusion of water across the snowline feeds the ice and thus increases the mass of solids just outside the water snowline (Stevenson & Lunine 1988). This not only provides additional mass to form planets, it could also trigger the streaming instability causing the dust particles to further concentrate and possible collapse to form larger bodies (Youdin & Goodman 2005; Johansen et al. 2007; Drażkowska & Alibert 2017; Schoonenberg & Ormel 2017). The dust grains outside the water snowline may be somewhat more prone to fragmentation due to their icy mantles, these mantles also increase the probability of two colliding grains to stick together and thus grow (Wada et al. 2011; Okuzumi et al. 2016).

Once planetesimals have formed, two main pathways to form planets are hypothesised: planetesimal accretion and pebble accretion (see Drażkowska et al. 2023, for a recent review). Both mechanisms have in common that they are driven by gravity, but their differences arise from the sizes of the initial bodies (planetesimals vs pebbles). In the case of planetesimal accretion, the formation of planets is

driven by collisions of planetesimals where the largest bodies have the largest gravitational pull and thus the highest accretion rates (Kokubo & Ida 1996; Tanaka & Ida 1999). However, this process can also lead to fragmentation and it is too slow to form a sufficiently massive solid core ($\gtrsim 10 M_{\text{Earth}}$) to accrete gas and form a giant planet at the distance of the ice giants in our Solar System (Pollack et al. 1996; Ikoma et al. 2000; Thommes et al. 2003). Pebble accretion provides a solution to this timescale problem as the accretion of pebbles onto a solid core is orders of magnitude faster than planetesimal accretion (Ormel & Klahr 2010; Lambrechts & Johansen 2012; Johansen & Lambrechts 2017). However, pebble accretion is only efficient if sufficiently massive cores to accrete onto are already present in the disk.

Comparing the exoplanet population that is observed to date to the planet forming disks could hold important clues to understand the planet formation process. One of these clues may be the disk mass as observations of protoplanetary disks in the Class II phase show that their masses are generally too low to explain the masses of the exoplanets around main sequence stars (e.g., Ansdell et al. 2016; Manara et al. 2018). The younger Class 0 and I disks are more massive and could reproduce the observed exoplanet population (e.g., Tychoniec et al. 2018, 2020; Tobin et al. 2020). However, these masses may be an underestimate of the true disk mass as the continuum emission is likely optically thick, hiding part of the dust mass, dust may have grown to larger sizes than those probed by the observations, and the dust opacity may be underestimated due to scattering (Zhu et al. 2019). Even though observations suggest that planet formation may start early, this does not mean that planet formation is finished before the Class II phase is reached.

1.2.3 Observations of disks with ALMA

Protoplanetary disks are observed with many different telescopes such as the VLT, NOEMA, SMA, VLA, ALMA, and recently JWST. ALMA is of particular interest for this thesis as its observing frequency, spatial and spectral resolution, and sensitivity are particularly well suited to spatially resolve the dust structures due to pressure traps and the weak molecular line emission probing the gas.

ALMA is a radio interferometer located on a plateau 5000 m above sea level in the Chilean desert. The 66 telescopes of ALMA are divided into three groups: the main array consisting of 50 antennas with a diameter of 12 m, the ACA consisting of 12 antennas of 7 m, and the Total Power array consisting of four 12 m antennas. As each group probes a larger angular scale on the sky, the main array, sometimes in combination with the ACA are most frequently used for protoplanetary disk observations.

The spatial resolution of the main array is tuned to the specific needs of observations as every ~ 20 days the telescopes of the main array are moved to a new configuration and thus a different spatial resolution. The highest resolution of $0''.01$ at 870 GHz or $0''.04$ at 230 GHz is achieved in the most extended configuration (C-8), whereas the lowest resolution of $3''.4$ at 100 GHz or $1''.5$ at 230 GHz is obtained in the most compact configuration (C-1). The maximum scale that

can be probed by these configurations is an order of magnitude larger than the respective spatial resolution as interferometers are not sensitive to extended emission. Therefore, multiple configurations are combined if a high dynamic range in spatial scales is expected.

ALMA covers a wide frequency range of 84 – 950 GHz divided into eight (non-continuous) frequency bands, Band 3 – 10. In addition, ALMA Band 1 (35 – 50 GHz) is currently being installed and expected to be offered from March 2024 and ALMA Band 2 (67 – 116 GHz) is in development. The wide range in available frequencies can not only be used for multi wavelength observations of the continuum to constrain e.g., the grain sizes and continuum optical depths but also to probe molecular lines with different upper energy levels. In particular, the high frequency bands, Band 8 – 10 can be used to probe warm molecular lines, such as the $^{13}\text{CO } J = 6 - 5$ transition that cannot be observed otherwise (see also Chapter 4). The wide frequency range together with the high spatial and spectral resolution and sensitivity of ALMA enable both detailed studies of individual disks (e.g., Qi et al. 2013; Cleeves et al. 2015b; Isella et al. 2016; Schwarz et al. 2016; Pinte et al. 2018b; Teague et al. 2018a,b; Wölfer et al. 2021; Keyte et al. 2023; Law et al. 2023a) and surveys of larger samples (Andrews et al. 2013; Miotello et al. 2014; Ansdell et al. 2016; Barenfeld et al. 2016; Miotello et al. 2016; Tripathi et al. 2017; Andrews et al. 2018; Ansdell et al. 2018; Long et al. 2018; Öberg & Bergin 2021; Anderson et al. 2022; van Terwisga et al. 2022; Stapper et al. 2022; Wölfer et al. 2023b).

1.2.4 Disks are not smooth in dust

The most striking direct proof of ongoing planet formation in a protoplanetary disk is the detection of two young, accreting planets in the PDS 70 disk (Keppler et al. 2018; Haffert et al. 2019; Benisty et al. 2021). These young planets are sufficiently massive to carve a wide gap and thus create a pressure trap just outside of their locations in the PDS 70 disk. Many of the structures seen in other protoplanetary disks to date can also be explained by embedded massive planets as rings and gaps are seen at almost all radii in large and bright disks observed with ALMA (see Fig. 1.3; e.g., Andrews et al. 2018; Long et al. 2018; Huang et al. 2018). However, even though the majority of structures can potentially be explained by planets, individual rings and gaps can be due a dust opacity change around the water snowline, a dead zone, and other processes forming pressure traps in disks (e.g., Huang et al. 2018).

In addition to rings and gaps, some disks show spiral arms in the sub-mm continuum (see e.g. IM Lup and Elias 27 in Fig. 1.3). Spiral arms are less common in the sub-mm emission than rings and gaps, and are likely generated by forming planets, binary companions, zonal flows, or a gravitationally unstable disk (e.g., Ogilvie & Lubow 2002; Rafikov 2002; Dong et al. 2015a; Uribe et al. 2015; Kratter & Lodato 2016; Bae & Zhu 2018). Another azimuthal structure that is sometimes seen in disks is an arc (see e.g., HD 143006 and HD 163296 in Fig. 1.3 and IRS 48 continuum in the top left panel of Fig. 1.5). These arcs can be the result of vortices due to a massive planer or stellar companion triggering the Rossby-Wave

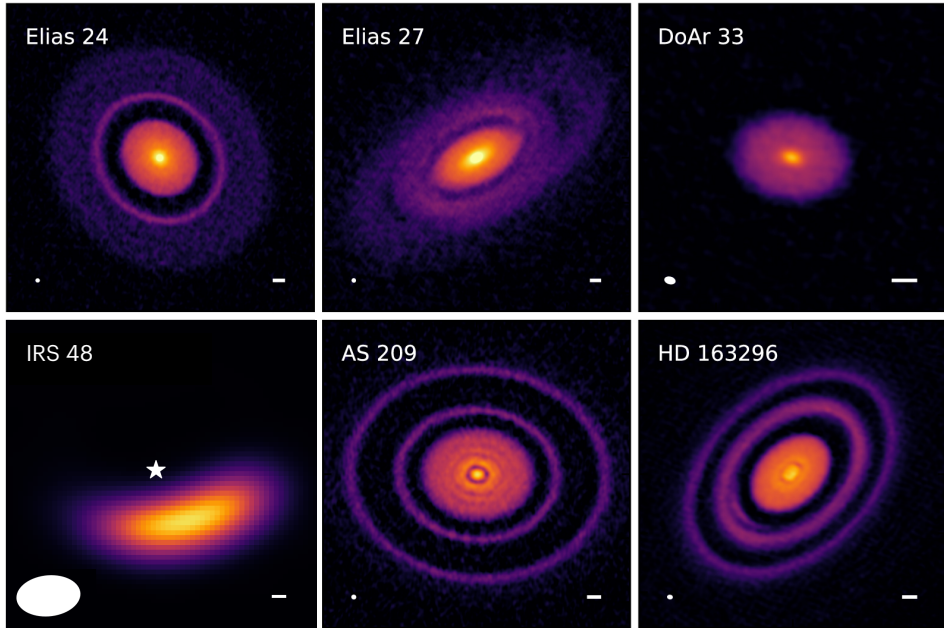


Figure 1.3: Continuum observations of structured protoplanetary disks. Rings, gaps, spirals, and an arc are seen. The resolution of the observations is indicated with the white ellipse in the bottom left corner and a 10 au scale bar is indicated in the bottom right corner. Figure adapted from van der Marel et al. (2013) and Andrews et al. (2018).

instability (Lovelace et al. 1999; Li et al. 2000, 2001; van der Marel et al. 2013).

Observing these rings, gaps, spirals, and arcs is now common with ALMA due to its high spatial resolution. However, even before the advent of ALMA disks with large cavities, transition disks, were identified based on their SED at IR to (sub-)mm wavelengths. The SED of transition disks is characterized by a low MIR and in some cases also NIR fluxes tracing the lack of the warm dust close to the central star. Excess emission at NIR wavelengths is indicative of a small dusty inner disk close to the central star. Gas observations with ALMA show that these disks not only have a deep cavity in the dust, but often also in the gas (e.g., Bruderer et al. 2014; Perez et al. 2015; van der Marel et al. 2015, 2016; Wölfer et al. 2021, see also Chapter 4). These cavities are likely due to one or more massive planets or a stellar companion but also photoevaporation can clear the inner disk regions from gas and dust (Owen et al. 2011; Ercolano & Pascucci 2017; Picogna et al. 2019). Interestingly, despite their large cavities, the observed accretion rates of these disk are often high, much higher than expected based on the mass of the dusty inner disk if present, suggesting that gas must flow through the cavity at high velocities (e.g., Najita et al. 2007; Espaillat et al. 2014; Francis & van der Marel 2020; Manara et al. 2020).

1.2.5 Disks are not smooth in gas

The dust in protoplanetary disks only makes up 1% of the total disk mass. Therefore, observations of the gas are needed to fully understand planet formation. Despite the fact that 99% of the disk mass consists of gas, observations of it are much more difficult than continuum observations. The reason for this is that a gas-phase molecule only emits at certain narrow frequency ranges (emission lines) set by quantum mechanics in contrast to the dust that emits at all wavelengths similar to or smaller than the grain itself (Draine 2006). Additionally, the flux of a specific gas line that is observed is set by the number molecules and the gas temperature. To further complicate gas observations, the most abundant molecule in a disk, molecular hydrogen, does not have a permanent dipole moment and thus no strong rotational transitions tracing the bulk of the disk. Therefore, less abundant molecules with a permanent dipole moment are used to trace the gas in disks.

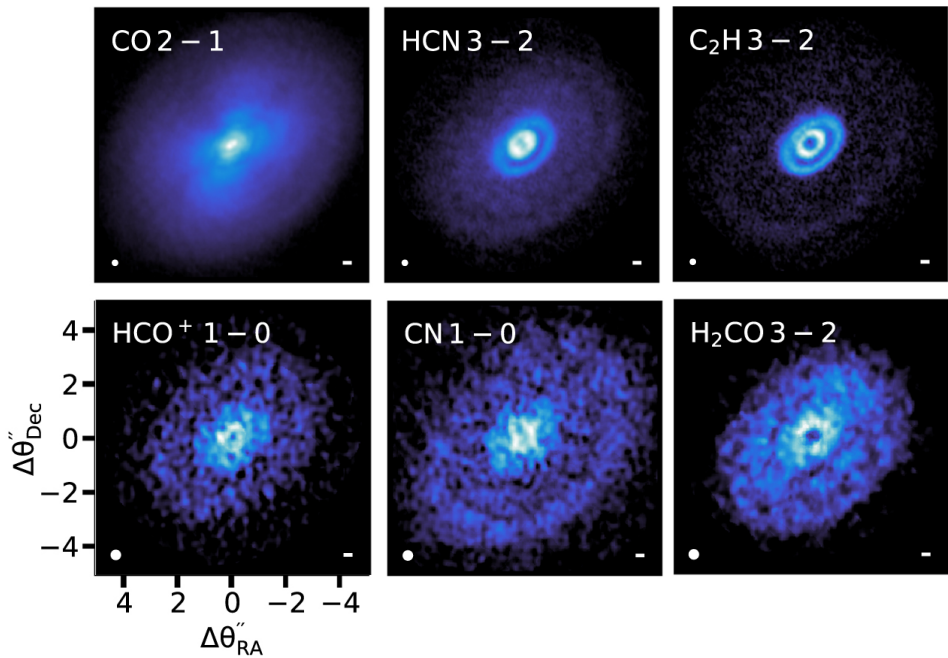


Figure 1.4: Diversity of structures in the HD 163296 disk. Figure adapted from Öberg & Bergin (2021).

One of the most commonly used tracers of the gas in a disk are CO and its isotopologues. CO is the second most abundant molecule with a typical abundance of only 10^{-4} with respect to hydrogen, yet CO rotational lines are often optically thick. As CO is abundant in almost all disk regions, CO and its isotopologues have often been used to estimate the radial extent of the disk as well as the mass.

In addition to CO and its isotopologues, over 40 other molecules and isotopologues have been detected in disks to date (McGuire 2022). A gallery of a few

different molecules in the HD 163296 disk is shown in Fig. 1.4. Similar to the diversity in dust substructures, these gas-phase molecules also all show rings and gaps at different radii that do not correlate with the dust in general (Law et al. 2021a; Jiang et al. 2022). Instead, their emission profiles are set by a combination of temperature and abundance that is controlled by chemical reactions in the disk, which opens the possibility to probe many different processes in the disk as is discussed in Sect. 1.3. However, not all disks conform to this general trend, such as the HD 100546 disk where molecular emission coincides with the dust rings as analysed in this thesis (Chapter 5 and 6).

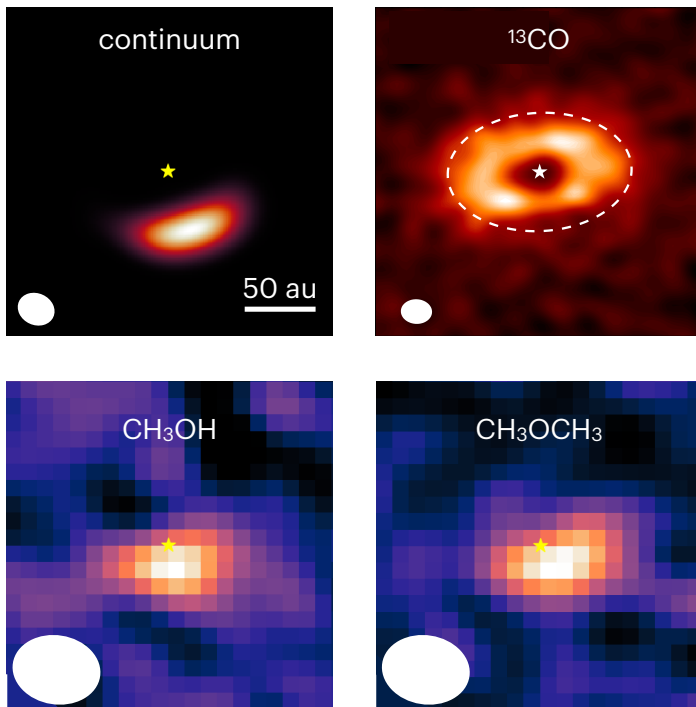


Figure 1.5: The major asymmetric ice trap IRS 48. The large dust (top left panel) is concentrated in the south, whereas the ^{13}CO gas disk is consistent with an azimuthally symmetric disk (top right panel). Emission from COMs (bottom row) is only seen at the dust trap, indicating an origin in the ice. Figure adapted from van der Marel et al. (2016) and (Brunken et al. 2022).

1.2.6 Dust traps are ice traps

Despite the general trend that gas and dust structures do not correlate, two disks are a notable exception: IRS 48 and HD 142527. Both of these disks are transition disks with an asymmetric dust trap but a gas disk that is consistent with an azimuthally symmetric disk (Casassus et al. 2013; van der Marel et al. 2013; Bruderer et al. 2014; van der Marel et al. 2021a). However, the molecular abundances

in these disks (anti-)correlate with the dust instead of the gas. In the IRS 48 disk, emission of H_2CO and COMs is only seen at the location of the dust trap, see Fig. 1.5 (van der Marel et al. 2021b; Booth et al. 2021b; Brunken et al. 2022), whereas in the HD 142527 disk, the emission of CS and H_2CO is seen opposite to the dust trap likely due to a misaligned inner disk shadowing parts of the outer disk (Temminck et al. 2023).

The emission of H_2CO together with multiple COMs at the dust trap in the IRS 48 disk suggests that the gas and dust interact through the thermal sublimation of ices on large dust grains and subsequent vertical mixing if the dust trap is sufficiently warm. The lack of COM emission in the HD 142527 dust trap is consistent with its much lower temperature due to the larger distance to its host star. The temperature of the dust trap can also have a significant impact on the ices that are transported to the inner disk and thus on the molecules and atoms available for forming planets inside the dust trap (e.g., van der Marel et al. 2021c).

1.2.7 Vertical structure in disks

The cartoon of a protoplanetary disk in Fig. 1.6 shows that disks do not only have a steep gradient in their density, temperature, and UV field in the radial direction but also in the vertical direction. The surface layers of the disk are directly exposed to the UV field of the central star, increasing their temperature. The intense UV field not only heats the disk, it also photodissociates many of the molecules present in this layer. Additionally, the X-rays impinging on this layer ionize the remaining atoms and molecules. In contrast, the cold and dense disk midplane is dominated by gas containing only the most volatile molecules such as H_2 and CO, and dust grains covered in icy layers.

At intermediate disk layers, the UV and X-ray fields are (partially) shielded allowing molecules to survive and react with each other. Therefore, this layer is characterized by a rich chemistry and will be further explored in Sect. 1.3. ALMA observations at high spatial and spectral resolution and sensitivity can directly measure the radial and vertical location at which a molecular line emits in a disk (e.g., Pinte et al. 2018a; Paneque-Carreño et al. 2022, 2023; Law et al. 2021b). This can not only be used to probe the emitting layer of different molecules or different lines of the same molecule, it can also be used to probe the 2D temperature structure in disks using multiple optically thick isotopologues of CO that probe deeper and deeper into the disk.

1.3 Astrochemistry

The composition of the gas and ice in protoplanetary disks and other objects is set by the chemical reactions between atoms and molecules. These chemical reactions are operating under very different conditions than those on Earth as typical densities in protoplanetary disks correspond to those in the highest vacuum that can be created in state of the art laboratories on Earth. Therefore, collisions between molecules are rare and the chemical timescales are long. Still a rich

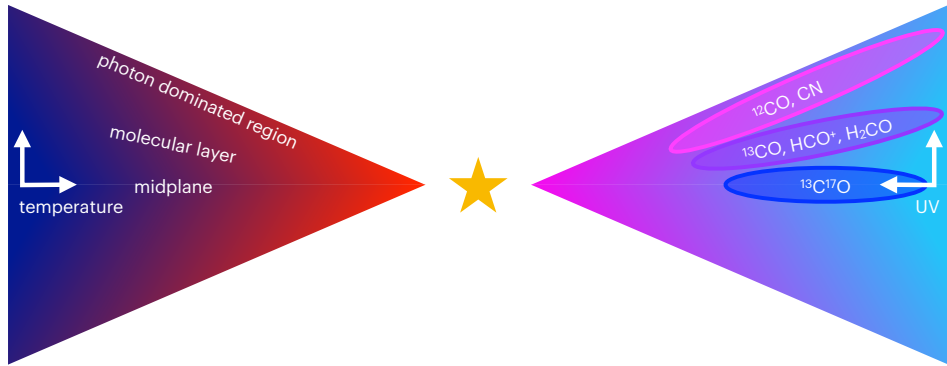


Figure 1.6: Schematic view of the radial and vertical structures in a protoplanetary disk. Left: temperature structure. Right: layering of molecules.

molecular complexity is seen across all stages of star and planet formation (e.g., Herbst & van Dishoeck 2009; Caselli & Ceccarelli 2012). The molecules that are detected vary from very simple molecules such as H_2 up to H_2O and the building blocks of life and other complex organic molecules (COMs, molecules that consist of at least six atoms of which at least one carbon and one hydrogen atom; see McGuire 2022 and references therein).

Understanding this rich molecular inventory not only requires observations of these molecules, but also laboratory research and quantum calculations to quantify the reaction rates, branching ratios, and reactions products. These reactions are collected in large databases to make predictions for the abundances of molecules in clouds and protoplanetary disks (e.g., UMIST and KIDA; Wakelam et al. 2012; McElroy et al. 2013). The reactions in most chemical networks are divided into two categories: gas-phase reactions and grain-surface reactions (see e.g., Tielens 2003; van Dishoeck 2014, for reviews).

1.3.1 Gas-phase chemistry

Two of the molecules that form predominantly through gas-phase reactions are CO and HCO^+ , but also other molecules like C_2H and O_2 are formed in the gas. The gas-phase reactions are dominated by two body reactions as the probability of three or more atoms or molecules meeting simultaneously is negligibly small due to the low gas density. Additionally, ions and molecules with a permanent dipole moment are more likely to react with other molecules due to their long range interactions (ion-molecule reactions), whereas the interactions between two neutral molecules are slower.

The low gas temperature in astronomical environments not only makes collisions between molecules rare due to their low velocities, it also heavily favours exothermic reactions over endothermic reactions and reactions with energy barriers as there is hardly any energy available. The additional energy that is produced during exothermic association reactions further limits the reactions that can take

place. This is due to the conservation of energy. If two molecules react to form a single new body, the excess energy from the bond can only be released through the emission of a photon in the gas phase, which is a very slow process. Therefore, the chance of immediate dissociation of the newly formed molecule is high and the efficiency of the initial reaction is thus low. Bond rearrangement on the other hand is much more efficient as not one but two reaction products are formed in a chemical reaction. The lightest of these two carries most of the excess energy as kinetic energy, thus stabilizing the molecule that has formed.

1.3.2 Grain surface chemistry

Reactions on the surfaces of grains are essential to form the most abundant molecule in the universe, H_2 as well as H_2O and COMs. Gas-phase atoms and molecules can land on a grain and freeze out if the temperature is sufficiently low. A light atom such as H is not bound to a specific site on the grain surface, but instead it can scan the surface. If another atom or molecule is encountered during this process this atom or molecule is hydrogenated. For instance, water is formed through $\text{O} + \text{H} \rightarrow \text{OH}$, where the excess energy is absorbed by the grain, allowing the OH radical to survive. When another hydrogen atom reacts with OH, H_2O is formed (Tielens & Hagen 1982; van Dishoeck et al. 2013). Similarly, many of the COMs likely form through the hydrogenation of CO ice (Watanabe & Kouchi 2002; Cuppen et al. 2009; Chuang et al. 2016). The processing of CO ice to CO_2 and other complex molecules in the ices could also be responsible for the very faint CO fluxes that are observed in protoplanetary disks (e.g., Favre et al. 2013; Ansdell et al. 2016; Miotello et al. 2017; Bosman et al. 2018b).

The molecules on the grain surfaces can desorb into the gas phase through excess energy produced during their formation (chemical desorption), an incident UV photon (photodesorption), or due to sublimation if the grain is heated (thermal desorption). Therefore, molecules that formed in the ice may also be observed in the gas-phase. The effect of freeze-out and desorption of the major volatiles on protoplanetary disk chemistry is discussed in detail in the next Section.

1.3.3 Inheritance or reset

As the long journey from clouds to protoplanetary disks and then planets mostly happens at temperatures below the freeze-out temperature of water, the question is raised whether the water seen in disks and comets is inherited from the earliest phases of star and planet formation or if the chemistry is reset along the way (e.g., Visser et al. 2009; Furuya et al. 2013; Cleeves et al. 2014b). In the inheritance scenario, the majority of the water that formed in the molecular cloud stage remains frozen out and unaltered through the four stages of star and planet formation until a planetary system is born (Visser et al. 2009; Drozdovskaya et al. 2016). On the other hand, in the reset scenario, water may still form in the molecular cloud stage, but this water is destroyed and later reformed during at least one of the stages (e.g., Yang et al. 2013). As the conditions under which water is destroyed and subsequently reformed may vary, the water content in e.g. protoplanetary

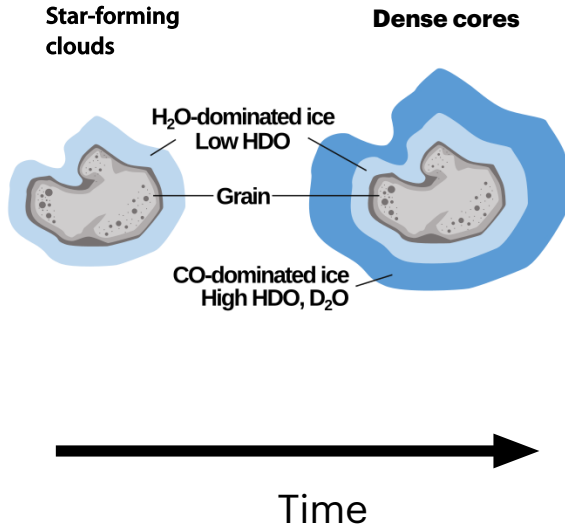
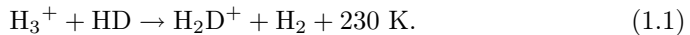


Figure 1.7: Deuteration of ices on a grain. The first layer mainly consists of H₂O ice as deuteration only becomes efficient when the cloud cools down and CO freezes-out creating a second layer dominated by CO ice with high levels of HDO and D₂O. Figure taken from van Dishoeck et al. (2021).

disk is expected to vary between isolated disks and disks in clusters whereas in the inheritance scenario each disk is born with a water abundance of 10^{-4} with respect to hydrogen. Therefore, inheritance vs reset is an important factor that sets the amount of water that is available for forming planets.

As measuring the water content in protoplanetary disks is difficult as discussed in previous sections, a different probe of inheritance vs reset is often used: deuteration of water. In the molecular cloud phase, water forms on the surfaces of grains through grain surface chemistry (see Sect. 1.3.2). Initially, the deuteration levels are low and the ice predominantly consists of H₂O, see Fig. 1.7. As the clouds cool down, the deuteration levels increase due to two main effects. First, the formation of almost all deuterated molecules is driven by H₂D⁺ formed through



The exothermicity of this reaction limits the backwards reaction at temperatures below ~ 25 K (Watson 1976; Aikawa & Herbst 1999). Second, at temperatures lower than ~ 20 K, the reaction of H₂D⁺ with CO is quenched (e.g., Pagani et al. 1992; Roberts et al. 2003). Therefore, deuteration is very efficient in the cold molecular cloud phase (Ceccarelli et al. 2014) and a second layer of ice is formed on the grains. This layer is dominated by CO ice and has high abundances of semi-heavy water (HDO) and heavy water (D₂O), see Fig. 1.7 (Furuya et al. 2016).

As this deuteration process is only efficient in the cold and dense cloud core, a high HDO/H₂O is only expected in the case of inheritance. Observations of HDO

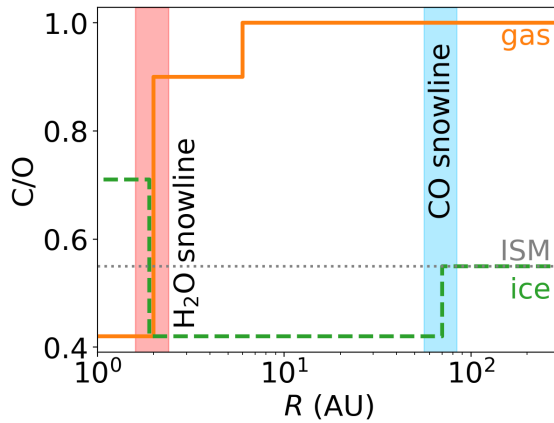


Figure 1.8: Snowlines and their effect on the chemical composition of planet forming material. Figure adapted from Öberg et al. (2011).

and the optically thin H_2^{18}O in Class 0 objects and comets in our Solar system show very similar deuteration levels of $\text{HDO}/\text{H}_2\text{O} \sim 10^{-3}$ (Persson et al. 2014; Altwegg et al. 2015; Jensen et al. 2019, 2021; Altwegg et al. 2019), suggesting that water may be inherited from clouds to comets. However, the destruction of water by UV photons and its subsequent reformation may lead to an $\text{HDO}/\text{H}_2\text{O}$ ratio similar to that in the inheritance case (Furuya et al. 2017). Therefore, the even rarer isotopologue D_2O may be used to distinguish these cases. The first measurement of the $\text{HDO}/\text{H}_2\text{O}$ ratio in a protoplanetary disk is presented in Chapter 3.

1.3.4 Snowlines

The freeze out and thermal desorption of the major volatiles has a large effect on the chemical composition of the planet forming material (e.g., Öberg et al. 2011; Öberg & Bergin 2021). Gas-phase water is one of the first molecules to freeze out as it only desorbs at a high temperature of $\sim 100 - 150$ K in protoplanetary disks. Therefore, the water snowline in a typical protoplanetary disk is located at only a few au from the host T Tauri star (Harsono et al. 2015). For the warmer Herbig disks, the snowline is expected at a somewhat larger distance of $5 - 10$ au. Other major snowlines in disks include those of NH_3 and CO_2 that are located a few au outside the water snowline, and the CO and N_2 snowlines that are located at tens of au, see the top bar in Fig. 1.8.

The chemical composition of the planet forming material is often measured as the C/O, C/H, and O/H ratios. The freeze-out of these major volatiles effectively moves carbon and oxygen atoms from the gas-phase into the ice and thus changing these ratios, see Fig. 1.8. In particular the water snowline is important as the largest change in the C/O ratio is seen at that location. In addition, grain growth may be enhanced around the water snowline (see Sect. 1.2.2) making the water snowline a crucial location in the disk. A few au further out, CO_2 freezes out and

the gas-phase C/O ratio approaches unity. A C/O ratio exceeding unity has a dramatic effect on the abundance of C_2H , a molecule that can only be abundant if the C/O ratio exceeds one (e.g., Bergin et al. 2016; Bergner et al. 2019; Miotello et al. 2019; Bosman et al. 2021a; Guzmán et al. 2021). Comparing the chemical composition of the gas and ice in protoplanetary disks to that of exo-planets can provide information on the location where these planets formed.

Directly observing the H_2O and CO snowline in protoplanetary disks is not trivial. First, the location where a molecule freezes-out is a function of both radius and height above the midplane, see Fig. 1.6 in Sect. 1.2.7 for a schematic view. The midplane radius where a 50% of a molecule is frozen out and 50% is in the gas-phase is defined as the water snowline. The water snow surface is the 2D equivalent of this. Therefore, gas phase H_2O and CO can be present out to radii well beyond their midplane snowline locations, hiding the midplane snowline behind a layer of gas in the disk surface. However, the recent detection of H_2O in a protoplanetary disk suggests that the water snow surface may instead be vertical due to vertical mixing causing all water to freeze-out close to the disk midplane (Carr et al. 2018; Bosman & Bergin 2021), the vertical cold finger phenomenon suggested by Meijerink et al. (2009).

Even if the water snow surface is vertical in some disks, locating it is even more challenging than the CO snowline as the water snowline is expected at only a few au from the host star in most protoplanetary disks. The spatial resolution required to resolve the snowline location can only be achieved by ground-based observatories such as ALMA. Even though these observatories are built on high and dry mountains on Earth, the remaining water in the Earth’s atmosphere absorbs most of the emission of water in protoplanetary disks and only one detection of gas-phase H_2O with ALMA has been reported to date (Carr et al. 2018; Bosman & Bergin 2021). These telluric lines are avoided by observing the rare isotopologues such as H_2^{18}O or HDO.

1.3.4.1 Tracers of snowlines

As observing these snowlines directly using H_2O or CO is very challenging or impossible, a tracer can be used. A tracer is a molecule that very strongly reacts to the desorption of either H_2O or CO, or a molecule that can only form in the vicinity of the respective snowline. For example, DCO^+ is a molecule that forms efficiently around the CO snowline (Mathews et al. 2013; Carney et al. 2018). Therefore, a ring of DCO^+ is expected around the CO snowline. Observations of the IM Lup disk revealed not one but two CO snowlines in this disk, the inner one due to the thermal structure of the disk and the outer one likely due to non-thermal desorption of CO ice (Öberg et al. 2015). However, DCO^+ also has a warm formation pathway unrelated to the CO snowline, thus careful chemical modelling is required to use it as a snowline tracer (Favre et al. 2015; Qi et al. 2015; Carney et al. 2018).

A molecule that reacts much stronger to the desorption of CO is N_2H^+ . This is because CO competes with N_2 to form N_2H^+ and CO also rapidly destroys N_2H^+ (Payzant et al. 1975; Rakshit 1982; Klippenstein et al. 2010). The main

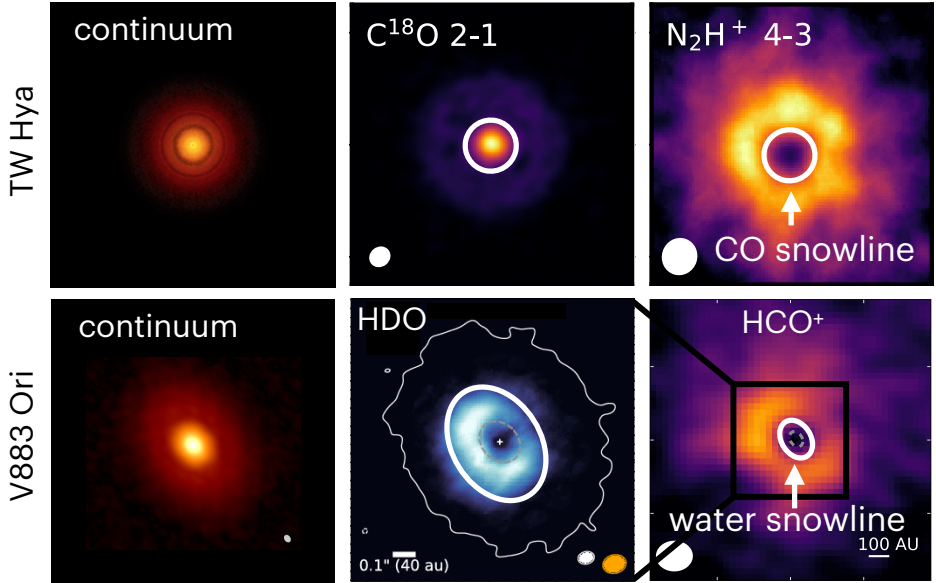
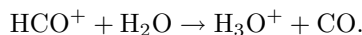


Figure 1.9: Observed anti-correlation between C^{18}O and N_2H^+ tracing the CO snowline (left) and between HDO and HCO^+ tracing the water snowline (right). ALMA observations of the TW Hya disk (left) and the V883 Ori disk (right) taken from (Qi et al. 2013; Andrews et al. 2016; Calahan et al. 2021; Ruíz-Rodríguez et al. 2022; Tobin et al. 2023).

formation pathway of N_2H^+ depends on the disk ionization, it is often used as a tracer of the disk ionization outside the CO snowline (e.g., Aikawa & Herbst 2001; Aikawa et al. 2015; Cleeves et al. 2015b). In addition, gas-phase N_2 is needed to form N_2H^+ . Therefore, ring-shaped N_2H^+ emission is expected outside the CO snowline and inside the N_2 snowline, see Fig. 1.9, though detailed chemical modelling is needed to infer these snowline locations (Qi et al. 2013, 2015; van 't Hoff et al. 2017). Observations of N_2H^+ and the rare CO isotopologue C^{18}O and $^{13}\text{C}^{18}\text{O}$ observationally confirm this anti-correlation (see Fig. 1.9) and thus establish N_2H^+ as a CO snowline tracer (Qi et al. 2013; Zhang et al. 2017). A small survey of N_2H^+ across six disks shows that the snowline locations vary from disk to disk even if a similar temperature is expected based on the spectral type of the host star (Qi et al. 2019).

Two tracers of the water snowline are COMs such as methanol and HCO^+ . Methanol has a very similar binding energy to water (e.g., Penteado et al. 2017; Minissale et al. 2022). Therefore, gas-phase methanol is only expected at or inside the water snowline. Following a similar mechanism to N_2H^+ as a CO snowline tracer, HCO^+ traces the water snowline in protoplanetary disks as water efficiently destroys HCO^+ , see Fig. 1.9 (Phillips et al. 1992; Bergin et al. 1998; van 't Hoff et al. 2018a) following



This destruction is so efficient that HCO^+ may peak slightly outside the water snowline.

To circumvent the extremely high spatial resolution needed to locate the water snowline in typical T Tauri and Herbig disks, HCO^+ and HDO, an isotopologue of H_2O , are observed in the V883 Ori disk. The central star recently experienced an outburst increasing its luminosity up to $\sim 400 L_\odot$ (Pickering 1890). Over the past century the luminosity has decreased by a factor of ~ 2 (Furlan et al. 2016), but the disk is still significantly warmer than disks around quiescent stars. Observations of the continuum suggested that the water snowline in this disk is located at 40 au based on a sudden change in the continuum opacity (Cieza et al. 2016). However, gas-phase methanol and HDO are seen out to 140 au and ~ 160 au (van 't Hoff et al. 2018a; Tobin et al. 2023). Moreover, ring-shaped HCO^+ emission is seen in this disk with a peak intensity well outside the methanol and HDO emission, see Fig. 1.9. The observed anti-correlation between HCO^+ and methanol are discussed in Chapters 2 and 3.

1.4 Thermometers in disks

The temperature structure of a disk does not only set the snowline locations, it also sets population of the energy levels of molecules and thus the expected line intensity assuming local thermodynamic equilibrium (LTE). Therefore, the temperature structure in a disk cannot only be probed by the abundance of snowline tracers such as HCO^+ , N_2H^+ , and DCO^+ but also by the intensity of the continuum and molecular line emission. In this section, two additional methods to probe the disk temperature are discussed, one for optically thick line and continuum emission and one for optically thin line emission.

1.4.1 Brightness temperature

The brightness temperature of continuum or molecular line emission is defined as the temperature of a blackbody that emits the observed intensity in the Rayleigh-Jeans limit. Therefore, the brightness temperature approximates the temperature of the disk material if the following conditions are satisfied: the emission is optically thick, spatially resolved, spectrally resolved, and the Rayleigh-Jeans approximation is appropriate. In case one of these requirements is not met, the brightness temperature (generally) underestimates the kinetic temperature.

If the emission is optically thin or marginally optically thick and the optical depth is known, the brightness temperature can be corrected for the optical depth τ using $1 - e^{-\tau}$. However, accurate measurements of the optical depth are challenging. Similarly, the brightness temperature can be corrected for unresolved emission if the emitting region is known from e.g., higher spatial resolution observations. As the brightness temperature is directly proportional to the observed intensity it provides a straight forward method to probe the disk temperature of both the dust and of the gas in the emitting layer of molecule.

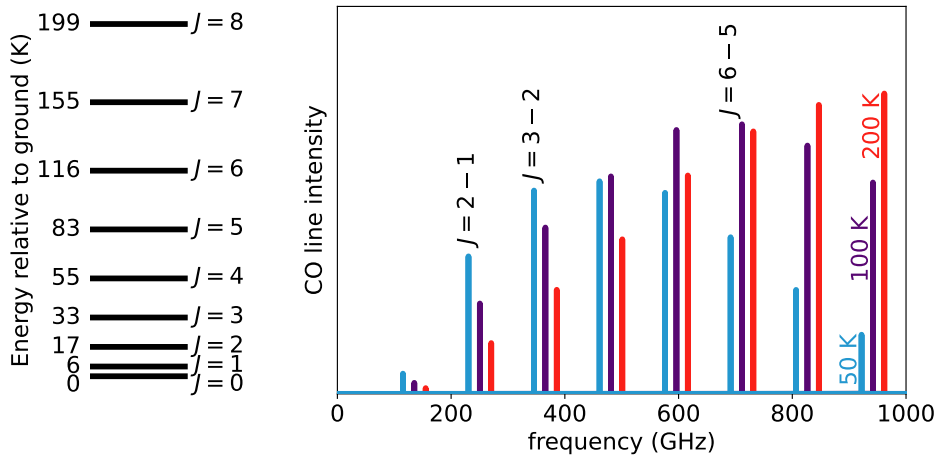


Figure 1.10: Left: CO rotational ladder. Right: the expected line intensities for three different temperatures of 50 K (blue), 100 K (purple), and 200 K (red). The 20 GHz frequency shift is applied to the purple and red spectra for visualisation purposes.

1.4.2 Line ratios

Another method to measure the temperature of the gas is to use line ratios of optically thin transitions (e.g., Goldsmith & Langer 1999; Loomis et al. 2018). The population of the energy levels of a molecule depends on its temperature if the density is sufficiently high:

$$\frac{N_u}{N_{\text{tot}}} = \frac{g_u}{Q(T_{\text{ex}})} e^{-E_u/(k_B T_{\text{ex}})}, \quad (1.2)$$

with N_u the column density of the upper energy level u , N_{tot} the total column density of the molecule, g_u the degeneracy, $Q(T_{\text{ex}})$ the partition function at excitation temperature T_{ex} , E_u the energy of level u , and k_B the Boltzmann constant. This also affects the expected line intensity as shown in Fig. 1.10.

The column density of the upper energy level can be measured directly from the observations as this is directly proportional to the integrated flux and not dependent on temperature. The right hand side of Eq. 1.2 only depends on molecular properties that can be found in databases such as CDMS and JPL (Pickett et al. 1998; Müller et al. 2001, 2005; Endres et al. 2016) and on the excitation temperature that is equal to the kinetic temperature if the gas is in LTE. Therefore, the gas temperature can be measured directly if two (or more) molecular lines of the same molecule are observed:

$$\frac{1}{k_B T_{\text{ex}}} = -\frac{1}{E_u - E_l} \ln \left(\frac{N_u g_l}{N_l g_u} \right). \quad (1.3)$$

This method is most sensitive to the temperature if the expected excitation temperature is similar to $(E_u - E_l)/k_B$. Therefore, high frequency ALMA Band 9

observations, probing warm CO isotopologue lines ($J = 6 - 5$, $E_u = 111$ K) are imperative to provide a lever arm when compared with cold ALMA Band 6 ($J = 2 - 1$, $E_u = 16$ K) or ALMA Band 7 ($J = 3 - 2$, $E_u = 32$ K).

In addition, this equation is only valid if the lines are optically thin and emit from the same region and thus probe the same parcel of gas. Even though a correction for optically thick lines is mathematically possible, the molecular lines likely become optically thick at different heights in the disk, causing them to probe different layers of gas. In summary, the brightness temperature is the most suited method for optically thick emission and the line ratios is best for optically thin emission lines, see Chapter 4 for a detailed discussion.

1.5 Modelling of protoplanetary disks using DALI

Models are key to improve our understanding of protoplanetary disks as the relevant physical and chemical processes can be implemented to find trends in observables such as the morphology of the HCO^+ and N_2H^+ emission as a function of stellar type. In addition, modelling specific sources to explain the disk specific observations will give a detailed view of the temperature, density, and chemical structure in that disk. Programs that model the disk gas temperature, chemical abundances, and molecular excitation self-consistently include e.g., ProDiMo (Woitke et al. 2009; Kamp et al. 2010; Thi et al. 2011) and RAC2D (Du & Bergin 2014). The focus of this thesis is on the thermochemical code DALI (Bruderer et al. 2009, 2012; Bruderer 2013) that also includes these quantities self-consistently.

The three main sets of input parameters for a DALI model are 2D gas and dust density structure, the spectrum of the host star, and the initial chemical abundances. These are then used to calculate the abundances of the molecules included in the chemical network and raytrace the continuum and molecular line emission that can then be compared with observations of e.g., ALMA.

The first step in the DALI modelling procedure is to calculate the dust temperature using Monte Carlo radiative transfer. This 2D temperature structure, together with the radiation field, is then used as an input for the chemical network. The chemical network solver computes an initial estimate of the atomic and molecular abundances and their excitation by assuming that the gas temperature is equal to the dust temperature. Different chemical networks can be used depending on the scientific question. The smallest and thus fastest network can be used to make predictions for temperature structure and the abundance of the most abundant CO isotopologues. Other networks include isotope selective reactions for CO and H_2 (Miotello et al. 2014, 2016; Trapman et al. 2017) or additional reactions to model nitrogen bearing molecules like CN, HCN and small carbon chains as C_2H (Visser et al. 2018; Cazzoletti et al. 2018; Long et al. 2021).

In the subsequent steps, the assumption that the gas and dust temperatures are equal is relaxed as the heating and cooling rates of the atoms and molecules are used to obtain a new estimate for the gas temperature by assuming that the heating is balanced by the cooling in the disk. The new gas temperature will cause a shift in the abundances as the rate of most chemical reactions depends on the

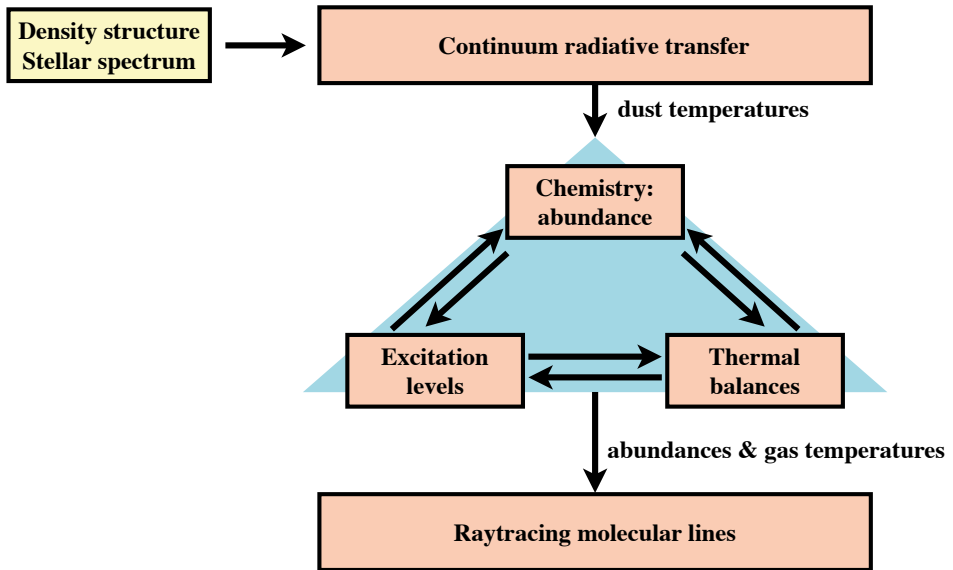


Figure 1.11: Schematic view of the work flow of DALI models (Bruderer et al. 2009, 2012; Bruderer 2013). Image credit: P. Cazzoletti, PhD thesis.

temperature. This in turn leads to new excitation levels and thus updated heating and cooling rates. Therefore, the cycle of chemistry, excitation, and thermal balance is repeated until convergence. The resulting gas and dust temperature, and abundance structure are then raytraced to create synthetic observations that can be compared to observations with ALMA or other telescopes.

The DALI modelling framework has been used to derive disk properties such as their mass and radius by comparing a population of disks observed in HD, CN, or CO isotopologues with model predictions for a set of typical disk parameters (e.g., Miotello et al. 2014, 2016; Cazzoletti et al. 2018; van Terwisga et al. 2019; Kama et al. 2020; Trapman et al. 2020). On the other hand, also in depth studies of individual disks have been used to investigate e.g., the different disk layers from the surface to the midplane, the abundance of specific atoms and molecules such as the depletion of carbon and the H₂O distribution in disks (e.g., Bruderer et al. 2012, 2014; Kama et al. 2016; van der Marel et al. 2016; Bosman et al. 2018b; Carney et al. 2018; Favre et al. 2019; Pirovano et al. 2022; Sturm et al. 2023a).

In case the modelled molecule is not included in chemical network or a specialized network is used, a parametrized abundance can be used as input for the DALI raytracer (van der Marel et al. 2021b, see also Chapter 2). Other raytracers that can be used for this are RADMC-3D (Dullemond et al. 2012), RADLite (Pontoppidan et al. 2009), LIME (Brinch & Hogerheijde 2010), and Hyperion (Robitaille 2011).

1.6 This thesis

The aim of this thesis is to shed light on the temperature structure in protoplanetary disks, a key parameter to understand their physical and chemical structure. ALMA has revealed that structures in both the gas and the dust are ubiquitous in the brightest and largest disks. One of the biggest questions in the field is what is causing these structures. Knowledge of the gas density and thus temperature structure is crucial to discriminate between these processes. In addition, characterizing the chemical composition of both the gas and the ice is needed to understand the chemical environment in which planets are forming.

Chapter 2 investigates HCO^+ as a tracer of the water snowline in protoplanetary disks. Detailed chemical modelling using a small network dedicated to HCO^+ shows that the abundance strongly anti-correlates with that of water. Synthetic images of HCO^+ and H^{13}CO^+ in a typical Herbig disk show that the lack of emission in the inner disk is only for a small part due to the water snowline and primarily due to optically thick dust that hides part of the molecular line emission. In addition, the molecular excitation has a small effect on the emission. Therefore, HCO^+ and its isotopologues are most suited as tracers in disks where no optically thick dust is expected around the water snowline. One of the disks where this is the case is the V883 Ori disk around a young outbursting star. Analysing archival HCO^+ observations shows that the water snowline is located at 75 – 120 au, which is much further out than the location of 40 au based on continuum observations and consistent with the radial extent of the methanol emission in this disk.

Chapter 3 further investigates the location of the water snowline in the V883 Ori disk and addresses the question if water is inherited from the earliest phases of star formation or reprocessed using the detections of HDO and H_2^{18}O in this disk. The emitting surface derived from the HDO channel maps shows that this layer is very steep suggesting that the water snow surface is close to vertical. In addition, gas-phase HDO is detected out to ~ 70 au close to the disk midplane, consistent with the snowline location derived from the HCO^+ observations.

Chapter 4 focuses on the origin of the cavities seen in two transition disks, LkCa 15 and HD 169142, using both ALMA Band 6 and high frequency observations. The ratio of the warm $^{13}\text{CO } J = 6 - 5$ to the cold $J = 2 - 1$ line shows that the LkCa15 dust cavity is warm. Additionally, no steep drop in the gas density is seen down to 10 au, resulting in a striking difference between the size of the gas cavity (10 au) and the dust cavity (68 au). Therefore, the LkCa 15 dust cavity is likely carved by multiple low-mass planets. The $^{13}\text{CO } J = 6 - 5/J = 2 - 1$ line ratio in the HD 169142 disk results in abnormally low temperatures likely due to the vertical structure in this disk. The brightness temperature of the optically thick ^{12}CO emission shows that the gas in the dust cavity in this disk is warm at ~ 200 K and that the gas cavity is very deep with a drop of at least 200 – 500 times less gas carved by a massive companion.

Chapter 5 analyses the first detection of NO in a protoplanetary disk. This disk is the major asymmetric ice trap IRS 48. A thermochemical model of this disk shows that additional NO beyond what can be produced by gas-phase chemistry is needed to explain the observations. The observed NO abundance is likely the

result of sublimating ices, indicating that the grains in protoplanetary disks carry the nitrogen and oxygen atoms that could be used in forming planets. Additionally, the non-detection of CN in this disk constrains the C/O ratio of the planet forming material to be < 1 , and ≤ 0.6 in most cases.

Chapter 6 further investigates the molecular structures across the gap in a planet forming disk using thermochemical modelling. In particular, the aim of this work is to distinguish physical rings, due to a change in the density or temperature structure, from chemical rings. The models are compared to the observations of molecular rings that coincide with those seen in the dust in the HD 100546 disk (Booth et al. in prep.). The models show that only the emission of rare CO isotopologues and HCO^+ directly correlate with the amount of gas in the dust gap, whereas the column density and observed intensity of C_2H , CN, HCN, and NO stays constant or even increases for deeper gas gaps. The morphology observed in all analysed molecular tracers in the HD 100546 disk is only reproduced if the gas in the gap is depleted by at least four orders of magnitude. In addition, the effect of an increased C/O ratio, a flatter disk, and an attenuated UV radiation field are investigated. The molecular rings in the HD 100546 disk likely have a chemical origin as a deep gas gap is excluded by the observations of CO isotopologues.

This leads to the following main conclusions of this thesis:

1. HCO^+ and its isotopologues are good tracers of the water snowlines if the dust around the snowline is optically thin.
2. The 2D snow surface of HDO and methanol are very steep in the disk around the outbursting star V883 Ori.
3. The gas in the dust cavities in the HD 169142 disk and the LkCa 15 disks is warm and the cavities are likely carved by a massive companion and multiple lower mass planets, respectively.
4. The emission of gas-phase molecules seen at the location of a dust trap can give clues about the chemical composition of the ice.

In summary, molecular line observations are crucial to understand the temperature and chemical structure in protoplanetary disks. Detailed knowledge of these two parameters is key to understand the density structure and thus what is causing the rings, gaps, spirals, arcs, and young planets that are observed.

1.6.1 Outlook

ALMA has opened our view into the physical and chemical structure in protoplanetary disks over the past decade and will continue to do so in the future. Observations at high spatial and spectral resolution and sensitivity show that substructures are common in the brightest and most massive disks. One of the leading hypotheses for the cause of these structures are embedded planets but other mechanisms like snowlines, photoevaporation, and instabilities can also be responsible for the observed cavities, rings, and arcs. To distinguish these mechanisms, the gas surface density and thus the temperature needs to be measured across the

disk. Observations of many molecular lines and their subsequent analysis in six dimensions – radial, vertical, azimuthal, and the velocity in those directions – will provide crucial constraints on the origin of disk structures. The potential upgrade of the ALMA receiver bands in 2030 will double their bandwidth, allowing for simultaneous observations of multiple molecular lines (Carpenter et al. 2023).

In addition, observations of gas-phase water and water ice will provide crucial information on the chemical composition of the planet forming material. This will not only shed light on the proposed enhancement of planet formation around the water snowline, it will also provide new insights in the origin of water on Earth and its expected abundance on other forming planets. A combination of detailed studies focusing on one or a few objects together with large surveys are needed to fully understand the chemical environment in which planets are forming. Detailed studies on a single object open the opportunity to observe the weak lines that contain the most exciting information, such as the discovery of new molecules or isotopologues. Thermochemical modelling is a powerful tool to constrain the temperature, density, and chemical structure across the disks radius and height. The combination with kinematic studies characterizing the flow of gas in the disk and potentially onto planets will help to constrain which elements are accreted by young planets. In particular, the trapping of dust and their icy mantles could leave an imprint on the carbon and water abundance and thus habitability of future exo-planets. Surveys of large samples will answer some of the fundamental questions regarding the effect of spectral type and age on the chemical composition of protoplanetary disks.

While ALMA observations probe the outer disk regions, the JWST probes the hot inner disk. The warm gas lines on top of a continuum shaped by ice absorption features and silicate features provides a new window into the relevant processes in disks. The abundance of specific gas-phase molecules can not only be used to infer that the gas emits from inside the snowline of that molecule, but also to put constraints on the dust structure in this disk on scales that ALMA cannot probe (Grant et al. 2023). Additionally, the ice absorption features seen across the continuum in these sources not only reveal what ices are present but also if these ices are pristine or if ice segregation through heating has occurred (Yang et al. 2022; McClure et al. 2023; Sturm et al. 2023b). Finally, comparing JWST observations with those of *Spitzer* can provide a new window into the physical and chemical processes during outbursts (Kóspál et al. 2023), similar to what may have happen for V883 Ori. As JWST only just started observing, there are many new and exciting opportunities to come. With these new and (un)expected results, also the modelling of protoplanetary disks will need to advance to understand the newly probed disk regions.

Chapter 2

Chemically tracing the water snowline in protoplanetary disks with HCO^+

M. Leemker, M. L. R. van 't Hoff, L. Trapman, M. L. van Gelder, M.
R. Hogerheijde, D. A. Ruíz-Rodríguez, and E. F. van Dishoeck

2021 A&A, 646, 3

Abstract

Context. The formation of planets is expected to be enhanced around snowlines in protoplanetary disks, in particular around the water snowline. Moreover, freeze-out of abundant volatile species in disks alters the chemical composition of the planet-forming material. However, the close proximity of the water snowline to the host star combined with the difficulty of observing water from Earth makes a direct detection of the water snowline in protoplanetary disks challenging. HCO^+ is a promising alternative tracer of the water snowline. The destruction of HCO^+ is dominated by gas-phase water, leading to an enhancement in the HCO^+ abundance once water is frozen out.

Aims. Following earlier observed correlations between water and H^{13}CO^+ emission in a protostellar envelope, the aim of this research is to investigate the validity of HCO^+ and the optically thin isotopologue H^{13}CO^+ as tracers of the water snowline in protoplanetary disks and the required sensitivity and resolution to observationally confirm this.

Methods. A typical Herbig Ae disk structure is assumed, and its temperature structure is modelled with the thermochemical code DALI. Two small chemical networks are then used and compared to predict the HCO^+ abundance in the disk: one without water and one including water. Subsequently, the corresponding emission profiles are modelled for the $J = 2 - 1$ transition of H^{13}CO^+ and HCO^+ , which provides the best balance between brightness and the optical depth effects of the continuum emission and is less affected by blending with complex molecules. Models are then compared with archival ALMA data.

Results. The HCO^+ abundance jumps by two orders of magnitude over a radial range of 2 AU outside the water snowline, which in our model is located at 4.5 AU. We find that the emission of H^{13}CO^+ and HCO^+ is ring-shaped due to three effects: destruction of HCO^+ by gas-phase water, continuum optical depth, and molecular excitation effects. Comparing the radial emission profiles for $J = 2 - 1$ convolved with a $0''.05$ beam reveals that the presence of gas-phase water causes an additional drop of only $\sim 13\%$ and 24% in the centre of the disk for H^{13}CO^+ and HCO^+ , respectively. For the much more luminous outbursting source V883 Ori, our models predict that the effects of dust and molecular excitation do not limit HCO^+ as a snowline tracer if the snowline is located at radii larger than ~ 40 AU. Our analysis of recent archival ALMA band 6 observations of the $J = 3 - 2$ transition of HCO^+ is consistent with the water snowline being located around 100 AU, further out than was previously estimated from an intensity break in the continuum emission.

Conclusion. The HCO^+ abundance drops steeply around the water snowline, when water desorbs in the inner disk, but continuum optical depth and molecular excitation effects conceal the drop in HCO^+ emission due to the water snowline. Therefore, locating the water snowline with HCO^+ observations in disks around Herbig Ae stars is very difficult, but it is possible for disks around outbursting stars such as V883 Ori, where the snowline has moved outwards.

2.1 Introduction

High resolution observations of protoplanetary disks show that many of them have rings, gaps, and other substructures (e.g. Andrews et al. 2010; van der Marel et al. 2015; Fedele et al. 2017; Huang et al. 2018; Long et al. 2018; and Andrews 2020 for a review). Different explanations have been proposed for these substructures, such as planets (e.g. Bryden et al. 1999; Zhu et al. 2014; Dong et al. 2018) and snowlines (e.g. Banzatti et al. 2015; Zhang et al. 2015; Okuzumi et al. 2016). A snowline is the midplane radius in a protoplanetary disk where 50% of a volatile is in the gas phase and 50% is frozen out onto the dust grains. These snowlines are related to planet formation because dust properties change around the snowlines of the major volatiles: H_2O , CO , and CO_2 (Pinilla et al. 2017). Even though water ice mantles may not always aid dust coagulation by collisions (Kimura et al. 2020), the sublimation, condensation, and diffusion of gas-phase water enhances the surface density around the water snowline, aiding planet formation and potentially triggering the streaming instability (e.g. Stevenson & Lunine 1988; Drażkowska & Alibert 2017; Schoonenberg & Ormel 2017).

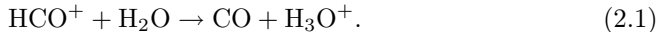
Snowlines do not only influence the formation of planets. They are also key in setting their chemical composition. The sequential freeze-out of the major volatile species changes the bulk chemical composition, often measured as the C/O ratio, of the planet-forming material, with the ice becoming more oxygen-rich than the gas (Öberg et al. 2011; Eistrup et al. 2016, 2018). The water snowline is of particular importance as water is crucial for the development of life.

Knowledge of the water snowline location is thus essential for the understanding of planet formation and composition. Yet observing water snowlines is challenging because their expected location is only a few AU from the host star for T Tauri disks (Harsono et al. 2015) and ~ 10 AU for disks around more luminous Herbig Ae stars. Therefore, observations with very high spatial resolution are necessary. On top of that, observing water snowlines directly from the ground by observing gas-phase water in protoplanetary disks is challenging because of the absorption of water in the Earth's atmosphere. The only detections of water in protoplanetary disks probe either the innermost hot regions of the disk ($\lesssim 5$ AU; e.g. Carr & Najita 2008; Salyk et al. 2008; Mandell et al. 2012) or the cold outer disk with space-based telescopes, analysing multiple water lines (Hogerheijde et al. 2011; Zhang et al. 2013; Blevins et al. 2016; Salinas et al. 2016; Du et al. 2017) or have used both ground-based and space-based telescopes (Banzatti et al. 2017; Salyk et al. 2019). Targeting less abundant isotopologues of water, for example H_2^{18}O , reduces the atmospheric absorption, but detecting these molecules at a significant signal-to-noise ratio greatly increases the required observing time (e.g. Notsu et al. 2019). Space-based telescopes circumvent this problem but for now lack the spatial resolution to resolve the water snowline.

Chemical tracers provide an alternative way of locating snowlines. Some detections of molecules in disks show ring-shaped emission even if the density of the disk is smooth. One example of such a molecule is CN, which is enhanced if a strong UV field is present (e.g. van Zadelhoff et al. 2003; Teague et al. 2016; Cazzoletti et al. 2018). Other examples are molecules that trace snowlines. Chemical

imaging has been used to locate the CO snowline in the disks around TW Hya and HD 163296 using N_2H^+ and DCO^+ (Mathews et al. 2013; Qi et al. 2013, 2015, 2019). Both tracers show ring-shaped emission but detailed chemical modelling is needed to infer the location of the CO snowline from these observations (Aikawa et al. 2015; van 't Hoff et al. 2017; Carney et al. 2018).

Water can be traced chemically using the HCO^+ ion, which is destroyed by gas-phase water (Phillips et al. 1992; Bergin et al. 1998):



Based on this reaction, HCO^+ is expected to be abundant when water is frozen out onto the grains, and HCO^+ is expected to be depleted when water is in the gas phase. This anti-correlation between water and HCO^+ has been verified observationally by the optically thin isotopologue H^{13}CO^+ and an isotopologue of water H_2^{18}O in a protostellar envelope (van 't Hoff et al. 2018a). Due to the high luminosity of young stellar objects at this early stage, the snowline is located further away from the star than in protoplanetary disks (Visser & Bergin 2012; Jørgensen et al. 2013; Vorobyov et al. 2013; Visser et al. 2015; Cieza et al. 2016; Hsieh et al. 2019). Similarly, the higher luminosity of Herbig Ae stars compared to T Tauri stars increases the temperature in the protoplanetary disks around them, which locates the water snowline further out in disks around the former type. Therefore, we focus on protoplanetary disks around Herbig Ae stars in this work.

The aim of this paper is to investigate HCO^+ as a tracer of the water snowline in protoplanetary disks. Compared to protostellar envelopes, the 2D temperature and density structure of disks complicates matters. First, the location of the water snowline in protoplanetary disks around Herbig Ae stars is expected around 10 AU, in contrast to $\gtrsim 100$ AU in protostellar envelopes. Second, the higher column density in disks increases the optical depth of the continuum and line emission. This complicates locating the water snowline as emission from HCO^+ can be absorbed by dust particles, mimicking the effect of depletion due to gas-phase water on the HCO^+ emission. Finally, the HCO^+ emission can also be ring-shaped when the J -level population of the low levels, which can be observed with ALMA, decreases towards the centre of the star due to the increase in temperature and density in the inner disk. This also mimics the effect of gas-phase water on the HCO^+ emission.

The validity of HCO^+ as a tracer of the water snowline in protoplanetary disks is investigated by modelling the physical and chemical structure of a disk around a typical Herbig Ae star with a luminosity of $36 L_\odot$ as described in Section 2.2. The predicted abundance structure of HCO^+ is presented in Section 2.3.1, and the corresponding emission profiles of HCO^+ and H^{13}CO^+ are described in Section 2.3.2 and 2.3.3. Archival ALMA observations of H^{13}CO^+ and HCO^+ in the outbursting source V883 Ori are discussed in Section 2.4. Finally, we conclude in Section 2.5 that it is difficult to use HCO^+ as a tracer of the water snowline in disks around Herbig Ae stars, but that it is possible for outbursting sources such as V883 Ori.

2.2 Protoplanetary disk model

The HCO^+ and H^{13}CO^+ radial emission profiles were modelled in several steps. First, a density structure for a typical disk around a Herbig Ae star was assumed. Second, the gas temperature was calculated using the thermochemical code DALI (Bruderer et al. 2009, 2012; Bruderer 2013). The gas density and gas temperature were then used as input for two chemical models, one without water and one with water, that predict the HCO^+ abundance in the disk. These abundance profiles together with the density and temperature structure of the disk were used to compute the HCO^+ and H^{13}CO^+ emission profiles with DALI.

2.2.1 Disk structure

The density structure of the disk was modelled with the thermochemical code DALI following the approach of Andrews et al. (2011). This approach is based on the self-similar solution for a viscously evolving disk, where the gas surface density of the disk outside the dust sublimation radius follows a power law with an exponential taper (Lynden-Bell & Pringle 1974; Hartmann et al. 1998):

$$\Sigma_{\text{gas}}(R) = \Sigma_c \left(\frac{R}{R_c} \right)^{-\gamma} \exp \left[- \left(\frac{R}{R_c} \right)^{2-\gamma} \right], \quad (2.2)$$

with Σ_c the gas surface density at the characteristic radius R_c , and γ the power law index. A sublimation radius of $R_{\text{subl}} = 0.05$ AU was assumed. Inside this radius, the surface density was set to $7 \times 10^2 \text{ cm}^{-3}$. An overview of all parameters used for the density and temperature structure can be found in Table 2.1.

The gas follows a Gaussian distribution in the vertical direction, where the temperature was calculated explicitly at each location in the disk. The scale height of the gas was set by the flaring index ψ and the characteristic scale height h_c at R_c ,

$$h = h_c \left(\frac{R}{R_c} \right)^\psi. \quad (2.3)$$

The resulting gas density of our model is shown in the top panel of Fig. 2.1.

The dust surface density was modelled with DALI by scaling the gas surface density with the disk-averaged gas-to-dust mass ratio, $\Delta_{\text{gas/dust}}$, which was set to the ISM value of 100. The vertical structure of the dust was modelled using two populations of dust grains following the approach of D'Alessio et al. (2006). Small grains with sizes between 5 nm and 1 μm are well mixed with the gas and therefore both follow the same vertical structure. Large grains with sizes from 5 nm to 1 mm are settled to the disk midplane. This was modelled by reducing the scale height of the large grains with a factor of $\chi < 1$. The fraction of the dust mass in large grains was controlled by f_{ls} and the size distribution of both grain populations was assumed to be proportional to $a^{-3.5}$, with a the size of the grains (MRN distribution, Mathis et al. 1977).

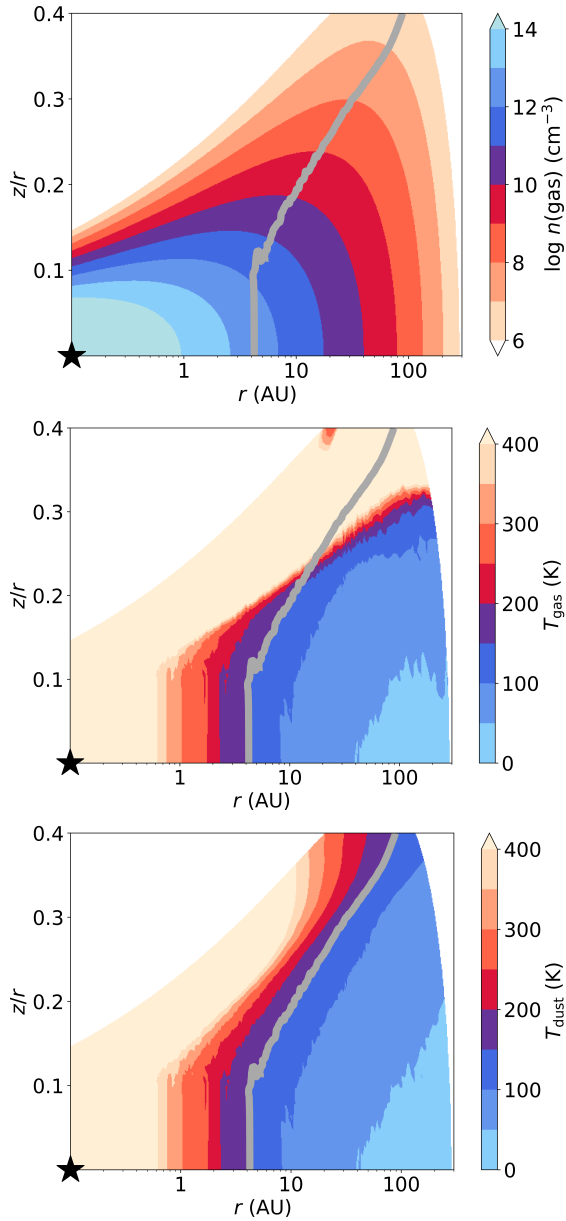


Figure 2.1: Assumed gas density (top) and computed gas and dust temperature (middle and bottom panels) in the DALI model for a typical disk around a Herbig Ae star with a luminosity of $36 L_{\odot}$. Only the region where $n(\text{gas}) > 10^6 \text{ cm}^{-3}$ is shown. The position of the star is indicated with the symbol of a black star and the $T_{\text{dust}} = 150$ K line, approximating the water snow surface, is indicated with the solid grey line.

Table 2.1: DALI model parameters for the disk around a typical Herbig Ae star.

Model parameter	Value
<i>Physical structure</i>	
R_{subl}	0.05 AU
R_{c}	50 AU
Σ_{c}	5.8 g cm^{-2}
M_{disk}	$0.01 M_{\odot}$
γ	1
h_{c}	0.1
ψ	0.25
<i>Dust properties</i>	
χ	0.2
f_{is}	0.85
$\Delta_{\text{gas/dust}}$	100
<i>Stellar spectrum</i> ⁽¹⁾	
Type	Herbig
L_{\star}	$36 L_{\odot}$
L_{X}	$8(28) \text{ erg s}^{-1}$
T_{eff}	$1(4) \text{ K}$
T_{X}	$7(7) \text{ K}$
$\zeta_{\text{c.r.}}$	$5(-17) \text{ s}^{-1}$
<i>Stellar properties</i>	
M_{\star}	$2.3 M_{\odot}$
<i>Observational geometry</i>	
i	38°
d	100 pc

Notes. $a(b)$ represents $a \times 10^b$. ⁽¹⁾ Spectrum of HD 100546 (Kama et al. 2016), which is well approximated by a 10^4 K black body spectrum.

The gas temperature needed to be computed separately as the abundances of the molecules that act as coolants of the gas in the disk affected the gas temperature, which in turn affected the chemistry. Therefore, DALI solves for the gas temperature by iterating over the chemistry and heating by the photoelectric effect and the cooling by molecules in the gas. The dust temperature was computed using Monte Carlo continuum radiative transfer. The gas and dust temperature calculated by DALI are shown in the middle and bottom panel of Fig. 2.1. The gas temperature exceeds the dust temperature in the surface layers only, whereas the gas and dust temperatures are equal in deeper layers of the disk.

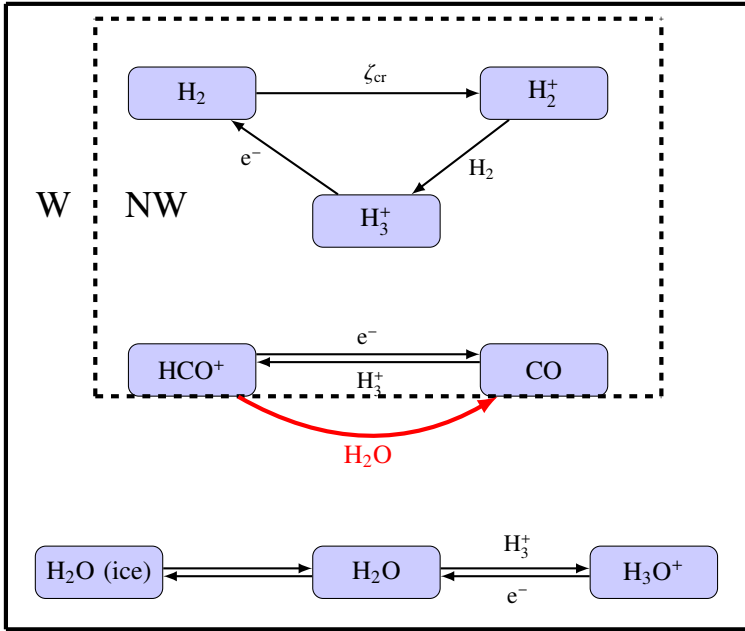
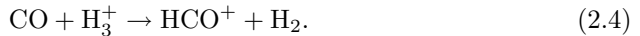


Figure 2.2: Schematic view of chemical networks NW (no water) and W (water) used to predict the abundance of HCO^+ . The first network, network NW, only includes the reactions enclosed in the dashed box. The second network, network W, includes all reactions present in the figure. The destruction of HCO^+ by gas-phase water is indicated with the thick red arrow.

2.2.2 Chemical models

The HCO^+ abundance with respect to the total number of hydrogen atoms in the disk was modelled with a small chemical network, which was solved time-dependently up to 1 Myr with the python function `odeint`¹. This allowed us to more easily study the effect of different parameters than with a computationally more expensive full chemical model. The HCO^+ abundance in protoplanetary disks is mainly controlled by three reactions. The main formation route of HCO^+ involves gas-phase CO:



Here, H_3^+ is produced by cosmic ray ionisation of molecular hydrogen at a rate of $\zeta_{\text{c.r.}}$. On the other hand, HCO^+ is destroyed by gas-phase water (Eq. 2.1) and by dissociative recombination with an electron:



¹The `odeint` function is part of the Scipy package in python and uses the LSODA routine from the ODEPACK library in FORTRAN.

Therefore, a jump in the HCO^+ abundance around the water snowline is expected if electrons are not the dominant destruction mechanism of HCO^+ .

To investigate the relationship between HCO^+ and H_2O , two small chemical networks were used. The first network, network *no water* (NW), is shown in the dashed box in Fig. 2.2. This network includes three reactions to model the ionisation in the disk (reactions $\zeta_{\text{c.r.}}$, k_2 , and k_3 in Table 2.2), and two reactions to model the HCO^+ abundance in the absence of gas-phase water (reactions k_4 and k_{e^-} (Eq. 2.4 and 2.5) in Table 2.2). As reaction $k_{\text{H}_2\text{O}}$ (Eq. 2.1) is not included in this network, HCO^+ is not expected to trace the water snowline in network NW. Therefore, this network serves as a baseline to quantify the effect of the gas-phase water on the HCO^+ abundance. The second network, network *water* (W), is shown in the solid box in Fig. 2.2 and contains all reactions present in Table 2.2. Network W includes those in network NW together with reactions to model the effect of water on the HCO^+ abundance. The most important reaction for our study is indicated in red in Fig. 2.2 and is the destruction of HCO^+ by gas-phase water (reaction $k_{\text{H}_2\text{O}}$ or Eq. 2.1). Therefore, HCO^+ is expected to trace the water snowline in network W. The other reactions present in network W include the freeze-out and desorption of water (reactions k_f and k_d), and the formation and destruction of gas-phase water from and to H_3O^+ (reactions k_7 and k_8). The equations for the freeze-out and desorption rates of water can be found in Appendix 2.A.

Initially, the abundance of all gas- and ice-phase species were set to 0 except for the abundance of gas-phase CO, which was set to 10^{-4} both in network NW and W, and the abundance of gas-phase water in network W, which was set to 3.8×10^{-7} , appropriate for a dark cold cloud (McElroy et al. 2013), see also Table 2.B.1. The rate coefficient for the freeze-out of water depends on multiple parameters, including the number density and size of the grains. Therefore, we assumed in chemical network NW and W a typical grain number density of $10^{-12} \times n(\text{H}_2)$ and a grain size of $0.1 \mu\text{m}$, which set the surface area available for chemistry on grains. Assuming a single grains size for the chemistry is an approximation, but the effect of grain growth in disks, which decreases this area, is cancelled by the dust settling in disks, which increases this area as there is more dust available for chemistry in the midplane (Eistrup et al. 2016). Finally, the H^{13}CO^+ abundance was taken to be a factor of 70 smaller than the abundance of HCO^+ , corresponding to the typical $^{12}\text{C}/^{13}\text{C}$ isotope ratio (Milam et al. 2005).

2.2.3 Radiative transfer

Predictions for multiple transitions of HCO^+ and H^{13}CO^+ were made using the ray tracer in DALI, where the outputs of the chemical networks discussed in Section 2.2.2 were used to set the abundance, and both line and continuum optical depth are included. The line radiative transfer did not assume LTE. Instead, the excitation was calculated explicitly, where we used the collisional rate coefficients in the LAMDA database (Botschwina et al. 1993; Flower 1999; Schöier et al. 2005).

Furthermore, the disk was assumed to be located at a distance of 100 pc and the inclination was taken to be 38° . Changing the inclination did not significantly

Table 2.2: Reaction coefficients of the reactions used in this paper. The last two columns indicate in which chemical networks the reactions are used.

reaction	α	β	γ	$k(100\text{ K})$	$k(150\text{ K})$	units	ref.	NW	W
$\zeta_{\text{c.r.}}$	$1(-17)$	0	0	$1(-17)$	$1(-17)$	s^{-1}		✓	✓
k_2	$2.1(-9)$	0	0	$2.1(-9)$	$2.1(-9)$	$\text{cm}^3\text{ s}^{-1}$	(a)	✓	✓
k_3	$2.3(-8)$	-0.5	0	$4.1(-8)$	$3.4(-8)$	$\text{cm}^3\text{ s}^{-1}$	(b)	✓	✓
k_4	$1.4(-9)$	-0.1	-3.4	$1.6(-9)$	$1.5(-9)$	$\text{cm}^3\text{ s}^{-1}$	(c)	✓	✓
k_{e^-}	$2.4(-7)$	-0.7	0	$5.1(-7)$	$3.9(-7)$	$\text{cm}^3\text{ s}^{-1}$	(d)	✓	✓
$k_{\text{H}_2\text{O}}$	$2.5(-9)$	-0.5	0	$4.3(-9)$	$3.5(-9)$	$\text{cm}^3\text{ s}^{-1}$	(e)	✓	✓
k_7	$7.1(-8)$	-0.5	0	$1.2(-7)$	$1.0(-7)$	$\text{cm}^3\text{ s}^{-1}$	(f)	✓	✓
k_8	$5.9(-9)$	-0.5	0	$1.0(-8)$	$8.3(-9)$	$\text{cm}^3\text{ s}^{-1}$	(g, h)	✓	✓
k_f	$1.2(-5)n(\text{H}_2)$	0.5	0	$6.7(-6)n(\text{H}_2)$	$8.3(-6)n(\text{H}_2)$	s^{-1}	(i)	✓	✓
k_d	$2.8(12)$	0	5.8(3)	$10(12)\text{cm}^{-3}$	$10(12)\text{cm}^{-3}$	s^{-1}	(i)	✓	✓

Notes. $a(b)$ represents $a \times 10^b$. NW is the chemical network without water, whereas W includes water. All reactions are given in the form $k = \alpha (T_{\text{gas}}/300\text{K})^\beta \exp(-\gamma/T_{\text{gas}})$, where the values of α , β , and γ for k_2 , k_3 , k_4 , k_{e^-} , k_7 , and k_8 are taken from the rate12 UMIST database (McElroy et al. 2013) and k_d uses T_{dust} instead of T_{gas} . References: (a) Theard & Huntress (1974), (b) McCall et al. (2004), (c) Klippenstein et al. (2010), (d) Mitchell (1990), (e) Adams et al. (1978), (f) Novotný et al. (2010), (g) Kim et al. (1974), (h) Anicich et al. (1975), and (i) Appendix 2.A and references therein.

change our results. The radial emission profiles were taken to be along the semi-major axis of the disk. The focus in the paper is on the $J = 2 - 1$ transition at 178.375 GHz and 173.507 GHz for HCO^+ and H^{13}CO^+ , respectively, because this transition provided the best balance between the brightness of the line and the effects of the continuum optical depth. Moreover, the higher transitions could be blended with emission from complex organic molecules. Predictions for the weaker $J = 1 - 0$ transition, as well as the brighter $J = 3 - 2$ and $J = 4 - 3$ transitions, that are more affected by the optical depth of the continuum emission and emission from complex organic molecules, can be found in Appendix 2.C. To mimic high resolution ALMA observations, the emission was convolved with a $0''.05$ beam, unless denoted otherwise.

2.3 Modelling results

2.3.1 Chemistry

The predicted abundances of HCO^+ by chemical networks NW and W are presented in Fig. 2.3. The water snow surface in network W is computed as the surface where 50% of the total water abundance is in the gas-phase and 50% is frozen-out onto the grains, and is indicated by the black line. In this model, the water snowline, the midplane location where water freezes-out, is located at 4.5 AU. The two networks predict very similar HCO^+ abundances outside and below the water snow surface. This is due to the fact that water is frozen out outside the water snow surface in network W, hence there is very little gas-phase water available for the destruction of HCO^+ . In network NW, the HCO^+ abundance drops inside the snowline, and is in general at least two orders of magnitude lower than in network NW. Up to 2 AU outside the water snowline HCO^+ is still efficiently destroyed by the small amount of water that is present in the gas-phase. Similar effects were found for N_2H^+ and CO (Aikawa et al. 2015; van 't Hoff et al. 2017). Therefore, HCO^+ is efficiently destroyed by gas-phase water, and is thus a good chemical tracer of the water snowline.

The morphology of the HCO^+ distribution predicted by chemical network W is similar to the morphology predicted by full chemical networks (Walsh et al. 2012, 2013; Agúndez et al. 2018). Chemical network W agrees with the full chemical networks quantitatively inside the water snowline, where all studies predict a low HCO^+ abundance of $\lesssim 10^{-14}$. Moreover, the full networks and network W all show a jump of at least one order of magnitude in the HCO^+ abundance over a radial range of 5 AU outside the water snowline. In addition, these models predict a layer starting at $z/r \sim 0.1$ where the HCO^+ abundance reaches a high abundance of $10^{-6} - 10^{-7}$ (Walsh et al. 2012, 2013, and Agúndez et al. 2018). Yet, this layer is not expected to contribute much to the column density and emission of HCO^+ because the gas densities are low in this layer of the disk. The midplane abundances at 10 AU are $\sim 10^{-12}$ in the full networks and 10^{-11} in network W, though the gradient in the HCO^+ abundance is very steep between the water snowline at 4.5 AU and a radius of 10 AU in network W complicating comparison.

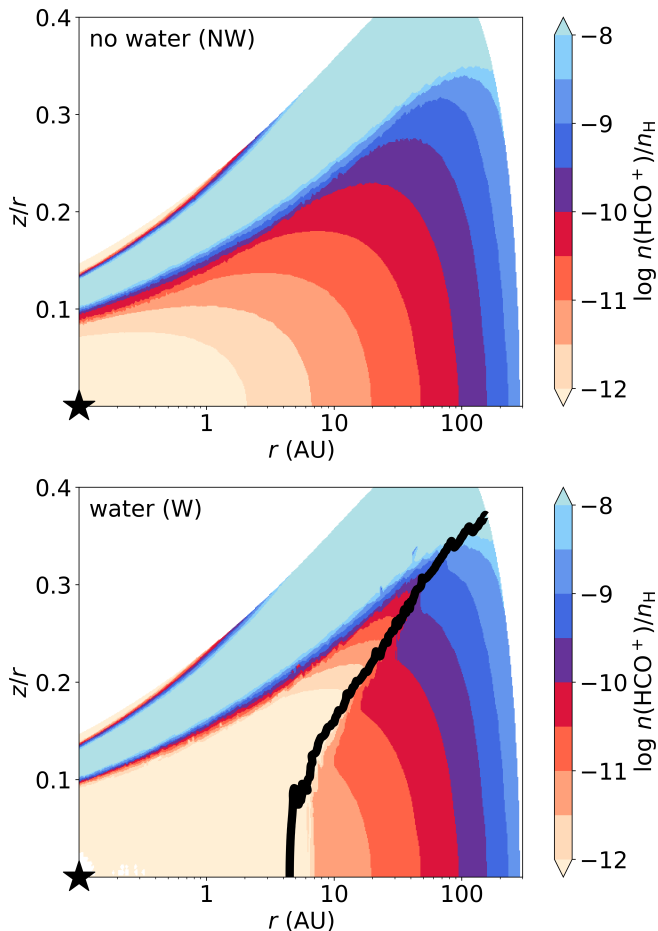


Figure 2.3: HCO^+ abundance calculated using chemical network NW (top) and network W (bottom). The water snow surface is marked with the black line in the bottom panel. The position of the star is indicated with the symbol of a black star.

An HCO^+ abundance of 10^{-12} is reached at 7 AU. The HCO^+ abundance at 100 AU lies within the range of HCO^+ abundances predicted by the full chemical models. Our small network is thus suited to study HCO^+ as a tracer of the water snowline.

2.3.1.1 Water versus electrons

HCO^+ only acts as a tracer of the water snowline if the destruction of HCO^+ by electrons is not dominant over the destruction by gas-phase water. The dissociative recombination of HCO^+ with an electron is included in both chemical networks. The rates of the reactions in Eq. 2.1 and Eq. 2.5, $R_{\text{H}_2\text{O}}$ and R_{e^-} , respectively, are

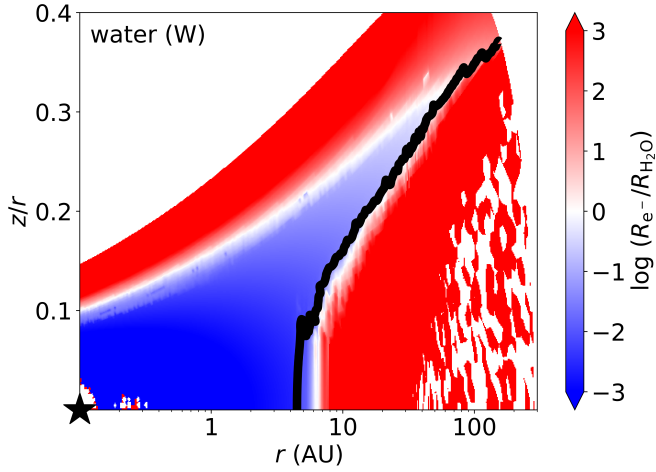


Figure 2.4: Relative reaction rates of HCO^+ destruction by electrons (R_{e^-}) and water ($R_{\text{H}_2\text{O}}$). Gas-phase water is the dominant destruction mechanism of HCO^+ in the blue regions and electrons are the dominant destruction mechanism in the red regions. The water snow surface is indicated by the black line.

given by:

$$R_{\text{H}_2\text{O}} = k_{\text{H}_2\text{O}} n(\text{HCO}^+) n(\text{H}_2\text{O}) \quad \text{and} \quad (2.6)$$

$$R_{e^-} = k_{e^-} n(\text{HCO}^+) n(e^-). \quad (2.7)$$

Using Table 2.2, the ratio of these reaction rates is given by:

$$\frac{R_{e^-}}{R_{\text{H}_2\text{O}}} = 96 \left(\frac{T_{\text{gas}}}{300\text{K}} \right)^{-0.19} \frac{n(e^-)}{n(\text{H}_2\text{O})}. \quad (2.8)$$

Therefore, gas-phase water is the dominant destruction mechanism of HCO^+ if the number density of gas-phase water is about two orders of magnitude larger than the number density of electrons.

Fig. 2.4 shows this ratio for chemical network W. The region where electrons are the dominant destruction mechanism ($R_{e^-} > R_{\text{H}_2\text{O}}$) is indicated in red and the region where water is dominant ($R_{e^-} < R_{\text{H}_2\text{O}}$) is indicated in blue. The first region exists mostly outside the water snow surface as water is frozen out. The latter region exists mostly inside and above the water snow surface because there is plenty of water to destroy HCO^+ in these regions. Therefore, HCO^+ is a good chemical tracer of the water snowline even though electrons are its dominant destruction mechanism in most of the disk.

2.3.1.2 Effect of the CO , H_2O abundance, and cosmic ray ionisation rate on the HCO^+ abundance

In this section we investigate the choice of initial conditions for chemical network W listed in Table 2.B.1. The HCO^+ abundance outside the water snow

surface in chemical network W can be approximated analytically (for details see Appendix 2.B.1):

$$x(\text{HCO}^+) = \sqrt{\frac{\zeta_{\text{c.r.}}}{k_{\text{e-}} n(\text{H}_2)}}. \quad (2.9)$$

Based on this equation, it is expected that the abundance of HCO^+ scales as the square root of the cosmic ray ionisation rate in the disk region outside the water snowline. This analytical prediction is consistent with the predictions made by the numerical solution to chemical network W (top left panel in Fig. 2.B.1), where the HCO^+ column density decreases by one order of magnitude if the cosmic ray ionisation rate decreases by two orders of magnitude.

Furthermore, the HCO^+ abundance is expected to be independent of the initial CO and H_2O abundance outside the water snow surface based on the analytical approximation. This is in line with the predictions by the numerical solution to chemical network W (see HCO^+ column density in Fig. 2.B.1). The only major difference between the analytical approximation and the numerical solution occurs inside the water snowline. If the initial abundance of gas-phase water increases up to $\sim 5 \times 10^{-5}$, as expected for water ice in cold clouds, the column density of HCO^+ inside the water snowline decreases. This is because the higher abundance of gas-phase water destroys more HCO^+ . There is no significant effect on the HCO^+ column density outside the water snowline as all water is frozen out in that region of the disk. In summary, HCO^+ shows a steep jump in its column density around the water snowline for all initial conditions discussed in this section. Therefore, the results in the following sections do not depend critically on the choice of initial conditions. Further details on the initial conditions can be found in Appendix 2.B.2.

2.3.2 HCO^+ and H^{13}CO^+ emission

Observations of gas in disks do not directly trace the local abundances, only the line emission that is closely related to the column densities if the line emission is optically thin. The column densities of HCO^+ and the predicted radial emission profiles of HCO^+ and H^{13}CO^+ in network NW and W are shown in Fig. 2.5. Similar to the abundance plots of HCO^+ , the total HCO^+ column density jumps by a factor of ~ 230 over a radial range of 3 AU outside the water snowline in network W (solid blue line, top panel). Therefore, the HCO^+ column density shows a clear dependence on the presence of gas-phase water, and the high HCO^+ abundance in the surface layers of the disk does not contribute much to the column density.

On the other hand, the shapes of the radial emission profiles of the HCO^+ $J = 2 - 1$ transition are very similar for networks NW and W, and the profiles peak at the same radius outside the water snowline (solid lines, middle panel). This is different from the HCO^+ column densities, where only network W predicts the HCO^+ column density to peak outside the water snowline. The drop in the column density around the water snowline translates into a relative maximum difference

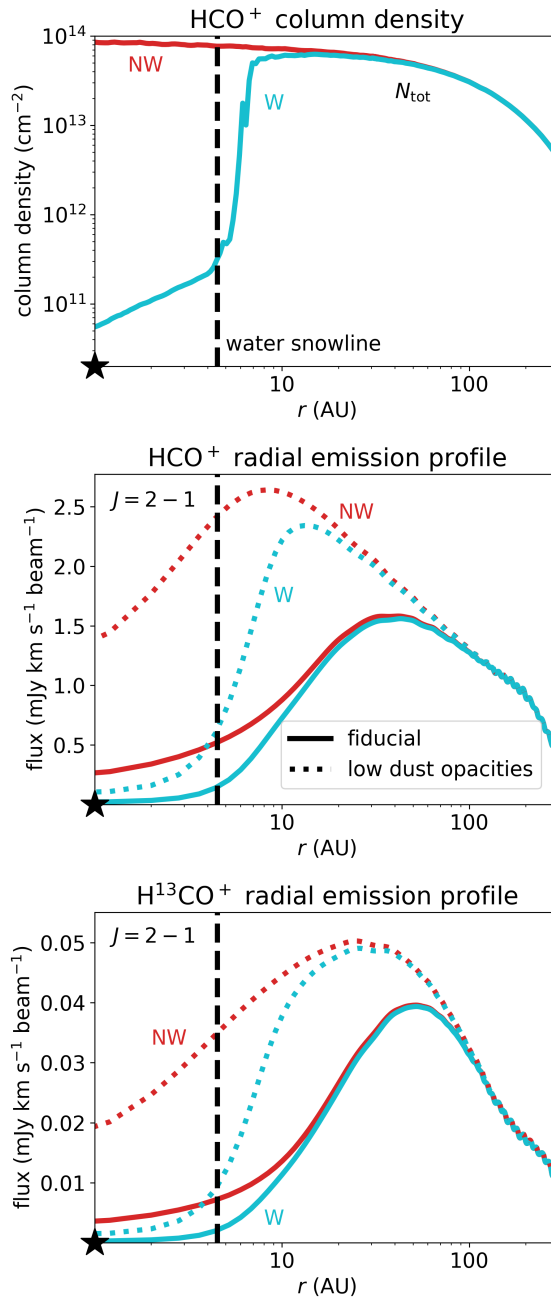


Figure 2.5: HCO⁺ column density and emission in a disk around a typical Herbig Ae star. Top panel: Total HCO⁺ column densities. Middle and bottom panels: HCO⁺ $J = 2 - 1$ radial emission profiles and H¹³CO⁺ $J = 2 - 1$ radial emission profiles along the major axis predicted for chemical network NW (red) and chemical network W (light blue). The dotted lines refer to a model with very low dust opacities to lower the effects of continuum optical depth (see Section 2.3.2.1). The water snowline is indicated with the dashed black line. The radial emission profiles are convolved with a 0^{''}.05 beam.

of only 24% between the radial emission profiles of the $J = 2 - 1$ transition of HCO^+ . This maximum relative difference is defined as the maximum difference between the flux predicted by network NW and W compared to the maximum flux predicted by network W, and is typically located at the water snowline.

HCO^+ is more abundant than H^{13}CO^+ , hence H^{13}CO^+ emission is expected to be optically thin, whereas the HCO^+ emission is optically thick. To test if this affects the ability to trace the water snowline, we predict emission from the less abundant isotopologue H^{13}CO^+ . The radial emission profiles of H^{13}CO^+ for both chemical networks are shown in the bottom panel of Fig. 2.5. Qualitatively the profiles are similar to the predicted emission for HCO^+ . Though the expected flux is about 39 times lower for H^{13}CO^+ than for HCO^+ . This difference in flux is less than a factor of 70, which indicates that the HCO^+ emission is indeed at least partially optically thick. The relative maximum difference between chemical network NW and W is 13% for H^{13}CO^+ , which is almost half of the corresponding number for HCO^+ . So the effect of the water snowline is also seen in the emission of the optically thin H^{13}CO^+ , but even less prominently than in HCO^+ . This is because H^{13}CO^+ emits from a lower layer in the disk due to its lower optical depth. Therefore, more dust is present above the layer where H^{13}CO^+ emits, hence the effect of dust is larger for H^{13}CO^+ than for HCO^+ .

These models show very similar radial emission profiles predicted for network NW and W with only a small difference in flux. Both networks predict ring shaped emission, regardless of the presence of the water snowline. This decrease in line flux towards the centre of the disk can have different origins. The first one is a decrease in the abundance of the observed molecule, discussed in the previous section, which is the effect we aim to observe. However, the optical depth of the continuum emission and molecular excitation effects can change the emission as well, potentially obscuring the effect we aim to trace.

2.3.2.1 Continuum optical depth

The continuum affects the line intensity when the optical depth of the continuum emission is larger than the optical depth of the line or when both are optically thick (Isella et al. 2016). To investigate the effect of the continuum emission, the $J = 2 - 1$ transition of HCO^+ and H^{13}CO^+ was ray traced in a disk model where the dust opacities (dust mass absorption coefficients κ_ν) were divided by a factor of 10^{10} , to cancel the effect of dust on the HCO^+ emission compared to the typical Herbig Ae disk model. The results are shown as the dotted lines in Fig. 2.5. Comparing these radial emission profiles with the fiducial model shows that the effect of dust is small for network W in the inner ~ 5 AU (solid versus dotted blue lines) even though the dust in the typical Herbig Ae disk model is optically thick out to ~ 14 AU (see the orange line in Fig. 2.6). The reason for this is that the HCO^+ abundance is low in the inner disk for network W. Therefore, little emission is expected, hence there is also little emission that can be affected by the dust.

However, the dust can mimic the effect of HCO^+ destruction by gas-phase water, which greatly complicates matters. That the effect of the dust is significant,

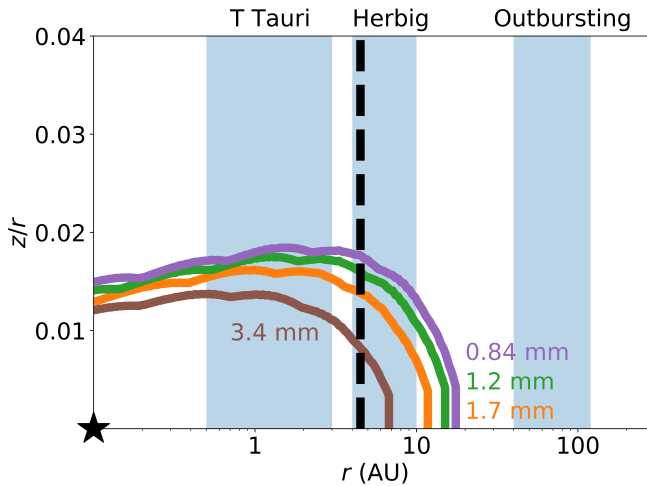


Figure 2.6: $\tau_{\text{dust}} = 1$ surface at the wavelength of the HCO^+ $J = 1 - 0$ transition (3.4 mm, brown), $J = 2 - 1$ (1.7 mm, orange), $J = 3 - 2$ (1.2 mm, green), and $J = 4 - 3$ (0.84 mm, purple). The radial range where the water snowline is expected for various types of sources is highlighted with the blue background. The water snowline in the model for a typical Herbig Ae disk is indicated with the dashed black line.

can be seen when the radial emission profiles predicted by network NW in the fiducial disk model and in the model with very low dust opacities (solid versus dotted red lines) are compared. This shows that the dust optical depth is largely responsible for the drop in emission in the centre in network NW and for the fact that the radial emission profiles for network NW and W look very similar in the fiducial disk model. Therefore, to locate the water snowline using HCO^+ , a disk with a high gas-to-dust mass ratio would be most suitable. However, recent work by Kama et al. (2020) has shown that disks with high gas-to-dust mass ratios around Herbig Ae stars are rare. Another option is to target HCO^+ in even warmer sources than Herbig Ae stars. Fig. 2.6 shows that in more luminous sources, such as outbursting Herbig sources, the snowline is expected to shift to radii where the dust is optically thin at the wavelengths of the $J = 1 - 0$ to $J = 4 - 3$ transitions of HCO^+ . We note, however, that the $\tau_{\text{dust}} = 1$ surfaces not only depend on the frequency but also on the mass of the disk. Nonetheless, typical disk masses are not expected to be more than an order of magnitude higher as that would make them gravitationally unstable (Booth et al. 2019; Booth & Ilee 2020; Kama et al. 2020).

2.3.2.2 Molecular excitation

Decreasing the dust opacities by a factor of 10^{10} cannot fully explain the unexpected ring-shaped emission found by network NW. A second effect that contributes to the decrease in flux in the centre is the temperature dependence of the J -level populations of HCO^+ . The column densities and midplane populations of

several J -levels of HCO^+ in chemical network NW are shown in Fig. 2.7. The column density of the $J = 2$ level of HCO^+ in chemical network NW peaks at a radius of ~ 30 AU, while the total HCO^+ column density, N_{tot} , peaks on-source (red line in top panel of Fig. 2.5).

The radius where the column density of the $J = 2$ level peaks roughly coincides with the radius where the emission of the $J = 2 - 1$ transition of HCO^+ associated with network NW with low dust opacities starts to drop. Therefore, both the optical depth of the continuum emission, as well as the temperature dependence of the J -level population contribute to the drop in emission seen in the centre.

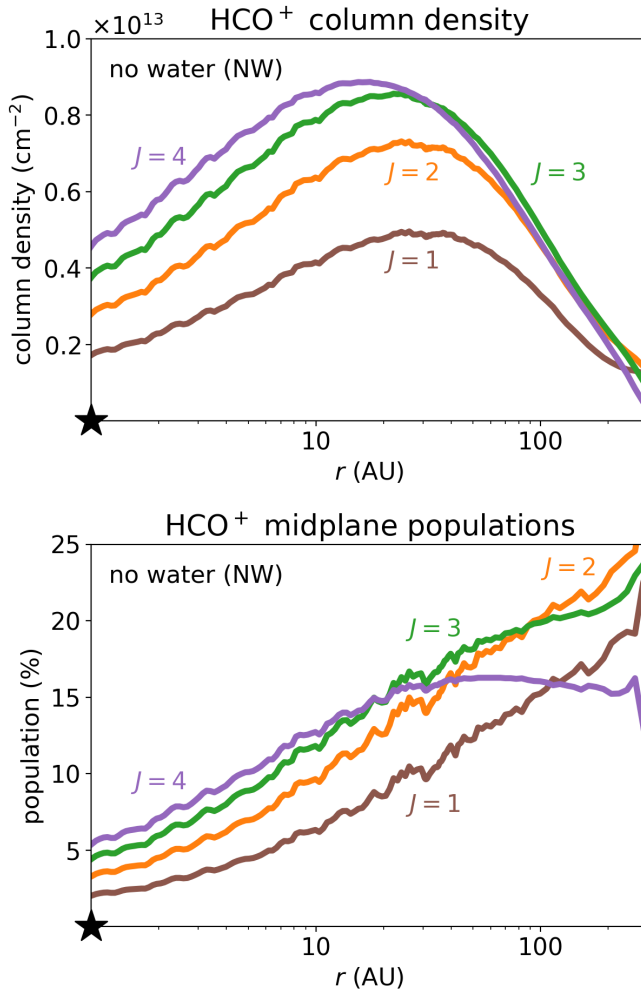


Figure 2.7: HCO^+ column density (top) and midplane populations (bottom) for the $J = 1$ (brown), $J = 2$ (orange), $J = 3$ (green), and $J = 4$ (purple) levels as a function of radius for chemical network NW in the typical Herbig disk model.

2.3.2.3 Chemistry

Finally, there could also be a chemical effect in network NW as the midplane abundance of HCO^+ decreases towards the centre of the disk. Yet, the total column density of HCO^+ keeps increasing up to a radius of 0.07 AU, which is too small to explain the decrease in flux out to ~ 50 AU seen in the radial emission profile associated with network NW in the fiducial model or to $\sim 10\text{-}25$ AU in the model with the low dust opacities. Still, the drop in the emission associated with network W is for a small part due to a decrease in the total HCO^+ column density.

2.3.2.4 What causes HCO^+ rings?

In summary, all three of the above discussed effects contribute to the decrease in HCO^+ flux in the inner regions of the disk model. Observing different transitions of HCO^+ and H^{13}CO^+ will give a different balance of these effects. Fig. 2.7 shows that the higher J -levels are more populated in the inner disk because the inner disk is too warm and dense to highly populate the $J = 2$ level of HCO^+ . However, the emitting frequency of HCO^+ increases as higher transitions are observed, so also the continuum optical depth increases.

Therefore, it is difficult, though crucial, to disentangle the effects of the water snowline and of the population of HCO^+ , and the optical depth of the continuum emission. The effect of the continuum optical depth can be quantified by observing another molecule that emits from the same region as HCO^+ or H^{13}CO^+ but does not decrease in column density towards the star, such as a CO isotopologue. The excitation and column density of HCO^+ need to be inferred from detailed modelling. In conclusion, the results in this section show that even though the HCO^+ abundance changes by at least two orders of magnitude around the water snow surface, it is observationally complicated to verify.

2.3.3 Line profiles

The discussion above has shown that locating the water snowline using the HCO^+ radial emission profile is difficult. The velocity resolved line profile may provide an alternative method as the removal of HCO^+ in the inner disk is expected to remove flux at the highest Keplerian velocities. Therefore, the line profile predicted by chemical network W is expected to be narrower than the line profile predicted by network NW.

The line profiles predicted by the two chemical networks for the $J = 2 - 1$ transition of HCO^+ and H^{13}CO^+ are shown in left column of Fig. 2.8. To show the difference between the models we subtracted the spectrum associated with network W from the spectrum associated with network NW. The result is shown in the right column of Fig. 2.8. This column shows that even though the line profiles look almost identical in the left column, there is an additional bump in the difference between them in the line wings (indicated with the black arrows). However, this difference is only 1.75 mJy for HCO^+ and 28 μJy for H^{13}CO^+ , that is, 0.6% and 0.3% of emission, which cannot be detected with a reasonable signal-to-noise ratio with current submillimetre observations. Moreover, detailed

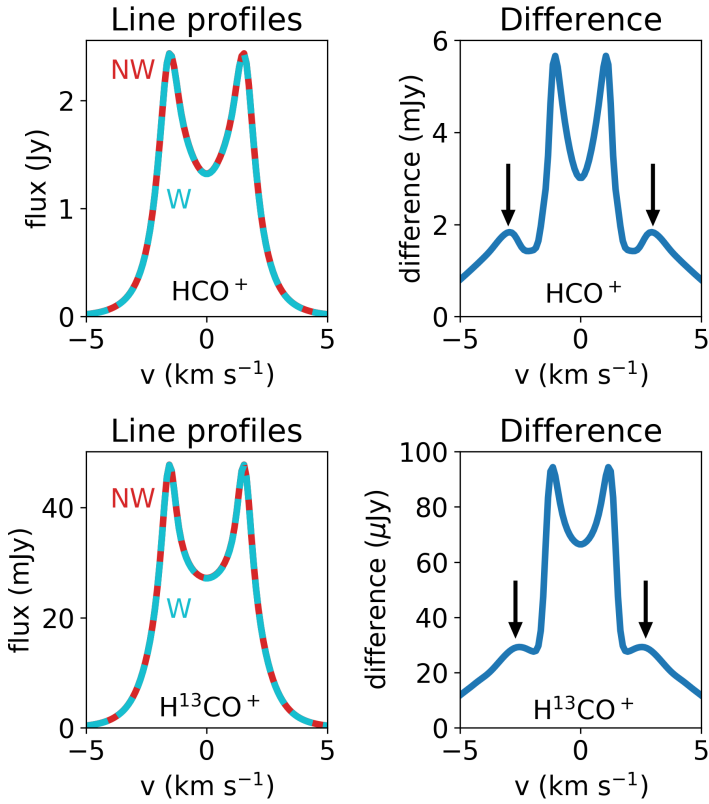


Figure 2.8: Predicted HCO^+ and H^{13}CO^+ line profiles in a typical Herbig Ae disk. Left panels: Line profile for the $J = 2 - 1$ transition of HCO^+ (top) and H^{13}CO^+ (bottom) for chemical network NW (red) and W (light blue). Right panels: Difference between the line profiles in the left column. The black arrows indicate where the effect of the water snowline is expected. We note the differences in the vertical axes.

comparison with the line profile associated with a molecule that does not show a decrease in the column density in the inner disk would be needed as only the flux associated with network W would be observed, and not the flux associated with network NW. Hence, it is very difficult to use the line profiles to locate the water snowline in disks around Herbig Ae stars.

2.4 Comparison with observations

The best targets to observe the water snowline using HCO^+ are warm disks because these disks have a water snowline at a large enough radius for ALMA to resolve. In addition, disks without deep gaps in the gas and dust surface density around

the expected location of the snowline are preferred, as these gaps complicate the interpretation of the HCO^+ emission.

One of the most promising targets to locate the water snowline in a disk is the young outbursting star V883 Ori, with a current luminosity of $\sim 218 L_{\odot}$ (Furlan et al. 2016). During the outburst, the luminosity is greatly increased, which heats the disk, shifting the water snowline outwards compared to regular T Tauri and even Herbig Ae disks. This not only allows for observations with a larger beam, it also mitigates the effects of the dust as the optical depth of the continuum emission decreases with radius. Previous observations of V883 Ori have inferred the location of the water snowline at 42 AU based on a change in the dust emission (Cieza et al. 2016). An extended hot inner disk region is consistent with the detection of many complex organic molecules (Lee et al. 2019). However, an abrupt change in the continuum optical depth or the spectral index are not necessarily due to a snowline, as shown for the cases of CO_2 , CO , and N_2 (Huang et al. 2018; Long et al. 2018; van Terwisga et al. 2018). Methanol observations suggest that the water snowline may be located at a much larger radius of ~ 100 AU, if the methanol observations are optically thin and most of its emission originates from inside the water snowline (van 't Hoff et al. 2018b). Observations of HCO^+ have the potential to resolve this discrepancy.

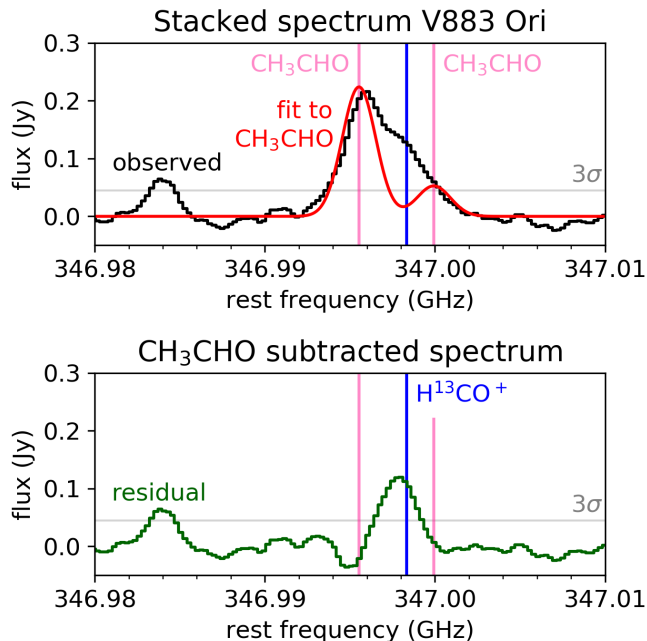


Figure 2.9: Observed and modelled spectrum of V883 Ori. Top panel: Observed and stacked spectrum of V883 Ori (black) and a fit of the CH_3CHO emission (red). Bottom panel: Spectrum where the CH_3CHO emission is subtracted. The H^{13}CO^+ $J = 4 - 3$ emission line (vertical dark blue line) is blended with the CH_3CHO lines (vertical pink lines). The 3σ noise level is indicated with the horizontal grey line.

2.4.1 H¹³CO⁺ observations

A promising dataset to locate the water snowline in V883 Ori is the band 7 observation by Lee et al. (2019) (project code: 2017.1.01066.T, PI: Jeong-Eun Lee), which contains the H¹³CO⁺ $J = 4 - 3$ line. To date, these observations are the only H¹³CO⁺ observations in a protoplanetary disk, to our knowledge, at sufficient spatial and spectral resolution and with enough sensitivity to potentially resolve the water snowline. The synthesised beam of these observations is 0''.2 (40 AU radius, 80 AU diameter at a distance of ~ 400 pc; Kounkel et al. 2017), and the spectral resolution is 0.25 km s⁻¹. The continuum is created using all line-free channels, which are carefully selected to exclude any line emission. The line data are continuum subtracted using these continuum solutions. Using the CASA 5.1.1 *tclean* task with a Briggs weighting of 0.5, line images are made with a mask of about 2'' in diameter centred on the peak of the continuum.

Following the approach of Lee et al. (2019), the line observations are velocity-stacked using a stellar mass, $M_{\star} = 1.3 M_{\odot}$, an inclination of 38°, and a position angle of 32° (Cieza et al. 2016). This technique reduces line blending because it makes use of the Keplerian velocity of the disk to calculate the Doppler shift of the emission in each pixel (Yen et al. 2016, 2018). This Doppler shift is then used to shift the spectrum of each pixel to the velocity of the star, before adding the spectra of all pixels. The noise level of ~ 15 mJy per spectral bin is determined using an empty region in the stacked image.

The resulting spectrum of the inner 0''.6 is shown as the black line in the top panel of Fig. 2.9. The rest frequency of the H¹³CO⁺ $J = 4 - 3$ transition lies between the rest frequencies of the 18_{7,12} - 17_{7,11}, E transition of acetaldehyde (CH₃CHO) ($v = 0$) at 346.9955 GHz and the two superimposed 18_{7,11} - 17_{7,10}, E and 18_{7,12} - 17_{7,11}, E transitions of CH₃CHO ($v_{\text{T}} = 2$) at 346.99991 GHz and 346.99994 GHz, respectively (Jet Propulsion Laboratory (JPL) molecular database; Pickett et al. 1998). In between these acetaldehyde transitions, a clear shoulder of emission is visible due to the $J = 4 - 3$ transition of H¹³CO⁺. To quantify this excess emission, two Gaussian profiles are fitted with `curve_fit`² to model the acetaldehyde emission. To reduce the number of free parameters in the fit, the line frequencies are fixed to their respective rest frequencies listed above and the widths of the lines are fixed to 2 km s⁻¹ following Lee et al. (2019). In addition, emission within 1 km s⁻¹ from the rest frequency of the $J = 4 - 3$ transition of H¹³CO⁺ is excluded from the fit. The result is shown as the red line in the top panel of Fig. 2.9. Subtracting this fit to the acetaldehyde emission from the observed spectrum clearly reveals emission of the $J = 4 - 3$ transition of H¹³CO⁺. Therefore, we conclude that H¹³CO⁺ is detected at $>5\sigma$ but is blended with lines that are expected to peak on-source, preventing a clean image.

The line blending of H¹³CO⁺ $J = 4 - 3$ with acetaldehyde prevents us from using the only available dataset covering a transition of H¹³CO⁺ at sufficient spatial and spectral resolution, and sensitivity to resolve the water snowline. The $J = 3 - 2$ transition of H¹³CO⁺ is likely blended with CH₃OCHO as both of them are bright in the Class 0 source B1-c (van Gelder et al. 2020). However, the

²The `curve_fit` function is part of the Scipy package in python.

H^{13}CO^+ $J = 2 - 1$ transition in the same Class 0 B1-c source is free from line blending (van 't Hoff et al. in prep.) and would therefore be the best line to target in sources with bright emission from complex organics.

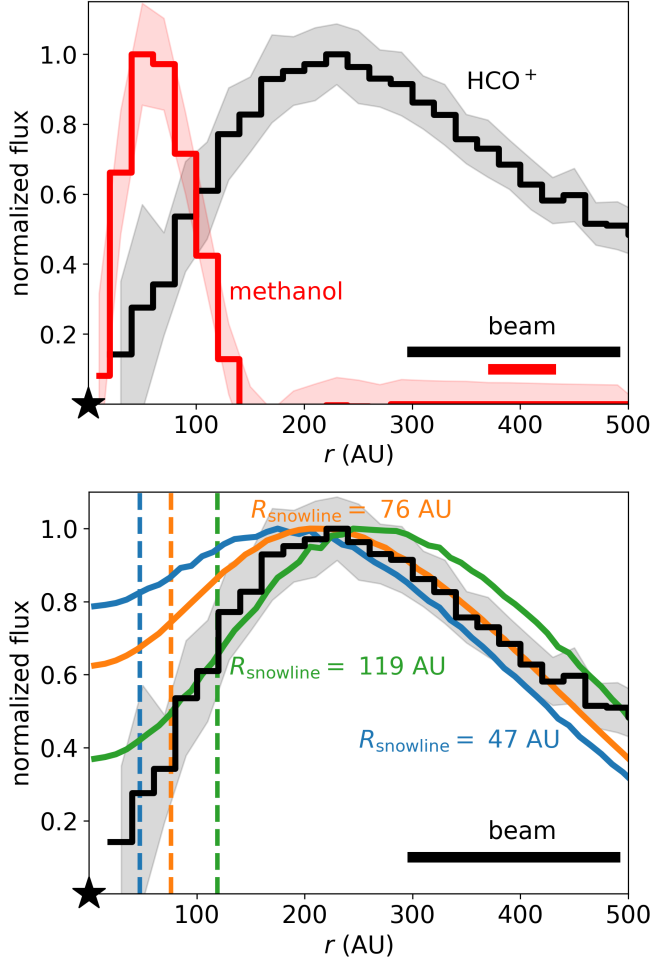


Figure 2.10: Observed and modelled emission from HCO^+ $J = 3 - 2$ and observed methanol in V883 Ori. Top: Normalised azimuthal average of the observed HCO^+ $J = 3 - 2$ flux in V883 Ori (black; Ruíz-Rodríguez et al. in prep. and this work) and methanol 18_3-17_4 flux (red; van 't Hoff et al. 2018b). Bottom: Normalised azimuthal average of the observed HCO^+ flux (black; as in top panel) and modelled HCO^+ flux for a snowline at 47 AU (blue), 76 AU (orange), and 119 AU (green). The snowline locations of the models are indicated with dashed lines in corresponding colours. The position of the star is indicated with a black star and the beam is indicated by the black bar in the bottom right corner.

2.4.2 HCO⁺ observations

Another promising dataset for HCO⁺ is a recent band 6 dataset (project code 2018.1.01131.S, PI: D. Ruíz-Rodríguez; Ruíz-Rodríguez et al. 2022). The $J = 3 - 2$ transition of HCO⁺ is detected with a high signal-to-noise ratio. The spatial resolution of $\sim 0''.5$ is insufficient to resolve the water snowline if it is located within a radius of ~ 90 AU (180 AU diameter).

An image of the HCO⁺ emission is presented in Ruíz-Rodríguez et al. (2022). Here, a normalised, deprojected azimuthal average of the observed emission from the product data of the $J = 3 - 2$ transition of HCO⁺ is presented in the top panel of Fig. 2.10. This azimuthal average shows that the HCO⁺ emission is ring shaped. Comparing the band 6 HCO⁺ emission with the band 7 emission from complex organic molecules presented in van 't Hoff et al. (2018b) and Lee et al. (2019), reveals that the emission from complex organic molecules such as methanol, 13-methanol, acetaldehyde, and H₂C¹⁸O peak inside the HCO⁺ ring, and in some cases is even centrally peaked. This is a strong indication that the lack of HCO⁺ emission in the centre is not only due to the optical depth of the continuum and that HCO⁺ is indeed tracing the water snowline in V883 Ori. Such an anti-correlation between HCO⁺ and methanol has also been seen in protostellar envelopes (Jørgensen et al. 2013).

2.4.3 Model HCO⁺ images: locating the snowline

To quantify the location of the water snowline, we model the HCO⁺ and H¹³CO⁺ emission in a representative model for V883 Ori. This model reproduces the previously observed flux of the $J = 2 - 1$ transition of C¹⁸O (van 't Hoff et al. 2018b), the HCO⁺ and H¹³CO⁺ total flux discussed in the previous Sections, and mm continuum fluxes within a factor of ~ 2 . The DALI model parameters are presented in Table 2.D.1. The main changes compared to the model for the typical Herbig Ae disk include the mass and radius of the disk, and the mass and luminosity of the star. The characteristic disk radius is set to 75 AU to match the radial extent of emission from the $J = 2 - 1$ transition of C¹⁸O presented by van 't Hoff et al. (2018b). The disk mass is estimated using the 9.1 mm continuum observations of the VANDAM survey (Tobin et al. 2020) and the relation between the continuum flux and the disk mass (Hildebrand 1983):

$$M = \frac{D^2 F_\nu}{\kappa_\nu B_\nu(T_{\text{dust}})}, \quad (2.10)$$

with D the distance to V883 Ori, F_ν the observed continuum flux, κ_ν the opacity, and $B_\nu(T_{\text{dust}})$ the Planck function for a dust temperature T_{dust} . As V883 Ori is an outbursting source, a dust temperature of 50 K is assumed. Following Tychoniec et al. (2020), a dust opacity of $0.28 \text{ cm}^2 \text{ g}^{-1}$ at a wavelength of 9.1 mm is used (Woitke et al. 2016). This results in an estimated disk mass of $0.25 M_\odot$.

The water snowline has been estimated at 42 AU from by Cieza et al. (2016), but it may be as far out as 100 AU based on CH₃OH observations (van 't Hoff et al. 2018b). The outburst likely began before 1888 (Pickering 1890) and has been

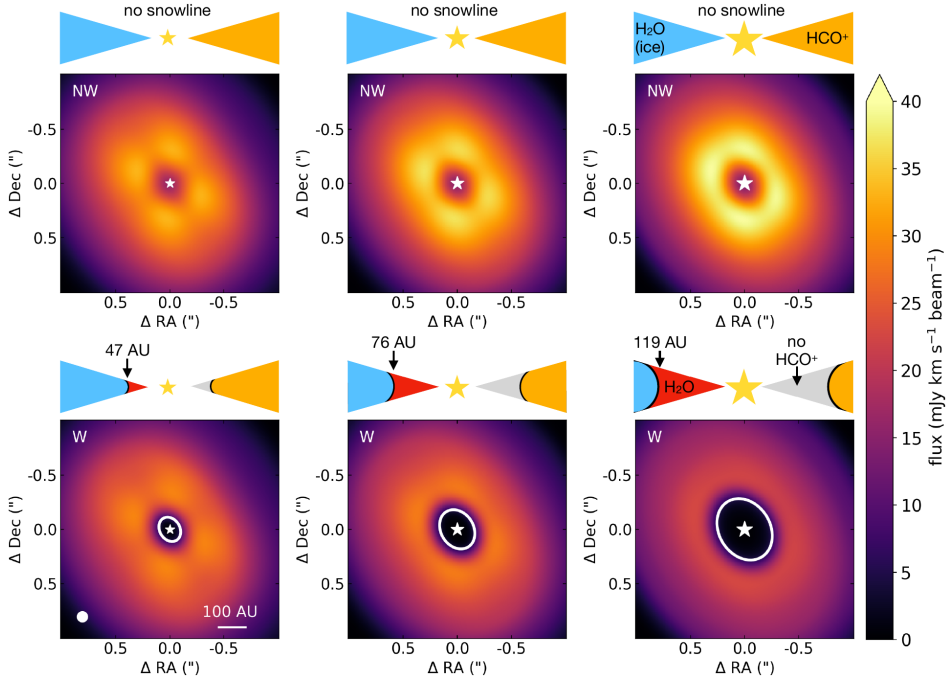


Figure 2.11: Integrated intensity maps for the $J = 3 - 2$ transition of HCO^+ predicted by network NW (top row) and network W (bottom row). The snowline is indicated with a white ellipse and is located at 47 AU (left column), 76 AU (middle column), and 119 AU (right column). The cartoons above the individual panels provide a sketch of the model, where blue indicates water ice, red indicates gas-phase water, orange indicates a high abundance of HCO^+ , and grey indicates a low abundance of HCO^+ . The position of the star is marked with a yellow star in each cartoon and with white star in each panel. We note that the size of the star increases with increasing luminosity of the star. The $0.1''$ beam and a scale bar are indicated in the bottom left panel.

decreasing since. Approximately 25 years ago the luminosity was measured to be $\sim 200 L_{\odot}$ higher than the current value (Strom & Strom 1993; Sandell & Weintraub 2001; Furlan et al. 2016). With a freeze-out time scale of 100-1000 yrs, the water snowline may thus not be at the location expected from the current luminosity (Jørgensen et al. 2013; Visser et al. 2015; Hsieh et al. 2019). We therefore use three different luminosities of 2×10^3 , 6×10^3 , and $1.4 \times 10^4 L_{\odot}$ in our models, which put the snowline at 47, 76, and 119 AU, respectively.

The resulting integrated intensity maps of the $J = 3 - 2$ transition of HCO^+ for these models are shown in Fig. 2.11. The corresponding figures for the weaker HCO^+ and H^{13}CO^+ $J = 2 - 1$ transitions are presented in Fig. 2.D.1 and Fig. 2.D.2. These lines are not expected to be contaminated by emission from complex organic molecules. The results in this section are convolved with a small $0.1''$ beam to make predictions for future high resolution observations.

The top row of Fig. 2.11 shows the expected emission for network NW for the

three different luminosities. The total HCO^+ emission does not depend strongly on the luminosity because the population of the $J = 3$ level decreases with luminosity but the increase in the temperature of the emitting region cancels this effect as the HCO^+ emission is marginally optically thick. Similar to the models for a disk around a typical Herbig Ae star, the moment 0 maps of network NW show ring shaped emission despite the fact that there is no snowline present in these models. The lack of emission in the centre is dominated by absorption by dust. On top of that, the column density of the $J = 3$ level of HCO^+ decreases in the inner parts of the disk. These two points are difficult to disentangle because the continuum optical depth is frequency and hence J -level dependent. However, most importantly, the location of the HCO^+ ring does not change as a function of luminosity in network NW.

This is different in the bottom row of Fig. 2.11, where emission associated with network W is shown. The water snowline is indicated with a white ellipse and shifts outwards as the luminosity of the star increases. This is also reflected in the HCO^+ emission as the ring of HCO^+ shifts outwards together with the water snowline. Therefore, the location of the HCO^+ ring can be used to locate the water snowline provided that another molecule is observed to show that the decrease in the HCO^+ flux in the centre is not solely due to molecular excitation effects and absorption by dust. The excitation effect needs to be inferred from disk modelling. The effect of the optical depth of the continuum emission can be estimated by observing another molecule, that emits from the same disk region as HCO^+ and whose column density does not drop in the inner disk. The most obvious molecule for this purpose is C^{18}O . However, the HCO^+ $J = 3 - 2$ emission comes from a layer closer to the midplane than the C^{18}O $J = 2 - 1$ and $J = 3 - 2$ emission. Therefore, the effect of the dust on the HCO^+ emission cannot be fully traced by the $J = 2 - 1$ or $J = 3 - 2$ transition of C^{18}O . Rarer isotopologues such as C^{17}O or $^{13}\text{C}^{18}\text{O}$ are more suited for this purpose, as well as other molecules such as complex organics as discussed in Section 2.4.2.

The model predictions for the observed flux of the $J = 3 - 2$ transition of HCO^+ in V883 Ori are compared with the observed flux in the bottom panel of Fig. 2.10. The model results are convolved to the same spatial resolution as the observations before calculating the deprojected azimuthal average. Even though the beam is too large to resolve the snowline if it is located inside ~ 90 AU, this figure clearly shows that the observed HCO^+ flux drops off steeper in the inner parts than that predicted by the model with a snowline at 47 AU. In addition, the HCO^+ ring shifts outwards with increasing snowline location. The observed peak location and gap depth in the centre best match with a snowline between 76 and 119 AU.

A central cavity (approx. 1 beam in diameter at $0''.35 \times 0''.27$ resolution corresponding to ~ 60 AU resolution in radius) was also observed for CO $J = 2 - 1$ and was attributed to the continuum optical depth by Ruíz-Rodríguez et al. (2017). However, it is unlikely that the cavity observed in HCO^+ is solely due to the continuum as the emission from complex organic molecules peaks inside the HCO^+ ring ($0''.23 \times 0''.17$; Lee et al. 2019). Similarly, the high resolution methanol emission ($0''.13 \times 0''.14$; van 't Hoff et al. 2018b) and the continuum emission ($0''.03$;

Cieza et al. 2016) peak well inside the HCO^+ cavity (Fig. 2.10). Furthermore, the continuum becomes optically thin well within 100 AU in all three of our models (Figs. 2.10 and 2.11), so the difference between the models is due to different snowline locations. Therefore, our analysis is consistent with a water snowline at ~ 75 -120 AU in V883 Ori, and thus suggests that the sudden change in continuum opacity at 42 AU is uncorrelated with the water snowline.

One effect that needs to be taken into account in outbursting sources like V883 Ori is viscous heating. This effect heats the disk midplane, hence the water snowline could be at a larger radius than expected based on radiative heating alone. The $J = 3 - 2$ transition of HCO^+ is marginally optically thick in our models. Targeting a low J transition of HCO^+ or targeting the optically thin H^{13}CO^+ , will allow us to directly trace the midplane. Another effect that could occur due to viscous heating is self-absorption of HCO^+ as the surface layers of the disk could have a lower temperature than the viscously heated midplane. This, again, could be resolved by observing multiple transitions of HCO^+ as higher J lines are more optically thick and hence trace a layer higher in the disk.

Taken together, our analysis of the observations suggests that HCO^+ is tracing the water snowline in the V883 Ori disk, and that the snowline is located outside the radius where the change in the continuum opacity is observed. Therefore, V883 Ori is the first example that shows that a change in the dust continuum opacity is not necessarily related to the water snowline, similar to what has been shown for the cases of CO, CO_2 , and N_2 snowlines (Huang et al. 2018; Long et al. 2018; van Terwisga et al. 2018).

2.5 Conclusions

Chemical imaging with HCO^+ is in principle a promising method to image the water snowline as it has been used successfully in a protostellar envelope (van 't Hoff et al. 2018a). This work examines the application of this to older protoplanetary disks. The HCO^+ abundance was modelled using two chemical networks, one with water (W) and one without water (NW). Predictions for the radial emission profiles of HCO^+ and H^{13}CO^+ were made to examine the validity of HCO^+ as a tracer of the water snowline. Moreover, archival observations of V883 Ori were examined to constrain the location of the water snowline in V883 Ori and make predictions for future high resolution observations.

Based on our models the following conclusions can be drawn:

- The HCO^+ abundance jumps two orders of magnitude around the water snowline.
- In addition to the water snowline, the optical depth of the continuum emission and molecular excitation effects for the low J -levels contribute significantly to the decrease in the H^{13}CO^+ and HCO^+ flux in the inner parts of the disk and result in ring shaped emission. Therefore, the effect of the continuum optical depth needs to be checked observationally, and the effects of the molecular excitation and HCO^+ abundance need to be modelled in

detail. Outbursting sources are the best targets, as the snowline is shifted to larger radii, where the dust optical depth is lower.

- HCO^+ and H^{13}CO^+ are equally good as tracers of the water snowline but the main isotopologue HCO^+ is more readily observable because of its higher abundance.
- For both HCO^+ and H^{13}CO^+ , the $J = 2 - 1$ transition is preferred because it provides the best balance between line strength and the negative effects of the continuum optical depth. Moreover, it is not expected to be blended with emission from complex organic molecules, unlike the $J = 3 - 2$ and $J = 4 - 3$ transitions of H^{13}CO^+ .
- Our analysis of the observations of the HCO^+ $J = 3 - 2$ transition and complex organic molecules suggest that HCO^+ is tracing the water snowline in V883 Ori. Based on our models, the snowline is located around 100 AU and is not correlated with the opacity change in the continuum emission observed at 42 AU.

Our results thus show that HCO^+ and H^{13}CO^+ can be used to trace the water snowline in warm protoplanetary disks, such as those found around luminous stars. Determining the snowline location in these sources is important to understand the process of planet formation and composition.

Acknowledgements

We thank the referee and the editor for the constructive comments, and Catherine Walsh and Jeong-Eun Lee for useful discussions. Astrochemistry in Leiden is supported by the Netherlands Research School for Astronomy (NOVA). M.L.R.H acknowledges support from a Huygens fellowship from Leiden University, and from the Michigan Society of Fellows. L.T. is supported by NWO grant 614.001.352. This paper makes use of the following ALMA data: ADS/JAO.ALMA#2017.1.01066.T. and ADS/JAO.ALMA#2018.1.01131.S. ALMA is a partnership of ESO (representing its member states), NSF (USA) and NINS (Japan), together with NRC (Canada), MOST and ASIAA (Taiwan), and KASI (Republic of Korea), in cooperation with the Republic of Chile. The Joint ALMA Observatory is operated by ESO, AUI/NRAO and NAOJ.

Appendix

2.A Freeze-out and desorption coefficients

The reaction coefficients of the freeze-out and desorption of water depend on the local conditions in the disk. The rate coefficient of the freeze-out of water, k_f can

be expressed as:

$$k_f = \langle v \rangle \pi a_{\text{grain}}^2 n(\text{grain}) S \quad (2.11)$$

$$= \sqrt{\frac{k_B T_{\text{gas}}}{m}} \pi a_{\text{grain}}^2 n(\text{grain}) S, \quad (2.12)$$

where $\langle v \rangle = \sqrt{k_B T_{\text{gas}}/m}$ is the thermal velocity of gas-phase water molecules with mass m in a gas at temperature T_{gas} , and k_B is the Boltzmann constant. The DALI models use a distribution of grain sizes, but for the chemistry, only the surface area of the grains matters. Therefore, a grain size of $a_{\text{grain}} = 0.1 \mu\text{m}$ and a number density, $n(\text{grain}) = 10^{-12} \times n(\text{H}_2)$ with respect to molecular hydrogen is used. Finally, a sticking coefficient, S , of 1 is assumed.

The reverse process, the desorption of water ice, is described by the desorption rate coefficient:

$$k_d = \nu_0 e^{-E_b/k_B T_{\text{dust}}} \quad (2.13)$$

$$= \sqrt{\frac{2n_s E_b}{\pi^2 m}} e^{-E_b/k_B T_{\text{dust}}}, \quad (2.14)$$

with $\nu_0 = \sqrt{2n_s E_b/\pi^2 m}$ the characteristic vibrational frequency of water ice on a grain. Here $n_s = 1.5 \times 10^{15} \text{ cm}^{-2}$ is the number density of surface sites where water can bind (Hasegawa et al. 1992). The binding energy, E_b , assumed in this work is 5775 K, corresponding to an amorphous water ice substrate (Fraser et al. 2001).

2.B Chemical network

2.B.1 Analytical approximation for network NW

Chemical network NW can be used to derive an analytical expression for the HCO^+ abundance because of its simplicity. The time evolution of the HCO^+ number density is given by the sum of the formation and destruction rates:

$$\frac{dn(\text{HCO}^+)}{dt} = k_4 n(\text{CO}) n(\text{H}_3^+) - k_{e^-} n(\text{HCO}^+) n(e^-), \quad (2.15)$$

with k_4 and k_{e^-} the reaction rates as listed in Table 2.2. This can be rewritten to

$$n(\text{HCO}^+) = \sqrt{\frac{k_4}{k_{e^-}}} n(\text{CO}) n(\text{H}_3^+) \quad (2.16)$$

under the assumption of steady state. Furthermore, it is assumed that metallic ions can be neglected as electron donors, and that HCO^+ is the main electron donor. HCO^+ has been found to be the dominant molecular ion protoplanetary disks (Teague et al. 2015), and the main charge carrier in starless cores (e.g. Caselli et al. 1998; Williams et al. 1998).

Following the approach of Lepp et al. (1987), the number density of H_3^+ , which is mainly governed by the ionisation, can be found in a similar way. The three reactions that regulate the ionisation in the disk: ionisation by cosmic rays (reaction $\zeta_{\text{c.r.}}$), the ion-molecule reaction to form H_3^+ (reaction k_2), and dissociative recombination of H_3^+ (reaction k_3), see also Table. 2.2. The first two reactions can be approximated as:



as the formation of H_3^+ is limited by the cosmic ray ionisation rate. Assuming CO is the main destroyer of H_3^+ and thus neglecting the dissociative recombination of H_3^+ , the time evolution and steady state abundance of H_3^+ can be expressed as:

$$\frac{dn(\text{H}_3^+)}{dt} = \zeta_{\text{c.r.}}n(\text{H}_2) - k_4n(\text{CO})n(\text{H}_3^+) \quad (\text{time-dependent}), \quad \text{and} \quad (2.18)$$

$$n(\text{H}_3^+) = \frac{\zeta_{\text{c.r.}}n(\text{H}_2)}{k_4n(\text{CO})} \quad (\text{steady state}). \quad (2.19)$$

Combining Eq. 2.16 and Eq. 2.19 gives the analytical approximation of the HCO^+ abundance in the disk:

$$x(\text{HCO}^+) = \sqrt{\frac{\zeta_{\text{c.r.}}}{k_{\text{e}} - n(\text{H}_2)}}. \quad (2.20)$$

The comparison of chemical network NW and W in Section 2.3.1 and Fig. 2.3 shows that the HCO^+ abundance in network NW is very similar to the HCO^+ abundance outside the water snow surface in network W. Therefore, the derived expression for the HCO^+ abundance can also be used in this disk region in chemical network W.

2.B.2 Initial conditions

The effects of the initial conditions on the abundance predicted by chemical network W were discussed in Section 2.3.1.2 and expected to be of little importance for HCO^+ 's ability to trace the water snowline. Here, the effects on the corresponding radial emission profiles of the $J = 2 - 1$ transition of HCO^+ and H^{13}CO^+ are discussed and shown in Fig. 2.B.1.

Previously, it was derived that the column density of HCO^+ scales with the square root of the cosmic ray ionisation rate (see Eq. 2.9). Similarly, the H^{13}CO^+ emission scales with the square root of the cosmic ray ionisation rate because it is optically thin, see Fig. 2.B.1. On the other hand, the HCO^+ emission does not scale with the cosmic ray ionisation rate as it is optically thick. As the column density of HCO^+ decreases, the HCO^+ emission becomes less optically thick and approaches the scaling for the column density.

In Section 2.3.1.2, it was found that the HCO^+ abundance or column density does not depend strongly on the initial abundance of CO or H_2O . This is also seen in the radial emission profiles both for HCO^+ and H^{13}CO^+ because the drop

Table 2.B.1: Initial conditions for chemical network NW (no water) and W (water).

Model parameter	Initial value NW	Initial value W	Ref.
$\zeta_{\text{c.r.}}$	1(-17)	1(-17)	
T_{gas}	DALI model	DALI model	
T_{dust}	DALI model	DALI model	
$n(\text{H}_2)$	DALI model	DALI model	
$x(\text{H}_2^+)$	0	0	
$x(\text{H}_3^+)$	0	0	
$x(\text{H})$	0	0	
$x(\text{e}^-)$	0	0	
$x(\text{CO})$	1(-4)	1(-4)	
$x(\text{HCO}^+)$	0	0	
$x(\text{H}_3\text{O}^+)$	0	0	
$x(\text{H}_2\text{O})$	0	3.8(-7)	(a)
$x(\text{H}_2\text{O}(\text{ice}))$	0	0	

Notes. $a(b)$ represents $a \times 10^b$. Abundances are defined with respect to molecular hydrogen. References: (a) McElroy et al. 2013.

in the HCO^+ emission in the centre is dominated by the effect of the optical depth of the continuum emission and molecular excitation. A small dependence of the HCO^+ emission on the initial abundance of gas-phase water is seen, but the abundance of gas-phase water seems to be low in the outer regions of protoplanetary disks (Bergin et al. 2010; Du et al. 2017; Notsu et al. 2019; Harsono et al. 2020). Moreover, the abundance of gas-phase water in the inner disk can be as high as 10^{-2} (Bosman et al. 2018a).

2.C HCO^+ and H^{13}CO^+ $J = 1 - 0$, $J = 3 - 2$, and $J = 4 - 3$ transitions

Radial emission profiles for the $J = 1 - 0$, $J = 3 - 2$, and $J = 4 - 3$ transitions of HCO^+ and H^{13}CO^+ are presented in Fig. 2.C.1.

2.D V883 Ori

An overview of the model parameters used for the representative DALI model for V883 Ori is given in Table 2.D.1. Predictions for the corresponding emission of the $J = 2 - 1$ transition of HCO^+ and H^{13}CO^+ are shown in Fig. 2.D.1 and Fig. 2.D.2.

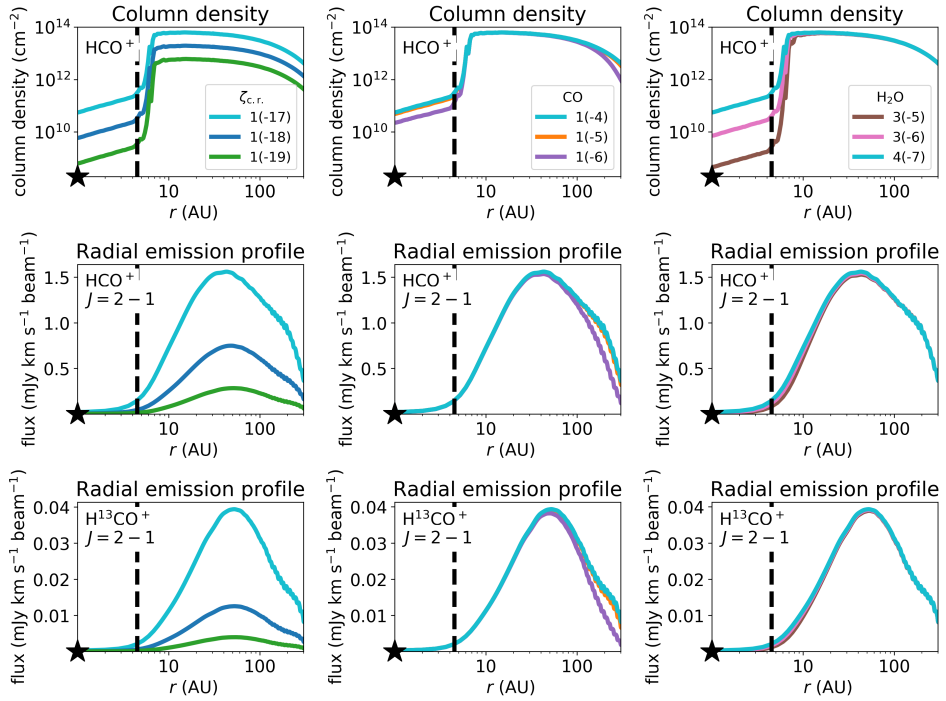


Figure 2.B.1: HCO⁺ column densities for different initial conditions in chemical network W (top row) and the corresponding radial emission profiles for the $J = 2 - 1$ transition of HCO⁺ (middle row) and H¹³CO⁺ (bottom row). The left-hand column shows the results for a cosmic ray ionisation rate of 10^{-17} s⁻¹, 10^{-18} s⁻¹, and 10^{-19} s⁻¹. The middle column shows the corresponding models for an initial CO abundance of 10^{-4} , 10^{-5} , and 10^{-6} . The right-hand column shows the corresponding models for an initial abundance of gas-phase water of 3×10^{-5} , 3×10^{-6} , and 3.8×10^{-7} . The fiducial model is indicated with the light blue line in each panel and uses an initial abundance of 3.8×10^{-7} for gas-phase water, 10^{-4} for gas-phase CO, and 10^{-17} s⁻¹ for the cosmic ray ionisation rate. The water snowline is indicated with a dashed black line and the position of the star is indicated by the symbol of a black star. The radial emission profiles are convolved with a $0''.05$ beam.

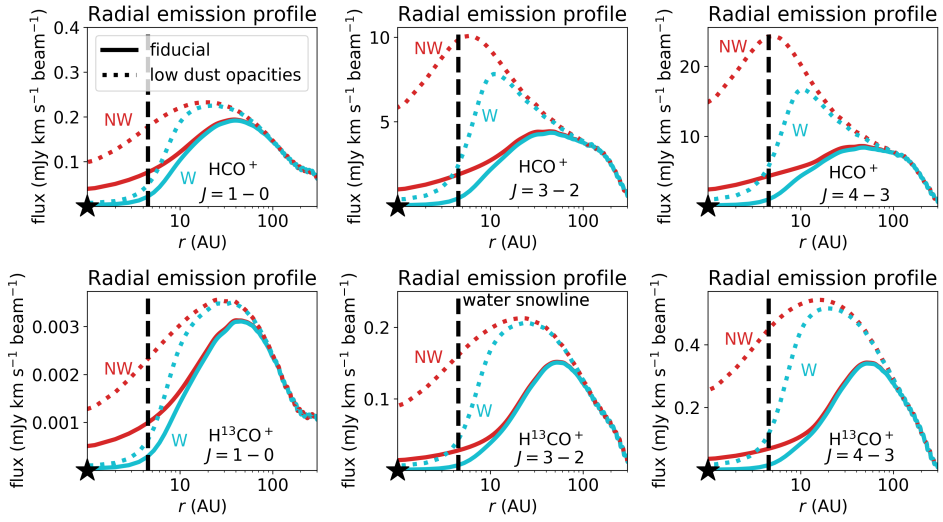


Figure 2.C.1: Same as the middle and bottom panel of Fig. 2.5, but then for the $J = 1 - 0$ (left column), $J = 3 - 2$ (middle column), and $J = 4 - 3$ (right column) transition of HCO^+ (top) and H^{13}CO^+ (bottom).

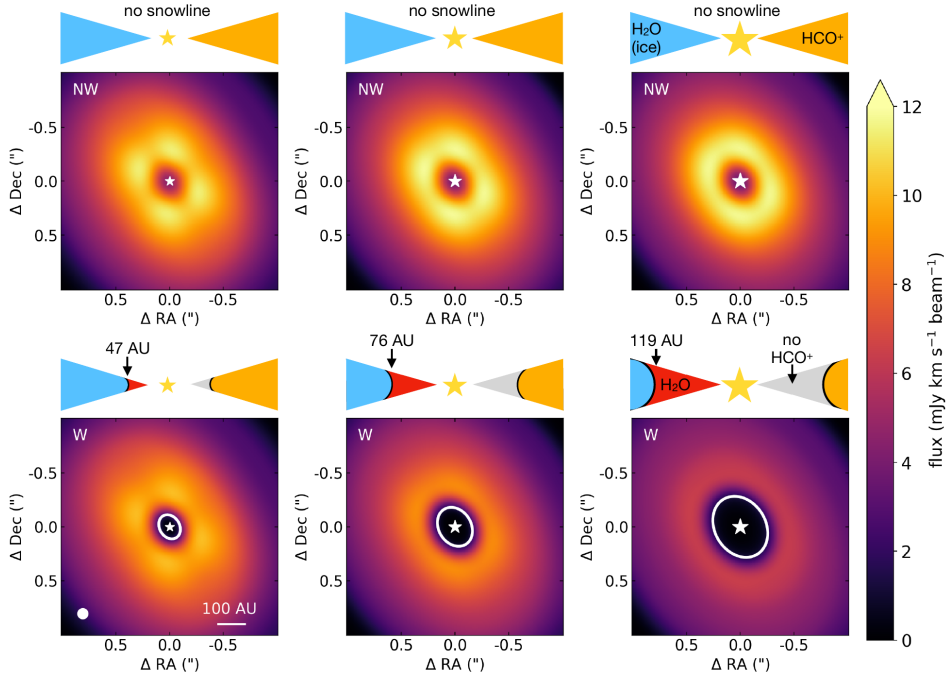


Figure 2.D.1: Same as Fig. 2.11 but then for the $J = 2 - 1$ transition of HCO^+ . The $0.1''$ beam and a scale bar are indicated in the bottom left panel.

Table 2.D.1: DALI model parameters for the representative model for V883 Ori.

Model parameter	Value	Ref.
<i>Physical structure</i>		
R_{subl}	1 AU	
R_{c}	75 AU	
Σ_{c}	35 g cm ⁻²	
M_{disk}	0.25 M _⊙	
γ	1	
h_{c}	0.1	
ψ	0.25	
<i>Dust properties</i>		
χ	0.2	
f_{ls}	0.9	
$\Delta_{\text{gas/dust}}$	100	
<i>Stellar spectrum</i> ⁽¹⁾		
Type	Outbursting	
$L_{\star+\text{acc}}$	2.0(3), 6.0(3), 1.4(4) L _⊙	
L_{X}	1.4(30) erg s ⁻¹	
T_{eff}	1(4) K	
T_{acc}	1(4) K	
T_{X}	7(7) K	
$\zeta_{\text{c.r.}}$	5(-17) s ⁻¹	
<i>Stellar properties</i> ⁽²⁾		
\dot{M}	5(-5) M _⊙ yr ⁻¹	
M_{\star}	1.3 M _⊙	(a)
R_{\star}	5.1 R _⊙	
<i>Observational geometry</i>		
i	38°	(a)
P.A.	32°	(a)
d	400 pc	(b)

Notes. $a(b)$ represents $a \times 10^b$. ⁽¹⁾The stellar spectrum is obtained by the sum of the accretion luminosity L_{acc} and an artificially high stellar luminosity L_{\star} to shift the snowline to 47, 76, and 119 AU. ⁽²⁾ R_{\star} is chosen to obtain an accretion luminosity of 4×10^2 L_⊙, consistent with Cieza et al. (2016). References: (a) Cieza et al. 2016, (b) Kounkel et al. 2017.

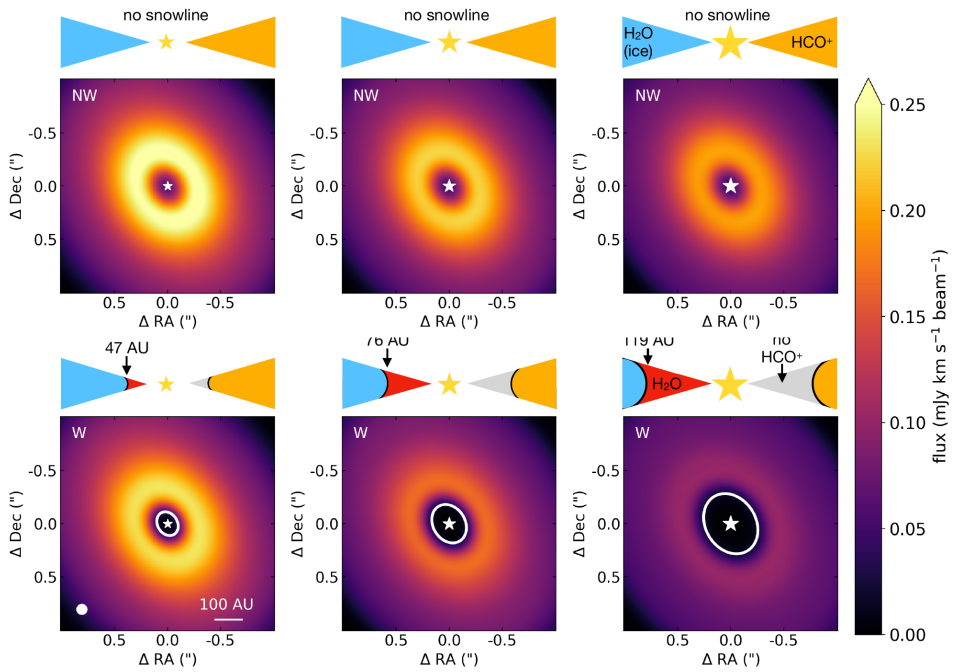


Figure 2.D.2: Same as Fig. 2.11 but then for the $J = 2 - 1$ transition of H^{13}CO^+ . The 0.1 beam and a scale bar are indicated in the bottom left panel.

Chapter 3

Resolving snow surfaces of water and methanol in the V883 Ori disk

M. Leemker, T. Paneque-Carreño, J. J. Tobin, M. L. R. van 't Hoff,
E. F. van Dishoeck, and A. S. Booth

In preparation

Abstract

Context. The chemical composition of the planet forming material changes around the major snowlines, those of water and CO, in a protoplanetary disk. The location and shape of the vertical snow surfaces of different molecules can be used to trace vertical mixing in disks and the structure of ices.

Aims. We aim to locate the snow surface of HDO and methanol in the V883 Ori disk in both the radial and vertical direction.

Methods. The ALFAHOR package is used to analyze the emitting height of HDO and methanol in the V883 Ori disk observed with ALMA.

Results. We find that the HDO and methanol snow surfaces are close to vertical, consistent with the vertical cold finger effect that transports water to the disk midplane due to diffusion and vertical mixing of grains. The HDO emission is seen in the midplane out to ~ 60 au pointing to a water snowline location beyond 60 au. Additionally, the methanol snow surface is located $\sim 10 - 20$ au outside that of HDO consistent with the lower binding energy of methanol to the grains. The separation between the two snow surfaces indicates that methanol is not co-desorbing with water ice.

Conclusions. The HDO and methanol snow surfaces in the V883 Ori disk are steep and radially separated indicating that methanol does not co-desorb with water. Therefore, the V883 Ori disk provides a unique laboratory to observationally determine the binding energies of other complex organic molecules.

3.1 Introduction

The thermal structure of protoplanetary disks has a large effect on the outcome of planet formation. In particular, snowlines, the midplane radii where 50% of a molecule is frozen out as ice and 50% is in the gas-phase, are important as they mark special locations in the disk where the chemical composition of the planet forming gas and ice changes due to selective freeze-out (see Öberg & Bergin 2021, for a recent review). In addition, the increase in the surface density of solids just outside the water snowline can aid planet formation by triggering the streaming instability leading to grain growth (e.g., Stevenson & Lunine 1988; Drażkowska & Alibert 2017; Pinilla et al. 2017).

Vertically the snowline is thought to follow the line where the freeze-out and desorption rates balance. This snow surface thus follows the temperature structure of the disk, and to some degree also its density structure, with the snow surface moving up as the radius increase. Recently, Bosman & Bergin (2021) proposed that the water snow surface may instead be vertical due to the continuous vertical mixing of grains in disks, following the idea of a vertical cold finger effect (Meijerink et al. 2009). In this scenario grains are mixed up to high layers in the disk where gas-phase water is abundant. Then water freezes-out and the grains settle to the disk midplane where these grains grow and become too heavy to be efficiently mixed up again. This causes a vertical water snow surface in disks and a similar process is expected for other molecules that freeze-out in disks such as CO and complex organic molecules (COMs).

COMs are suggested to desorb sequentially due to the different binding energies on the grains for different COMs. For example, observations of young and massive protostars show warm formamide at 300 – 400 K, whereas an isotopologue of methanol $\text{CH}_3^{18}\text{OH}$ is seen at only 100 K (e.g., Jørgensen et al. 2018; Nazari et al. 2022). As the temperature profile of protostellar envelopes decreases with increasing distance to the star, the $\text{CH}_3^{18}\text{OH}$ traces colder and thus more extended material than the warmer formamide. Similarly, differences are expected for other COMs such as acetaldehyde (CH_3CHO) that has a lower binding energy than e.g., methanol (Penteado et al. 2017; Minissale et al. 2022) and its snow surface is thus expected to be further away from the central star. However, the binding energy of a molecule depends on the surface to which it is bound. Therefore, acetaldehyde ice that is frozen on top of a methanol ice layer may have a different sublimation temperature than if it is frozen out onto a water ice layer.

The ice on grains in disks likely consists of multiple layers with different molecules in each layer. This is due to the formation of ices in the parent molecular cloud and the formation of molecules on the icy surfaces. For example, laboratory research shows that some COMs like acetaldehyde and ethanol formed in a layer with both water and C_2H_2 ice, may be trapped in the water ice matrix whereas COMs that form through CO hydrogenation e.g., CH_2OHCHO , $(\text{CH}_2\text{OH})_2$, and CH_3OCHO may be trapped in methanol ice that is also formed through CO hydrogenation (Chuang et al. 2020; Simons et al. 2020). Two molecules that may also have a common formation pathway are NH_2CHO and HCNO as they have a very similar spatial distribution in the HH 212 protostellar disk system (Lee et al.

2022). Therefore, information on the order in which molecules desorb in a protostellar envelope and at which disk locations can shed light on the ice structure and thus the formation pathways of COMs and other molecules on the grains.

The midplane location where water and CO desorb have been located using chemical tracers such as HCO^+ (for water) and N_2H^+ , DCO^+ , and very rare CO isotopologues (for CO) (van 't Hoff et al. 2017; Carney et al. 2018; van 't Hoff et al. 2018a; Qi et al. 2019; Leemker et al. 2021). A second method to derive the water snowline location is to use the emission of COMs that desorb at approximately the same temperature as water (van 't Hoff et al. 2018b; Booth et al. 2023c). However, these methods only work for molecules like water and CO for which tracers are available. Observations of embedded edge-on disks show the 2D snow surface of each molecule that is observed as the column density in the disk midplane and beyond will be greatly reduced due to freeze-out (e.g., Podio et al. 2020; van't Hoff et al. 2020; Lee et al. 2022). Yet, models by Sturm et al. (2023c) show that the situation is much more complicated in Class II disks at infrared wavelengths.

Recently, a new method has become available to study the emitting surfaces in moderately inclined protoplanetary disks using the Keplerian rotation that can be seen in high spatial and spectral resolution channel maps (Pinte et al. 2018a). This work presented the emitting surfaces of ^{12}CO , ^{13}CO , and C^{18}O in the IM Lup disk and found that the latter two are co-located at roughly 20 K. This is a direct indication that the emitting surfaces trace snow surfaces if the emission is not highly optically thick. In addition, analyses of many different molecules across the disks shows that the molecules span a wide range of vertical emitting heights depending on the optical depth (e.g., for CO isotopologues), upper energy level of the transition (e.g., $^{13}\text{CO } J = 2 - 1$ vs $J = 6 - 5$), and the abundance structure (e.g, for CN) (Law et al. 2021b; Leemker et al. 2022; Paneque-Carreño et al. 2022, 2023; Law et al. 2023b).

In this work we focus on the V883 Ori disk. This disk is located around an outbursting star with a luminosity of $\sim 200 L_{\odot}$ that has heated the disk and shifted the water snowline out to at least 40 au but possibly as far as 120 au (Cieza et al. 2016; Furlan et al. 2016; van 't Hoff et al. 2018b; Leemker et al. 2021). The disk is located in Orion at ~ 400 pc (Kounkel et al. 2017) and has a moderate inclination of 38° (Cieza et al. 2016). This disk is the most COM rich disk to date (Lee et al. 2019). Additionally, other molecules such as the potential precursor of methanol, and both HDO and methanol have been observed at high spatial and spectral resolution and sensitivity in this disk (Ruíz-Rodríguez et al. 2022; Tobin et al. 2023). In addition to the circumstellar disk, the system is surrounded by a remnant envelope (e.g., Ruíz-Rodríguez et al. 2017).

This paper is organised as follows. In Sect. 3.2 we outline the method used to derive the emitting surfaces of HDO and methanol in the V883 Ori disk. The results are presented in Sect. 3.3 and in Sect. 3.4 the implications for the structure of the ice on the dust in protoplanetary disks are discussed and compared to other sources. Finally, our conclusions are summarised in Sect. 3.5.

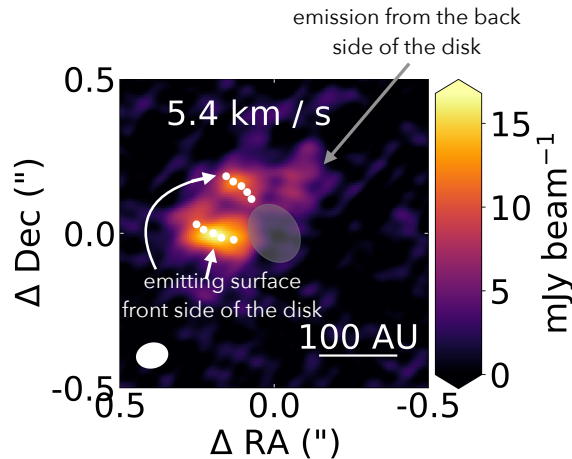


Figure 3.1: Channel map of the HDO 225 GHz emission at 5.4 km s^{-1} which is 1.3 km s^{-1} from the source velocity of 4.3 km s^{-1} (van 't Hoff et al. 2018b). The white dots indicate the emission peaks of the near and far side of the disk's front side. The grey arrow indicates the emission from the near and back side of the disk. The grey ellipse in the center indicates a 40 au radius within which the continuum emission is optically thick and the HDO emitting surface cannot be traced.

3.2 Methods

To derive the emitting heights, observations with a high signal-to-noise ratio taken at a high spatial ($\lesssim 0''.15$) and a high spectral resolution ($\lesssim 0.2 \text{ km s}^{-1}$) of unblended lines. Most archival ALMA data sets do not satisfy at least one of these criteria. Therefore, we focus here on the HDO and methanol presented in Tobin et al. (2023, ALMA project code: 2021.1.00186.S). In particular, the HDO 225 GHz line is used as the 241 GHz line is heavily blended confusing the HDO and COM emission in the channel maps. For methanol we used the stacked channel maps of the six isolated methanol lines to increase the signal-to-noise ratio, see Table 3.1. Both lines were imaged at a spatial resolution of $0''.10 \times 0''.08 (-76.6^\circ)$ and $0''.09 \times 0''.07 (-75.2^\circ)$ for HDO and methanol, respectively, and a spectral resolution of 0.16 km s^{-1} . Details about the imaging of the data can be found in Tobin et al. (2023).

The emitting height of the HDO and methanol emission is inferred directly from the channel maps using the ALFAHOR package (Paneque-Carreño et al. 2023), based on Pinte et al. (2018a). Masks encompassing the upper emitting surface in the near and far side of the disk were created after visual inspection of the data to exclude emission from the lower disk surface and from neighbouring COMs. Subsequently, the emission maxima along the major axis are located within these masks in the near and far side of the disk by the ALFAHOR package. Fig. 3.1 shows the resulting peak locations for the HDO channel at 5.4 km s^{-1} , whereas the source velocity is 4.3 km s^{-1} (van 't Hoff et al. 2018b). The channel maps of the

Table 3.1: HDO and methanol lines used in this work.

Molecule	Frequency (GHz)	Transition	$\log_{10} A_{ij}$ (s^{-1})	E_{up} (K)
HDO	225.897	$3(1, 2) - 2(2, 1)$	-4.9	168
CH ₃ OH	241.807	$5(4)^- - 4(4)^- v_t = 0$	-4.7	115
CH ₃ OH	241.807	$5(4)^- - 4(4)^- v_t = 0$	-4.7	115
CH ₃ OH	241.813	$5(-4) - 4(-4) E_2 v_t = 0$	-4.7	123
CH ₃ OH	241.852	$5(-3) - 4(-3) E_2 v_t = 0$	-4.4	98
CH ₃ OH	241.879	$5(1) - 4(1) E_1 v_t = 0$	-4.2	56
CH ₃ OH	241.888	$5(2)^+ - 4(2)^+ v_t = 0$	-4.3	73

The line properties are obtained from the JPL database (Johns 1985; Pickett et al. 1998; Xu et al. 2008).

methanol and HDO emission with the masks and traced maxima are presented in Fig. 3.A.1 and 3.A.2. For each pair of points the spatial location of the maxima is converted to an emitting height using an position angle of 32.4° , an inclination of 38.3° and a distance of 400 pc. A linear fit was made to the resulting data points that lie above the midplane and inside 80 au. Furthermore, the emitting heights are binned to increase the signal-to-noise ratio.

3.3 Results

The resulting emitting heights of the HDO and methanol emission are presented in Fig. 3.2. The scatter points in this figure indicate the emitting height derived from each pair of a near and a far side emission peak. To increase the signal-to-noise ratio, these data points are binned resulting in the thick blue line with the shaded region indicating the scatter. The emitting surfaces are only traced outside 40 au where the dust is not highly optically thick at mm-wavelengths (Cieza et al. 2016). Outside this region, the emitting surfaces trace the snow surfaces of HDO and methanol, respectively, as these molecules are expected to be frozen out in the disk midplane. If the emission is optically thin or marginally optically thick, the traced surface is set by the region with the highest density of HDO or methanol molecules. As the gas density increases towards the disk midplane and the HDO and methanol emission is marginally optically thick (see Appendix 3.B for details), the highest HDO and methanol densities are found just above their respective snow surfaces.

Gas-phase water is seen close to the disk midplane out to ~ 60 au. This is close to consistent with the 75 – 120 au midplane snowline location derived from previously observed methanol and HCO⁺ emission (van 't Hoff et al. 2018b; Leemker et al. 2021), whereas this is 20 au further out than sudden change in the continuum opacity at 40 au attributed to the water snowline (Cieza et al. 2016).

The resulting emitting surface of both HDO and methanol are very steep, rising $\gtrsim 30$ au in height over a radial region of 20 au. This is much steeper and more

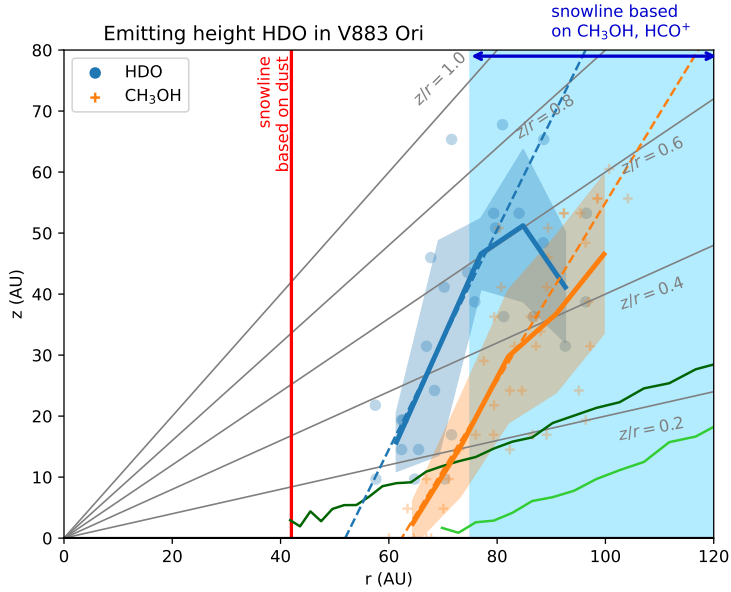


Figure 3.2: Emitting surface of the HDO 225 GHz and methanol emission in the V883 Ori disk. The scatter points indicate the measured height and the thick blue and orange lines the binned surface of HDO and methanol, respectively. The dashed lines indicate a linear fit to the points inside 80 au. The vertical red line indicates the ~ 40 au midplane water snowline location based on the continuum (Cieza et al. 2016) and the blue shaded region indicates the midplane water snowline based on previously detected methanol and HCO^+ emission (van ’t Hoff et al. 2018b; Leemker et al. 2021). Finally, the dark and light green lines indicate the water snow surfaces for the V883 Ori disk radiative transfer models with a snowline at 47 au and 76 au presented in Leemker et al. (2021).

vertically extended than expected based on the temperature of thermochemical models (green lines in Fig. 3.2, Leemker et al. 2021). This is likely not due to molecular excitation as the HDO line at 225 GHz has an upper energy level of 167 K, similar to the desorption temperature of H_2O (Penteado et al. 2017). Therefore, even if the measured emitting surface would mainly trace gas at this temperature, this would still coincide with the water snow surface. Moreover, the stacked methanol lines cover a range of different upper energy levels (56 – 123 K) and still trace similar disk regions.

The emitting surfaces above the disk midplane and inside 80 au follow an approximately linear relation. Outside 80 au the scatter increases and the emitting heights cannot be traced accurately. A linear fit to the surfaces inside 80 au and above the midplane shows that the slope of both surfaces are similar with an increase of 1.8 au and 1.5 au in height for every au in radius for HDO and methanol, respectively. Extrapolating this to the disk midplane shows that the last radius where gas-phase HDO and methanol are present is 52 au and 62 au,

respectively.

The radial off-set between HDO and methanol persists above the disk midplane with the emitting surface of methanol being shifted to larger radii by $\sim 10 - 20$ au than that of HDO. Such an off-set is expected as the binding energy of H_2O of 5770 K is higher than that of methanol of 3800 K (Penteado et al. 2017). Therefore, H_2O is expected to desorb at a higher temperature and thus closer to the central star than methanol. The clear separation between the measured emitting surfaces also indicates that most of the methanol ice desorbs at its own desorption temperature rather than being locked up in a water ice matrix.

3.4 Discussion

The distinct difference between the location of the HDO and methanol snow surfaces indicates a true difference in the abundance structure of the two molecules in the disk or a difference in the excitation of the two molecules. The HDO emitting surface is traced using a 167 K line whereas the methanol surface is traced using a stacked image of six methanol lines with upper energy levels ranging from 56 to 123 K. Observations of CO isotopologue emission in other protoplanetary disks around T Tauri and Herbig stars show that transitions with low upper energy levels generally emit from lower disk layers as the disk temperature decreases towards the disk midplane (Leemker et al. 2022; Paneque-Carreño et al. 2023). This could contribute to the observed difference in the emitting surfaces of HDO and methanol. However, the methanol surface is derived from a stacked image of six transitions to increase the signal-to-noise ratio. A low signal-to-noise analysis of the individual transitions did not reveal large differences between the emitting layers of lines with high (~ 123 K) and low (~ 56 K) upper energy levels. Therefore, excitation may contribute but is not expected to be the dominant driver of the radial offset between HDO and methanol. Thus, a difference in the underlying abundance structure due to the snow surface of HDO and methanol is likely responsible for the different emitting surfaces.

3.4.1 Layered or mixed ices on the grains

A difference in the underlying abundance structure could be caused by a difference in the sublimation temperature of HDO and methanol. Modelling of ice layers on grains shows that water and methanol are expected to be abundant in different layers as water is formed the hydrogenation of O and methanol through hydrogenation of CO ice (Taquet et al. 2012). Laboratory studies show that methanol sublimates at a temperature 20 K lower than water if the methanol ice is deposited on top of the water ice matrix (Collings et al. 2004). On the other hand, if the ices are mixed, methanol and water sublime at the same temperature. However, other laboratory experiments show that for a pre-cometary ice mixture ($\text{H}_2\text{O}:\text{CH}_3\text{OH}:\text{CO}:\text{CO}_2:\text{NH}_3=100:5.7:8.7:20.2:5.7$), the methanol desorbs in multiple stages including desorption at the temperature of a pure ice matrix and co-desorption with water (Martín-Doménech et al. 2014). Co-desorption of methanol

with the much more volatile CO ice has not been seen in experiments (Ligterink et al. 2018b). Therefore, the radial offset between the HDO and methanol snow surfaces in the V883 Ori disk could point to a layered ice structure instead of a mixed one. Whether this also holds for other molecules requires high spatial and spectral resolution observations of multiple molecules at high sensitivity.

In addition to the structure of the ices (segregated layers or mixed), the amount of ice on the grains also affects the sublimation temperature, as only the top layer of ice can sublimate efficiently. Zeroth order sublimation is the process for a thick ice layer consisting of multiple mono-layers. This ice desorbs at a temperature depending on the concentration with an increasing temperature for thicker ices. First order sublimation is relevant for ices that cover less than one mono-layer on the surface. Because this is the top layer, the desorption temperature is independent of the fractional coverage of the grain surface. As the ice on grains in protoplanetary disks is dominated by water ice, the desorption of water may follow a zeroth order profile, whereas the less abundant methanol ice could be dominated by a first order process. In particular, Minissale et al. (2022) find that in this case a monolayer of methanol ice on an amorphous water ice layer desorbs at a somewhat lower temperature than water in the laboratory, consistent with the results in the V883 Ori disk. Observations of $^{13}\text{CH}_3\text{OH}$ and H_2^{18}O in the V883 Ori disk show that the water to methanol ratio is 6 after correcting for the isotopologue ratios but not correcting for the optical depth of the dust (Lee et al. 2019; Tobin et al. 2023). Therefore, the difference between zeroth and first order desorption could contribute to the difference in the HDO and methanol snow surfaces that are observed. However, the abundance of HDO is much lower than that of H_2O so both HDO and methanol are much less abundant than H_2O in the ice. In addition, methanol ice generally extends multiple monolayers. Therefore, the effect of zeroth and first order desorption may contribute somewhat to the difference in the emitting surfaces, but it is not expected to be the dominant driver.

3.4.2 HDO and methanol snow surfaces in other disks

HDO and methanol have both been observed in the edge-on protostellar disk around the HH 212 system. The emitting region of methanol is constrained to a ~ 15 au thick layer that is elevated above the disk midplane at radii larger than 19 au up to a radius of ~ 40 au where the layer extends from 15 – 30 au (Lee et al. 2022). Therefore, the largest midplane radius where gas-phase methanol is seen in this disk is 19 au. Additionally, the emitting region of HDO in the same disk is constrained to be < 60 au using a warm transition (Codella et al. 2018). As the < 60 au radius of the water emitting region in this disk is potentially much larger than that of methanol, the upper limit is not sufficiently stringent to determine the order of the snowlines in the HH 212 disk, though the results could be consistent with those found in the V883 Ori disk presented in this work.

The snow surface of other molecules such as CO, CS, and H_2CO have been spatially resolved in the edge-on disks L1527 IRS and IRAS 04302+2247 (van't Hoff et al. 2020; Podio et al. 2020). Additionally, a tentative detection of methanol in the L1527 IRS disk has been reported, though similar observations did not detect

methanol in the same disk. The emitting surfaces of CO, CS, and H₂CO in these edge-on disks are much more shallow with a slope $\Delta z/\Delta r \lesssim 1$ than those seen in the V883 Ori disk. This could be due to a difference in the evolutionary stage of the objects as the V883 Ori disk is located around an outbursting Class I/II star whereas the L1527 IRS and IRAS 04302+2247 disks are not and are still embedded. Additionally, the difference in the slope of the snow surfaces could be due to a difference in vertical mixing between the disks. Bosman & Bergin (2021) suggested that the water snowline in the AS 205 disk may be vertical due to continuous vertical mixing, locking the water as ice in the disk midplane. If this mechanism is the dominant mechanism driving the slope of the snowline in these three disks, then the vertical mixing may be more efficient in the V883 Ori disk than in the L1527 IRS and IRAS 04302+224 disks.

3.5 Conclusions

In this work we present the emitting surfaces of HDO and methanol, the only two molecules observed at sufficiently high spatial and spectral resolution and sensitivity that are not dominated by the remnant envelope emission to derive the emitting heights. The emitting surfaces are measured using the ALFAHOR package (Paneque-Carreño et al. 2023) and provide the first direct measurement of the HDO and methanol snow surfaces in a moderately inclined disk, V883 Ori. In summary we find that:

1. The snow surfaces of HDO and methanol are directly traced by the emitting surface and are close to vertical.
2. Gas-phase HDO is seen in the disk midplane up to ~ 60 au, consistent with a water snowline location > 60 au.
3. The emitting surface of methanol is consistently at a $\sim 10 - 20$ au larger radius than that of HDO indicating a difference in their desorption temperatures likely due to a layered ice structure.

The steep snow surfaces seen in the V883 Ori disk could hint at efficient vertical mixing in protoplanetary disks. Observations of other COMs together with optically thin CO isotopologue emission at high spatial and spectral resolution and sensitivity are needed to derive their snow surfaces and the structure of the disk as traced by CO isotopologues. This will provide insights in the ices present on the grains together with crucial information to interpret unresolved observations of e.g. protostellar envelopes. The V883 Ori disk is a unique laboratory to observationally determine the (relative) binding energies of COMs.

3.6 Acknowledgements

We would like to thank Niels Ligterink for useful discussions. This work is supported by grant 618.000.001 from the Dutch Research Council (NWO). Astrochemistry in Leiden is supported by funding from the European Research Council

(ERC) under the European Union’s Horizon 2020 research and innovation programme (grant agreement No. 101019751 MOLDISK), by the Netherlands Research School for Astronomy (NOVA). This paper makes use of the following ALMA data: ADS/JAO.ALMA#2021.1.00186.S. ALMA is a partnership of ESO (representing its member states), National Science Federation (NSF) (USA) and NINS (Japan), together with NRC (Canada), MOST and ASIAA (Taiwan), and KASI (Republic of Korea), in cooperation with the Republic of Chile. The Joint ALMA Observatory is operated by ESO, AUI/NRAO and NAOJ. The National Radio Astronomy Observatory is a facility of the National Science Foundation operated under cooperative agreement by Associated Universities, Inc.

Appendix

3.A Channel maps

In this section the channel maps of the HDO and the stacked methanol lines are presented, see Fig. 3.A.1 and 3.A.2. The blue and white contours indicate the masks drawn after visual inspection of the emission in the near and far side of the disk respectively.

3.B Optical depth

The optical depths of the HDO and methanol lines is estimated using RADEX (Schöier et al. 2005). The typical peak intensity of the 225 GHz HDO line is 20 mJy beam^{-1} with a maximum of $\sim 25 \text{ mJy beam}^{-1}$. Using a line width of 2 km s^{-1} following Lee et al. (2019), and excitation temperature of 200 K following Tobin et al. (2023), and assuming local thermodynamic equilibrium, we find that the typical line optical depth in the disk is 0.3 with a maximum of 0.4. The six stacked methanol lines all have similar Einstein- A coefficients of $(2-6) \times 10^{-5} \text{ s}^{-1}$. Therefore, only the warmest (123 K) and coldest (56 K) methanol lines used in the stacking are considered. The resulting optical depths for the methanol lines are typically 0.4 (56 K line) and 0.3 (123 K line) with a maximum of 0.4 for both lines. As the other methanol lines have similar Einstein- A coefficients, identical upper state degeneracies, and upper energy levels that fall within the explored range, their optical depth is expected to fall in the same range as well. The stacked methanol image is thus composed of six unblended lines that are marginally optically thick. However, the similar intensity of the six lines may indicate that the emission on the other hand is more optically thick than suggested by this simple calculation. Therefore, the HDO line and probably also the methanol lines with the highest (123 K) and lowest (56 K) upper energy levels are likely marginally optically thick and thus trace the snow surface.

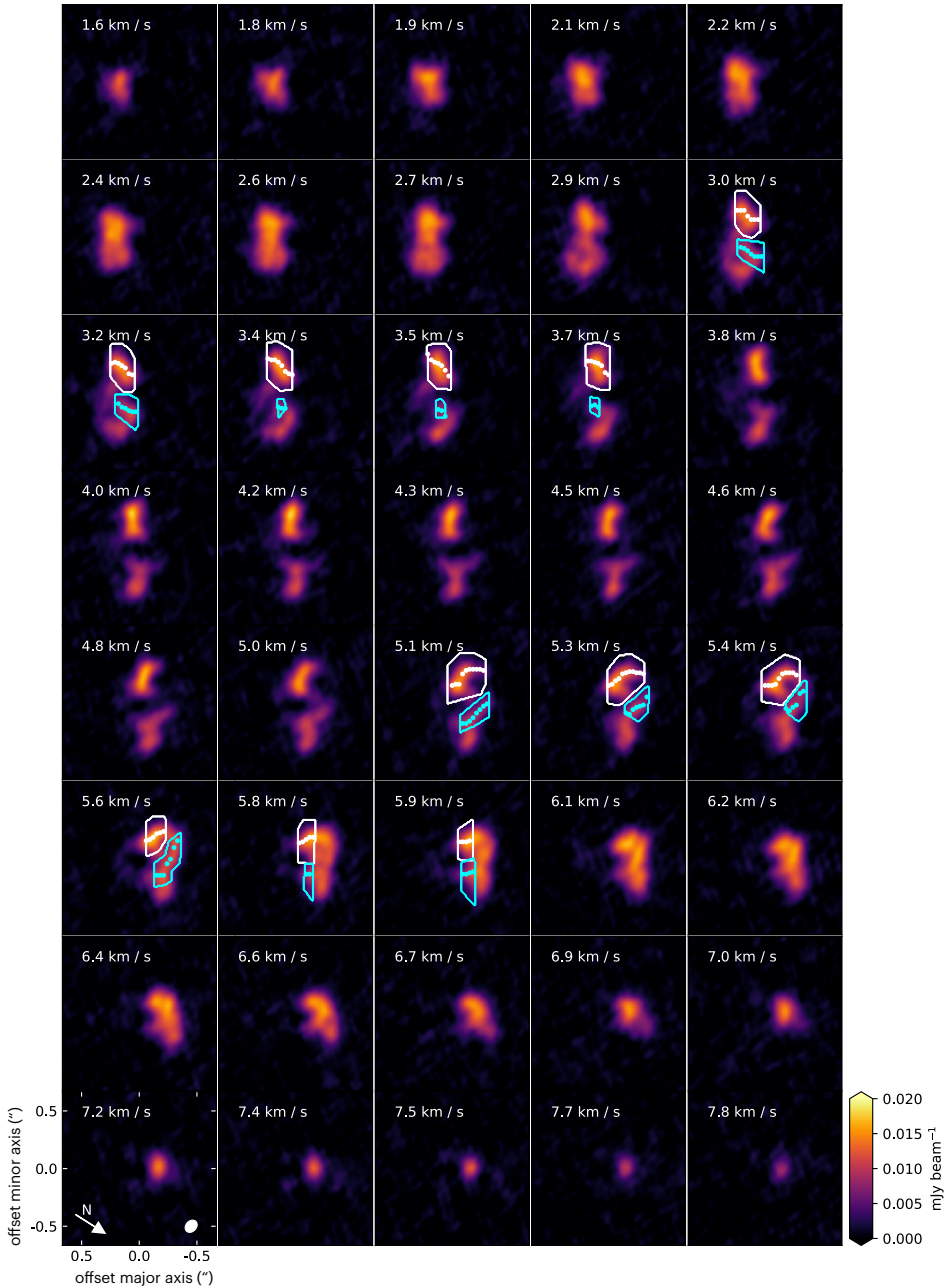


Figure 3.A.1: Channel maps of the stacked methanol emission in the V883 Ori disk. The channel maps are rotated such that the disk major axis is horizontal. North and the beam of the observations are indicated in the bottom left panel by the white arrow and the white ellipse, respectively. The blue (white) contours indicate the masks encompassing the emission from the near (far) side of the disk after visual inspection. The blue (white) dots within the mask trace the emission peak in the direction of the disk major axis.

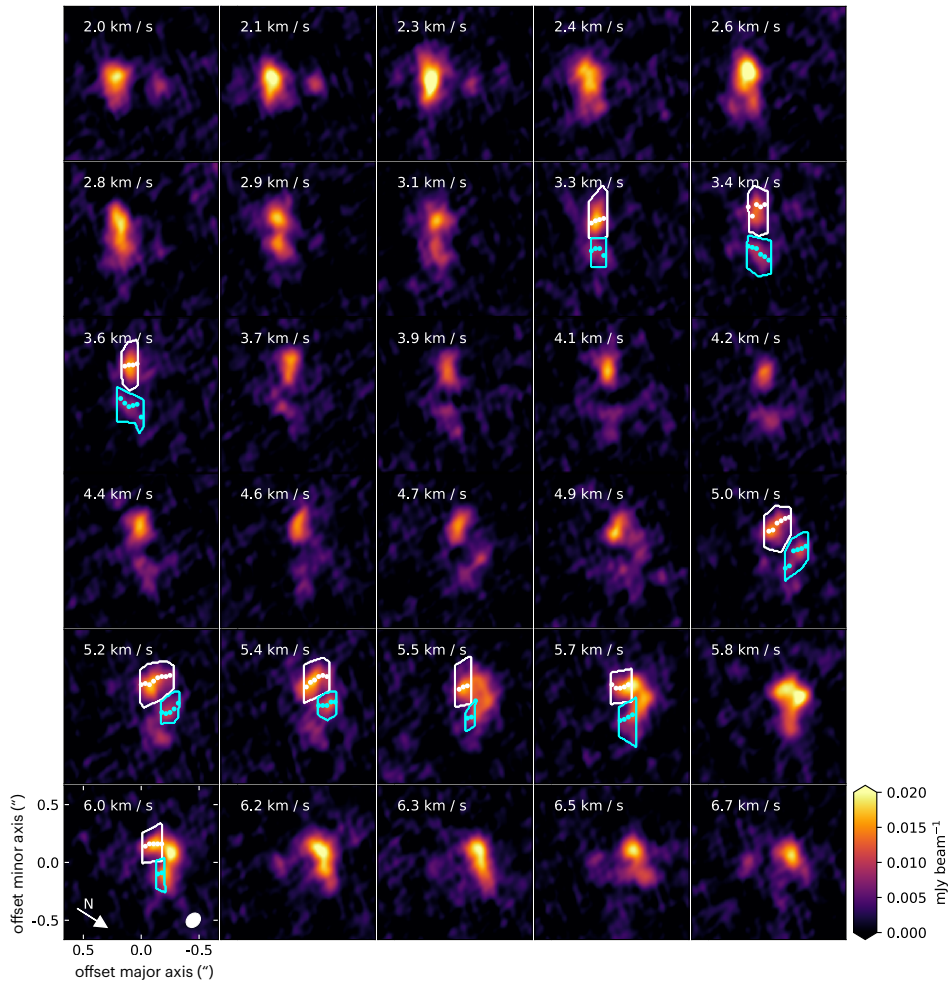


Figure 3.A.2: Same as Fig. 3.A.1 but then for the HDO line at 225 GHz.

Chapter 4

Gas temperature structure across transition disk cavities

M. Leemker, A. S. Booth, E. F. van Dishoeck, A. F. Pérez-Sánchez,
J. Szulágyi, A. D. Bosman, S. Bruderer, S. Facchini, M. R.
Hogerheijde, T. Paneque-Carreño, J. A. Sturm

2022 A&A, 663, 23

Abstract

Context. Most disks observed at high angular resolution show signs of substructures, such as rings, gaps, arcs, and cavities, in both the gas and the dust. To understand the physical mechanisms responsible for these structures, knowledge about the gas surface density is essential. This, in turn, requires information on the gas temperature.

Aims. The aim of this work is to constrain the gas temperature as well as the gas surface densities inside and outside the millimeter-dust cavities of two transition disks: LkCa15 and HD 169142, which have dust cavities of 68 AU and 25 AU, respectively.

Methods. We use some of the few existing ALMA observations of the $J = 6 - 5$ transition of ^{13}CO together with archival $J = 2 - 1$ data of ^{12}CO , ^{13}CO , and C^{18}O . The ratio of the ^{13}CO $J = 6 - 5$ to the $J = 2 - 1$ transition is used to constrain the temperature and is compared with that found from peak brightness temperatures of optically thick lines. The spectra are used to resolve the innermost disk regions to a spatial resolution better than that of the beam of the observations. Furthermore, we use the thermochemical code DALI to model the temperature and density structure of a typical transition disk as well as the emitting regions of the CO isotopologs.

Results. The ^{13}CO $J = 6 - 5$ and $J = 2 - 1$ transitions peak inside the dust cavity in both disks, indicating that gas is present in the dust cavities. The kinematically derived radial profiles show that the gas is detected down to 10 and 5–10 AU, much farther in than the dust cavities in the LkCa15 and HD 169142 disks, respectively. For LkCa15, the steep increase toward the star in the ^{13}CO $J = 6 - 5$ transition, in contrast to the $J = 2 - 1$ line, shows that the gas is too warm to be traced by the $J = 2 - 1$ line and that molecular excitation is important for analyzing the line emission. Quantitatively, the $6 - 5/2 - 1$ line ratio constrains the gas temperature in the emitting layers inside the dust cavity to be up to 65 K, warmer than in the outer disk, which is at 20–30 K. For HD 169142, the lines are optically thick, complicating a line ratio analysis. In this case, the peak brightness temperature constrains the gas in the dust cavity of HD 169142 to be 170 K, whereas that in the outer disk is only 100 K. The data indicate a vertical structure in which the ^{13}CO $6 - 5$ line emits from a higher layer than the $2 - 1$ line in both disks, consistent with exploratory thermochemical DALI models. Such models also show that a more luminous central star, a lower abundance of polycyclic aromatic hydrocarbons, and the absence of a dusty inner disk increase the temperature of the emitting layers and hence the line ratio in the gas cavity. The gas column density in the LkCa15 dust cavity drops by a factor of > 2 compared to the outer disk, with an additional drop of an order of magnitude inside the gas cavity at 10 AU. In the case of HD 169142, the gas column density drops by a factor of 200–500 inside the gas cavity.

Conclusions. The gas temperatures inside the dust cavities steeply increase toward the star and reach temperatures of up to 65 K (LkCa15) and 170 K (HD 169142) on scales of ~ 15 –30 AU, whereas the temperature gradients of the emitting layers in the outer disks are shallow, with typical temperatures of 20 – 30 and 100 K,

respectively. The deep drop in gas column density inside the HD 169142 gas cavity at <10 AU could be due to a massive companion of several M_J , whereas the broad dust-depleted gas region from 10-68 AU for LkCa15 may imply several lower mass planets. This work demonstrates that knowledge of the gas temperature is important for determining the gas surface density and thus whether planets, and if so what kinds of planets, are most likely to be carving the dust cavities.

4.1 Introduction

High angular resolution observations of protoplanetary disks show structures in both gas and dust (e.g., Andrews et al. 2010; van der Marel et al. 2015; Fedele et al. 2017; Andrews et al. 2018; Huang et al. 2018; Long et al. 2018; Öberg et al. 2021; see Andrews 2020 for review). One favored mechanism that can explain most of these substructures is planet-disk interactions ($> 20 M_{\text{Earth}}$) (e.g., Bryden et al. 1999; Zhu et al. 2014; Dipierro et al. 2015; Rosotti et al. 2016; Dong et al. 2018; Zhang et al. 2018; Szulágyi et al. 2018; Binkert et al. 2021). If these structures are caused by embedded planets, these gaps should be deep in both gas and dust (at least a factor of 10 depletion in the gas). However, the structures could also be caused by a change in the temperature that is unrelated to a potential embedded planet. Therefore, knowledge of the temperature profile across these structures is needed to distinguish truly empty gaps from emission drops related to temperature decreases.

There are only a few cases where young exoplanets have been caught in the act of formation. Two young planets and their disks have recently been directly imaged in the central dust cavity of the PDS 70 disk (Keppler et al. 2018; Haffert et al. 2019; Isella et al. 2019; Benisty et al. 2021), and three more have been located in gaps in the HD 163296 and HD 97048 disks based on localized azimuthal perturbations in the disk velocity structure traced by CO kinematics (Teague et al. 2018a; Pinte et al. 2019; Teague et al. 2019; Izquierdo et al. 2021). Two of these disks are typical transition disks with large millimeter-dust cavities, supporting the expectation that planets are present in most (transition) disks. The presence of massive planets ($>$ several M_{Jup}) in a number of other disks, including those around HD 100546 and HD 169142, has been suggested, but confirmation by direct imaging is still lacking (e.g., Quanz et al. 2013a,b; Osorio et al. 2014; Reggiani et al. 2014; Walsh et al. 2014a; Currie et al. 2017; Follette et al. 2017; Rameau et al. 2017; Casassus & Pérez 2019; Toci et al. 2020). Similarly, planets have been proposed and refuted in the LkCa15 disk (Kraus & Ireland 2012; Sallum et al. 2015; Currie et al. 2019). Other explanations for the structures seen in disks include disk winds, internal photoevaporation, opacity variations, chemical effects, and magnetohydrodynamics (e.g., Clarke et al. 2001; Birnstiel et al. 2015; Zhang et al. 2015; Flock et al. 2015; Simon et al. 2016). Spatially resolved observations of gas in and near a gap or cavity can help us distinguish between these scenarios. In particular, the presence of massive planets should result in deep gas cavities (gas depleted by at least a factor of 10) that are somewhat smaller than the deep dust cavities.

In this work we focus on transition disks with large cavities as they are more easily resolved by current Atacama Large Millimeter/submillimeter Array (ALMA) observations. Fully resolving the cavity with multiple beams is crucial for deriving the properties of the gas and dust in the cavities (Bruderer 2013; Szulágyi et al. 2018). The gas shows a different morphology than the dust, with the gas cavity indeed typically smaller than that in the dust (e.g., Bruderer et al. 2014; Perez et al. 2015; van der Marel et al. 2015, 2016; Wölfer et al. 2021). However, observations do not trace the column density of the gas and dust directly. A gas cavity seen in molecular line emission can be due to an actual decrease in the surface density, but it can also be caused by a drop in the gas temperature in that region of the disk or a combination of both (Facchini et al. 2017, 2018). Therefore, the temperature needs to be known to accurately derive the surface density in the gas cavity.

The gas temperature inside and outside the cavity is controlled by a number of heating and cooling processes, including the photoelectric effect on polycyclic aromatic hydrocarbons (PAHs) and small grains exposed to UV radiation, gas-grain coupling, and atomic and molecular line emission (e.g., Bakes & Tielens 1994; Kamp & van Zadelhoff 2001; Weingartner & Draine 2001; Gorti & Hollenbach 2004; Woitke et al. 2009; Bruderer et al. 2012; Bruderer 2013). A crucial ingredient is the local UV field. The radiation field at each point in the disk depends on a number of parameters: the stellar type of the host star, the UV luminosity from accretion of material onto the star, the abundance of dust and PAHs and their properties, and the presence of an inner disk that shields radiation from the host star. Polycyclic aromatic hydrocarbons that heat the gas through the photoelectric effect and dusty inner disks are commonly observed in transition disks (Habart et al. 2006; Brown & Bolina 2007; Geers et al. 2007a,b; Merín et al. 2010; Isella et al. 2019; Pérez et al. 2019; Facchini et al. 2020; Francis & van der Marel 2020). Detailed modeling by Jonkheid et al. (2006), Woitke et al. (2009), Bruderer et al. (2012), Bruderer (2013), Facchini et al. (2017), Facchini et al. (2018), Alarcón et al. (2020), and Rab et al. (2020) shows that the temperature of the gas changes when a gap or cavity is introduced in the model. Whether the gas becomes warmer or colder than the gas in the full disk model depends on parameters such as the grain sizes and on the gas-to-dust ratio. A planet in the gap can locally increase the temperature by several tens of kelvins (Cleeves et al. 2015a; Szulágyi et al. 2018).

Pre-ALMA, the gas temperature in the emitting layers was derived by comparing observations of various CO lines, up to $J_u \geq 14$ lines observed with ground-based telescopes and *Herschel* (e.g., van Zadelhoff et al. 2001; Sturm et al. 2010; Bruderer et al. 2012; Dent et al. 2013; Fedele et al. 2013b; Meeus et al. 2012; Green et al. 2013; Meeus et al. 2013). These observations mainly probe the temperature in intermediate disk layers ($z/r \sim 0.5$) at 10-200 AU from the central star (Fedele et al. 2016).

With the advent of ALMA, spatially resolved observations have been used together with detailed modeling of individual disks with large dust cavities (e.g., Bruderer et al. 2012; van der Marel et al. 2015, 2016; Kama et al. 2016; Schwarz et al. 2021) and without large dust cavities (e.g., Schwarz et al. 2016; Pinte et al. 2018a; Calahan et al. 2021). The temperature of the (outer) disk midplane is

derived from the location of the snow lines of major species such as H_2O and CO (Mathews et al. 2013; Qi et al. 2013; van 't Hoff et al. 2017, 2018b; Qi et al. 2019; Leemker et al. 2021). Additionally, rotational diagrams are used to derive the temperature of intermediate layers in disks (e.g., Schwarz et al. 2016; Loomis et al. 2018; Pegues et al. 2020; Terwisscha van Scheltinga et al. 2021). In this work we study the rarely observed $J = 6 - 5$ transition of ^{13}CO ($E_u = 111.1$ K) in two transition disks, LkCa15 and HD 169142, which have spatially resolved ALMA data. The combination of this high transition with the more commonly observed ^{13}CO $J = 2 - 1$ ($E_u = 15.9$ K) transition allows us to study the temperature and column density in the cavities of two transition disks and link them to the rest of the disk. The very high resolution of the ^{13}CO $J = 6 - 5$ data provides a unique opportunity to study the gas temperature in these disks in detail.

The sources and observations are discussed in Sect. 4.2. Next, the continuum and molecular line emission across the cavities of LkCa15 and HD 169142 are presented in Sect. 4.3. The relevant equations for the temperature analysis are summarized and applied to the data in Sect. 4.4, where we derive the temperature, column density, and optical depth using CO isotopologs. We put the derived temperature structure in context using a representative thermochemical model in Sect. 4.5. Finally, we discuss and summarize our findings in Sects. 4.6 and 4.7, respectively.

4.2 Observations

In this paper we analyze ALMA observations of CO isotopologs in the LkCa15 and HD 169142 disks. An overview of the stellar parameters is given in Table 4.1 and an overview of the observations is presented in Table 4.2. The sources and data reduction are discussed in this section.

4.2.1 The sources

LkCa15 is a transition disk with a large dust cavity up to 68 AU radius. The system is located at 157.2 ± 0.7 pc (Gaia Collaboration et al. 2018). The disk surrounding the K3 type T Tauri star LkCa15 is inclined by $\sim 50 - 55^\circ$ (Wolk & Walter 1996; van der Marel et al. 2015; Facchini et al. 2020). High resolution ALMA Band 6 observations reveal that, in addition to the cavity, the dust is highly structured with multiple narrow rings observed at high resolution (Facchini et al. 2020). Small grains, traced by scattered light observations, have been seen out to ~ 30 AU radius inside the millimeter-dust cavity, suggesting that gas is present in this disk region (Thalmann et al. 2016; Oh et al. 2016). Furthermore, ALMA observations have revealed that the dust cavity is not completely devoid of millimeter grains as the continuum intensity in the dust cavity peaks at $73.7 \pm 6.9 \mu\text{Jy beam}^{-1}$ (Facchini et al. 2020). Here we present the first ALMA observations of a gas cavity in the LkCa15 disk. Previous observations by van der Marel et al. (2015) do not have the spatial resolution to resolve this gap in the gas. Furthermore, CO ro-vibrational lines at $5 \mu\text{m}$ also indicate a low CO gas column in the inner 0.3 AU of the LkCa15

Table 4.1: Source properties.

Disk	RA <i>J</i> 2016	Decl. <i>J</i> 2016	M_* (M_\odot)	M (M_\odot)	L_* (L_\odot)	spectral type	age (Myr)	distance (pc)	v_{sys} (km s^{-1})	incl. ($^\circ$)	PA ($^\circ$)	Refs.
LkCa15	04:39:17.79	22:21:03.39	1.3	$10^{-9.2}$	1.1	K3	~ 5	157.2	6.25	50	62	1-5
HD 169142	18:24:29.78	-29:46:49.33	1.7	$10^{-7.4}$	10	F1	~ 6	114.9	6.9	13	5	1,6-13

Notes. References. (1) Gaia Collaboration et al. 2018, (2) Donati et al. 2019, (3) Wolk & Walter 1996, (4) this work, (5) Facchini et al. 2020, (6) Blondel & Djie 2006, (7) Following Fedele et al. 2017, based on the optical and UV extinction (Malfait et al. 1998) and the new Gaia distance, (8) Gray et al. 2017, (9) Grady et al. 2007, (10) Fedele et al. 2017, (11) Raman et al. 2006, (12) Panić et al. 2008, and (13) Guzmán-Díaz et al. 2021.

Table 4.2: Molecular line and continuum observations used in this work.

Disk	Transition	Int. flux ⁽¹⁾ (Jy km s ⁻¹)	Channel width (km s ⁻¹)	Channel rms (mJy beam ⁻¹)	Beam	MRS ⁽²⁾ Robust	Project code	PI	
LkCa15	¹² CO $J = 2 - 1$	16 ± 2	0.04	8.9	0 ^{''} .34 × 0 ^{''} .25 (−9.7°)	3 ^{''} .7	2018.1.01255.S	M. Benisty	
	¹³ CO $J = 2 - 1$	1.4 ± 0.2	0.17	4.4	0 ^{''} .17 × 0 ^{''} .13 (−13.7°)	0 ^{''} .5	2018.1.00945.S	C. Qi	
	¹³ CO $J = 2 - 1$	5.8 ± 0.6	0.33	3.1	0 ^{''} .35 × 0 ^{''} .25 (26.6°)	4 ^{''} .0	2018.1.00945.S	C. Qi	
	¹³ CO $J = 6 - 5$	7.5 ± 0.8	0.5	2.8	0 ^{''} .08 × 0 ^{''} .05 (−18.6°)	1 ^{''} .2	2017.1.00727.S	J. Szulágyi	
	¹³ CO $J = 6 - 5$	8.2 ± 0.9	0.44	25	0 ^{''} .32 × 0 ^{''} .30 (−31.2°)	2 ^{''} .1	2017.1.00727.S	J. Szulágyi	
	C ¹⁸ O $J = 2 - 1$	1.0 ± 0.1	0.33	3.9	0 ^{''} .36 × 0 ^{''} .27 (26.6°)	4 ^{''} .0	2018.1.00945.S	C. Qi	
	0.45 mm cont.		0.16		0 ^{''} .071 × 0 ^{''} .048 (−23.5°)	1 ^{''} .2	2017.1.00727.S	J. Szulágyi	
	HD 169142	¹² CO $J = 2 - 1$	9.3 ± 0.9	0.17	1.7	0 ^{''} .05 × 0 ^{''} .029 (78.8°)	0 ^{''} .6	2016.1.00344.S	S. Pérez ⁽³⁾
		¹³ CO $J = 2 - 1$	4.3 ± 0.4	0.17	2.3	0 ^{''} .054 × 0 ^{''} .035 (78.4°)	0 ^{''} .6	2016.1.00344.S	S. Pérez ⁽³⁾
		¹³ CO $J = 6 - 5$	6.1 ± 0.7	0.44	12	0 ^{''} .055 × 0 ^{''} .054 (86.2°)	0 ^{''} .6	2017.1.00727.S	J. Szulágyi
C ¹⁸ O $J = 2 - 1$		2.0 ± 0.2	0.17	1.4	0 ^{''} .052 × 0 ^{''} .031 (78.6°)	0 ^{''} .6	2016.1.00344.S	S. Pérez ⁽³⁾	
0.45 mm cont.			0.52		0 ^{''} .038 × 0 ^{''} .037 (−72.0°)	0 ^{''} .6	2017.1.00727.S	J. Szulágyi	
1.3 mm cont.			0.022		0 ^{''} .036 × 0 ^{''} .018 (73.0°)	0 ^{''} .6	2016.1.00344.S	S. Pérez ⁽³⁾	

Notes. ⁽¹⁾ Disk integrated flux calculated from the region within the Keplerian mask. The error includes the 10% absolute flux calibration error but not any uncertainty due to resolved-out large-scale emission. ⁽²⁾ The maximum recoverable scale (MRS) is estimated as $\sim 0.983\lambda/L_5$, with λ the wavelength and L_5 the fifth percentile baseline of the configuration. ⁽³⁾ Data first presented by Pérez et al. (2019). ⁽⁴⁾ Data first presented in Facchini et al. (2020). ⁽⁵⁾ Natural weighting with a 0^{''}.15 uv taper. ⁽⁶⁾ ALMA image for which high and intermediate spatial resolution ALMA data are combined. ⁽⁷⁾ Product data. R. refers to the robust parameter used for the imaging of the data.

disk (Salyk et al. 2009).

The dust in HD 169142 is highly structured, similar to the LkCa15 disk (Fedele et al. 2017; Pérez et al. 2019). Yet, HD 169142 is a Herbig F1 star (Gray et al. 2017) with a mass of $1.7 M_{\odot}$ (Blondel & Dje 2006) at 114.9 ± 0.4 pc (Gaia Collaboration et al. 2018) with its surrounding disk seen almost face-on ($i = 13 \pm 1^{\circ}$, Raman et al. 2006; Panić et al. 2008). A small (~ 0.3 AU) and variable near-IR inner dust disk has been observed in HD 169142 (Wagner et al. 2015; Chen et al. 2019). This inner dust disk has also been detected in high resolution ALMA observations (Pérez et al. 2019). The HD 169142 disk not only has structures in the dust, but also in the gas with rings and gaps. A gas cavity is seen in CO isotopologs, and DCO^+ is found to have an inner component and a ring at $\sim 50 - 230$ AU (Fedele et al. 2017; Carney et al. 2018).

4.2.2 Data

In this work we used new ALMA observations of the $^{13}\text{CO } J = 6 - 5$ transition in the LkCa15 and HD 169142 disks (2017.1.00727.S; PI: J. Szulágyi) as well as archival ALMA observations of the CO, ^{13}CO , and $\text{C}^{18}\text{O } J = 2 - 1$ lines (see Table 4.2). The continuum images were used to identify the dust cavity in both disks. All CO transitions for LkCa15 are consistent with a source velocity of 6.3 km s^{-1} . For HD 169142, a source velocity of 6.9 km s^{-1} is found. The line ratio of the $^{13}\text{CO } J = 6 - 5$ to the $J = 2 - 1$ transition was used to constrain the temperature across the cavities of both disks, and the optical depth of the $J = 2 - 1$ transition was determined from the ratio with the $\text{C}^{18}\text{O } J = 2 - 1$ transition. Finally, we also used the brightness temperature of optically thick lines as a temperature probe. Subtracting the continuum may remove line flux from the CO isotopologs as the continuum and the molecular lines may be optically thick in these disks. In this case, the continuum flux at the frequencies of the CO isotopolog emission is overestimated as it is absorbed by the CO isotopologs (Isella et al. 2016; Weaver et al. 2018). Hence, we did not subtract the continuum for the calculation of the peak brightness temperatures, but we did subtract it for the ratios of not very optically thick lines.

The spatial resolutions of the data for LkCa15 range from $\sim 0''.07$ to $0''.36$. The $\sim 0''.07$ data resolves the dust cavity with ~ 12 beams along the major axis of the bright ring in the Band 9 continuum, but $0''.36$ resolution is comparable to the minor axis of the dust cavity, causing the flux of the outer disk to be smoothed into the dust cavity. All data in the HD 169142 disk have a high spatial resolution of $\sim 0''.05$ used in this work, resolving the dust cavity fully with ~ 9 beams within the first ring in the Band 9 continuum. The Band 9 data for LkCa15 were taken in two different ALMA configurations. The first one had a very high spatial resolution of $\sim 0''.05$ and a small maximum recoverable scale (MRS) of $0''.6$, and the second one had an intermediate spatial resolution of $\sim 0''.3$ and a larger MRS of $2''.1$. The latter data were self-calibrated using two rounds of phase calibration and one round of phase and amplitude calibration. We refer to these data as the intermediate resolution data. These self-calibrated data were also combined with the high resolution data to create a combined high resolution image with a large

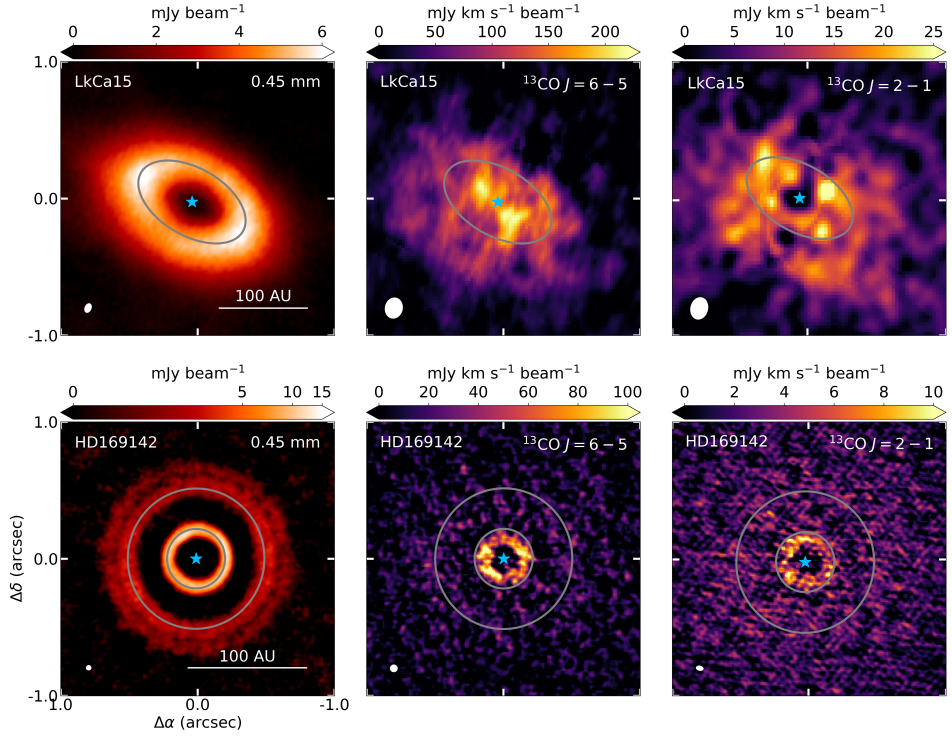


Figure 4.1: Band 9 continuum (left) and moment 0 maps of $^{13}\text{CO } J=6-5$ (middle) and $^{13}\text{CO } J=2-1$ (right) after Keplerian masking in the LkCa15 (top) and HD 169142 (bottom) disks. An asinh stretch is applied to the 0.45 mm continuum for HD 169142 to highlight the outer ring. We note the difference in the emission morphologies for the different panels, especially between the gas and dust. The position of the star is marked with a blue star in the center, and the rings in the continuum are indicated with gray ellipses in each panel. The beam is indicated by the white ellipse in the bottom-left corner of each panel, and a 100 AU scale bar is indicated in the bottom-right corner.

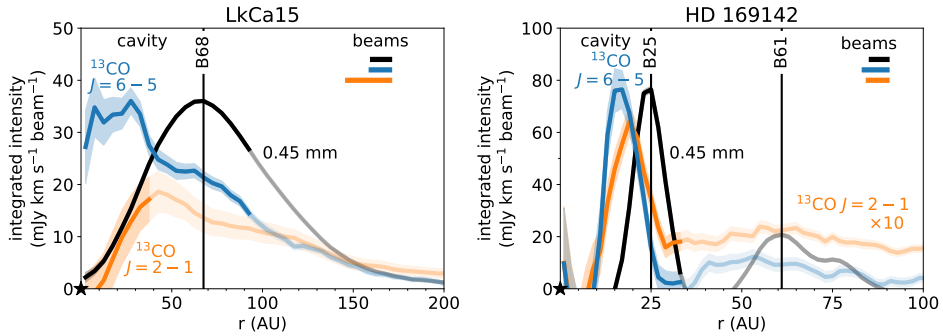


Figure 4.2: Deprojected azimuthally averaged radial profiles of the $^{13}\text{CO } J = 6 - 5$ and $J = 2 - 1$ transitions and the scaled 0.45 mm continuum in the LkCa15 (left) and HD 169142 disks (right). We note that, in the left-hand panel, the $^{13}\text{CO } J = 6 - 5$ line intensity is roughly constant in the inner ~ 30 AU in the LkCa15 disk, whereas the 0.45 mm continuum shows a dust cavity. The intensity outside the MRS of the observations is shown in a lighter shade of the corresponding colors. The position of the star is indicated by the black star in the bottom-left corner, and the beam sizes are indicated by horizontal bars in corresponding colors. Furthermore, the rings in the dust are indicated with the vertical black lines. We note that the MRS of the $^{13}\text{CO } J = 2 - 1$ line is small compared to the beam size due to the uv taper applied to this data set.

MRS. We refer to this as the combined high resolution image. Following the works of Czekala et al. (2021) and Öberg et al. (2021), we applied the Jorsater & van Moorsel (1995) (JvM) correction ($\epsilon = 0.20$ for the $^{13}\text{CO } J = 6 - 5$ transition, and $\epsilon = 0.23$ for the continuum) to the residuals to correct for the difference between the dirty and clean beams. Other data sets where both high and intermediate spatial resolution data are available were not combined, instead they were imaged separately. None of the other images were self-calibrated, but all images were corrected for the primary beam response.

For HD 169142, only the high spatial resolution scheduling block was observed. Similar to the intermediate spatial resolution data for LkCa15, we self-calibrated the data covering the $^{13}\text{CO } J = 6 - 5$ transition using two rounds of phase calibration and one round of phase and amplitude calibration. For the continuum, we used the product data from the ALMA archive as these data were taken during excellent weather conditions and the maximum possible bandwidth was used for the product data, leading to a very good signal-to-noise ratio.

To constrain the temperature in the cavities of both disks, we not only need the $^{13}\text{CO } J = 6 - 5$ transition, but also a lower J transition, as this provides a good lever arm in upper energy levels. Both disks have suitable archival ALMA observations of the $J = 2 - 1$ transition of CO isotopologs. Therefore, we compared the $^{13}\text{CO } J = 6 - 5$ transition ($E_{\text{up}} = 111.1$ K) to the $J = 2 - 1$ transition ($E_{\text{up}} = 15.9$ K). For HD 169142, we reimaged the data presented in Pérez et al. (2019) and for LkCa15, we use two different data sets. One covers ^{12}CO at a moderate spatial resolution of $\sim 0''.35$, and the other one covers ^{13}CO and C^{18}O at moderate ($\sim 0''.35$) and high spatial resolution ($\sim 0''.15$). The high spatial

resolution of the latter data set lowered the signal-to-noise ratio greatly compared to the intermediate spatial resolution images. Therefore, the high resolution ^{13}CO $J = 2 - 1$ transition was imaged using natural weighting and an $0''.15$ uv taper. This enhanced the signal-to-noise ratio while still resolving the gas cavity.

All observations were imaged using `multiscale` in the `tclean` function within the Common Astronomy Software Applications package (CASA) version 5.4.0. (combined image of ^{13}CO $J = 6 - 5$ for LkCa15), 5.6.0 (self-calibration) or 5.7.0 (all lines except the combined image of ^{13}CO $J = 6 - 5$ for LkCa15) (McMullin et al. 2007; Cornwell 2008). For each image, we chose the robust parameter that provides the best balance between the signal-to-noise ratio and the angular resolution. In order to compare the gas cavity with the outer disk, it is crucial to resolve the inner gas cavity. Therefore, we favored high angular resolution over a high signal-to-noise ratio. Each cube is imaged both before and after continuum subtraction, with the former image used to find the brightness temperature and the latter used for the other data products.

A Keplerian mask¹ was used to create a mask for the data while cleaning. The robust parameters, resulting disk integrated fluxes, beam sizes, sensitivities, and MRSs can be found in Table 4.2 for the observations in the LkCa15 and HD 169142 disks. The integrated flux of the high resolution ^{13}CO $J = 2 - 1$ transition in LkCa15 is a factor of 5 smaller than the intermediate resolution counterpart because most of the flux at scales larger than $0''.5$ (79 AU diameter) is resolved out in the high resolution data set. The integrated fluxes of the ^{12}CO , ^{13}CO , and C^{18}O $J = 2 - 1$ transitions for HD 169142 are 34-49% lower than those reported in Fedele et al. (2017), due to the smaller MRS of the data used in our work. The shortest baseline of the $J = 2 - 1$ data used in this work is 41.1 m, which is identical to the shortest baseline of the data set covering the ^{13}CO $J = 6 - 5$ transition in the HD 169142 disk. Furthermore, the MRS of our two data sets are both $0''.6$ (35 AU radius), and therefore the $J = 6 - 5$ and $J = 2 - 1$ data sets are expected to have a similar sensitivity to larger scales. The MRSs of the data used in this work are typically smaller than the size of the LkCa15 and HD 169142 disks. Therefore, the brightness temperatures may be underestimated at radii similar to the MRSs. The line ratios may also be affected by the MRSs causing small differences, for example, between the ^{13}CO $J = 6 - 5$ to $J = 2 - 1$ line ratio at (combined) high spatial resolution and that at intermediate spatial resolution in the LkCa15 disk. This is because the MRS of the combined high resolution ^{13}CO $J = 6 - 5$ image is larger than that of the high resolution $J = 2 - 1$, whereas the opposite is the case for the intermediate resolution data. Therefore, the ^{13}CO $J = 6 - 5$ to $J = 2 - 1$ line ratio of the (combined) high resolution will be slightly higher than that of the intermediate resolution data.

Finally, the data were imaged to specific beam sizes to compare the ^{13}CO $J = 6 - 5$ data to the corresponding ^{13}CO $J = 2 - 1$ transition. For LkCa15, a common restoring beam parameter of $0''.36 \times 0''.30$ (26.6°) was used to compare the azimuthally averaged radial profiles of different transitions and isotopologs. This procedure increased the beam size by at most $0''.05$. Similarly, a $0''.057 \times 0''.054$ (88.6°) restoring beam was used for the Band 6 and Band 9 data for HD 169142. As the

¹https://github.com/richteague/keplerian_mask

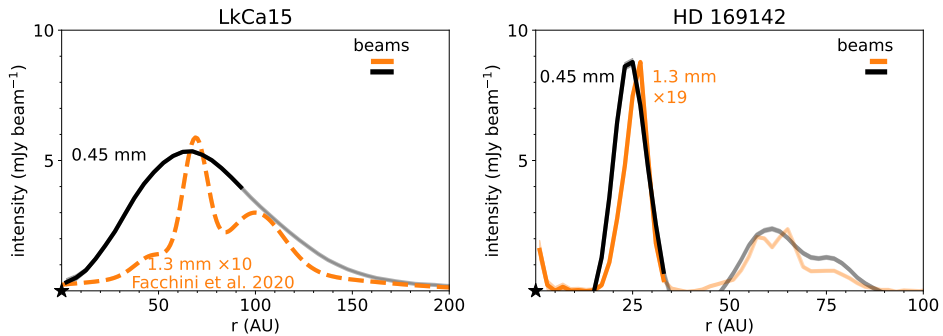


Figure 4.3: Deprojected azimuthally averaged profiles of the (combined) high resolution Band 9 continuum (black) in the LkCa15 (left) and HD 169142 disks (right). The intensity outside the MRS of the observations is shown in a lighter shade of the corresponding colors. For comparison, the fit to the LkCa15 Band 6 continuum by Facchini et al. (2020) (multiplied by 10 for the ease of comparison) and the observed HD 169142 Band 6 continuum (multiplied by 19 to match the Band 9 absolute intensity) are shown in orange. The beams are indicated in corresponding colors in the top-right corner, and the position of the star is marked with the black star in the bottom-left corner. We note that the Band 6 continuum in the LkCa15 disk is highly structured, whereas the Band 9 continuum shows a single ring.

combined high resolution $^{13}\text{CO } J = 6 - 5$ data for LkCa15 is a combined data product, these were not convolved using the restoring beam parameter but a uv taper was applied. This resulted in a cube with a $0''.15 \times 0''.13$ (-12.2°) beam, which was then smoothed using the `imsmooth` function in CASA to match the $0''.17 \times 0''.13$ (-13.7°) beam of the high resolution $^{13}\text{CO } J = 2 - 1$ data.

To improve the signal to noise in the moment 0 and peak intensity maps and on the azimuthally averaged radial profiles we used the same Keplerian mask that was also used during the cleaning process to mask any pixels that are not expected to contribute based on the Keplerian rotation of the disk. The noise on the azimuthally averaged radial profile is calculated from the channel rms using error propagation. First, the noise on the moment 0 map, σ_{mom0} (in $\text{mJy km s}^{-1} \text{ beam}^{-1}$), was calculated using the noise in one channel, σ_{chan} (in mJy beam^{-1}), the number of channels included for each pixel in the moment 0 map, N_{chan} , and the velocity resolution ΔV (in km s^{-1}):

$$\sigma_{\text{mom0}} = \sigma_{\text{chan}} \sqrt{N_{\text{chan}}} \Delta V. \quad (4.1)$$

Then we averaged this over an annulus and corrected for the number of independent measurements using the beam size

$$\sigma_{\text{azimuthal average}} = \sqrt{\frac{1}{N_{\text{beams}}} \sum_{\text{pix}} \sigma_{\text{mom0}}^2}, \quad (4.2)$$

where N_{beams} is the number of independent beams per annulus, restricted to be

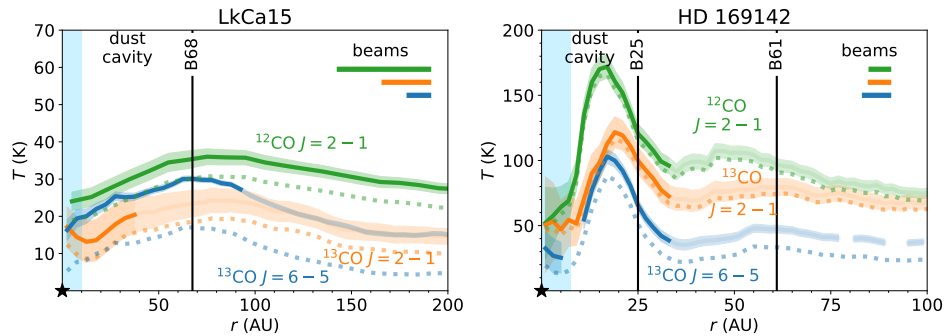


Figure 4.4: Deprojected azimuthally averaged radial profiles of brightness temperatures of the $^{12}\text{CO } J = 2 - 1$ (green), $^{13}\text{CO } J = 2 - 1$ (orange), and $^{13}\text{CO } J = 6 - 5$ (blue) transition for LkCa15 (left) and HD 169142 (right). The solid lines show the brightness temperature calculated using the Planck function, and the faded dotted colors show the Rayleigh-Jeans approximation. The vertical black lines indicate the rings seen in the Band 9 continuum, and the light blue region starting from 0 AU indicates the gas cavity. The MRS of the HD 169142 $J = 6 - 5$ data corresponds to a radius of 35 AU.

≥ 1 . The 10 % absolute calibration error was not included in these estimates, but it was included in the error on the total flux.

In summary, both the Band 9 and Band 6 LkCa15 data have spatial resolutions of $\sim 0''.07 - 0''.36$, with the $0''.36$ beam similar to the size of the dust cavity. The potential effects of this are discussed in Sect. 4.4.2. The data for HD 169142 have a much higher angular resolution of $\sim 0''.05$. Therefore, the dust cavity in the HD 169142 disk is fully resolved with ~ 9 beams inside the first ring in the Band 9 continuum data and 5 beams inside the ring in the $^{13}\text{CO } J = 6 - 5$ data.

4.3 Results

The (combined) high resolution Band 9 continuum and the $^{13}\text{CO } J = 6 - 5$ and $J = 2 - 1$ Keplerian masked integrated intensity maps are presented in Fig. 4.1. The Band 9 continuum data show a very clear dust cavity in both disks. This is in contrast to the $^{13}\text{CO } J = 6 - 5$ and $J = 2 - 1$ transitions that clearly peak inside the cavity seen in the dust, as shown in Fig. 4.2. Channel maps of the $^{13}\text{CO } 6 - 5$ data are presented in Figs. 4.A.1 and 4.A.2 and the deprojected azimuthally averaged radial profiles of the ^{12}CO and $\text{C}^{18}\text{O } J = 2 - 1$ transitions in Fig. 4.A.3.

4.3.1 Dust

The Band 9 continuum is compared to the Band 6 continuum in both disks in Fig. 4.3. The Band 6 continuum in the LkCa15 disk (left-hand panel) is the fit from Facchini et al. (2020) and clearly shows two narrow bright rings at 69 and 100 AU and a weaker ring at 47 AU. The Band 9 data on the other hand only show a broad single ring at 68 AU, regardless of the similar beam compared to

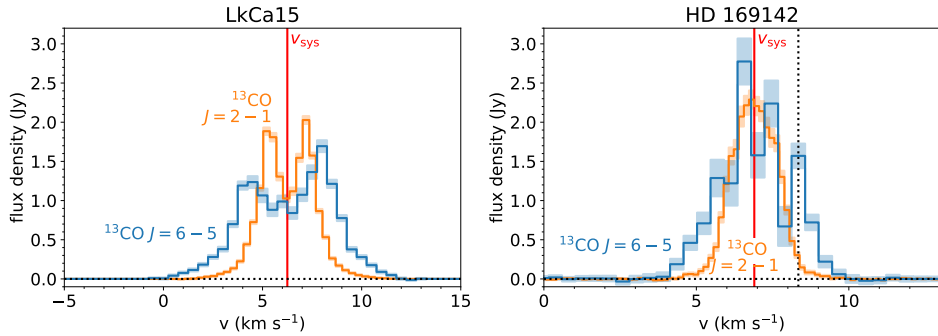


Figure 4.5: Keplerian masked spectrum of $^{13}\text{CO } J = 6 - 5$ (blue) and $^{13}\text{CO } J = 2 - 1$ (orange) of the LkCa15 (left) and HD 169142 disk (right). The shaded area indicates the 1σ uncertainty on the spectra. The vertical dotted black line in the HD 169142 panel indicates the bump in the spectrum corresponding to the inner ring at 17 AU seen in the azimuthally averaged radial profile of the $^{13}\text{CO } J = 6 - 5$ transition. We note that for S/N considerations, we show the $^{13}\text{CO } J = 2 - 1$ data at intermediate spatial resolution for LkCa15. The spectrum of the $^{13}\text{CO } J = 6 - 5$ transition for LkCa15 is obtained from the combined data sets.

the Band 6 data, suggesting that the Band 9 continuum is highly optically thick, hiding variations in the column density. Alternatively, the larger grains could be trapped in pressure traps whereas the somewhat smaller grains are not (e.g., Pinilla et al. 2016).

In contrast, the morphologies of the very high resolution 0.45 mm and 1.3 mm continuum for HD 169142 are very similar and only differ by a constant factor of 19 in intensity across the disk (right-hand panel Fig. 4.3). This factor of 19 in intensity is 2.3 times larger than what is expected for optically thick emission. The great similarity in morphology indicates that the trapping mechanism is more efficient in the HD 169142 disk than in the LkCa15 disk. Both the Band 6 and Band 9 continuum observations in the HD 169142 disk peak at very similar radii of 27 AU and 25 AU, respectively. The three rings seen at 57, 64, and 76 AU in the high resolution Band 6 data (Pérez et al. 2019) are observed as two marginally separated rings at 59 AU and 75 AU in the Band 9 data. The fact that we do not see three individual rings is likely due to the slightly larger beam size of our data set. Finally, we note that the high resolution data have some emission with negative intensity between the bright rings. This is likely due to the very high angular resolution, which results in a MRS smaller than the disk. The continuum data will be analyzed in more detail in a future paper.

4.3.2 Gas

4.3.2.1 Radial profiles

The $^{13}\text{CO } J = 6 - 5$ and $J = 2 - 1$ transitions in the LkCa15 disk (top row in Fig. 4.1 and left panel in Fig. 4.2) show very different morphologies compared to

the 0.45 mm continuum and to each other. The $^{13}\text{CO } J = 6-5$ data have a roughly constant integrated intensity in the inner ~ 30 AU, whereas the continuum and the $J = 2-1$ data both show a clear cavity. The $^{13}\text{CO } J = 2-1$ gas cavity is marginally resolved at our spatial resolution. These data suggest that there is still some gas in the dust cavity. Furthermore, they show that the line ratio of the $^{13}\text{CO } J = 6-5$ to the $J = 2-1$ line increases steeply inside the dust cavity, highlighting that molecular excitation, controlled by the gas temperature, and the gas surface density play a role in the molecular line emission.

The C^{18}O emission for LkCa15 decreases with decreasing radius between 50 and 100 AU but there appears to be some emission inward of 50 AU (see Fig. 4.A.3). This is likely due to the low signal-to-noise ratio and due to beam dilution of the gas cavity as the major axis of the C^{18}O beam is comparable to the minor axis of the dust cavity. Accordingly, C^{18}O emission from the region just outside the dust cavity is smoothed into the cavity, which affects our further analysis in Sect. 4.4.2. Therefore, we proceed to treat this as a 3σ upper limit on the C^{18}O emission inside the dust cavity.

In the case of the HD 169142 disk, the $^{13}\text{CO } J = 6-5$ and $J = 2-1$ lines peak ~ 10 AU inside the dust ring and just inside the ring seen in scattered light (Tschudi & Schmid 2021). Both ^{13}CO lines show a clear gas cavity inward of 10 AU, similar to the structure seen in other transition disks, such as DoAr44, IRS 48, HD 135344B, HD 142527, and PDS 70 (Bruderer et al. 2014; Perez et al. 2015; van der Marel et al. 2015, 2016, 2018; Facchini et al. 2021). Finally, the $^{13}\text{CO } J = 2-1$ transition is detected out to much larger radii than the $J = 6-5$ transition and the continuum data in both disks.

4.3.2.2 Brightness temperatures

The brightness temperatures of the two ^{13}CO and the $^{12}\text{CO } J = 2-1$ transition are presented in Fig. 4.4. First, we highlight the difference between the Rayleigh-Jeans approximation (dotted lines) and the full Planck curve (solid lines). The results are different because the Rayleigh-Jeans approximation is only valid if $h\nu \ll kT$, which results in $T \gg 32$ K for the $^{13}\text{CO } J = 6-5$ and $T \gg 11$ K for the ^{12}CO and $^{13}\text{CO } J = 2-1$ transitions. This criterion is not met for these observations except for the $J = 2-1$ data in the HD 169142 disk. Therefore, care should be taken when using the Rayleigh-Jeans approximation for high frequency observations and observations with low peak intensities.

Comparing their brightness temperatures directly shows that the disk around the Herbig star HD 169142 is warmer than that around the T Tauri star LkCa15. The brightness temperature of ^{12}CO is highest in both disks as this line becomes optically thick highest up in the disk and hence traces a warmer layer closer to the surface of the disk. The $^{13}\text{CO } J = 2-1$ transition traces a lower and hence colder layer due to its lower optical depth (see Fig. 4.B.1). The brightness temperature of both $^{13}\text{CO } J = 6-5$ lines is lower than that of the $^{12}\text{CO } J = 2-1$ lines. This is due to the lower optical depth of the $J = 6-5$ transition and due to its lower spectral resolution. This lower resolution lowers the peak flux by 6-13 K (40-60%) in LkCa15 and by 10-15 K (10-30%) in HD 169142 (see Appendix 4.A.3). All CO

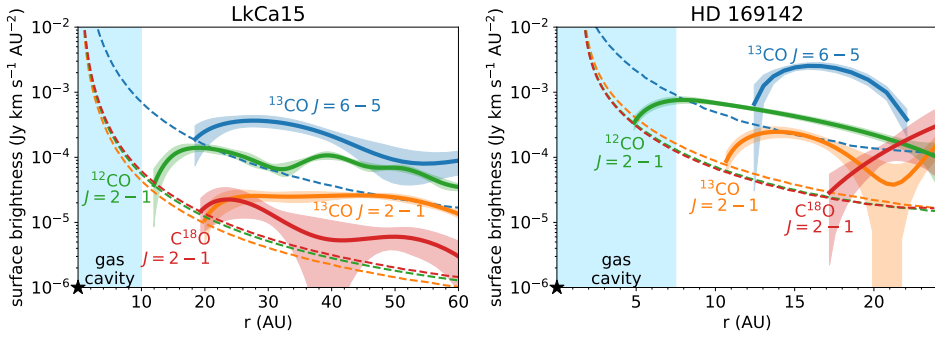


Figure 4.6: Surface brightness of the $^{13}\text{CO } J = 6 - 5$ (blue), $^{13}\text{CO } J = 2 - 1$ (orange), $^{12}\text{CO } J = 2 - 1$ (green), and $\text{C}^{18}\text{O } J = 2 - 1$ (red) lines inside the dust cavities derived using the kinematics. The dashed lines in corresponding colors indicate the detection limit for each line.

lines may become more optically thin in the outer disk and in the gas cavities, which lowers their brightness temperature. In the case of LkCa15, the gas inside the dust cavity may be similarly warm as in the HD 169142 disk, but this cannot be determined from the brightness temperatures presented here due to beam dilution and, optical depth effects in the inner disk.

For HD 169142, the ^{12}CO line indicates gas as warm as 170 K. The brightness temperature of the $^{13}\text{CO } J = 6 - 5$ transition for HD 169142 is somewhat lower than the corresponding $^{13}\text{CO } J = 2 - 1$ transition, which is not what is expected. The $J = 2 - 1$ emission is optically thick (see also Fig. 4.B.1), and hence its brightness temperature traces the kinetic temperature in the disk layer where its optical depth equals 1. For these temperatures, the molecular excitation is such that the optical depth of the $J = 6 - 5$ line is comparable to or larger than that of the $J = 2 - 1$ line. Therefore, the $J = 6 - 5$ transition should trace a higher layer and warmer temperatures. The reason that we do not observe this is likely due to the small MRS of $0''.6$ (35 AU radius) of the high resolution data, which resolves out some of the flux inside this radius. Furthermore, the shortest baseline of the $^{13}\text{CO } J = 6 - 5$ data is longer than that of the $J = 2 - 1$, causing the $J = 6 - 5$ data to be less sensitive to larger spatial scales. This is not reflected in the MRS of $0''.6$, because the MRS is calculated using the 5th percentile of the baseline distribution and is calculated assuming that the morphology of the emission resembles a uniform disk. Our observations show that the morphology of the $^{13}\text{CO } J = 6 - 5$ and $J = 2 - 1$ lines is different. Therefore, the low $^{13}\text{CO } J = 6 - 5$ brightness temperature may be partially due to the small MRS. Finally, we note that the $^{13}\text{CO } J = 6 - 5$ transition is not spectrally resolved for radii larger than ~ 30 AU, lowering the peak flux and hence the brightness temperature by 10-15 K (~ 10 -30%; see Appendix 4.A.3).

4.3.2.3 Spectra

The azimuthally averaged radial profiles discussed in the previous section show a very clear difference between the morphology of the $^{13}\text{CO } J = 6 - 5$ transition and the $J = 2 - 1$ transition for LkCa15. The spectra extracted from the Keplerian masked images of these two transitions are presented in Fig. 4.5.

Both disks clearly show that the $^{13}\text{CO } J = 6 - 5$ line profile is broader than that of the $J = 2 - 1$ line. This is another indication that the $J = 6 - 5$ transition is brighter than the $J = 2 - 1$ transition in the inner disk, as the innermost regions of the disk are rotating at the highest Keplerian velocity:

$$R = GM_{\star} \left(\frac{\sin(i)}{V_{\text{Kep}}} \right)^2, \quad (4.3)$$

with G the gravitational constant, M_{\star} the mass of the star, i the disk inclination, and V_{Kep} the Keplerian velocity of the gas.

Bosman et al. (2021c) used this principle to derive the surface brightness of molecular line emission in the innermost disk regions with a spatial resolution smaller than the beam. Using this kinematics fitting program, we are able to reconstruct the surface brightness of the molecular line emission in the innermost regions of the LkCa15 and HD 169142 disks. A $1''.0$ region was used to extract the spectrum for LkCa15 and a $0''.5$ region for HD 169142. No Keplerian mask was applied. Furthermore, the spectral resolution of the model was set to the native spectral resolution of the data and the spectra were modeled out to $\pm 60 \text{ km s}^{-1}$ from the velocity corresponding to the peak flux density. The surface brightness is fitted up to 80 AU (LkCa15) and 25 AU (HD 169142). Finally, ≥ 2 (LkCa15) and ≥ 3 (HD 169142) velocity resolution elements per model fitting point were used for the surface brightness. The model fitting points are separated by ≥ 6 AU (LkCa15) and ≥ 2 AU (HD 169142), effectively increasing the signal-to-noise ratio in the LkCa15 disk.

The resulting radial profiles for the ^{12}CO , ^{13}CO , and $\text{C}^{18}\text{O } J = 2 - 1$ and the $^{13}\text{CO } J = 6 - 5$ lines are presented in Fig. 4.6. The dashed lines indicate the detection limit for each radial profile in corresponding colors. In the LkCa15 disk, all transitions except for $^{12}\text{CO } J = 2 - 1$ drop below their detection limit around 20 AU. This is consistent with the azimuthal averages presented in Fig. 4.2 but now resolving the emission to a smaller spatial scale than what is obtained with the traditional azimuthally averaged radial profiles presented in Fig. 4.A.3. The $^{12}\text{CO } J = 2 - 1$ line is detected down to 12 AU, as ^{12}CO has the highest column density and hence the highest signal-to-noise ratio in the line wings, making it easier to detect than the less abundant isotopologs. As no steep increase in the surface brightness in the inner disk is detected in any of the lines presented here and the turnover of each line at 10 – 20 AU is significant compared to the corresponding detection limit, the results from the kinematically derived radial profiles can be interpreted as a ~ 10 AU cavity in the gas in the LkCa15 disk. Notably, this is significantly smaller than the cavity seen in the dust that peaks at 68 AU.

In the HD 169142 disk, the $^{13}\text{CO } J = 6 - 5$ and $J = 2 - 1$ transitions both drop below the detection limit at $\sim 10 - 12$ AU, similar to what is seen in the traditional

azimuthally averaged radial profiles. The C^{18}O $J = 2 - 1$ emission is only detected from 17 AU outward due to its low signal-to-noise ratio. On the other hand, ^{12}CO $J = 2 - 1$ is detected down to the smallest radius of 5 AU, similar to LkCa15. This is supported by the signal-to-noise ratio in the line wings (right-hand panel Fig. 4.A.5), where the ^{12}CO $J = 2 - 1$ transition is detected out to the largest velocities. As all lines quickly drop below their detection limits and their turn overs are significant, the results from the kinematically derived radial profiles in the HD 169142 disk can be understood as a deep gas cavity at $\sim 5 - 10$ AU.

In summary, the derived gas cavity radii in the LkCa15 and HD 169142 disks are smaller by $\sim 15 - 60$ AU than their dust cavity radii, consistent with models of planet-disk interaction and formation of dust traps (e.g., Pinilla et al. 2012a; de Juan Ovelar et al. 2013). Furthermore, the brightness temperature indicates that the gas in the dust cavity in the HD 169142 disk is warmer than that in the outer disk. This is not seen in the brightness temperature in the LkCa15 disk due to beam dilution that lowers the peak intensity inside the dust cavity. The gas temperature inside these regions will be further constrained in the next section.

4.4 Analysis

To analyze the data in terms of physical quantities, we first briefly reiterate the relevant equations to derive the temperature, column density, and estimates of the optical depth using CO line ratios and assuming that all levels are characterized by a single excitation temperature, that is, the common assumption that the lines are emitting from the same layer in the disk. Next, we apply this to the observations to investigate the differences between the cavities and the outer disks of LkCa15 and HD 169142.

4.4.1 Temperature and column density determination

The temperature structure inside and outside the dust cavity can be found by analyzing the ^{13}CO $6 - 5$ and ^{13}CO $2 - 1$ transitions, as these transitions are far apart in upper energy level ($E_u = 15.9$ K vs. $E_u = 111.1$ K). The column density structure can then be derived using the less optically thick C^{18}O $2 - 1$ emission together with the temperature structure from the ^{13}CO analysis.

If the emission is optically thin, the column density is proportional to the integrated intensity (e.g., Goldsmith & Langer 1999):

$$N_u^{\text{thin}} = \frac{4\pi F_\nu \Delta V}{A_{ul} \Omega h c}, \quad (4.4)$$

with N_u^{thin} the column density of the upper level (u), $F_\nu \Delta V$ the integrated intensity, A_{ul} the Einstein A coefficient, Ω the emitting region, h the Planck constant, and c the speed of light. If the emission is optically thick, a correction factor needs to be applied:

$$N_u = N_u^{\text{thin}} C_\tau, \quad (4.5)$$

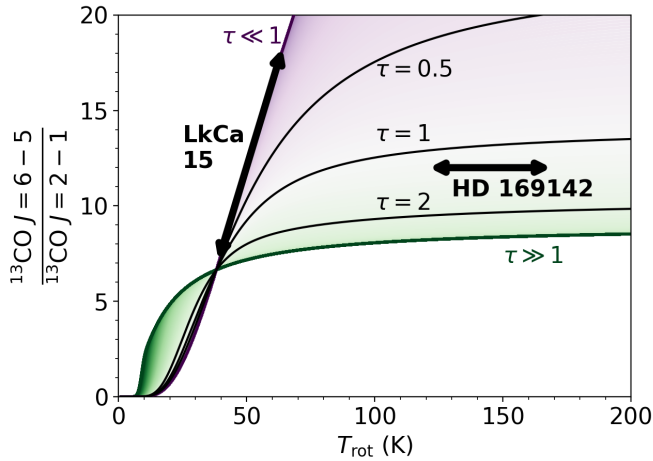


Figure 4.7: Model line ratio of $^{13}\text{CO } J = 6 - 5$ to $^{13}\text{CO } J = 2 - 1$ as a function of rotational temperature for very low (purple) to very high (green) optical depths of $^{13}\text{CO } 2-1$. The contours highlight the line ratio for a $^{13}\text{CO } J = 2 - 1$ optical depth of 0.5, 1, and 2 (black). We note that the line ratio scales linearly with temperature if the emission is optically thin and $25 \text{ K} \lesssim T_{\text{rot}} \lesssim 150 \text{ K}$ and that it becomes independent of temperature at a value of 9 if the emission is optically thick and $T_{\text{rot}} \gtrsim 40 \text{ K}$. The typical values for the line ratio and rotational temperature (LkCa15) and brightness temperature (HD 169142) in their dust cavities are indicated in the figure.

where the correction factor is defined as

$$C_{\tau} \equiv \frac{\tau_{\nu}}{1 - e^{-\tau_{\nu}}}. \quad (4.6)$$

We note that this expression approaches 1 for $\tau \ll 1$, such that N_u approaches N_u^{thin} . On the other hand, if the emission becomes optically thick, this correction factor scales with τ , whose precise value is uncertain in this regime.

The estimate of the column density of the upper state can also be related to the total column density assuming local thermodynamic equilibrium (LTE):

$$\frac{N_u}{g_u} = \frac{N_{\text{tot}}}{Q(T_{\text{rot}})} e^{-E_u/kT_{\text{rot}}}, \quad (4.7)$$

with $Q(T_{\text{rot}}) \approx kT_{\text{rot}}/(hB_0) + 1/3$ the partition function of CO at a rotational temperature T_{rot} with rotational constant B_0 , and k is the Boltzmann constant. Local thermodynamic equilibrium excitation is a valid assumption for $^{13}\text{CO } J = 6 - 5$ and $J = 2 - 1$ line emission in protoplanetary disks as the critical density is $\sim 10^6 \text{ cm}^{-3} - 3 \times 10^4 \text{ cm}^{-3}$ for the two lines, respectively, which is easily reached even in higher layers. This equation can be solved for the temperature (and column density) as we have observations of both $^{13}\text{CO } J = 6 - 5$ and $J = 2 - 1$. A detailed description of the methods used to solve this equation and to estimate the optical depth can be found in Appendix 4.B.

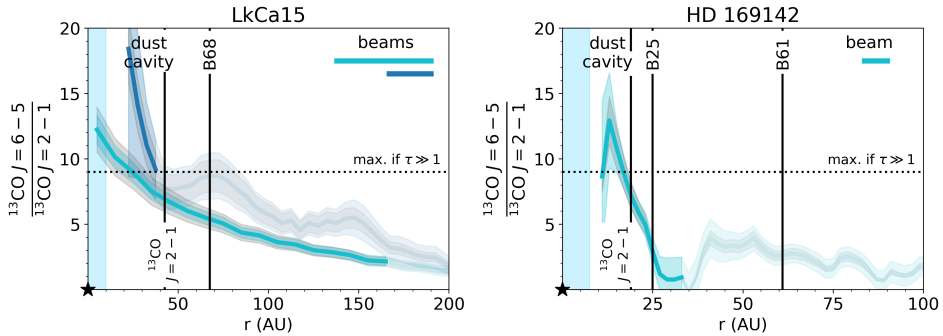


Figure 4.8: Radially resolved $^{13}\text{CO } J = 6-5$ to $^{13}\text{CO } J = 2-1$ line ratio in the LkCa15 (left; (combined) high and intermediate resolution data) and HD 169142 disk (right). The rings in the continuum and the radius where the $^{13}\text{CO } J = 2-1$ transition peaks are indicated with the vertical black lines. The horizontal dotted black line indicates the theoretical maximum line ratio if both lines are optically thick and emit from the same disk region. The beam is indicated with the horizontal bar in the top-right corner. The gray shaded region shows the 10 % absolute calibration error. The line ratio is not shown for radii where the $^{13}\text{CO } J = 6-5$ or the $J = 2-1$ integrated intensity is below 1.5σ . Furthermore, the intensity outside the MRS of the observations is shown in a lighter shade of the corresponding colors.

The result of this analytical analysis is shown in Fig. 4.7. If the emission is optically thin, the line ratio is linearly proportional to the rotational temperature for $T \gtrsim 25$ K. If, on the other hand, the emission is optically thick, the line ratio is only very weakly dependent on the temperature. The predicted line ratio only increases from 8 to 8.5 between temperatures of 90 to 200 K. For higher temperatures, the line ratio approaches $(\nu_{65}/\nu_{21})^2 = 9$, complicating the determination of the temperature.

The line ratio analysis requires that both ^{13}CO lines emit from the same disk layer. The emitting surfaces of molecular line emission in inclined protoplanetary disks can actually be inferred directly from the channel maps, as emission from an elevated layer appears offset compared to the disk center (Pinte et al. 2018a; Law et al. 2021b; Paneque-Carreño et al. 2022). The upper surface in the disk was traced within hand-drawn masks in each channel containing line emission. For each position along the disk major axis, the locations where the emission peaks in the near and far side of the disk were converted to an emitting height using their offset compared to the disk center, the Keplerian velocity and the parameters listed in Table 4.1. Subsequently, the resulting emitting surface was binned in radius to increase the signal-to-noise ratio.

4.4.2 Results for LkCa15

The observed line ratio for LkCa15 is presented in Fig. 4.8, where the lines used for the ratio were convolved to the same beam of $0''.36 \times 0''.30$ (26.6°) or $0''.17 \times 0''.13$ (-13.7°) in case of the intermediate and (combined) high resolution

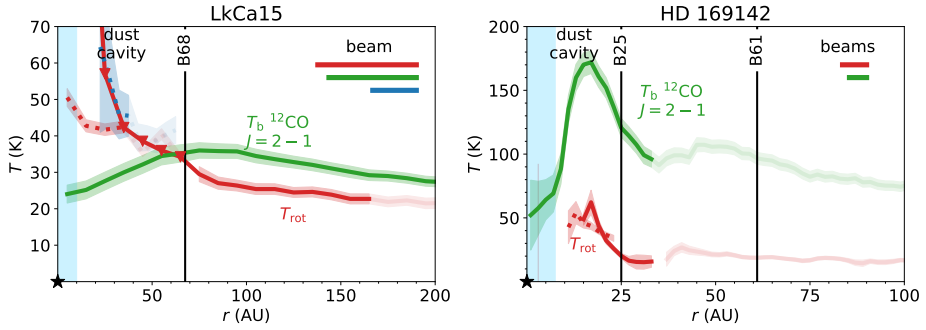


Figure 4.9: Temperature derived from the line ratio analysis. The rotational temperature (red) is derived from the $^{13}\text{CO } J = 6 - 5$ to $J = 2 - 1$ line ratio, including optical depth constraints (solid lines), for LkCa15 (left) and HD 169142 (right). The dotted lines in corresponding colors indicate the rotational temperature inside the dust cavity if the emission were optically thin. For comparison, the brightness temperature of the optically thick $^{12}\text{CO } J = 2 - 1$ transition is shown. We note the difference in the vertical temperature axes. In the case of LkCa15, the dotted blue line shows the rotational temperature assuming optically thin emission for the (combined) high resolution observations. The downward triangles indicate the upper limit on the rotational temperature due to the upper limit on the integrated $\text{C}^{18}\text{O } J = 2 - 1$ intensity in the dust cavity. The intensity outside the MRS of the observations is shown in a lighter shade of the corresponding colors.

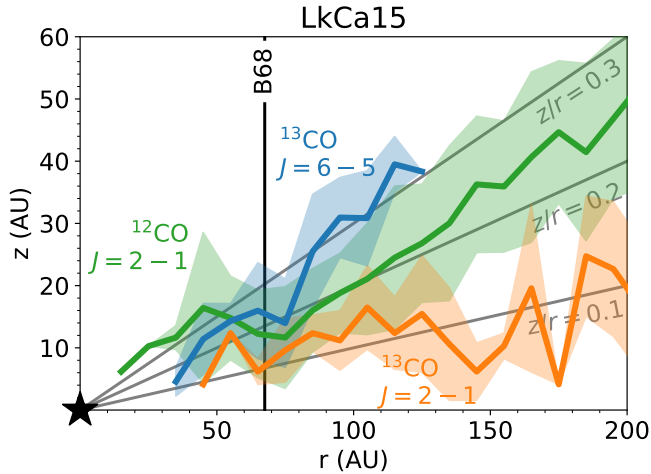


Figure 4.10: Emitting surface of $^{12}\text{CO } J = 2 - 1$ (green), $^{13}\text{CO } J = 2 - 1$ (orange), and $^{13}\text{CO } J = 6 - 5$ (blue) for LkCa15. The gray lines indicate the emitting surface for $z/r = 0.1, 0.2,$ and 0.3 .

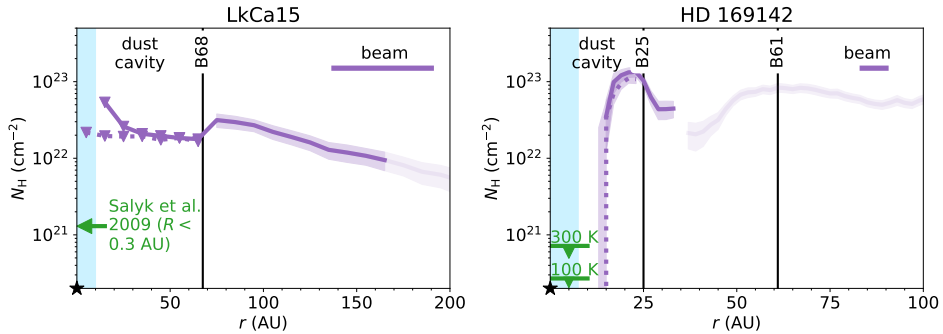


Figure 4.11: Total hydrogen column density (purple) derived from the $^{13}\text{CO } J = 6 - 5$ to $J = 2 - 1$ line ratio, the integrated $\text{C}^{18}\text{O } J = 2 - 1$ line intensity, and the optical depth for LkCa15 (left) and HD 169142 (right). The dotted line indicates the rotational temperature and column density inside the dust cavity if the emission were optically thin. The purple downward triangles in the left panel indicate the upper limit on column density due to the upper limit on the integrated $\text{C}^{18}\text{O } J = 2 - 1$ intensity in the dust cavity. The green bars with downward triangles in the right panel indicate the 3σ upper limit on the hydrogen column density derived from the non-detection of $^{12}\text{CO } J = 2 - 1$ in this region and assuming a temperature of 100 K and 300 K, respectively.

observations, respectively. The line ratio of the $^{13}\text{CO } J = 6 - 5$ to $J = 2 - 1$ transition decreases with radius in the outer disk. This is expected as the temperature of the gas decreases with radius. Furthermore, the data show an increase in the slope inside the dust cavity compared to outside the dust cavity, driven by the drop in $^{13}\text{CO } J = 2 - 1$ inside 40 AU. Whether this indicates an actual increase in the temperature in the dust cavity or if it is just an optical depth effect is investigated below. The line ratio found from the (combined) high resolution data is consistent with the intermediate resolution data outside 45 AU, within the limitations of the data. The line ratio of the $^{12}\text{CO } J = 6 - 5$ transition presented in van der Marel et al. (2015) and the $^{12}\text{CO } J = 2 - 1$ transition in a common beam of $0''.35 \times 0''.25$ (-37.5°) is similar in value and trend with radius to the intermediate resolution line ratio of the ^{13}CO isotopolog.

The optical depths of the $^{13}\text{CO } J = 6 - 5$, $J = 2 - 1$ and the $\text{C}^{18}\text{O } J = 2 - 1$ transitions at moderate spatial resolution were derived using Eq. 4.13 and using a 3σ upper limit on the integrated C^{18}O intensity inside the dust cavity (≤ 68 AU; see Fig. 4.B.1) as the radial profile derived from the kinematics clearly suggests a much smaller gas cavity of only ~ 10 AU. The optical depth $^{13}\text{CO } J = 2 - 1$ and $\text{C}^{18}\text{O } J = 2 - 1$ transition differ by their isotopolog ratio as this is one of the assumptions used to find the optical depth. The $\text{C}^{18}\text{O } J = 2 - 1$ emission is marginally optically thick in the outer disk with an optical depth between ~ 0.1 and ~ 0.4 between 70 AU and 200 AU. Consequently, the $^{13}\text{CO } J = 2 - 1$ emission is optically thick throughout the same disk region. Inside the dust cavity, the optical depths of ≤ 2 for the ^{13}CO and ≤ 0.3 for the $\text{C}^{18}\text{O } J = 2 - 1$ are upper limits. The optical depth of the $^{13}\text{CO } J = 6 - 5$ transition follows from the line

ratio analysis and lies typically between the optical depth from the aforementioned transitions in the outer disk. Inside the dust cavity, an upper limit on the ^{13}CO $J = 6 - 5$ optical depth is given. The ^{13}CO and C^{18}O lines could be close to optically thin inside the dust cavity, and thus their brightness temperatures are only lower limits to the kinetic temperature.

The rotational temperature is presented in the left-hand panel of Fig. 4.9 and increases toward the dust cavity. For comparison, the ^{12}CO $J = 2 - 1$ brightness temperature is also shown. This transition is surely optically thick outside the dust cavity so the brightness temperature traces the kinetic temperature in the emitting layer of the outer disk. This brightness temperature is 5 – 10 K higher than the rotational temperature of ^{13}CO in the outer disk. In the inner disk, the line ratio steeply increases toward the star, indicating a steep increase in the gas temperature.

The (combined) high resolution data for LkCa15 do not have an C^{18}O $J = 2 - 1$ counterpart. Therefore, the optical depth cannot be determined following the same method as for the intermediate resolution data. Still, the steep increase in the line ratio in the dust cavity and the upper limit on the ^{13}CO $J = 2 - 1$ optical depth of ~ 2 in the dust cavity at moderate spatial resolution suggest that the gas in the dust cavity is likely optically thin in the two ^{13}CO and the C^{18}O $J = 2 - 1$ lines. In this case, the temperature derived from the line ratio (blue dotted line in Fig. 4.9) is very similar to the rotational diagram analysis on the moderate spatial resolution data.²

The hypothesis that the ^{13}CO $J = 6 - 5$ and $J = 2 - 1$ transitions emit from the same disk region inside the dust cavity is supported by the emitting surfaces presented in Fig. 4.10. First, we note that the LkCa15 disk is very flat with $z/r \sim 0.1$ for the ^{13}CO $J = 2 - 1$ transition similar to, for example, AS 209, HD 163296, and MWC 480 (Law et al. 2021b). At radii smaller than 85 AU, the emitting surfaces of these two transitions measured from the (combined) high resolution data are consistent within the error bars. Moreover, their brightness temperatures are very similar (Fig. 4.4), which is as expected if the same layer is traced. Outside this radius of 85 AU, the ^{13}CO $J = 6 - 5$ and ^{12}CO $J = 2 - 1$ lines emit from a similar layer at $z/r \sim 0.2 - 0.3$, whereas the ^{13}CO $J = 2 - 1$ line emits from a lower layer at $z/r \sim 0.1$. This is the first time that we derive directly from the data that the ^{13}CO $J = 6 - 5$ line indeed emits from a higher layer than the ^{13}CO $J = 2 - 1$ line.

Finally, the total hydrogen column density in the LkCa15 disk is derived using the rotational temperature and the absolute integrated C^{18}O intensity at intermediate resolution, assuming a CO abundance of 10^{-4} with respect to the total number of hydrogen atoms. As the C^{18}O emission is marginally optically thick throughout the outer disk, the optical depth of the line is explicitly taken into account. The total column density, presented in Fig. 4.11, increases toward the central star up to ~ 75 AU. However, the exact radius where the gas column density peaks is smaller as argued in Sect. 4.3.2.3. Inside the dust cavity, the C^{18}O upper limit gives an upper limit of $5 \times 10^{22} \text{ cm}^{-2}$ at 15 AU, consistent with the

²The 40 AU radius MRS of the high resolution ^{13}CO $J = 2 - 1$ line is not expected to affect this result as it covers most of the dust cavity. Therefore, most flux is recovered in this region.

value of $1.3 \times 10^{21} \text{ cm}^{-2}$ in the inner 0.3 AU using the CO column density derived by Salyk et al. (2009), and with the modeling result found by van der Marel et al. (2015). Furthermore, the derived drop in gas column density inside the dust cavity is a factor of ≥ 2 , consistent with the modeling by van der Marel et al. (2015). Finally, we note that the total hydrogen column density in the LkCa15 disk may be higher than the values derived here depending on whether CO is transformed to other species resulting in a CO abundance lower than the assumed value of 10^{-4} (Sturm et al. in prep.).

4.4.3 Results for HD 169142

The fact that $^{13}\text{CO } J = 6 - 5$ is detected just inside the dust cavity, but drops steeply inward of ~ 15 AU indicates that the gas cavity is likely very depleted in gas (Figs. 4.2, 4.6). Therefore, we focus on the region outside ~ 10 AU. The line ratio of $^{13}\text{CO } J = 6 - 5$ to $^{13}\text{CO } J = 2 - 1$ for HD 169142 increases to a value of ~ 13 at the inner edge of the gas cavity and rapidly decreases further out in the disk (Fig. 4.8).

The results of the line ratio analysis are shown in the right-hand panels of Figs. 4.9 and 4.B.1. The optical depths of the lines are comparable to the values found for LkCa15, that is to say, the $^{13}\text{CO } J = 2 - 1$ transition has an optical depth of a few. Furthermore, the temperature in the outer disks of HD 169142 and LkCa15 are similar at ~ 30 K as derived from the line ratio. This derived temperature in the outer disk of HD 169142 is likely very low due to the small MRS of the Band 6 and Band 9 data, which lowers the $^{13}\text{CO } J = 6 - 5$ and $J = 2 - 1$ integrated intensities in the outer disk outside ~ 35 AU. Furthermore, at the location of the bright continuum rings, the temperature from the line ratio may be affected by the continuum subtraction of the $^{13}\text{CO } J = 6 - 5$ and $J = 2 - 1$ lines used for the line ratio. The bright rim just inside the dust cavity of the HD 169142 disk is warm and (marginally) optically thick in $^{13}\text{CO } J = 6 - 5$. The line ratio analysis predicts an increase to ~ 50 K compared to the outer disk, but the uncertainty on the line ratio and optical depth are large. In contrast with the LkCa15 case, the $^{12}\text{CO } J = 2 - 1$ brightness temperature suggests that the dust cavity is much warmer, up to 170 K, compared to the outer disk (~ 100 K).

The total hydrogen column density, derived using the rotational temperature and the integrated C^{18}O intensity (purple line in Fig. 4.11, right panel), shows similar values at the location of the two rings detected in this disk and a few times higher than in the LkCa15 disk. The HD 169142 column density at 23 AU is a factor of 2.5 lower than that modeled by Fedele et al. (2017). This difference is due to the lower spatial resolution and larger MRS of the data used in that work. The drop in the gas column density by a factor of 40 in the gap at 56 AU found by Fedele et al. (2017) is not constrained in our work due to the small MRS. The signal-to-noise ratio and MRS of the data are not high enough to determine the expected steady decrease in gas column density in the outer disk outside of ~ 35 AU.

4.5 Thermochemical models

The analysis in Sect. 4.4 shows that the temperature increases inside the dust cavity compared to outside for both the LkCa15 and HD 169142 disks. Furthermore, it is found that the gas is located at smaller radii, ~ 10 AU, than the dust cavity and that the gas cavity is very deep ($\geq 100\times$ drop in gas column density) in the HD 169142 disk. The gas in the dust cavity for LkCa15 could be optically thin, but only an upper limit on the column density could be obtained due to the beam size being comparable to the dust cavity and because the line ratio exceeded the maximum possible value of 9 if both lines are optically thick. Finally, a difference between the temperature derived from the line ratio and the brightness temperature was found. Although this could be due to the MRS being smaller than the angular size of the gas and dust disk in the case of HD 169142, another explanation would be a difference in the emitting layers of the ^{13}CO $J = 6 - 5$ and $J = 2 - 1$ transitions. This is in line with the expectation that different lines do not emit from the same disk region due to optical depth and excitation effects (e.g., van Zadelhoff et al. 2001) as also derived directly in the LkCa15 disk (see Fig. 4.10). In order to investigate this situation, we present some exploratory DALI models following Bruderer (2013). Then we compare our results to other sources and finally discuss the implications.

The thermochemical code DALI was used to model the line ratio of the ^{13}CO $J = 6 - 5$ to $J = 2 - 1$ transition in the cavities of typical transition disks. A detailed description of the DALI modeling setup is given in Appendix 4.C and in Table 4.C.1. We do not attempt to model the individual sources, but look for trends in a set of representative disk models and study the sensitivity to parameters. The fiducial Herbig disk model is a transition disk with a gas cavity with variable gas drop inside 30 AU. The dust cavity extends to 50 AU and a small inner disk of 1 AU is present. The ALMA observations presented in this work mainly probe the region inside the dust cavity but outside the gas cavity corresponding to 30 – 50 AU in this model. The density and temperature structure of this model are presented in Fig. 4.C.2. The cyan and orange lines show the $\tau = 1$ surfaces of the ^{13}CO $J = 6 - 5$ and $J = 2 - 1$ transitions, respectively. For gas density drops by factors of 0.1 – 0.001, both ^{13}CO lines are (marginally) optically thin in the gas cavity. Outside the gas cavity and in the model with no gas drop in the dust cavity, both lines are optically thick and trace a slightly different layer in the disk.

The predicted ^{13}CO $J = 6 - 5$ to $J = 2 - 1$ line ratios for this model with four different gas drops inside 30 AU are presented in the top-left panel of Fig. 4.12. This figure shows that the line ratio can reach up to the maximum possible value of 80 for optically thin gas in the gas cavity, due to the high gas temperatures in the gas cavity midplane and both ^{13}CO lines being optically thin. The temperature in the gas cavity midplane increases due to the increased UV radiation field if less gas is present. We note that PAHs are present in the gas even if at small amounts and absorb the UV radiation from the star. This increased radiation field for lower gas densities also changes the chemistry in the cavity by photodissociating CO, the major coolant at a height of ~ 1 AU inside the gas cavity. Therefore, the gas inside 30 AU in the models with a deep gas cavity, cools less efficiently than in

the full gas disk model. This results in an increased midplane temperature inside 30 AU with deeper gas cavity depth (compare $0.1 - 0.001\times$ drops in Fig. 4.12 right-hand panel). In these models with a gas density drop ($\geq 10\times$), the line ratio is a direct probe of the temperature.

Outside the gas cavity but inside the dust cavity and in the outer disk ($R > 30$ AU), the line ratio is larger than 9, which is the maximum theoretical value that is expected when the emission is optically thick. This is because the $J = 6 - 5$ line emits from a layer with a higher temperature than the $J = 2 - 1$ line (bottom panel Fig. 4.C.2 and 4.12, top-right panel), increasing the line ratio with respect to the $J = 2 - 1$ transition up to 20 in the outer disk. In summary, the line ratio analysis can be used if both lines are emitting from the same disk region. If the lines become optically thick, their emitting regions will deviate, and the brightness temperature becomes a good probe of the temperature of that layer.

The effect of the host star is investigated as LkCa15 is a $1.1 L_{\odot}$ T Tauri star and HD 169142 is a $10 L_{\odot}$ Herbig star. The higher luminosity of the Herbig star heats the surrounding disk to higher temperatures as shown in the left two panels of Fig. 4.13. One of the main heating agents in the disk is molecular hydrogen that is vibrationally excited by the absorption of a far-UV photon. The collisional de-excitation then releases this energy to the gas causing it to heat up. This process is most effective in the gas cavity midplane, and at $z/r \sim 0.1$ for radii >30 AU. The disk midplane in the T Tauri model is colder than the corresponding region in the Herbig model because the main heating agents, far-UV pumped H_2 and the photoelectric effect on small grains and PAH, are less effective due to the weaker far-UV field and lower luminosity in the T Tauri model.

The line ratio and temperature at the $\tau = 1$ surface for the T Tauri models are presented in the bottom row of Fig. 4.12. The line ratios in the T Tauri disk models are smaller than the values in the Herbig disk models. This is due to the lower gas temperature in the T Tauri models (Fig. 4.12, right-hand panel). Another difference between the Herbig and the T Tauri models is the temperature of the emitting layers. In the outer disk of the Herbig models, the temperature of the ^{13}CO $J = 6 - 5$ layer is $\sim 1.3 - 2\times$ higher than in the $J = 2 - 1$ layer, but in the T Tauri models the layers have nearly the same temperature of $50 - 100$ K. Inside the dust cavity, the temperatures of the $J = 6 - 5$ and $J = 2 - 1$ layers differ from each other except within the 30 AU gas cavity for the models with a deep gas cavity (drop ≥ 0.01), as the lines become optically thin in this region. The effects of the PAH abundance, the presence of a dusty inner disk and the effects of grain growth are investigated in Appendix 4.C.2.

The exploratory DALI models show that the UV field and the amount of gas in the gas cavity are important for the temperature of the gas in the cavity. The disk models by Bruderer et al. (2009), Bruderer et al. (2012), Bruderer (2013), and Alarcón et al. (2020) do not distinguish between a gas and dust cavity or gap and show that the gas in this region is warmer than the gas outside the cavity or gap. In contrast, the models by Facchini et al. (2017) and Facchini et al. (2018) show lower temperatures. The main difference between these models are the heating and cooling rates that are taken to be independent of grain sizes and gas-to-dust ratios in the cavities and gaps in the models by Bruderer (2013), whereas they

are dependent on grain sizes in the models by Facchini et al. (2017) and in this work. In our models, we show that the gas temperature not only depends on these choices, but also on the stellar luminosity (Fig. 4.13). In our T Tauri models with a gas cavity the emitting layer of $^{13}\text{CO } J = 6 - 5$ and $J = 2 - 1$ inside the dust cavities (10 – 50 AU) have a temperature similar to or colder than the outer disk, whereas in the Herbig disk models, we find that the temperature of the emitting layers is generally warmer than the outer disk.

4.6 Discussion

4.6.1 Comparing models and observations

The DALI models show that the $^{13}\text{CO } J = 6 - 5$ to $J = 2 - 1$ line ratio is a sensitive tracer of the gas temperature in the gas cavity of transition disks if the emission is optically thin. Outside the gas cavity and in the outer disk regions of the models, the two ^{13}CO lines are optically thick, complicating the line ratio analysis, but in this case the brightness temperature can be used to constrain the temperature. The line ratio inside the gas cavity is especially sensitive to the amount of gas in the gas cavity, the presence of a dusty inner disk, the abundance of small grains and PAHs in the gas cavity, as these are all important parameters to set the temperature. A higher line ratio points toward a low PAH abundance, no dusty inner disk, and grain growth.

Our ALMA observations in the HD 169142 disk trace the disk region outside the gas cavity but inside the dust cavity (from 30 to 50 AU in the models and from 5 – 10 to 25 AU in the data). In this region, the line ratio is not very sensitive to the amount of gas in the gas cavity due to optical depth effects and because its temperature structure is not affected much when a gas cavity is introduced. In contrast, the line ratio in this disk region is affected by the presence of a dusty inner disk, the abundance of PAHs and grain growth similar to the disk region inside the gas cavity. Therefore, the ALMA line ratio in the HD 169142 disk mainly traces the effects of these parameters rather than the amount of gas in the gas cavity.

The ^{12}CO brightness temperature indicates that the gas is 170 K in this region in the HD 169142 disk, which is consistent with the 80 – 300 K temperature range predicted by the DALI models inside the dust cavity but outside the gas cavity. Similarly, the observed brightness temperature of ~ 100 K in the outer disk of HD 169142 is consistent with the typical temperature of the ^{13}CO emitting layers in the fiducial Herbig disk model.

In the case of LkCa15, the gas cavity of ~ 10 AU is unresolved by ALMA observations. Therefore, the observed line ratio likely traces a combination of all effects (gas cavity depth, abundance of PAHs, presence of a dusty inner disk and grain growth) discussed above, complicating the interpretation of the observations. The T Tauri models have a typical temperature of 50 – 100 K in the outer disk at their $\tau = 1$ heights, which is higher than the typical temperature of 20 – 30 K in the outer disk of LkCa15. Still, the models predict a steep increase in the gas

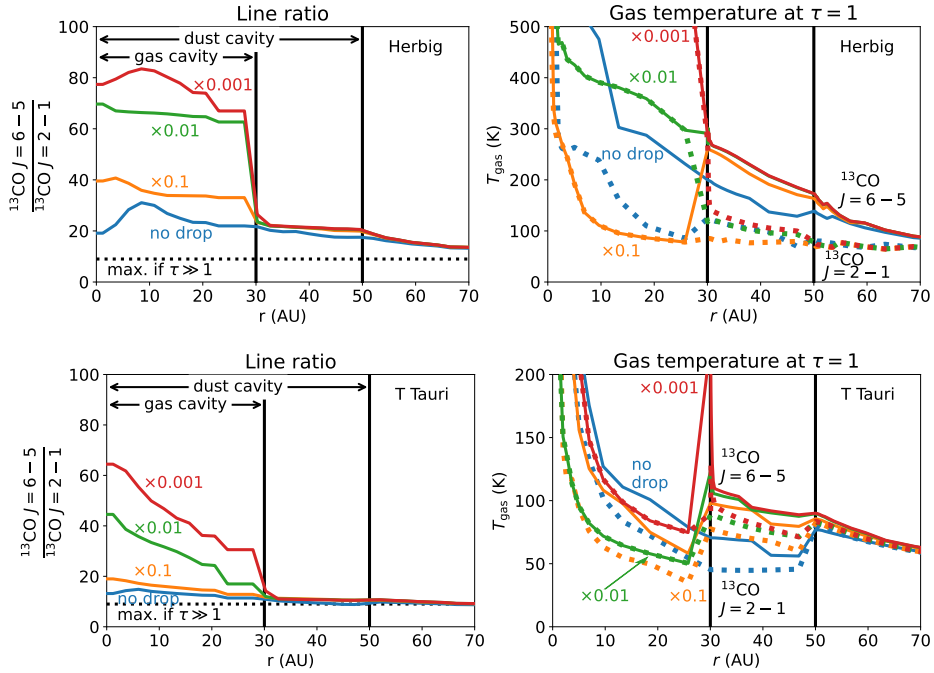


Figure 4.12: Predicted line ratio (left) and gas temperature (right) at the height where the $^{13}\text{CO } J = 6 - 5$ (solid) and $J = 2 - 1$ (dotted) transitions become optically thick for different gas cavity depths (no drop to a factor of 0.001, colors) in the Herbig disk models (top) and T Tauri models (bottom). We note the different temperature scales for the two types of stars. If the transitions are optically thin, the midplane temperature is shown, as that is the region that optically thin CO lines trace in the gas cavity. The dotted horizontal line in the left panels indicates the theoretical maximum value for the line ratio if both ^{13}CO lines are optically thick and emit from the same disk layer.

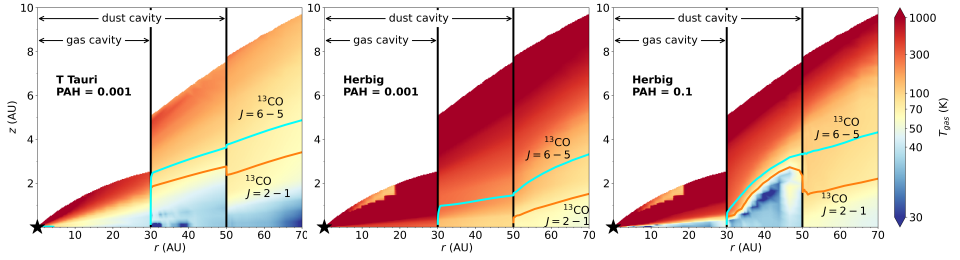


Figure 4.13: Gas temperature of our model for a T Tauri star and a PAH abundance of 0.001 with respect to the ISM (left), the fiducial Herbig model with a PAH abundance of 0.001 with respect to the ISM, and a Herbig model with a high PAH abundance of 0.1 with respect to the ISM (right). All models have a factor of 100 drop in gas density inside 30 AU. The cyan and orange contours indicate the $\tau = 1$ surface of the ^{13}CO $J = 6 - 5$ and $J = 2 - 1$ lines, respectively. The ^{13}CO $J = 2 - 1$ transition is optically thin inside the dust cavity, and the $J = 6 - 5$ is optically thin inside the gas cavity, and hence these lines trace the midplane at these radii. We note that the dust cavity starts from 50 AU inward and the gas cavity from 30 AU. Only the regions with a gas density above 10^7 cm^{-3} are shown.

temperature inside the gas cavity. This is likely also traced by our observations, but the large beam smears this out to larger radii up to the dust cavity radius.

4.6.2 Comparison to other sources

The temperature structure of few other sources has been studied in detail. Recent work on the temperature structure in the transition disk GM Aur has shown that an additional increase of a factor of up to 10 in the gas temperature in the surface layers in the inner disk, inside its dust cavity at 40 AU, compared to the thermochemical model prediction is needed to fit the observed intensities (Schwarz et al. 2021). In contrast, that same model overpredicts the gas temperature in the outer disk by a factor of 2. The increase in temperature inside the GM Aur dust cavity is similar to the steep increase in gas temperature inside the dust cavity found in the LkCa15 and HD 169142 disks. One of their proposed explanations is that the PAH abundance in the surface layer is too low in the GM Aur models. Our models confirm that the abundance of PAHs is important together with the UV field to effectively heat the gas through the photoelectric effect. On the other hand, a high PAH abundance also shields the gas from stellar UV radiation causing a lower gas temperature in the emitting layer. The disk region inside the inner most beam for LkCa15 may even be warmer than what we derived using the ^{13}CO $J = 6 - 5$ to $J = 2 - 1$ line ratio, because of beam dilution. This effect is less relevant for HD 169142 as its gas cavity is very depleted in gas.

High resolution ^{13}CO $J = 6 - 5$ observations probing the inner few AU in the TW Hya disk are not available. The temperature in the outer disk of TW Hya, derived using a similar method to this work, it is also consistent with excitation temperature derived from formaldehyde and methyl cyanide emission (Schwarz et al. 2016; Loomis et al. 2018; Pegues et al. 2020; Terwisscha van Scheltinga et al.

2021). As all of these temperatures are similar to each other, the molecules used likely emit from similar disk regions as the disk is very flat. This situation is similar to our case for LkCa15, which has similar outer disk temperatures as the TW Hya disk and also a shallow vertical temperature gradient.

Modeling by Fedele et al. (2016) shows that the temperature in four Herbig disks depends on their vertical structure (flaring and scale height) as well as the dust distribution (gas-to-dust ratio and dust settling). Comparing the temperature of the HD 169142 disk to the temperatures found in Herbig disks using *Herschel* observations of the CO ladder shows that HD 169142 is $\sim 50 - 100$ K warmer than the HD 163296 disk at the emitting heights. Furthermore, HD 169142 falls within the range of all four Herbig disks analyzed in Fedele et al. (2016).

4.6.3 Implications for the cause of the gas cavity

Our results have shown that temperature plays a role in lowering the low- J lines. One of the most popular alternative explanations for cavities and rings in protoplanetary disks are planets. The deep gas cavity in the HD 169142 disk could be carved by a massive companion. The high signal-to-noise ratio of the ^{12}CO $J = 2 - 1$ transition constrains the total hydrogen column density in the inner 10 AU to be $\leq (3 - 7) \times 10^{20} \text{ cm}^{-2}$ using a 3σ upper limit on the integrated ^{12}CO $J = 2 - 1$ intensity and assuming an average gas temperature of $100 - 300$ K, respectively. This upper limit shows that the deep gas cavity that is depleted by at least a factor of $(2 - 5) \times 10^2$, with respect to the bright ring seen in the gas. If this cavity is carved by a massive companion, its mass can be estimated using the following equation (Zhang et al. 2018):

$$\frac{K}{24} = \frac{q}{0.001} \left(\frac{h/r}{0.07} \right)^{-2.81} \left(\frac{\alpha}{10^{-3}} \right)^{-0.38}, \quad (4.8)$$

with q the mass ratio of the companion to the star, α the viscosity, and h/r the scale height of the disk. The K is a dimensionless parameter that describes the depth of the gas cavity, δ , as $\delta - 1 = CK^D$. The values of $C = 0.002$ and $D = 2.64$ are the best fitting parameters to the hydro simulations of both the gas and the dust performed by Zhang et al. (2018). Fedele et al. (2017) find from models that the disk scale height h/r is 0.07, independent of radius. Assuming a typical disk viscosity of 10^{-3} constrains the mass of the potential companion to be $\geq 8.0 M_{\text{J}}$ for a gas temperature of 100 K in the gas cavity and $\geq 5.5 M_{\text{J}}$ for 300 K. The mass of the potential planet and the disk viscosity are degenerate. Therefore, a lower disk viscosity of 10^{-4} , results in the mass of the potential planet to be $\geq 3.3 M_{\text{J}}$ (100 K) or $\geq 2.3 M_{\text{J}}$ (300 K). A cartoon of the proposed scenario is presented in Fig. 4.14. It is also possible that multiple smaller planets carve the cavity seen in the gas (Dodson-Robinson & Salyk 2011).

LkCa15 may be hosting multiple low mass planets, as the gas cavity (~ 10 AU) is much smaller than the dust cavity (68 AU). In LkCa15, the gas column density drops by at least a factor of 2 inside the dust cavity, though the exact drop cannot be inferred from the observations due to large beam of the C^{18}O data. Still, the CO column density inside 0.3 AU derived by Salyk et al. (2009) constrains the

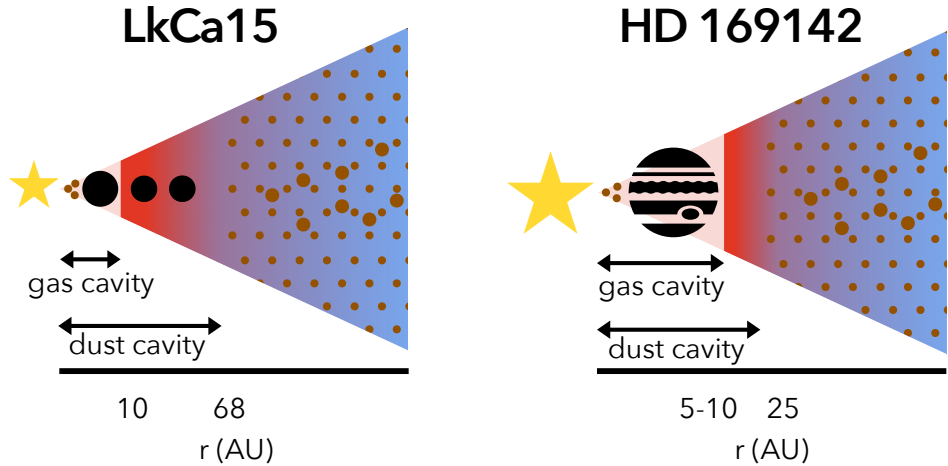


Figure 4.14: Cartoon of the proposed scenario for LkCa15 (left) and HD 169142 (right). The black circles represent the proposed planets that may be carving the dust cavities of both disks. The colored background indicates the radial gas temperature structure in both disks. The brown circles indicate where the dust is present.

total drop in gas column density inside the gas cavity with respect to the outer disk to be a factor of 24. The gas detection up to ~ 10 AU points to the presence of multiple low mass planets that are massive enough to carve a cavity in the dust up to 68 AU but not (yet) in the gas (Dong et al. 2015b and see our Fig. 4.14).

Another possible mechanism to create cavities in transition disks is internal photoevaporation. In this case, low accretion rates of $\lesssim 10^{-9} M_{\odot} \text{ yr}^{-1}$ are expected since the gas is evaporated from the cavity, preventing it from being accreted onto the central star (Owen et al. 2011; Picogna et al. 2019; Ercolano et al. 2021). The mass-accretion rate of $10^{-9.2} M_{\odot} \text{ yr}^{-1}$ for LkCa15 can be consistent with internal photoevaporation, but we find that the gas cavity of ~ 10 AU is much smaller than the dust cavity of 68 AU, which is inconsistent with what is expected for a cavity carved by photoevaporation (Donati et al. 2019). These models predict that small grains are removed from the cavity together with the gas, while the larger grains remain present (Franz et al. 2020), such that the cavity seen in gas and small dust is larger than the cavity seen in large dust grains. This is the opposite of what is observed in the LkCa15 disk as the millimeter-sized grains peak at larger radii (68 AU) than the micron-sized grains (56 AU; Thalmann et al. 2014) and our gas data (10 AU). In the case of the HD 169142 disk, the mass accretion rate of $10^{-7.4} M_{\odot} \text{ yr}^{-1}$ (Guzmán-Díaz et al. 2021) is at least one order of magnitude larger than what can be explained by photoevaporation models.

Dead zones can also cause a drop in the gas column density in the inner disk, but the drops due to dead zones are expected to be on the order of a factor of a few (Lyra et al. 2015). The deep drops in the gas column density inside the dust cavities of LkCa15 and HD 169142, together with the presence of gas well inside the dust cavity points to the presence of one or more lower mass planets

that are hard to detect. Moreover, multiple planets can produce a gap that has a similar width to a gap with a massive planet, making their detection even more challenging.

4.7 Conclusions

In this work we have used the observed $^{13}\text{CO } J = 6 - 5$ to $J = 2 - 1$ line ratio to determine the temperature in the cavities for LkCa15 and HD 169142 with ALMA. The line ratio in the LkCa15 and HD 169142 disks steeply increases inside the dust cavity toward the position of the star in the (combined) high resolution data. Outside the dust cavity, both disks have a relatively low ratio of $\lesssim 6$. The temperature is derived from the line ratio and brightness temperature analysis. Also, DALI models are used to investigate the effect of a drop in the dust and gas column density in the dust and gas cavity on the line ratio. Furthermore, we also investigated the effect of the stellar spectrum, PAH abundance, grain growth, and a dusty inner disk on the line ratio as these parameters affect the local UV field. Our conclusions are summarized as follows:

1. The gas cavity is smaller than the dust cavity for both disks. Based on the kinematically derived radial profiles, we find that the gas in the LkCa15 disk extends down to at least 10 AU, much farther than the dust ring at 68 AU. The results for HD 169142 are consistent with a $\sim 5 - 10$ AU gas cavity and a dust ring at 25 AU.
2. The integrated intensity of the $^{13}\text{CO } J = 6 - 5$ transition is relatively flat in the dust cavity of the LkCa15 disk, whereas the $J = 2 - 1$ transition shows a steep decrease. Therefore, gas is present inside the dust cavity, and the excitation is important for determining its column density. The molecular excitation can be constrained directly by the $^{13}\text{CO } J = 6 - 5$ to $J = 2 - 1$ line ratio if both lines are optically thin.
3. The line ratio of $^{13}\text{CO } J = 6 - 5$ to $J = 2 - 1$ reaches a high value of 13 at the inner rim of the HD 169142 gas (15 AU) disk, and it steeply increases toward the position of the star inside the dust cavity of the LkCa15 disk. This indicates that these disk regions are warm compared to the dusty outer disk. The dust cavity of the LkCa15 disk (up to 65 K) is warmer than the outer disk ($\sim 20 - 30$ K), based on the line ratio analysis. For HD 169142 this analysis is not possible as the lines are optically thick.
4. The brightness temperature of optically thick lines is a good alternative probe of the temperature across the cavity for HD 169142 and indicates that the gas in the dust cavity is warmer, up to 170 K, than in the outer disk, up to ~ 100 K. For LkCa15, the brightness temperature is only a good probe of the temperature in the outer disk due to beam dilution.
5. The factor of $(2 - 5) \times 10^2$ drop in gas column density in the HD 169142 cavity indicates that a massive ($\geq 2.3 - 8.0 M_{\text{J}}$) planet may be present in

this region. For LkCa15, the extended gas-rich region inside the dust cavity may be indicative of several lower mass planets.

6. The DALI models show that the $^{13}\text{CO } J = 6 - 5$ and $J = 2 - 1$ transitions emit from different layers in the disk if the lines are optically thick. Their line ratio in the cavities of transition disks can reach high values, up to the theoretical maximum value of 80, depending on the model. In general, models with a high luminosity, a low PAH abundance, no dusty inner disk, and a large fraction of large grains predict the highest temperatures and line ratios.
7. The vertical structure inferred from the channel maps in the LkCa15 disk is very flat, with a typical scale height of $z/r \sim 0.1$ for the $^{13}\text{CO } J = 2 - 1$ transition. Furthermore, the $^{13}\text{CO } J = 6 - 5$ transition emits from a higher disk layer ($z/r \sim 0.2 - 0.3$) than the $^{13}\text{CO } J = 2 - 1$ transition, consistent with thermochemical models.

In summary, the brightness temperature is a good probe of the disk temperature if the (low- J) CO lines are optically thick (e.g., for HD 169142). If the lines are optically thin, the $^{13}\text{CO } J = 6 - 5$ to $J = 2 - 1$ line ratio is a sensitive probe of the gas temperature. The intermediate case, where these lines are marginally optically thin or not very optically thick, the analysis is more difficult (e.g., for LkCa15). The line ratio analysis in LkCa15 clearly shows that an intensity drop in a low- J CO line does not necessarily require a drop in the CO column density. This work also highlights that resolving the cavities with more than one beam and with good sampling of the relevant scales is crucial for the analysis. High spatial resolution ALMA observations of high- J CO isotopologs (both optically thick and thin) of a much larger sample of transition disks is needed to nail down the combined temperature and column density structure of the gas inside dust cavities and thus, ultimately, the mechanism responsible for carving them.

Acknowledgements

We thank the referee for the constructive comments. Astrochemistry in Leiden is supported by the Netherlands Research School for Astronomy (NOVA), by funding from the European Research Council (ERC) under the European Union’s Horizon 2020 research and innovation programme (grant agreement No. 101019751 MOLDISK), and by the Dutch Research Council (NWO) grants 618.000.001 and TOP-1 614.001.751. Support by the Danish National Research Foundation through the Center of Excellence “InterCat” (Grant agreement no.: D NRF150) is also acknowledged. A.D.B. acknowledges support from NSF AAG grant No. 1907653. This paper makes use of the following ALMA data: ADS/JAO.ALMA #2016.1.00344.S, #2017.1.00727.S, #2018.1.00945.S, and #2018.1.01255.S. ALMA is a partnership of ESO (representing its member states), NSF (USA) and NINS (Japan), together with NRC (Canada), MOST and ASIAA (Taiwan), and KASI (Republic of Korea), in cooperation with the Republic of Chile. The Joint ALMA Observatory is operated by ESO, AUI/NRAO and NAOJ.

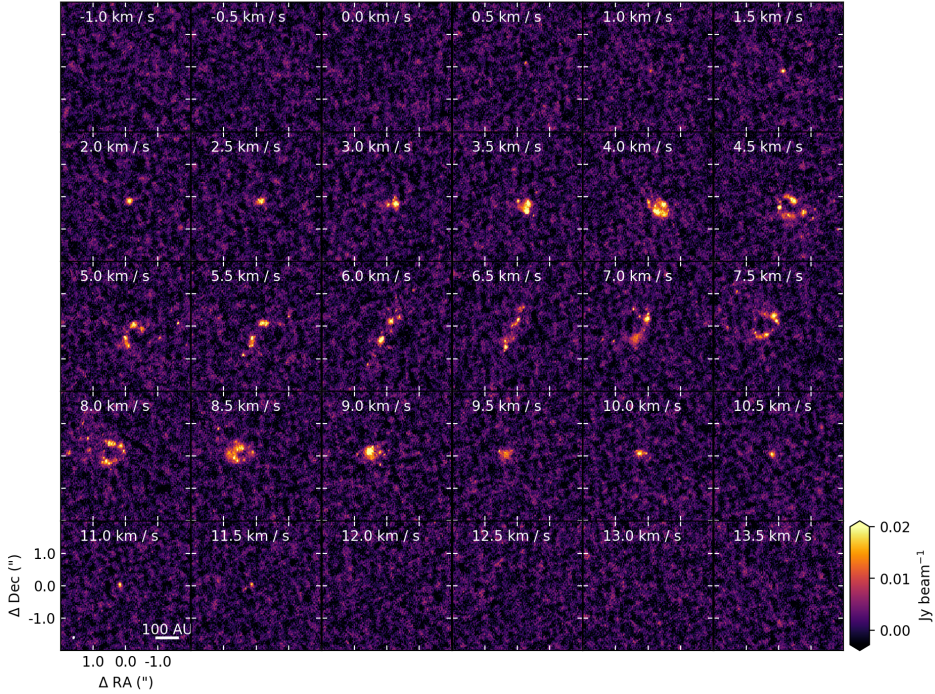


Figure 4.A.1: Channel maps of the combined data set for the $^{13}\text{CO } J = 6 - 5$ transition in the LkCa15 disk.

Appendix

4.A Observations

4.A.1 Channel maps $^{13}\text{CO } J = 6 - 5$

The channel maps of the $^{13}\text{CO } J = 6 - 5$ transition in the LkCa15 and HD 169142 disks are presented in Figs. 4.A.1 and 4.A.2, respectively.

4.A.2 Azimuthally averaged radial profiles

The deprojected azimuthal averages of the CO isotopolog emission are presented in Fig. 4.A.3.

4.A.3 Brightness temperature

The brightness temperature of an optically thick line was calculated using the peak flux. However, a low spectral resolution can lower this peak flux compared to the true value. In this section we quantify this effect for the ^{13}CO emission. The

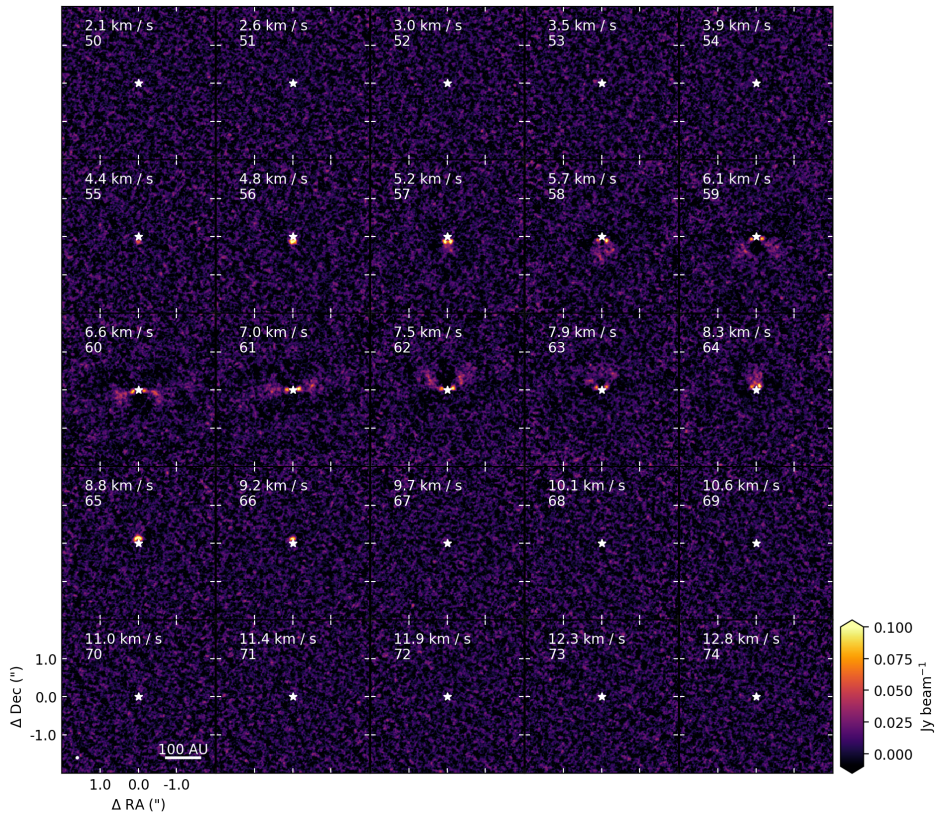


Figure 4.A.2: Same as Fig. 4.A.1 but in the HD 169142 disk.

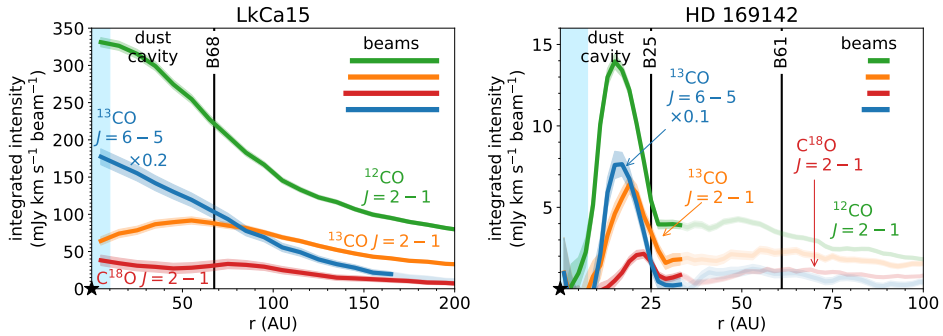


Figure 4.A.3: Azimuthally averaged radial profiles of ^{12}CO , ^{13}CO , and C^{18}O $J = 2 - 1$ and ^{13}CO $J = 6 - 5$ at intermediate resolution profiles for LkCa15 (left) and at high resolution for HD 169142 (right). The gas cavity (light blue shaded region) is unresolved at these spatial resolutions. We note that, in the left-hand panel, the morphology of the ^{13}CO $J = 6 - 5$ is very different from the ^{13}CO $J = 2 - 1$ line. Furthermore, the integrated ^{13}CO $J = 6 - 5$ line intensity was multiplied by 0.2 (LkCa15) and 0.1 (HD 169142) for visibility. The (combined) high resolution data for the LkCa15 disk is presented in Fig. 4.2.

spectral resolution of the data set covering the ^{13}CO $J = 2 - 1$ line is 0.17 km s^{-1} , whereas that of the $J = 6 - 5$ data set is 0.44 km s^{-1} in HD 169142. Therefore, the former data set better samples the line profile and hence the peak flux of the ^{13}CO emission than the latter. The effect of underestimating the peak flux due to a lower spectral resolution is shown in Fig. 4.A.4, where the brightness temperature of the ^{13}CO $J = 2 - 1$ transition is shown at two spectral resolutions: 0.17 km s^{-1} (native resolution solid orange line) and 0.44 km s^{-1} (binned, dashed orange line). This figure shows that binning lowers the brightness temperature by 10-15 K, corresponding to $\sim 10\text{-}30\%$, compared to the brightness temperature at the native spectral resolution. For comparison the brightness temperature of the ^{13}CO $J = 6 - 5$, at 0.44 km s^{-1} is shown as the blue dashed line. This figure shows that the low spectral resolution of the ^{13}CO $J = 6 - 5$ data is partially responsible for the difference between the $J = 2 - 1$ and $J = 6 - 5$ brightness temperatures discussed in Sect. 4.3.2.2. Similarly, in the LkCa15 disk, the lowering the spectral resolution of the high spatial resolution ^{13}CO $J = 2 - 1$ line from 0.17 km s^{-1} to 0.5 km s^{-1} , lowers the peak brightness temperature by 6-13 K or 40-60%. Therefore, the ^{13}CO $J = 6 - 5$ brightness temperature in LkCa15 is likely underestimated due to the spectral resolution.

4.A.4 Spectra

The signal-to-noise ratio of the spectra used for the kinematically derived radial profiles is presented in Fig. 4.6. The signal-to-noise ratio is the highest for the ^{12}CO $J = 2 - 1$ and ^{13}CO $J = 6 - 5$ transitions in the line wings, and therefore these lines are also detected out to the smallest radii.

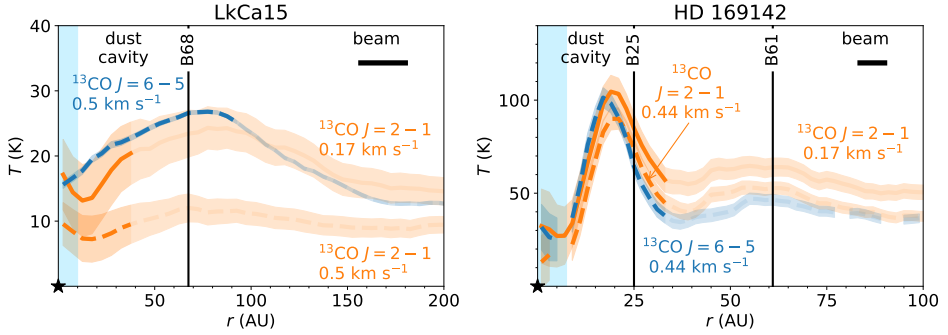


Figure 4.A.4: Deprojected azimuthally averaged radial profiles of the brightness temperature of the $^{13}\text{CO } J = 2 - 1$ (orange) and $^{13}\text{CO } J = 6 - 5$ (blue) transition in LkCa15 (left) and HD 169142 (right). The dashed lines show them at a spectral resolution of 0.5 km s^{-1} (LkCa15) and 0.44 km s^{-1} (HD 169142). The solid line shows the $^{13}\text{CO } J = 2 - 1$ transition at the native spectral resolution of 0.17 km s^{-1} . The difference between the solid and dashed orange lines is due to the spectral resolution as the cubes are convolved to a beam of $\sim 0''.17 \times 0''.13$ (-13.7°) (LkCa15) and $0''.057 \times 0''.054$ (88.6°) (HD 169142), respectively. The vertical black lines indicate the rings seen in the Band 9 continuum, and the light blue region starting from 0 AU indicates the gas cavity. The MRS of the HD 169142 $J = 6 - 5$ data corresponds to a radius of 35 AU.

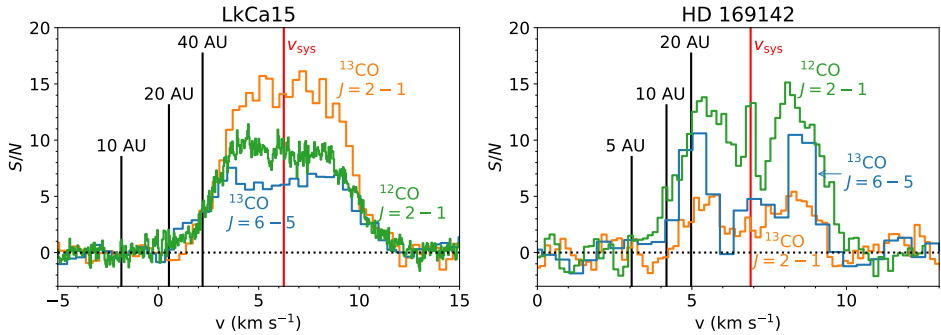


Figure 4.A.5: Signal-to-noise ratio of the $^{12}\text{CO } J = 2 - 1$, $^{13}\text{CO } J = 2 - 1$, and $^{13}\text{CO } J = 6 - 5$ spectra in the inner $1''.0$ and $0''.5$ for LkCa15 (left) and HD 169142 (right), resp. The systematic velocity is indicated with the vertical red line. The vertical black lines indicate the maximal velocities where emission at that radius is expected based on the Keplerian velocity profile. We note the difference in horizontal axes.

4.B Line ratio analysis

4.B.1 Temperature and column density

Rotational diagrams can be used to derive the temperature and column density of the gas observationally (e.g., Goldsmith & Langer 1999; Schwarz et al. 2016; Loomis et al. 2018; Pegues et al. 2020; Terwisscha van Scheltinga et al. 2021). The relation between the column density and rotational temperature, as discussed in Sect. 4.4, can best be solved in log-space:

$$\ln\left(\frac{N_u}{g_u}\right) = \ln N_{\text{tot}} - \ln Q(T_{\text{rot}}) - \frac{E_u}{kT_{\text{rot}}} \quad (4.9)$$

$$\ln\left(\frac{N_u^{\text{thin}}}{g_u}\right) + \ln C_\tau = \ln N_{\text{tot}} - \ln Q(T_{\text{rot}}) - \frac{E_u}{kT_{\text{rot}}}, \quad (4.10)$$

where we used the correction factor for the optical depth in the last line. The optical depth is discussed in the next section.

4.B.2 Optical depth

The observations cover both the $^{13}\text{CO } J = 2-1$ and the $\text{C}^{18}\text{O } J = 2-1$ transitions. Therefore, the ratio of these two lines can be used to derive the optical depth of $^{13}\text{CO } J = 2-1$. The equation of radiative transfer can be written as

$$T_{\text{b}} = T_{\text{ex}}(1 - e^{-\tau_\nu}), \quad (4.11)$$

with T_{b} the brightness temperature obtained from the non-continuum subtracted map and T_{ex} the excitation temperature of the line. The excitation temperatures of $^{13}\text{CO } J = 2-1$ and $\text{C}^{18}\text{O } J = 2-1$ are similar if both emit from the same region of the disk. Therefore, we can write

$$\frac{T_{\text{b},^{13}\text{CO } 2-1}}{T_{\text{b},\text{C}^{18}\text{O } 2-1}} = \frac{1 - e^{-\tau_{^{13}\text{CO } 2-1}}}{1 - e^{-\tau_{\text{C}^{18}\text{O } 2-1}}}. \quad (4.12)$$

As the line widths of the ^{13}CO and $\text{C}^{18}\text{O } J = 2-1$ transitions are similar, this line ratio is similar to the ratio of their integrated intensities, $I_\nu \Delta v$:

$$\frac{I_{^{13}\text{CO } 2-1} \Delta v}{I_{\text{C}^{18}\text{O } 2-1} \Delta v} = \frac{1 - e^{-\tau_{^{13}\text{CO } 2-1}}}{1 - e^{-\tau_{\text{C}^{18}\text{O } 2-1}}}. \quad (4.13)$$

Furthermore, the ratio of the optical depths of ^{13}CO and C^{18}O is identical to the isotopolog ratio, which we assume to be 8 (Wilson 1999). The isotopolog ratio for ^{12}CO to ^{13}CO is assumed to be 70 (Milam et al. 2005). The uncertainty on the optical depths is dominated by the uncertainty on the line ratio of the ^{13}CO to the $\text{C}^{18}\text{O } J = 2-1$ transition. Assuming a 10 % higher $^{12}\text{C}/^{13}\text{C}$ ratio of 77, lowers the optical depths of the ^{13}CO and $\text{C}^{18}\text{O } J = 2-1$ transitions slightly but the values remain consistent within the error bars in the disk region where C^{18}O

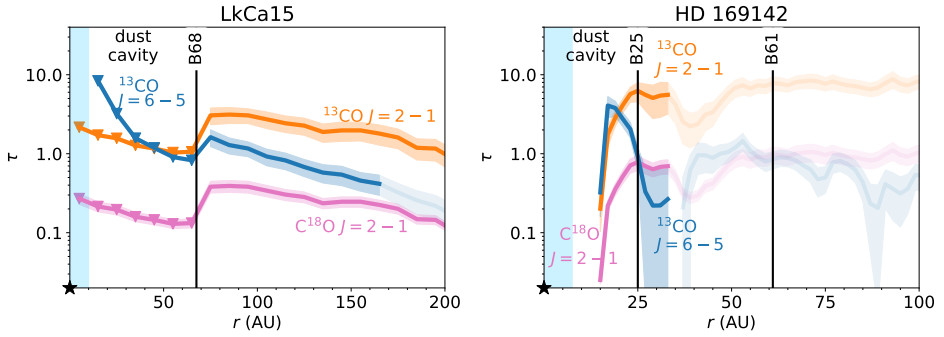


Figure 4.B.1: Optical depth of the ^{13}CO $J = 6 - 5$ and $J = 2 - 1$ transitions and the C^{18}O $J = 2 - 1$ transition for LkCa15 (left) and HD 169142 (right). The optical depth of the $J = 2 - 1$ transitions is derived from their respective line ratio, and the optical depth of the ^{13}CO $J = 6 - 5$ transition is derived using the line ratio analysis (see text for details).

is detected inside the MRS. Therefore, the uncertainty on the isotopolog ratio is neglected.

The optical depth of the ^{13}CO $J = 6 - 5$ line cannot be estimated in this way as no C^{18}O $J = 6 - 5$ observations are available. Therefore, we used an analytical expression for the optical depth (Goldsmith & Langer 1999):

$$\tau_\nu = \frac{A_{ul}c^3}{8\pi\nu^3\Delta V} \left(e^{h\nu/kT} - 1 \right) N_u. \quad (4.14)$$

This can be related to the optical depth of ^{13}CO $J = 2 - 1$, by taking the ratio of the two optical depths:

$$\frac{\tau_{65}}{\tau_{21}} = \frac{A_{65}\nu_{21}^3\Delta V_{21}}{A_{21}\nu_{65}^3\Delta V_{65}} \frac{e^{h\nu_{65}/kT_{65}} - 1}{e^{h\nu_{21}/kT_{21}} - 1} \frac{N_6}{N_2}. \quad (4.15)$$

This expression can be simplified by using the Planck function, assuming that the line widths are similar, and using that the ratio of the column densities is determined by a Boltzmann distribution:

$$\frac{\tau_{65}}{\tau_{21}} = \frac{A_{65}}{A_{21}} \frac{B_{21}(T)}{B_{65}(T)} \frac{g_6}{g_2} e^{-(E_6 - E_2)/kT}, \quad (4.16)$$

with $g_J = 2J + 1$ the degeneracy of level J for CO. The derived optical depths are presented in Fig. 4.B.1. The ^{13}CO $J = 2 - 1$ emission outside the dust cavity is optically thick in both disks as expected, the C^{18}O $J = 2 - 1$ transition is moderately optically thick. The optical depths of all transitions in the dust cavity of LkCa15 are upper limits as an upper limit on the integrated C^{18}O $J = 2 - 1$ intensity was used. In the case of HD 169142, the optical depth estimates outside 35 AU may be affected by the maximum resolvable scale of these observations.

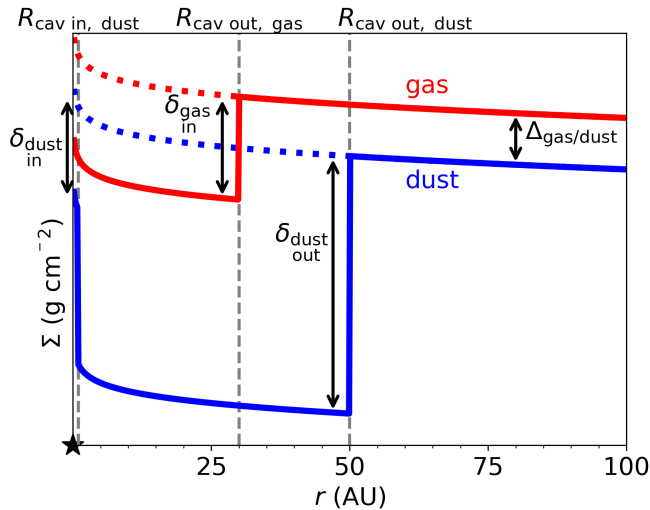


Figure 4.C.1: Generic structure of the DALI models. The gas surface density is indicated in red, and the dust surface density is indicated in blue.

4.C DALI

4.C.1 Model setup

The exploratory models for the ^{13}CO $J = 6 - 5$ to $J = 2 - 1$ line ratio discussed in Sect. 4.5 and Appendix 4.C.2 were computed using the thermochemical code DALI (Bruderer et al. 2009, 2012; Bruderer 2013). The disk gas and dust structure together with the stellar spectrum were used to calculate the thermal and chemical structure across the disk and predict the flux that can be observed by, for example, ALMA.

The radial structure of the gas and dust in DALI is based on the self-similar solution to a viscously evolving disk (Lynden-Bell & Pringle 1974; Hartmann et al. 1998):

$$\Sigma_{\text{gas}}(R) = \Sigma_c \left(\frac{R}{R_c} \right)^{-\gamma} \exp \left[- \left(\frac{R}{R_c} \right)^{2-\gamma} \right], \quad (4.17)$$

with $\Sigma_{\text{gas}}(R)$ the gas surface density at radius R , Σ_c , the gas surface density at the characteristic radius R_c , and γ is the power-law index, similar to the approach of Andrews et al. (2011). An overview of the gas and dust surface density structure is presented in Fig. 4.C.1 and an overview of all model parameters is presented in Table 4.C.1. The inner radius of the protoplanetary disk is set to the sublimation radius that can be approximated as

$$R_{\text{subl}} \approx 0.07 \text{ AU} \sqrt{\frac{L_\star}{L_\odot}}, \quad (4.18)$$

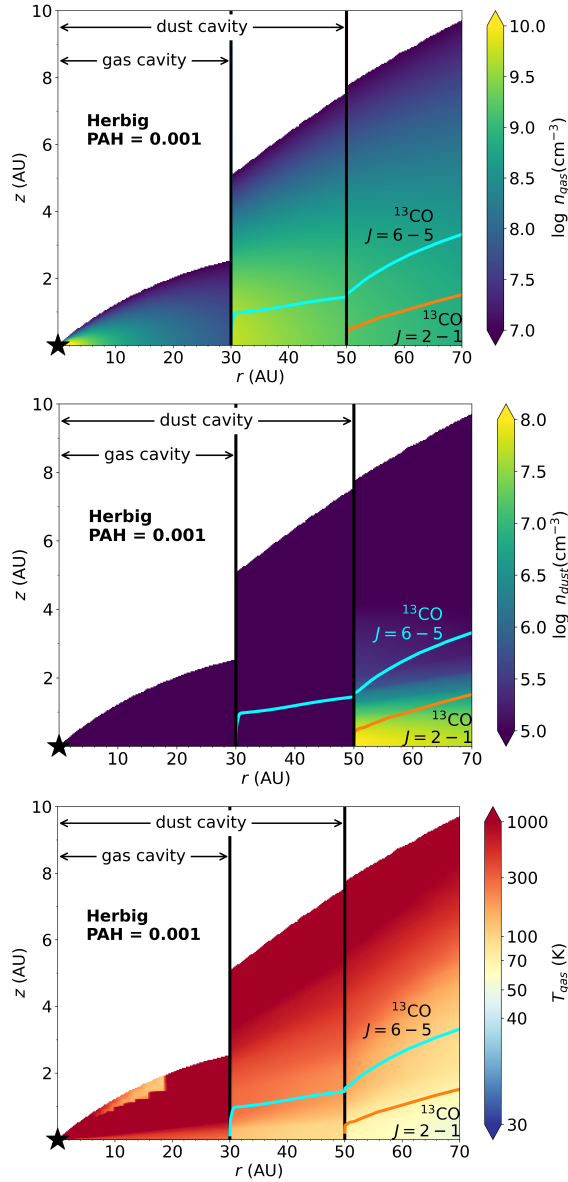


Figure 4.C.2: Gas number density (top), dust density (middle), and gas temperature (bottom) of our fiducial model for a Herbig star with a factor of 100 drop in gas density inside 30 AU. The cyan and orange contours indicate the $\tau = 1$ surface of the ^{13}CO $J = 6 - 5$ and $J = 2 - 1$ lines, respectively. The ^{13}CO $J = 2 - 1$ transition is optically thin inside the dust cavity, and the $J = 6 - 5$ is optically thin inside the gas cavity; hence, these lines trace the midplane at these radii. We note that the dust cavity starts from 50 AU inward and the gas cavity from 30 AU. Only the regions with a gas density above 10^7 cm^{-3} are shown. We note that the bottom panel is identical to the middle panel in Fig. 4.13.

with L_\star the luminosity of the star (Dullemond et al. 2001).

The vertical structure of the gas in the disk is assumed to follow a Gaussian distribution, where the scale height of the gas at each radius is given determined by the flaring, ψ , of the disk:

$$h = h_c \left(\frac{R}{R_c} \right)^\psi, \quad (4.19)$$

with h the scale height angle and h_c the scale height angle at R_c . This scale height angle can be converted to a physical height above the disk midplane, H , by $H \sim hR$.

The dust is modeled using two populations of dust grains following Andrews et al. (2011): small grains (5 nm–1 μ m) and large grains (5 nm–1 mm). Both dust populations follow the Mathis, Rumpl, and Nordseick (MRN) distribution ($a^{-3.5}$ with a the grain size; Mathis et al. 1977) and the mass fraction of large grains is controlled by f_{ls} . The small dust grains are assumed to be well-coupled to the gas and hence follow the same radial and vertical distribution. The larger grains are assumed to be settled to the midplane, as recent observations have shown (e.g., Villenave et al. 2020), and therefore the scale height of the large grains is reduced by a factor of $\chi < 1$. Finally, the total dust mass is scaled such that the global gas-to-dust mass ratio in the outer disk, $\Delta_{\text{g/d}}$, matches the interstellar medium (ISM) value of 100.

The transition disk structure was parametrized as presented in Fig. 4.C.1. The gas cavity was modeled by reducing the gas column density inside $R_{\text{cav out,gas}}$ by a factor of $\delta_{\text{gas in}} < 1$. The cavity in the dust was modeled in a similar way by a drop in column density controlled by $\delta_{\text{dust out}} < 1$ between $R_{\text{cav in,dust}}$ to $R_{\text{cav out,dust}}$. The dusty inner disk between R_{subl} and $R_{\text{cav in,dust}}$ was modeled with a factor of $\delta_{\text{dust in}} < 1$ with respect to the outer disk. The gas cavity is typically smaller than the dust cavity (Bruderer et al. 2014; Perez et al. 2015; van der Marel et al. 2015, 2016); therefore, we used $R_{\text{cav out,gas}} \leq R_{\text{cav out,dust}}$.

Polycyclic aromatic hydrocarbons are assumed to be well mixed with the gas. The abundance of PAHs was modeled as a step function where PAHs can only exist in the disk regions where the integrated far-UV flux is at most $10^6 G_0$, with G_0 the interstellar radiation field. In this region where PAHs are abundant, they provide an additional source of opacity. Thus, PAHs act both as a heating agent as well as a source for attenuation of UV radiation. A more detailed discussion on the treatment of PAHs with respect to the gas can be found in Bruderer et al. (2012) and Visser et al. (2007).

The stellar spectrum was modeled as a 4000 K (10000 K) black body for a T Tauri (Herbig) star. In the case of the T Tauri star, the UV-luminosity from accretion onto the star was modeled as an additional 10000 K black body and a mass accretion rate of $10^{-8} M_\odot \text{ yr}^{-1}$, corresponding to a UV luminosity of $0.15 L_\odot$. This is a typical mass accretion rate for a T Tauri type star (Francis & van der Marel 2020 and references therein).

The temperature structure in DALI was calculated in an iterative manner, starting with the dust temperature. The dust temperature was calculated using Monte Carlo continuum radiative transfer. Initially, the abundances of the

species in the chemical network were calculated assuming that the gas temperature is equal to the dust temperature. The chemical network used to calculate these abundances is based on the UMIST06 network (Woodall et al. 2007) and has previously been presented in Bruderer (2013). No isotope-selective chemistry was included and the network was evaluated assuming steady state. Instead, the isotopolog abundances were scaled to their main isotopolog using their elemental ratios given in Table 4.C.1. Finally, the heating and cooling rates, depending on the grain sizes following Facchini et al. (2017) and Facchini et al. (2018), were used to calculate the gas temperature independent of the dust temperature. The calculations of the abundances and gas temperatures were repeated until they are consistent.

Finally, the ^{13}CO $J = 6 - 5$ and $J = 2 - 1$ transitions were ray-traced using non-LTE excitation adopting the collisional rate coefficients from the LAMDA database (Botschwina et al. 1993; Flower 1999; Schöier et al. 2005). Our fiducial disk was located at 150 pc and has a face-on orientation.

Table 4.C.1: Other DALI model parameters.

Model parameter	T Tauri	Herbig	Description
<i>Physical structure</i>			
R_{subl}	0.07 AU	0.2 AU	Sublimation radius, calculated as $0.07 \text{ AU} \sqrt{L_*/L_\odot}$. ⁽¹⁾
$R_{\text{cav in, dust}}$	1 AU		Inner radius of the dust cavity.
$R_{\text{cav out, gas}}$	30 AU		Outer radius of the gas cavity.
$R_{\text{cav out, dust}}$	50 AU		Outer radius of the dust cavity.
R_c	100 AU		Characteristic radius of the surface density profile.
R_{out}	600 AU		Outer radius of the disk.
Σ_c	0.28 g cm ⁻²		Sets the gas surface density at the characteristic radius R_c .
M_{disk}	1.5(-3) M _⊙		Mass of the disk.
γ	1		Power law index of the surface density profile.
h_c	0.05		Scale height angle at the characteristic radius R_c .
ψ	0.05		Flaring index of the disk surface density.
PAH abundance	1(-3), 1(-1)		Abundance of PAHs w.r.t. to ISM value, in gas.
$\delta_{\text{gas, in}}$	1(-3), 1(-2), 1(-1), 1		Relative drop in gas density inside the gas cavity ($R_{\text{subl}} < R < R_{\text{cav out, gas}}$).
$\delta_{\text{gas, out}}$	1		Relative drop in gas density inside the dust cavity, but outside the gas cavity ($R_{\text{cav out, gas}} < R < R_{\text{cav out, dust}}$).
$\delta_{\text{dust, in}}$	1(-10), 1(-4)		Relative drop in dust density in the dusty inner disk w.r.t. the outer disk ($R_{\text{subl}} < R < R_{\text{cav in, dust}}$).
$\delta_{\text{dust, out}}$	1(-10)		Relative drop in dust density inside the dust cavity ($R_{\text{cav in, dust}} < R < R_{\text{cav out, dust}}$).

Table 4.C.1: Continued.

Model parameter	T Tauri	Herbig	Description
<i>Dust properties</i>			
χ	0.2		Settling of large grains.
f_{ls}	1(-10), 0.85, 0.98		Mass-fraction of grains that is large.
$\Delta_{\text{gas/dust}}$	100		Global gas-to-dust mass ratio.
<i>Stellar properties</i>			
M_{\star}	0.9 M_{\odot}	2.5 M_{\odot}	Mass of the central star.
$\dot{M}_{\star}^{(2)}$	1(-8) $M_{\odot} \text{ yr}^{-1}$	0 $M_{\odot} \text{ yr}^{-1}$	Mass accretion rate of the central star.
<i>Stellar spectrum</i>			
L_{\star}	1 L_{\odot}	10 L_{\odot}	Luminosity of the central star.
L_X		1(30) erg s^{-1}	X-ray luminosity of the central star.
T_{eff}	4000 K	10000 K	Effective temperature of the central star.
T_X		7(7) K	Effective temperature of the X-ray radiation.
$\zeta_{\text{c.r.}}$		5(-17) s^{-1}	Cosmic ray ionization rate.
<i>Observational geometry</i>			
i		0$^{\circ}$	Disk inclination (0° is face-on).
d		150 pc	Distance to the star.
<i>Chemistry</i>			
H		1	Abundance w.r.t. the total number of hydrogen atoms.

Table 4.C.1: Continued.

Model parameter	T Tauri	Herbig	Description
He		7.6(-2)	Abundance w.r.t. the total number of hydrogen atoms.
C		1.4(-4)	Abundance w.r.t. the total number of hydrogen atoms.
N		2.1(-5)	Abundance w.r.t. the total number of hydrogen atoms.
O		2.9(-4)	Abundance w.r.t. the total number of hydrogen atoms.
Mg		4.2(-7)	Abundance w.r.t. the total number of hydrogen atoms.
Si		7.9(-6)	Abundance w.r.t. the total number of hydrogen atoms.
S		1.9(-6)	Abundance w.r.t. the total number of hydrogen atoms.
Fe		4.3(-7)	Abundance w.r.t. the total number of hydrogen atoms.
$^{12}\text{C}/^{13}\text{C}$		70	Carbon isotope ratio.
$^{16}\text{O}/^{18}\text{O}$		560	Oxygen isotope ratio.

Notes. $a(b)$ represents $a \times 10^b$. Boldface indicates the fiducial value. ⁽¹⁾ Following Dullemond et al. (2001). ⁽²⁾ The stellar accretion rate is converted to a 10^4 K black body and then added to the stellar spectrum. An accretion rate of $10^{-8} M_{\odot} \text{ yr}^{-1}$ corresponds to a UV luminosity of $0.15 L_{\odot}$.

4.C.2 DALI models for other parameters

The effect of the gas cavity depth is discussed in Sect. 4.5. In this section the effect of other parameters such as the abundance of PAHs, the presence of a dusty inner disk and the mass fraction of large grains is investigated.

The results for the Herbig disk model with a deep ($\times 0.01$) gas cavity and a dusty inner disk³ are presented in Fig. 4.C.3. The dusty inner disk shields the cavity from UV-radiation, and therefore the gas between 30 and 50 AU is warmer in the model without a dusty inner disk, which is also reflected in the line ratio. This effect is even more pronounced in the region inside 30 AU, where the gas density is low.

The importance of PAHs is highlighted in the two rightmost panels of Fig. 4.13 and in the middle panel of Fig. 4.C.3. Increasing the PAH abundance increases the gas temperature in a thin layer at $z/r \sim 0.15$, but it decreases the gas temperature in the midplane and in intermediate layers due to attenuation of UV radiation. Furthermore, the two ^{13}CO transitions emit from higher disk layers due to this temperature change and because CO is abundant to higher disk layers. Together these two effects result in a lower line ratio of ~ 20 in the gas cavity, whereas the model with a lower PAH abundance of 10^{-3} with respect to the ISM predicts a high line ratio inside 30 AU. This is again due to the underlying temperature structure. The high abundance of PAHs in the former model effectively shields the midplane where the optically thin ^{13}CO lines are emitting from. The lack of UV radiation is responsible for the low temperatures.

Finally, the effect of grain growth is investigated by varying the fraction of large grains, f_{ls} , from 98% in the fiducial model to 85% and 0% in the models mimicking disks with smaller grains. The disk models with many small grains are colder because of the efficient shielding of UV radiation by these grains and PAHs that are abundant to larger scale heights. Therefore, heating through the photoelectric effect on PAH and far-UV pumped H_2 is less efficient in these regions, causing the line ratio to decrease when more grains are small.

³Other parameters as listed in Table 4.C.1.

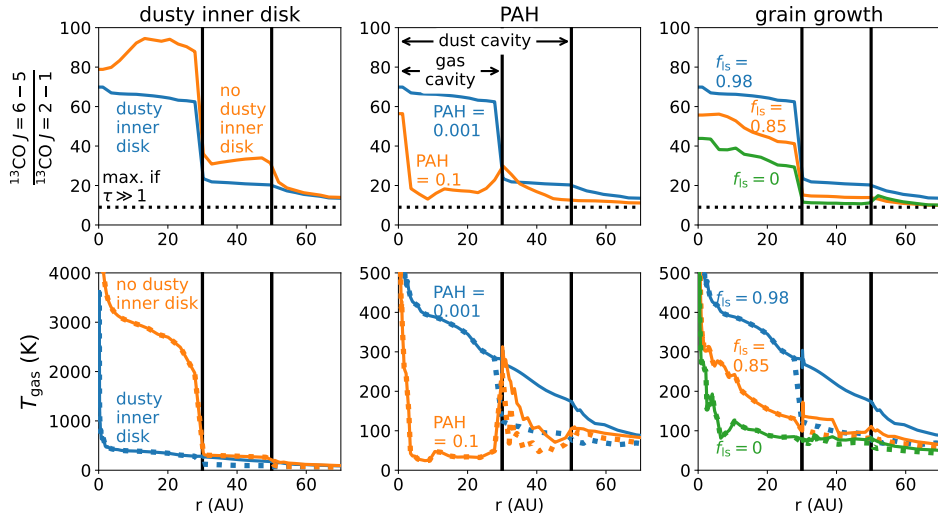


Figure 4.C.3: Modeled line ratio for the Herbig disk model (top), where the absence of a dusty inner disk (left), the PAH abundance with respect to the ISM (middle), and the fraction of large grains (right) are compared to the fiducial Herbig disk model with a 0.01 times drop in gas density inside 30 AU (blue). The bottom row shows the temperature at the $\tau = 1$ surface for the $^{13}\text{CO } J = 6 - 5$ (solid) and $J = 2 - 1$ (dotted) transitions. Both ^{13}CO lines are (moderately) optically thin inside the gas cavities of these models. Therefore, the midplane temperature is shown in this region. We note the difference in the temperature axes.

**A major asymmetric ice trap
in a planet-forming disk. IV.
Nitric oxide gas and a lack of
CN tracing sublimating ices
and a C/O ratio < 1**

M. Leemker, A. S. Booth, E. F. van Dishoeck, N. van der Marel, B. Tabone, N. F. W. Ligterink, N. G. C. Brunken, M. R. Hogerheijde

Abstract

Context. Most well-resolved disks observed with the Atacama Large Millimeter/submillimeter Array (ALMA) show signs of dust traps. These dust traps set the chemical composition of the planet-forming material in these disks, as the dust grains with their icy mantles are trapped at specific radii and could deplete the gas and dust at smaller radii of volatiles.

Aims. In this work, we analyse the first detection of nitric oxide (NO) in a protoplanetary disk. We aim to constrain the nitrogen chemistry and the gas-phase C/O ratio in the highly asymmetric dust trap in the Oph-IRS 48 disk.

Methods. We used ALMA observations of NO, CN, C₂H, and related molecules in the Oph-IRS 48 disk. We modeled the effect of the increased dust-to-gas ratio in the dust trap on the physical and chemical structure using a dedicated nitrogen chemistry network in the thermochemical code DALI. Furthermore, we explored how ice sublimation contributes to the observed emission lines. Finally, we used the model to put constraints on the nitrogen-bearing ices.

Results. Nitric oxide (NO) is only observed at the location of the dust trap, but CN and C₂H are not detected in the Oph-IRS 48 disk. This results in an CN/NO column density ratio of < 0.05 and thus a low C/O ratio at the location of the dust trap. Models show that the dust trap cools the disk midplane down to ~ 30 K, just above the NO sublimation temperature of ~ 25 K. The main gas-phase formation pathways to NO through OH and NH in the fiducial model predict NO emission that is an order of magnitude lower than what has been observed. The gaseous NO column density can be increased by factors ranging from 2.8 to 10 when the H₂O and NH₃ gas abundances are significantly boosted by ice sublimation. However, these models are inconsistent with the upper limits on the H₂O and OH column densities derived from *Herschel* PACS observations and the upper limit on CN derived from ALMA observations. As the models require an additional source of NO to explain its detection, the NO seen in the observations is likely the photodissociation product of a larger molecule sublimating from the ices. The non-detection of CN provides a tighter constraint on the disk C/O ratio than the C₂H upper limit.

Conclusions. We propose that the NO emission in the Oph-IRS 48 disk is closely related to the nitrogen-bearing ices sublimating in the dust trap. The non-detection of CN constrains the C/O ratio both inside and outside the dust trap to be < 1 if all nitrogen initially starts as N₂ and ≤ 0.6 , consistent with the Solar value, if (at least part of) the nitrogen initially starts as N or NH₃.

5.1 Introduction

Almost all bright and well-resolved disks observed with the Atacama Large Millimeter/submillimeter Array (ALMA) show dust traps seen as rings or cavities that have possibly been generated by planets forming in the disk (e.g., van der Marel et al. 2016; Huang et al. 2018; Long et al. 2018; Andrews 2020). These dust traps are the result of a local maximum in the gas pressure, causing the dust to drift to these regions (Whipple 1972; Pinilla et al. 2012a). These pressure maxima can be caused by a planet – but possibly also by dead zones, magnetic fields, gravitational instability, Rossby wave instability, or snowlines (e.g., Stevenson & Lunine 1988; Boss 1997; Paardekooper & Mellema 2006; Rice et al. 2006; Regály et al. 2012; Zhu et al. 2012; Meheut et al. 2013; Alexander et al. 2014; Suzuki et al. 2016; Stammerl et al. 2017). Once dust traps are formed, trapped dust pebbles may continue to grow to planetesimals, comets, and planets.

These dust traps can affect the global chemical composition of the planet-forming material, as the dust grains beyond the major snowlines are covered in icy mantles (McClure et al. 2020). Therefore, they trap ices at specific radii in the disk making the dust traps act as ice traps. The freeze-out and desorption of the major volatiles, H_2O , NH_3 , and CO , at their respective snowlines changes the chemical composition of the gas and dust (e.g., Öberg et al. 2011; Pinilla et al. 2017; Öberg & Bergin 2021; van der Marel et al. 2021c). Inside the water snowline in a smooth disk, the C/O ratio of the gas is expected to be close to the stellar value as all major volatiles are in the gas-phase, whereas outside the CO_2 or CO snowlines, the C/O ratio in the gas is higher because oxygen is locked up in the icy mantles. Similarly, the C/O ratio of the ices changes across the snowlines and is expected to be low compared to the gas. However, if a dust trap is present in the disk, this C/O ratio may change as a result of transport of icy pebbles. One extreme example of such a dust trap is the Oph-IRS 48 disk, hereafter the IRS 48 disk, making it a unique laboratory to study icy chemistry in disks.

The relative volatile carbon to oxygen budget in disks can be traced by the emission of [C I], [O I] observed by the PACS instrument on *Herschel* (Thi et al. 2010; Fedele et al. 2013a; Howard et al. 2013) and C_2H as these carbon species only become bright when the C/O ratio exceeds unity (Bergin et al. 2016; Kama et al. 2016; Bergner et al. 2019; Miotello et al. 2019; Bosman et al. 2021a; Guzmán et al. 2021). Other tracers of the C/O ratio are the ratio of CS to SO (Dutrey et al. 2011; Semenov et al. 2018; Facchini et al. 2021; Booth et al. 2021b; Le Gal et al. 2021) and the less explored CN to NO ratio (e.g., Hily-Blant et al. 2010a; Daranlot et al. 2012; Le Gal et al. 2014). The commonly observed CN radical is destroyed by atomic oxygen (Cazzoletti et al. 2018), whereas NO is enhanced if the gas is oxygen-rich because it is mainly formed through the reaction:



(Millar et al. 1991). NO is destroyed by photodissociation and the reaction:



Therefore, NO is expected to be bright when the gas-phase C/O ratio is low (Schwarz & Bergin 2014).

Ices that have a low C/O ratio are considered to be nitrogen-poor as 70 – 85% of the total available nitrogen is not identified in ices and could thus be in the form of gas-phase N or N₂ (Öberg et al. 2011; Boogert et al. 2015). The main carrier of nitrogen is NH₃, which typically has an abundance of only 5% compared to H₂O (Boogert et al. 2015). Other nitrogen-bearing ices seen in the comet 67P are HCN (21% w.r.t. NH₃), N₂ (13%) and HNCO, NH₂CHO, and CH₃CN (all < 5%), as well as ammonia salts (Rubin et al. 2019; Altwegg et al. 2020, 2022).

An extreme example of an asymmetric dust trap is the IRS 48 dust disk (van der Marel et al. 2013). The large mm-sized dust is concentrated in an arc in the south of this disk, possibly due to a vortex generated by a massive companion. Recent works have shown many complex organic molecules (COMs) such as CH₃OH and CH₃OCH₃, but also smaller species such as SO. In addition, for the first time in a disk, SO₂ and NO are seen in the gas-phase at the location of the dust trap (van der Marel et al. 2021b, hereafter Paper I, Booth et al. 2021b; Brunken et al. 2022, hereafter Paper II). The excitation temperature of CH₃OH and H₂CO of 100-200 K indicates that these molecules are thermally sublimated just inside the water snowline (Paper I and II). Furthermore, the detections of SO and SO₂ and the non-detection of CS point toward a low C/O ratio of < 1 (Booth et al. 2021b). Therefore, the dust trap is an ice trap, making this disk a unique laboratory to study the ice content in this disk. The snowlines of these COMs are most likely at the dust cavity edge that is heated by stellar radiation. The detection of NO further points to the presence of nitrogen-bearing ices on the dust.

ALMA dust polarization observations together with VLA data show that the dust surface density in the IRS 48 dust trap is very high at 2 – 8 g cm⁻² (Ohashi et al. 2020). Together with the low gas surface density of 0.07 g cm⁻² at this location (van der Marel et al. 2016), the local gas-to-dust ratio in this disk region is 0.04 – 0.009 instead of the nominal gas-to-dust ratio of 100 in the interstellar medium (ISM). In contrast to the large mm-sized grains, the small micron-sized dust and the gas traced by CO isotopologs are seen throughout the full 360° of the disk (e.g., Geers et al. 2007a; van der Marel et al. 2013; Bruderer et al. 2014; van der Marel et al. 2016). Modeling these CO isotopologue observations has constrained the IRS 48 disk mass to be as low as $5.5 \times 10^{-4} M_{\odot}$ (van der Marel et al. 2016), with an inclination of 50° and a position angle of 100° (Bruderer et al. 2014) based on ¹²CO observations.

IRS 48 is likely is an A0 ± 1 type star with a stellar luminosity of 14.3 L_⊙, using a dereddening slope of $R_v = 5.5$ (Brown et al. 2012; Follette et al. 2015). The high visual extinction of $A_V = 11.5$ makes a precise measurement uncertain. Schworer et al. (2017) inferred a stellar luminosity that was about three times higher, as more flux was attributed to the star instead of a ~ 1 AU inner disk, and a higher visual extinction of $A_v = 12.9$, together with a dereddening slope of $R_v = 6.5$ were used. Given the high extinction and for consistency with previous work modeling the IRS 48 disk, we used a stellar luminosity of 14.3 L_⊙. The star is located in the Ophiuchus star-forming cloud at a distance of 135 pc (Gaia Collaboration et al. 2018).

In this paper, we analyse the impact of the dust trap on the chemistry in the IRS 48 disk and, in particular, we focus on the detection of NO. To complement this search, we looked for other carbon- and nitrogen-bearing species and combined these with upper limits on OH, H₂O, CN, C₂H, N₂O, NO₂, and NH₂OH (Sect. 5.2). We modeled the molecular abundances using a thermochemical model where we explore different scenarios in Sect. 5.4. Finally, the observational and modeling results are discussed in Sect 5.5 and our conclusions are summarized in Sect. 5.6.

5.2 Observations and methods

5.2.1 Data

We used ALMA observations covering transitions of ¹³CO, NO, N₂O, NO₂, NH₂OH, CN, and C₂H. Only ¹³CO and NO are detected. A summary of the transitions covered with ALMA, details of the observations, and an overview of the line strengths obtained from the CDMS and JPL databases is presented in Table 5.1 (Pickett et al. 1998; Müller et al. 2001, 2005; Endres et al. 2016).

Six emission lines of NO with upper energy levels of 36 K at 350.7 GHz (3 lines), 351.04 GHz (1 line), and 351.05 GHz (2 lines) were observed as part of the ALMA project 2017.1.00834.S (PI: A. Pohl; see Table 5.1; Ohashi et al. 2020). Additionally, the data cover transitions of N₂O, NO₂, and NH₂OH. This data set has a sensitivity of ~ 1.2 mJy beam⁻¹ channel⁻¹ and a spectral resolution of 1.7 km s⁻¹. The imaging is described in detail in Papers I and II.

The CN $3_{0,7/2,7/2} - 2_{0,5/2,5/2}$, $3_{0,7/2,9/2} - 2_{0,5/2,7/2}$, and $3_{0,7/2,5/2} - 2_{0,5/2,3/2}$ transitions with $E_u = 33$ K at 340.248 GHz (2 lines) and 340.249 GHz (1 line), and ¹³CO 3 – 2 transition with $E_u = 32$ K at 330.588 GHz in Band 7 have not been published before. These two molecules were targeted as part of the ALMA program 2013.1.00100.S (PI: N. van der Marel). The IRS 48 disk was observed on June 14 2015 for 27 minutes on-source with 41 antennas and baselines ranging from 21.4 m to 783.5 m. The spectral windows covering the CN and the ¹³CO transitions have a resolution of 282.23 kHz (0.25 km s⁻¹). Both were self-calibrated using CASA version 4.2.2 (McMullin et al. 2007) with four rounds of phase calibration down to a solution interval of 24 s and subsequently one round of amplitude calibration with a solution interval of 48 s. This increased the signal-to-noise ratio (S/N) on the continuum from 217 to 804. The continuum and the ¹³CO are both detected and were imaged using the `clean` function in casa with used-defined masks and Briggs weighing with `robust = 0.5`. The images were `cleaned` to a noise threshold of 3× the rms that was measured in the line-free channels. The CN emission is imaged using natural weighing (equivalent to `robust = 2.0`) to maximize the sensitivity but it is not detected. Furthermore, the CN data were binned to 1 km s⁻¹ and the ¹³CO to 0.5 km s⁻¹ bins. The resulting 0.89 mm continuum image has a spatial resolution of $0''.19 \times 0''.14$ (65.4°) with the position angle of the beam indicated within the brackets, and a sensitivity of 56 μJy beam⁻¹. The ¹³CO and CN images have a spatial resolution of $0''.19 \times 0''.14$ (64.8°) and $0''.25 \times 0''.20$ (80.9°) and a sensitivity of 2.2 mJy beam⁻¹ and 1.8 mJy beam⁻¹, respectively.

Table 5.1: Molecular line and continuum ALMA observations used in this work

Molecule	Transition ^(a)	A_{ul} (s^{-1})	E_u (K)	Frequency (GHz)	Int. flux ^(b) ($mJy km s^{-1}$)	Channel width ($km s^{-1}$)	Channel rms ($mJy beam^{-1}$)	Beam	Ref.
NO ^(c)	$4_{-1,7/2,9/2} - 3_{1,5/2,7/2}$	5.4×10^{-6}	36	350.689	CH ₃ OH blend	1.7	~ 1.2	$0''.55 \times 0''.44$ (-79.8°)	(1)
NO ^(c)	$4_{-1,7/2,7/2} - 3_{1,5/2,5/2}$	5.0×10^{-6}	36	350.691	CH ₃ OH blend	1.7	~ 1.2	$0''.55 \times 0''.44$ (-79.8°)	(1)
NO ^(c)	$4_{-1,7/2,5/2} - 3_{1,5/2,3/2}$	4.8×10^{-6}	36	350.695	CH ₃ OH blend	1.7	~ 1.2	$0''.55 \times 0''.44$ (-79.8°)	(1)
NO ^(d)	$4_{1,7/2,9/2} - 3_{-1,5/2,7/2}$	5.4×10^{-6}	36	351.044	31	1.7	~ 1.2	$0''.55 \times 0''.44$ (-79.8°)	(1)
NO ^(d)	$4_{1,7/2,7/2} - 3_{-1,5/2,5/2}$	5.0×10^{-6}	36	351.052	23	1.7	~ 1.2	$0''.55 \times 0''.44$ (-79.8°)	(1)
NO ^(d)	$4_{1,7/2,5/2} - 3_{-1,5/2,3/2}$	4.8×10^{-6}	36	351.052	16	1.7	~ 1.2	$0''.55 \times 0''.44$ (-79.8°)	(1)
N ₂ O	$14_{0,0} - 13_{0,0}$	6.3×10^{-6}	127	351.668	< 45	1.7	~ 1.2	$0''.55 \times 0''.44$ (-79.8°)	(2)
NO ₂ ^(e)	$5_{1,5,11/2,13/2}$ $4_{0,4,9/2,11/2}$	1.4×10^{-5}	29	348.821	< 65	1.7	~ 1.2	$0''.56 \times 0''.44$ (80.2°)	(2)
NH ₂ OH ^(e)	$7_{1,7} - 6_{1,6}$	8.1×10^{-5}	76	352.298	< 46	1.7	~ 1.2	$0''.55 \times 0''.44$ (79.8°)	(2)
CN ^(f)	$3_{0,7/2,7/2} - 2_{0,5/2,5/2}$	3.8×10^{-4}	33	340.248	< 51	1.0	1.8	$0''.25 \times 0''.20$ (80.9°)	(3)
CN ^(f)	$3_{0,7/2,9/2} - 2_{0,5/2,7/2}$	4.1×10^{-4}	33	340.248	< 69	1.0	1.8	$0''.25 \times 0''.20$ (80.9°)	(3)
CN ^(f)	$3_{0,7/2,5/2} - 2_{0,5/2,3/2}$	3.7×10^{-4}	33	340.249	< 37	1.0	1.8	$0''.25 \times 0''.20$ (80.9°)	(3)
C ₂ H ^(g)	$4_{9/2,5} - 3_{7/2,4}$	1.3×10^{-4}	42	349.338	< 26	1.7	1.0	$0''.64 \times 0''.51$ (80.1°)	(4)
C ₂ H ^(g)	$4_{9/2,4} - 3_{7/2,3}$	1.3×10^{-4}	42	349.339	< 26	1.7	1.0	$0''.64 \times 0''.51$ (80.1°)	(4)
¹³ CO	$3 - 2$	2.2×10^{-6}	11	330.588	4.5×10^3	0.5	2.2	$0''.19 \times 0''.14$ (64.8°)	(3)
cont. ^(h)	0.89 mm			336	0.18		0.056	$0''.19 \times 0''.14$ (65.4°)	(3)

Notes. ^(a) Quantum numbers are formatted for NO as N_{K,J,F_1} and line strengths taken from CDMS and Varberg et al. 1999, NH_2OH as N_{K_u,K_c} (CDMS, Tsumekawa 1972), N_2O as $N_{K,v}$ (JPL, Burrus & Gordy 1956), NO_2 as $J_{\Omega,\Lambda,(F1),(F2),(F)}$ (JPL, Bowman & de Lucia 1982; Semmoud-Monnanteuil et al. 1989), CN as N_{v,J,F_1} (CDMS, Skatrud et al. 1983), C_2H as N_{J,F_1} (CDMS, Sastry et al. 1981), and ^{13}CO as J (CDMS Klapper et al. 2000). ^(b) Disk-integrated flux within the Keplerian mask. Blended lines are corrected for their expected line strength by scaling the total integrated flux with $A_{ij} \times g_u$ neglecting the dependence on E_u , unless denoted otherwise. ^(c) Detected but blended with the two other NO lines at 350.7 GHz and a methanol line. ^(d) Blended with the two other NO lines at 351.04 – 351.05 GHz. ^(e) Only the line that is expected to be brightest is listed. This line is blended with two weak 266 K lines, that are neglected for the calculation of the integrated flux. ^(f) Blended with another CN line at 340.2 GHz. ^(g) Blended with another C_2H line at 349.3 GHz. ^(h) Unit of the integrated continuum flux is Jy.

References. (1) ALMA project code: 2017.1.00834.S (Paper II). (2) ALMA project code: 2017.1.00834.S (this work). (3) ALMA project code: 2013.1.00100.S (this work). (4) ALMA project code: 2017.1.00834.S (van der Marel et al. 2021c).

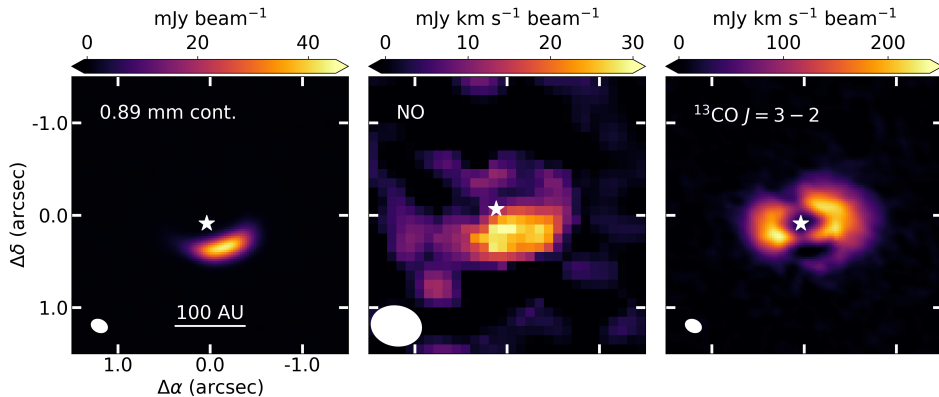


Figure 5.1: Dust and gas observations in the IRS 48 disk. *Left:* 0.89 mm continuum emission showing the major asymmetric dust trap in the south. *Middle:* Moment 0 map of the sum of the three NO lines at 351.1 GHz. *Right:* Moment 0 map of the ^{13}CO 3 – 2 transition. The position of the star and the beam of the observations are indicated with the white star and the white ellipse, respectively, in each panel. A 100 AU scale bar is indicated in the bottom of the left panel.

In addition to the ALMA observations, we also use the observations of the IRS 48 disk in the *Herschel* PACS DIGIT survey (Fedele et al. 2013a). These observations cover H_2O and OH far infrared lines in the spectral range of 51 – 220 μm , but neither of these molecules is detected, with H_2O fluxes lower than $(1.6 - 8) \times 10^{-17} \text{ W m}^{-2}$ and OH fluxes lower than $(1.2 - 9.6) \times 10^{-17} \text{ W m}^{-2}$. A full description of the data reduction is reported in Fedele et al. (2013a). As the $9''.4 \times 9''.4$ spaxels of the *Herschel* PACS data are much larger than the IRS 48 disk, only a disk-integrated analysis was carried out using these H_2O and OH data.

5.2.2 Data analysis

To increase the S/N of the NO and ^{13}CO integrated intensity (moment 0) maps, as well as that of the ALMA data covering the lines that were not detected, we used a Keplerian mask (Teague 2020)¹. The mask for each line is created using a stellar mass of $2 M_{\odot}$, a position angle of 100° , an inclination of 50° , a distance of 135 pc, and a source velocity of 4.55 km s^{-1} (Bruderer et al. 2014). Furthermore, the mask for the moment 0 maps has a large maximum radius of $4''.0$ to avoid any loss of diffuse emission in the outer disk. Additionally, the mask is smoothed with a beam 1.5 times larger than the spatial resolution of the data and assumes all emission is coming from the disk midplane. Finally, the line width in the mask is calculated as $0.5 \text{ km s}^{-1} \times (r/1''.0)^{-0.5}$ to encompass both the ^{13}CO 3 – 2 (presented in this work) and the previously published 6 – 5 line (van der Marel et al. 2016). For the uncertainty on the integrated fluxes, a Keplerian mask with a smaller outer radius of $0''.9$, fitting the $^{13}\text{CO } J = 3 - 2$ and $J = 6 - 5$ transitions, was used.

¹https://github.com/richteaue/keplerian_mask

This ensures that we include all pixels that could have emission, but as few of those without as possible. Furthermore, in the case of the blended NO lines at 351.05 GHz, we use the union of two Keplerian masks centered at the frequencies of the NO lines at 351.043 GHz and 351.051 GHz.

The error on the integrated intensity maps are calculated using the channel rms $\sigma_{\text{channel rms}}$:

$$\sigma_{\text{mom0}} = \sigma_{\text{channel rms}} \times \Delta V_{\text{channel}} \times \sqrt{N_{\text{channel}}}, \quad (5.3)$$

with $\Delta V_{\text{channel}}$ the spectral resolution of the image cube in km s^{-1} and N_{channel} the number of channels in the Keplerian mask in that pixel. To increase the S/N of the radial profile, the average over a 100° wedge is taken, following van der Marel et al. (2021b). This wedge is centered at position angle of 192° , close to the disk minor axis in the south to encompass the emission of the dust, NO, ^{13}CO , and CH_3OH . The error on this radial profile is propagated from that on the integrated intensity map:

$$\sigma_{\text{radial profile}} = \sqrt{\frac{1}{N_{\text{beams bin}} N_{\text{pix bin}}} \sum_{\text{pix}} \sigma_{\text{mom0}}^2}, \quad (5.4)$$

with $N_{\text{beams bin}} \geq 1$ as the number of independent beams in one radial bin within the wedge and $N_{\text{pix bin}}$ as the number of pixels used in that bin. For the azimuthal profile, the same equation is used but then with the number of beams and pixels in one azimuthal bin in a ring.

The error on the integrated flux, $\sigma_{F_\nu \Delta V}$, and the upper limits on the integrated fluxes of the non-detections are calculated as follows:

$$\sigma_{F_\nu \Delta V} = 1.1 \times \sigma_{\text{channel rms}} \times \Delta V_{\text{channel}} \times \sqrt{\frac{N_{\text{pix mask}}}{N_{\text{pix beam}}}}, \quad (5.5)$$

for an extended region, and as follows:

$$\sigma_{F_\nu \Delta V} = 1.1 \times \sigma_{\text{mom0}}, \quad (5.6)$$

for the spectra within one beam. The factor of 1.1 accounts for the 10% absolute flux calibration error of ALMA, which is necessary to include when comparing data from different observing projects, $N_{\text{pix mask}}$ is the total number of pixels included in the Keplerian mask and $N_{\text{pix beam}}$ is the number of pixels per beam. For the data used in this work, $N_{\text{pix mask}}/N_{\text{pix beam}} = 80 - 320$. In the case of a non-detection, a $3\sigma_{F_\nu \Delta V}$ upper limit is used.

5.2.3 Column densities

To compare our observations to other disks and disk models, we converted the (upper limits on) velocity-integrated fluxes to a column density following for instance, Goldsmith & Langer (1999):

$$N_u^{\text{thin}} = \frac{4\pi F_\nu \Delta V}{A_{ul} h c \Omega}, \quad (5.7)$$

Table 5.2: Derived column densities

Molecule	T_{ex} (K)	N_{ext} (cm^{-2})	N_{peak} (cm^{-2})
NO (north)	40		$< 3.0 \times 10^{14}$
NO (north)	100		$< 5.0 \times 10^{14}$
NO (south)	40	$\sim 6.7 \times 10^{14}$	7.7×10^{14}
NO (south)	100	$\sim 1.1 \times 10^{15}$	1.3×10^{15}
N ₂ O	40	$< 1.8 \times 10^{15}$	$< 1.7 \times 10^{15}$
N ₂ O	100	$< 6.6 \times 10^{14}$	$< 6.4 \times 10^{14}$
NO ₂	40	$< 2.1 \times 10^{15}$	$< 2.0 \times 10^{15}$
NO ₂	100	$< 5.6 \times 10^{15}$	$< 5.2 \times 10^{15}$
NH ₂ OH	40	$< 1.3 \times 10^{14}$	$< 1.4 \times 10^{14}$
NH ₂ OH	100	$< 1.7 \times 10^{14}$	$< 1.8 \times 10^{14}$
CN	40	$< 2.7 \times 10^{12}$	$< 4.1 \times 10^{13}$
CN	100	$< 4.1 \times 10^{12}$	$< 6.2 \times 10^{13}$
C ₂ H	40	$< 1.5 \times 10^{12}$	$< 1.1 \times 10^{13}$
C ₂ H	100	$< 2.1 \times 10^{12}$	$< 1.5 \times 10^{13}$
OH	< 100	no constraint	
OH	150	$\lesssim 6 \times 10^{14}$	
OH	> 200	$\lesssim 10^{14}$	
H ₂ O	< 100	no constraint	
H ₂ O	150	$\lesssim 1 \times 10^{14}$	
H ₂ O	> 200	$\lesssim 10^{14}$	

Notes. The upper limits on the column densities of N₂O, NH₂OH, OH, and H₂O derived in the extended region covered by the Keplerian mask N_{ext} are derived assuming an emitting region of 1.4×10^{-11} sr, similar to NO. This is because these species are expected to be closely related to the emitting region of NO. The emitting regions of CN and C₂H are assumed to be 8.0×10^{-11} sr (3.4 square arcseconds) and 1.6×10^{-10} sr (7.0 square arcseconds), respectively, using the area covered in the Keplerian mask. The peak column densities N_{peak} are derived using a spectrum within one beam at the location where the emission is brightest.

with N_u^{thin} as the column density of the upper energy level, u ; $F_\nu \Delta V$ is the integrated flux; A_{ul} is the Einstein A coefficient; c is the speed of light; h is the Planck constant; and Ω the emitting region. The column density of the upper level is set by the total column density, N , of the molecule assuming local thermodynamical equilibrium (LTE) and optically thin emission. The total column density N then follows from:

$$N = \frac{N_u Q(T_{\text{ex}})}{g_u} e^{E_u/kT_{\text{ex}}}, \quad (5.8)$$

with $Q(T_{\text{ex}})$ the partition function at excitation temperature, T_{ex} ; g_u as the degeneracy of the upper energy level; E_u is the energy; and k is the Boltzmann constant. The column density for each molecule is computed four times: we compute N for two different assumed excitation temperatures and for two different regions in the disk. The first temperature of 40 K corresponds to the assumed excitation temperature of NO in Paper II and the second temperature of 100 K corresponds to the excitation temperature of methanol (Paper I) in the IRS 48 disk. The excitation temperature of NO cannot be derived from the observations as all detected NO lines have an upper energy level energy of $E_u = 36$ K.

For the two regions, the column density within 1 beam (N_{peak}) and within an extended region (N_{ext}) are computed. The column density within 1 beam is computed using the spectrum extracted from the brightest pixel. To compute column densities, the physical size of the beam area is used. For comparison to other work, the column density is also calculated in an extended region, N_{ext} , using the total flux in the small Keplerian mask listed in Table 5.1 and an assumed emitting region. For the molecules that are directly related to the dust trap (NO, N_2O , NO_2 , NH_2OH , H_2O , and OH) an emitting area of 1.4×10^{-11} sr (0.6 square arcseconds, typically 10 times smaller than that covered by the Keplerian mask) is used as done in Paper I, II, and Booth et al. (2021b); for the molecules where this is not necessarily the case (CN and C_2H), the area covered by the Keplerian mask is used (8.0×10^{-11} sr, equivalent to 3.41 square arcseconds, and 1.6×10^{-10} sr equivalent to 7.0 square arcseconds, respectively). An overview of the resulting column densities at 40 and 100 K is presented in Table 5.2, the column densities at a range of temperatures are presented in Fig. 5.A.1.

5.3 Observational results

5.3.1 Detected lines

The observational results are presented in Figs. 5.1 and 5.2. We display the detections of the 0.89 mm continuum, the ^{13}CO 3 – 2 transition, and six transitions of NO. We provide upper limits for CN, N_2O , NO_2 , NH_2OH , and C_2H . The three NO lines at 350.7 GHz are blended with the $4_{0,4} - 3_{1,3}$ transition of CH_3OH (Paper II, see left panel in Fig. 5.2). Therefore, we focus on the three NO lines at 351.1 GHz, that are blended with each other, but not with any emission from other molecules (see right panel in Fig. 5.2). A spectrum in units of K can be found in Fig. 5.A.2.

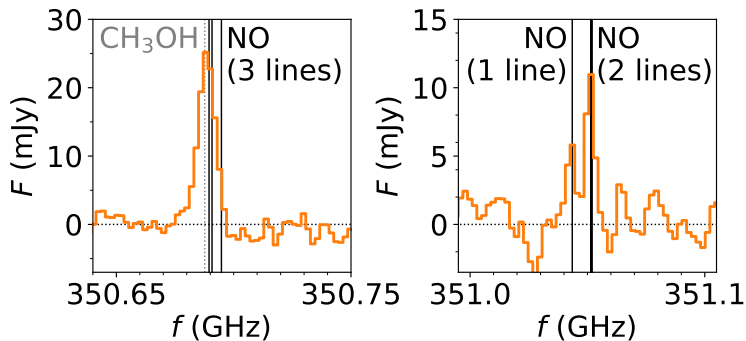


Figure 5.2: Continuum-subtracted and stacked spectra of the six NO transitions detected inside 115 AU. Left: Three NO lines at 350.7 GHz, indicated with the thick black vertical line, are blended with methanol (dotted grey line). Right: Two NO lines at 351.05 GHz are slightly blended with the final NO line at 351.04 GHz.

The Keplerian-masked integrated intensity maps of these three NO lines, together with the Keplerian masked ^{13}CO 3 – 2 transition and the 0.89 mm continuum, are presented in Fig. 5.1. Both the NO and the continuum emission are only detected in the south of the IRS 48 disk, where the dust trap is located. In contrast, the ^{13}CO emission does not show this asymmetry. Thus, there is no indication that the IRS 48 gas disk is azimuthally asymmetric apart from cloud absorption along the minor axis (Bruderer et al. 2014; van der Marel et al. 2016). The lack of ^{13}CO emission at the location of the dust trap is likely due to ^{13}CO 3 – 2 and continuum optical depth effects and not due to a lack of ^{13}CO gas at that location (see Fig. 5.A.3; Isella et al. 2016; Weaver et al. 2018). Additionally, the 25 AU gas cavity in this disk is also seen in the ^{13}CO $J = 3 - 2$ transition (van der Marel et al. 2016). The emission from COMs and NO is (close to) optically thin as this depression at the location of the dust trap is not seen in those moment 0 maps. The small depression of ^{13}CO emission along the disk minor axis is likely due to foreground cloud absorption at 3 – 4.5 km s $^{-1}$ that is seen in the ^{13}CO $J = 3 - 2$ channel maps (Fig. 5.A.4) and in the ^{12}CO 6 – 5 transition (van Kempen et al. 2009; Bruderer et al. 2014).

To further support the investigation of emission in the dust trap, the radial profiles are presented in Fig. 5.3. These profiles were extracted from an 100° wide wedge centered around a position angle of 192° east of north, following Paper I. The NO and methanol emission peak at the same location as the continuum. Furthermore, the emission of NO and methanol decreases slightly or stays relatively constant towards the position of the star due to the large beam of the NO and methanol observations. The steep decrease in the ^{13}CO 3 – 2 emission towards the star is indicative of the 25 AU gas cavity that is also seen in the ^{12}CO , ^{13}CO , and C^{18}O 6 – 5 transitions as these all have a high spatial resolution compared to that of the NO and methanol observations (Bruderer et al. 2014; van der Marel et al. 2016). The azimuthal profile is presented in Fig. 5.A.5.

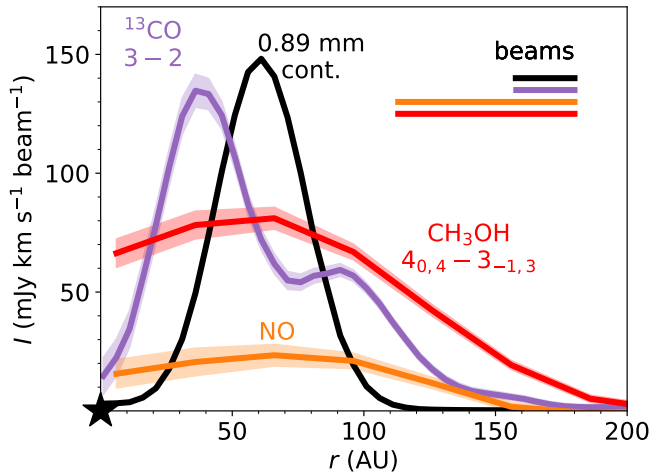


Figure 5.3: Radial profile of the continuum (black), NO (orange), ^{13}CO 3–2 (purple), and CH_3OH $4_{0,4} - 3_{-1,3}$ (red) emission averaged over an 100° angle, centered at 192° east of north where the large dust is located.

5.3.2 NO column density

The peak NO column density derived in this work is $7.7 \times 10^{14} \text{ cm}^{-2}$ and the NO column density assuming all NO emission is emitted from the same region as the continuum ($1.4 \times 10^{-11} \text{ sr}$) N_{ext} is $\sim 6.7 \times 10^{14} \text{ cm}^{-2}$ for an assumed $T_{\text{ex}} = 40 \text{ K}$. As the NO and continuum emission are unresolved in the radial direction, the true emitting area may be smaller than this value. The NO column densities found in this work are a factor of 4–10 lower than the value of $3 \times 10^{15} \text{ cm}^{-2}$ found in Paper II. The analysis in Paper II was done using a spectrum in K. This spectrum was computed by applying the Rayleigh Jeans law to the data cube and then integrating the emission over an $3.4 \times 10^{-11} \text{ sr}$ region, instead of the regular method of first applying the Rayleigh Jeans law and then averaging over these pixels. As the region used to compute the spectrum was five times larger than the $0''.55 \times 0''.44$ ($6.4 \times 10^{-12} \text{ sr}$) ALMA beam, the fluxes – and hence the column densities reported in Paper II – are overestimated by a factor of 5. The corrected NO spectrum in K is presented in Fig. 5.A.2. The abundance ratios reported in Paper II are not affected by this inconsistency as the difference of a factor of 5 drops out.

5.3.3 Upper limits on nitrogen-bearing molecules and C/O ratio

N_2O , NO_2 , and NH_2OH are expected to be closely linked to the chemistry of NO as NH_2OH is the product of its hydrogenation on icy grains and N_2O and NO_2 are the byproducts (Congiu et al. 2012; Fedoseev et al. 2012), however, none of these have been detected. In Table 5.2, the upper limits on their column densities are

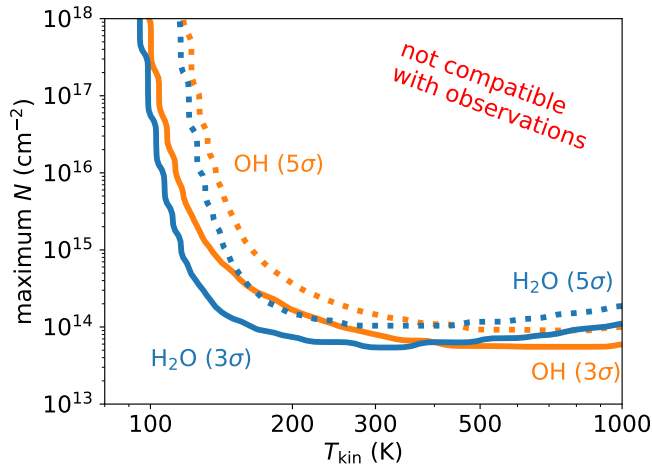


Figure 5.4: Maximum H₂O (blue) and OH (orange) column density above the optically thick dust that is compatible with the 3 σ (solid) and 5 σ (dotted) upper limits on the H₂O and OH flux using *Herschel* PACS observations.

reported for two different temperatures of 40 and 100 K, following the excitation temperature used to model the NO in Paper II and the excitation temperature found for CH₃OH in Paper I. As the NO lines listed in Table 5.1 all have an upper energy level of 36 K, its excitation temperature is not tightly constrained. Increasing the assumed excitation temperature of NO to 100 K increases the (upper limit) on its column density by a factor of ~ 2 . For both temperatures, the upper limits on the N₂O, NO₂, and NH₂OH column densities are comparable to the NO column density at the dust trap.

In contrast to many other disks, CN is not detected in the IRS 48 disk and its peak column density is constrained to be $< 4.1 \times 10^{13} \text{ cm}^{-2}$, assuming a temperature of 40 K. This is a factor of 6.6 – 47 lower than the peak CN column densities derived for the five disks that were observed as part of the MAPS large program with masses 8 – 360 times larger than that of the IRS 48 disk (Bergner et al. 2021; Öberg et al. 2021; Zhang et al. 2021). Our assumed emitting region is similar to the emitting region of ¹³CO as both CN and ¹³CO are expected to trace large radial extents of the disk (e.g., Law et al. 2021a; Nomura et al. 2021), although some radial differences may be expected (Cazzoletti et al. 2018; van Terwisga et al. 2019; Paneque-Carreño et al. 2022). A CN/NO ratio of < 0.05 was found. This points to a low C/O ratio that is consistent with that found from the CS/SO ratio Booth et al. (2021b). This conclusion is strengthened by the non-detection of C₂H, a molecule that becomes abundant when C/O > 1 (Bergin et al. 2016; Bergner et al. 2019; Miotello et al. 2019; Bosman et al. 2021a). We further explore this in a qualitative way in Sects. 5.4.2 and 5.4.4, as well as Appendix 5.B.2.2 using thermo-chemical disk models.

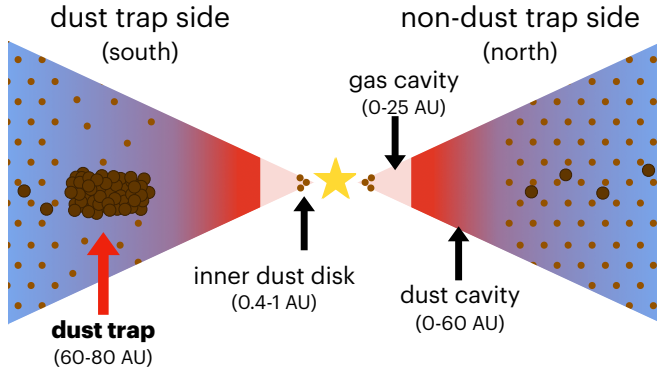


Figure 5.5: Cartoon of the dust trap side (south) and non-dust trap side (north) of the disk. The background color indicates the gas and its temperature. The faded red inside 25 AU indicates the deep gas cavity. The small and large brown circles indicate the small and large dust, respectively. Large amounts of dust are mainly present between 60 and 80 AU in the dust trap side (south) of the disk.

5.3.4 Upper limits on H₂O and OH

Far-infrared lines of H₂O and OH are covered in the *Herschel* DIGIT survey using the PACS instrument (Fedele et al. 2013a). Similarly to the carbon- and nitrogen-bearing molecules CN, C₂H, N₂O, NO₂, and NH₂OH, the IRS 48 disk shows no detection of H₂O and OH lines. We revisited these upper limits using the LTE model of Fedele et al. (2013a), assuming that the emission originates from a slab with homogeneous column density and temperature, and including line opacity effects (see Bruderer et al. 2010 for further details). The emitting area of H₂O and OH is assumed to be that of the trap (5000 AU² or 1.4×10^{-11} sr). This allows us to convert the non-detection into constraints on the column density of H₂O and OH, and temperature. The joint constraints on the column density above the optically thick dust are presented in Fig. 5.4, using the 3σ and 5σ upper limits.

In this figure, two regimes can be distinguished, depending on the assumed temperature. First, if the temperature of the H₂O and OH emitting regions is < 100 K, no constraint can be set and the trap may be rich in H₂O and OH. On the other hand, if the temperature exceeds 200 K, both the H₂O and OH column densities are constrained to be $\lesssim 10^{14}$ cm⁻², with H₂O and OH far-IR lines being optically thin. The excitation temperature of H₂CO of 173_{-9}^{+11} K derived in Paper I shows that there is a layer of gas above the dust trap where the gas reaches these high temperatures and H₂CO can exist. Furthermore, H₂O is expected to be frozen out on the dust grains if the temperature is lower than $\lesssim 100$ K based on its 5770 K binding energy (Fraser et al. 2001). Therefore, the temperature range of $\sim 150 - 200$ K is likely the most relevant range for our analysis given the complementary observations. Finally, the *Herschel* PACS observations only probe the column of H₂O and OH above the optically thick dust at 51 – 220 μ m, therefore, the full H₂O and OH column density may be higher than the upper limits derived here.

5.4 Models

The observations show a clear north-south asymmetry in the NO emission that is possibly related to the dust trap. To investigate the origin of this asymmetry and the chemical composition of the gas and ice in the IRS 48 disk we ran a grid of thermochemical models using DALI (Bruderer et al. 2012; Bruderer 2013). We tested three scenarios: (1) a fiducial model, (2) a model with sublimating H₂O and/or NH₃ ice, and (3) a model with sublimating NO ice.

The models are based on the previously published, azimuthally symmetric IRS 48 disk model with a fixed gas density and a high dust surface density in the dust trap (Bruderer et al. 2014; van der Marel et al. 2016). More details can be found in Fig. 3 and Fig. C.1 of Paper I. We improved on this model by modeling the chemistry in the dust trap (south side) and the non-dust trap (north side) of the disk separately, using the model parameters in Table 5.B.1 for models 1-3. In particular, we modeled the effect of the ice trap by increasing the initial abundance of gas-phase species to O/H and N/H ratios above the typical ISM values, mimicking their enhanced abundances due to radial drift and subsequent sublimation.

The typical gas number density at the dust trap edge is 10^8 cm^{-3} and the corresponding dust number density n_{dust}^2 in that region increases up to $7.5 \times 10^{10} \text{ cm}^{-3}$. Furthermore, the large dust is settled to the disk midplane with a scale height that is a factor of 0.1 of that of the gas and small dust. The midplane dust temperature in Fig. 5.6 increases from 52 K at the inner edge of the dust trap at 60 AU to 58 K at 60.3 AU, then decreases to 31 K at 64 AU and increases again slightly, reaching 38 K at the outer edge at 80 AU. A full description of the model is given in Appendix 5.B together with an overview of the gas and dust density, temperature, and the UV field (Fig. 5.B.2). A cartoon of the gas and dust distribution is presented in Fig. 5.5.

First, we describe our investigation of the effect of the dust trap on the model in Sect. 5.4.1. Second, the effects of sublimating H₂O and NH₃ ices are given in Sect. 5.4.2. Third, the effect of additional NO in the disk is explored in Sect. 5.4.3.

The chemical abundances are computed using an updated version of the nitrogen chemistry network first presented in Visser et al. (2018), Cazzoletti et al. (2018), and Long et al. (2021), (for details see Appendix 5.B.1.3). This network is suited to evaluate the abundance of nitrogen-bearing species such as NO and CN, but also small hydrocarbons such as C₂H. This network includes freeze-out and desorption but it does not include any ice-phase chemistry, except for the formation of H₂, H₂O, CH₄, NH₃, and HCN ices. More complex nitrogen-bearing molecules such as N₂O, NO₂, and NH₂OH are not included in this network. Carbon-bearing molecules up to C₂H₃ (ethylenyl) are included in this model. The binding energy of C₂H₃ is set to 10^4 K to mimic the effect of C₂H₃ being converted to other larger carbon-chain molecules that have a high binding energy. A lower binding energy results in gas-phase C₂H₃ that photodissociates into smaller molecules producing unphysically high abundances of other molecules such as C₂H. Thus C₂H₃ acts as

²Defined as $n_{\text{gas}}/n_{\text{dust}} = \rho_{\text{gas}}/\rho_{\text{dust}} = 0.04 - 0.009$, with ρ the mass density in g cm^{-3} (van der Marel et al. 2016; Ohashi et al. 2020).

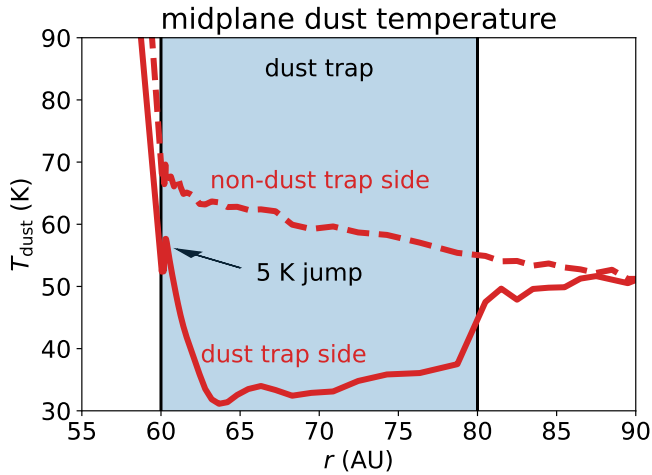


Figure 5.6: Midplane dust temperature in the DALI model for the dust trap side (solid) and non-dust trap side (dashed). Note: there is a 5 K jump at the edge of the dust trap.

a sink of hydrocarbons in this model (Wei et al. 2019). For NO, we used a binding energy of 1600 K, consistent with its 40-50 K desorption temperature in laboratory experiments (Collings et al. 2004; Garrod & Herbst 2006; Wakelam et al. 2017). Typically, NH_2OH desorbs at a much higher temperature of 170 – 250 K under laboratory conditions (Zheng & Kaiser 2010; Congiu et al. 2012; Ioppolo et al. 2014; He et al. 2015; Fedoseev et al. 2016; Jonusas & Krim 2016; Tsegaw et al. 2017). Using the Redhead equation (Redhead 1962), a binding energy of ~ 6500 K can be derived assuming a pre-exponential factor of 10^{13} s^{-1} (Congiu et al. 2012). Similarly, for N_2O , the Redhead equation, together with an assumed pre-exponential factor of 10^{13} s^{-1} and a measured peak desorption temperature of ~ 75 K under laboratory conditions, results in a binding energy of ~ 2500 K, which is consistent with the literature value (Congiu et al. 2012; Ioppolo et al. 2014).

The fiducial network starts with molecular initial conditions where all nitrogen starts in gas-phase N_2 with an abundance of 3.1×10^{-5} with respect to hydrogen, and all oxygen is initially distributed over gas-phase CO (1.3×10^{-4} w.r.t hydrogen) and H_2O (1.9×10^{-4} w.r.t. hydrogen; see Table 5.B.1). The models start with all molecules initially in the gas-phase to mimic the very quick sublimation from the ices. The models are run time dependently up to 100 yr and 10^3 yr inside the dust trap. These time scales correspond to the typical freeze-out time scale just above the dust trap at $r = 70$ AU and $z = 5$ AU, and the time scale on which the dust trap could have been formed based on hydrodynamical models (van der Marel et al. 2013), respectively. The default time scale is 100 yr. Outside the dust trap in the south and in the entire north side of the disk, the disk chemistry is evolved to 1 Myr, the typical disk formation timescale of a protoplanetary disk. As the youngest Keplerian rotating disks are detected in Class 0 objects with an

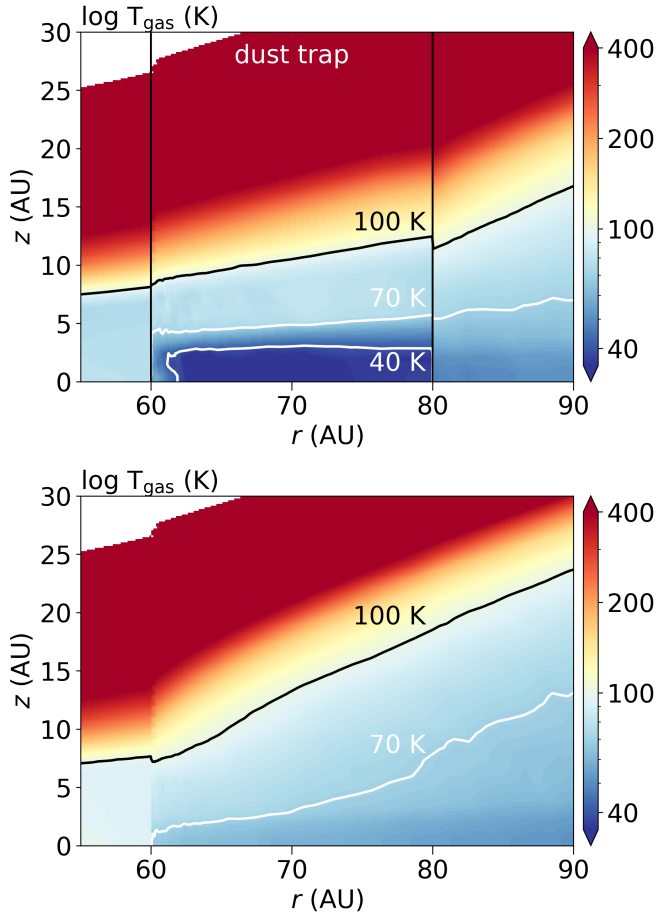


Figure 5.7: Gas temperature structure in the IRS 48 disk model with (top) and without (bottom) a dust trap between 60 and 80 AU. The dust trap midplane is up to ~ 30 K colder than the corresponding region in the non-dust trap side of the disk. At $z > 10$ AU the dust trap model is warmer than the non-dust trap side due to the intense radiation field above the dust trap. The gas and dust temperature are similar below the $T_{gas} = 70$ K contour. Note: these figures are zoomed in on the dust trap region. The vertical black lines in the left hand panel indicate the inner and outer radius of the dust trap.

approximate age on the order of 10^5 yr (Evans et al. 2009; Tobin et al. 2012; Murillo et al. 2013) and the typical disk life time is ~ 6 Myr (e.g., Haisch et al. 2001). Evolving the disk for shorter (0.5 Myr) or longer (up to 10 Myr) timescales does not change the NO column density in the south side of the disk outside the dust trap by more than 1.4%.

Synthetic images are made using the raytracer in DALI to compare the models to the observations. The excitation temperature in each cell is calculated explicitly, without assuming LTE, using the collisional rate coefficients for NO with He, scaled down with a factor 1.4 to account for collisions with H_2 from the LAMDA database (Varberg et al. 1999; Schöier et al. 2005; Lique et al. 2009). The images cubes are then convolved to the $0''.55 \times 0''.44$ (79.8°) beam of the observations. The DALI raytracer does not take line blending into account. Instead, the three NO lines at ~ 351.05 GHz were raytraced separately and added afterwards. This is appropriate if these NO lines are optically thin, which is the case for all models except those with a very high initial NO abundance.

5.4.1 Dust trap cools the disk midplane

The resulting gas temperature structure in the dust trap (south) and the non-dust trap side (north) are presented in Fig. 5.7. The gas temperature is up to 32 K lower inside the bulk of the dust trap than it is in the same disk region without the dust trap. This is due to the very high dust density of the large grains in the dust trap shielding the UV radiation that heats the disk. Therefore, despite their 30-60 times lower opacity to UV radiation, the large grains absorb almost all UV that is incident on the dust trap, lowering the temperature. Notably, a small jump of 5 K in the temperature is seen at 60.3 AU due to the intense radiation field (see Fig. 5.6). Furthermore, both sides of the disk are too warm for CO freeze-out (at ~ 20 K).

The 32 K drop in the dust temperature in the dust trap is not sufficiently cold for NO freeze-out ($T \sim 25$ K in the dust trap). As the non-dust trap side is warmer, NO is not freezing out in the IRS 48 disk model. The dust trap could still contain ices that have formed from NO in earlier phases, for example, N_2O , NO_2 , and NH_2OH that are products formed in NO hydrogenation experiments and have larger binding energies (Congiu et al. 2012; Yıldız et al. 2013; Fedoseev et al. 2012, 2016) but as N_2O , NO_2 , and NH_2OH are not included in the chemical network, their contributions cannot be studied directly with our model. Therefore, the dust trap can contain a reservoir of nitrogen-bearing ices build up from the colder earlier phases.

The NO abundance predicted by the dust-trap model is presented in the top panel of Fig. 5.8. The NO has a moderate abundance of 1.4×10^{-8} in the surface layer at $z/r = 0.3$ (indicated with the dashed white line). In the top half of this layer, NO is mainly formed in the gas through:



The OH is formed through the photodissociation of water as water photodissociates into OH, H, and O, where the latter reacts with molecular hydrogen to form more

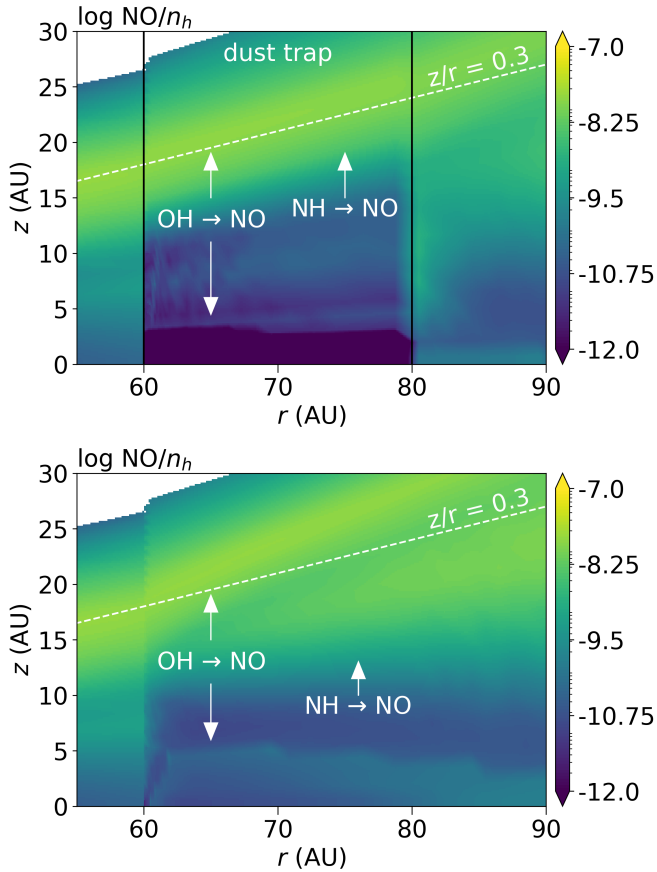


Figure 5.8: NO abundance in the model with a dust trap (top) and without a dust trap (bottom). Note: the NO abundance inside the dust trap is lower than in the model without a dust trap except for a thin layer at $z/r \sim 0.3$ (white dashed line), opposite of what is observed in the observations. This shows that the fiducial model is not sufficient to reproduce the observations.

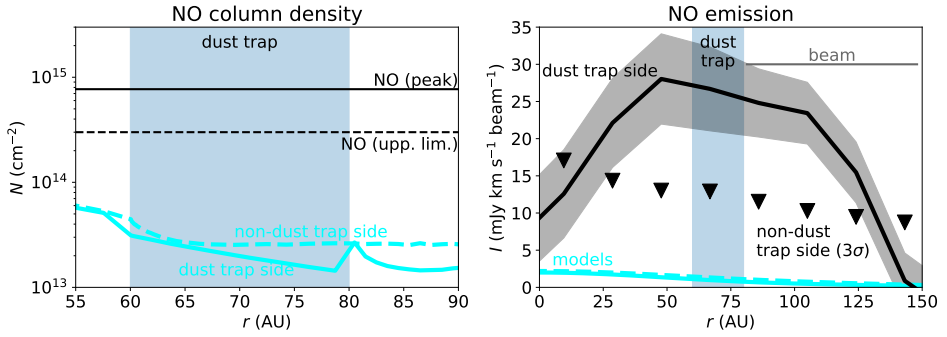


Figure 5.9: NO column density (left) and emission (right) predicted by the model for the dust trap side (solid blue) and non-dust trap side (dashed blue). The horizontal black lines in the left panel indicate the NO column density or the upper limit derived by the observations. The black line in the right panel indicates the horizontal cut of the NO emission through the dust trap and the triangles indicate the 3σ upper limit on the intensity in the north. The horizontal grey line in the right panel indicates the beam size. Note: the two panels have a different horizontal axis.

OH. In the lower half of the NO surface below $z/r = 0.3$, a second pathway through NH appears:



where NH is formed from the reaction of N with vibrationally excited H₂. Deeper down in the disk including the dust trap itself, the NO abundance decreases due to a lack of OH and NH, the two main ingredients needed to form NO. The main destruction path of NO is through photodissociation.

The NO abundance in the non-dust trap side of the model is presented in the bottom panel of Fig. 5.8. The formation and destruction pathways for NO are similar in the north side of the disk. The surface layer of NO splits into two layers: one where NO is mainly formed through OH and one where NO is mainly formed through NH. Furthermore, between the midplane and $z = 5$ AU, an NO layer with an abundance of $\sim 10^{-10}$ is present, indicated by the downward arrow in the bottom panel of Fig. 5.8. This layer is located just above the water snow surface, where some sublimating water photodissociates into OH and then forms NO. This layer can also be seen just above the dust trap in the dust trap model (top panel of Fig. 5.8).

The column density and emission predicted by the model are compared to the observations in Fig. 5.9. The model column density in the non-dust trap side (dashed blue line) is 7 – 12 times lower than the upper limit that is derived by the observations. Similarly, the emission predicted by the non-dust trap side is consistent with the non-detection of the NO in the north. On the other hand, the dust-trap side of the model underpredicts the NO column density by a factor of 25 – 50 and the emission by a factor of 15. Furthermore, the dust trap model does not reproduce the characteristic shape of the NO emission that is only present at

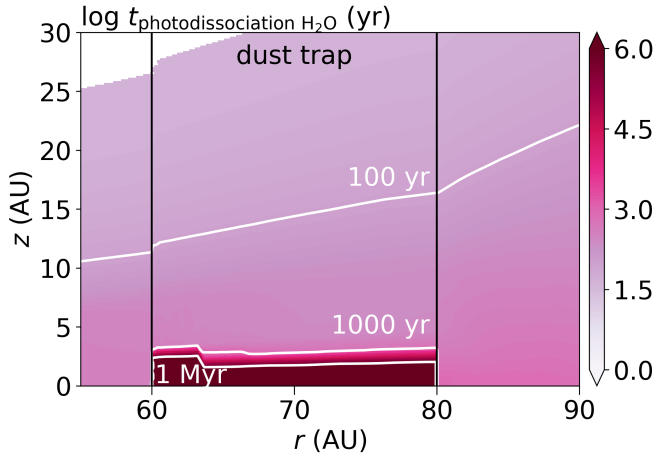


Figure 5.10: Photodissociation timescale of H_2O . In the dust trap midplane the photodissociation timescale is long due to the shielding of UV radiation by dust. Above the dust trap, the photodissociation timescale is much shorter, from 10^3 yr just above to trap to < 100 yr above ~ 15 AU.

the location of the dust trap. Therefore, the NO abundance in the south needs to be enhanced compared to the fiducial model to explain the observations.

5.4.2 Effect of sublimating ices: H_2O and NH_3

Observations of ices in young stellar objects and in comets show that oxygen is primarily locked up in water ice, whereas nitrogen is mostly stored in NH_3 ice (Boogert et al. 2015; Rubin et al. 2019). The gas-phase detections of CH_3OH , H_2CO , SO, and SO_2 , as well as other complex organic molecules in the IRS 48 disk show that the dust trap is an ice trap (Paper I and II, Booth et al. 2021b). Therefore, H_2O ice is also likely sublimating above the dust trap. The photodissociation timescale of water is presented in Fig. 5.10 using a photodissociation rate attenuated by grown dust particles appropriate for protoplanetary disks:

$$t = \frac{1}{kE_2(\gamma A_V)}, \quad (5.11)$$

with t as the photodissociation timescale, $k = 7.7 \times 10^{-10} \text{ s}^{-1}$ as the photodissociation rate of H_2O , $E_2(x)$ as the second order exponential integral, $\gamma = 0.41$ as the dust shielding factor for H_2O for large grains, and A_V as the visual extinction (Heays et al. 2017). Water dissociates in less than 10^3 years just above the dust trap and in less than 100 years for the layers above the dust trap at $z > 15$ AU, providing a reservoir of OH that is partially used to form NO.

Increasing the initial ice and, thus, the gas-phase water abundance by a factor of 2 and 5 only increases the NO column density with a factor of 1.6 – 2.8, up to a peak column density of $8.6 \times 10^{13} \text{ cm}^{-2}$, as presented in the top left panel of

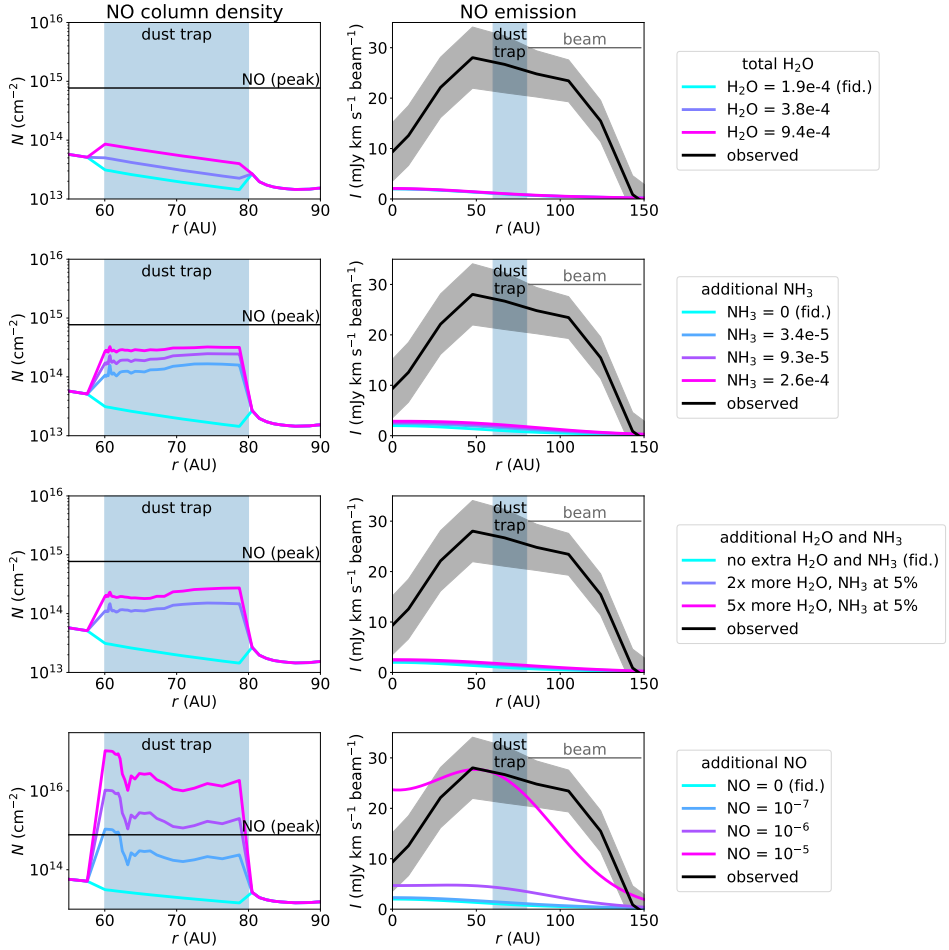


Figure 5.11: NO column density (left) and emission (right) for the dust trap models with different initial conditions. The different rows indicate the effect of additional H₂O (first row), NH₃ (second row), H₂O and NH₃ (third row), and NO (final row). The NO column density in the bottom row is dominated by that hidden underneath the $\tau_{\text{dust}} = 1$ layer. The chemical network inside the dust trap is evolved for 100 yr whereas that outside is evolved for 1 Myr. The horizontal black line in the left column indicates the NO column density derived from the observations and the black line in the right column indicates the observed emission. Note: a difference is apparent in the vertical axis of the bottom left panel.

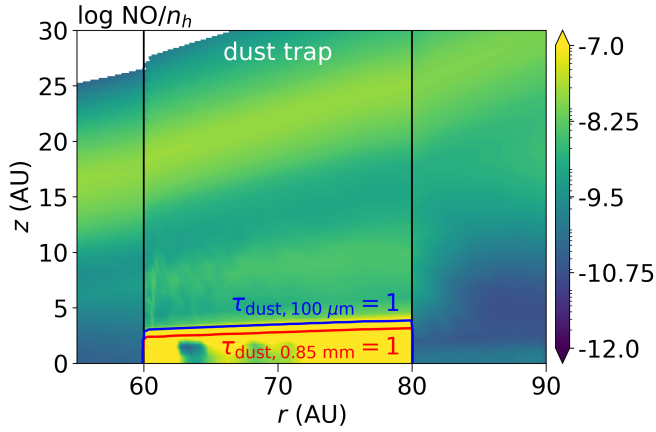


Figure 5.12: NO abundance after 100 yr in the dust trap model with an initial NO abundance of 10^{-5} . Most of the NO is hidden below the $\tau_{\text{dust},0.85 \text{ mm}} = 1$ surface at 0.85 mm indicated by the red contour. The blue contour indicates $\tau_{\text{dust},100 \text{ }\mu\text{m}} = 1$ at 100 μm , representative of the wavelength of the H₂O and OH upper limits.

Fig. 5.11. This is still an order of magnitude smaller than the NO column density found from the observations. Thus, much higher initial abundances of water ice, translating into enhanced gas-phase water that would be needed to explain the NO column density. However, this is inconsistent with the upper limit on the warm H₂O and OH column density derived from the *Herschel* PACS observations, suggesting that a different formation pathway of NO is dominant.

The column density of warm ($> 150 \text{ K}$) water predicted by the fiducial model and the models with additional H₂O is a factor of ~ 14 higher than the upper limit derived from *Herschel* at that temperature (see Figs. 5.4, 5.B.7, and 5.B.8). Similarly, the warm OH column density is a factor of ~ 30 higher than its observed upper limit. Additionally, the upper limit on the CN column density constrains the minimum initial water abundance to be $\sim 1.9 \times 10^{-5}$ if all nitrogen starts as N₂ and $\gtrsim 9.4 \times 10^{-5}$ if this is not the case. This is because lower water abundances overproduce the upper limit on the CN column density (see Fig. 5.B.5). Hence, the C/O is constrained to be $\lesssim 1$ (if all nitrogen starts as N₂) or $\lesssim 0.6$ (if some nitrogen starts as N or NH₃) at the dust trap. Thus, sublimating water alone cannot explain the high NO column density.

The second pathway to NO in the model is through NH. In the disk surface layers, NH is created by the reaction of N with vibrationally excited H₂, but in the dust trap it could be created through sublimating NH₃ that photodissociates. This is modeled as an additional gas-phase NH₃ abundance of $3.4 \times 10^{-5} - 2.6 \times 10^{-4}$. At the dust trap edge and in the bulk of the dust trap, the NO column density predicted by these models is a factor of 3 – 8 lower than that derived from the observations (see second row in Fig. 5.11). Additionally, the highest initial NH₃ abundance of 2.6×10^{-4} matches the upper limit on the CN column density so the abundance cannot be higher. Finally, the observed NO emission predicted by

these models is an order of magnitude too low (see the second row of Fig. 5.11).

All in all, adding gas-phase water or adding gas-phase NH_3 leads to an increase in the NO column density, but neither pathway is sufficient to explain the observed NO emission because the level required is inconsistent with the upper limits on OH, H_2O , and CN. In astronomical ices, the abundance of NH_3 with respect to water is typically 5% (Boogert et al. 2015). This is modeled by adding a water abundance of 1.9×10^{-4} and 7.6×10^{-4} and an NH_3 abundance that is 5% of that to the fiducial initial water abundance of 1.9×10^{-4} and initial NH_3 abundance of 0 (i.e., increasing water by a factor of 2 and 5 and increasing NH_3 accordingly to 1.9×10^{-5} and 4.7×10^{-5}). The results are very similar to what would happen if just NH_3 were added, which can be seen in the third row of Fig. 5.11. In summary, sublimating H_2O and/or NH_3 ices alone cannot explain the NO observations, even if the NO inside the dust trap would be mixed up to higher layers.

5.4.3 Effects of sublimating ices: Additional NO

The formation pathways to form NO from simple molecules are not efficient enough to explain the observations. Here, we investigate the opposite scenario, namely, of NO as the photodissociation product of a larger molecule with an NO bond that is frozen out in the dust trap. As our chemical network does not include species such as this, we modeled this scenario as an initial NO abundance of 10^{-7} , 10^{-6} , and 10^{-5} . The resulting column densities are presented in the bottom left panel of Fig. 5.11. An initial NO abundance of 10^{-7} results in an NO column density that matches that of the observations between 60 and 62 AU, but it underpredicts the column density by a factor of ~ 4 in the bulk of the dust trap. Increasing the NO abundance by one and two additional orders of magnitude results in an NO column density that increases that same amount up to a peak NO column density of 10^{16} cm^{-2} and 10^{17} cm^{-2} , respectively.

Only the model with an initial NO abundance of 10^{-5} matches the observed NO emission (see bottom right panel of Fig. 5.11). The three NO lines in this model are optically thick with optical depth of 1.4 – 2.7. As the raytracer in DALI does not do line blending, we raytraced these lines separately and added the intensities of these three lines. If line blending was taken into account, the expected intensity of the three blended NO lines would be at least the intensity of one NO line raytraced separately and, at most, the sum of the three NO lines raytraced separately. As the three NO lines have similar line strengths, the predicted line intensity is expected to be a factor of 2 – 3 lower when line blending is taken into account. In the observations, the 351.044 GHz line can marginally be separated from the other two at 351.052 GHz. Therefore, the true NO intensity expected from this is expected to be a factor 2 – 3 lower than the value plotted in the bottom right panel of Fig. 5.11. The NO intensity in the model with an initial NO abundance of 10^{-6} is only marginally optically thick with a maximum optical depth of 0.3. In summary, a high initial NO abundance is needed to match the observations within a factor of 2 – 3.

The discrepancy in the column density needed in the models compared to that derived from the observations is likely due to the different emitting layers. Fig-

ure 5.12 shows that most of the NO is distributed inside the dust trap where the dust hides the NO emission. The NO column density above the $\tau_{\text{dust},0.85 \text{ mm}} = 1$ surface is a few 10^{15} cm^{-2} , which is consistent with the observations within a factor of 5. This factor of 5 could be due to beam dilution indicating that the true emitting region of NO is five times smaller than that assumed in Sect. 5.3.2. Therefore, the NO column density is higher than the inferred value of $7.7 \times 10^{14} \text{ cm}^{-2}$. Another possibility is that the initial NO abundance in the IRS 48 disk is lower at $10^{-7} - 10^{-6}$ and that the NO located below the optically thick dust is mixed up to higher layers, which is not included in our models. Possible parent molecules that could photodissociate into NO are considered in Sect. 5.5.

5.4.4 Chemical composition of the non-dust trap side

In this section the chemical composition of the north side of the IRS 48 disk is explored. As the large grains with their icy mantles are trapped in the south, the north side of the disk could be depleted in gas-phase water. This is modeled as an initial abundance of gas-phase water of 9.4×10^{-5} , 3.8×10^{-5} , and 1.9×10^{-5} . As these models start without atomic oxygen initially present, the main oxygen reservoir is CO with an abundance of 1.3×10^{-4} w.r.t. hydrogen. The overall carbon (1.3×10^{-4} w.r.t. hydrogen), and nitrogen abundances (6.2×10^{-5} w.r.t. hydrogen) are identical to the fiducial model and follow the typical ISM values. The resulting column densities are presented in Fig. 5.B.9, 5.B.10, and 5.B.11. Interestingly, the upper limit on the CN column density is more constraining than that of NO in the north and also more constraining than that of C₂H. Depleting H₂O by a factor of 2 increases the CN column density by that same factor causing the model to be slightly lower than the derived upper limit. Depleting water with a factor of 5 – 10 increases the CN column density to $(6 - 8) \times 10^{13} \text{ cm}^{-2}$ in the bulk of the dust trap. This is consistent with the CN upper limit if all nitrogen initially starts as N₂. On the other hand, if nitrogen starts as solely N, solely NH₃ or a mix of N₂, N, and NH₃, the CN constrains the water abundance to be at least 9.4×10^{-5} . Therefore, the C/O ratio in this disk region is ≤ 1 if all nitrogen is initially in N₂ and ≤ 0.6 if not all nitrogen is initially in N₂.

5.5 Discussion

5.5.1 Possible parent molecules of NO

The NO emission is only seen at the location of the dust trap in the observations, indicating that the presence of NO is directly related to the dust trap. Additionally, modeling of the IRS 48 dust trap has shown that an additional source of NO relative to the fiducial model is needed to explain the observations. As the photodissociation timescale in these surface layers of the disk is short, this NO is likely the photodissociation product of a larger molecule that carries an NO bond and is frozen out in the dust trap.

One candidate for this is NH₂OH that can be formed by hydrogenation of NO ice (Fedoseev et al. 2012). However, NH₂OH gas photodissociates primarily into

$\text{NH}_2 + \text{OH}$ (Betts & Back 1965). The two-step photodissociation pathway to form NO is less efficient (Gericke et al. 1994; Fedoseev et al. 2016). Although NH_2OH has a higher binding energy of ~ 6500 K (Penteado et al. 2017) than CH_3OH (3800 K), its snowline is only 5 AU higher, just above the region where CH_3OH is expected to be abundant in the models (see Fig. 5.13 and Paper I). The fact that NH_2OH is not detected in the IRS 48 disk with an upper limit on the column density that is four times lower than that of NO suggests that it is not present in the gas-phase. Furthermore, the only detection of NH_2OH in the ISM yields a low abundance of only a few 10^{-10} (Rivilla et al. 2020). Therefore, NH_2OH , if present, likely remains frozen onto the dust grains. This, coupled together with the presence of a minor route that produces NO after photodissociation, makes NH_2OH an unlikely parent molecule of the detected NO.

Three other molecules that photodissociate into NO are N_2O , NO_2 , and HNO. No HNO lines are covered in our data so no constraint can be made on its column density. Its photodissociation cross-section is $1.7 \times 10^{-10} \text{ s}^{-1}$, which is two times smaller than that of NO. Therefore, HNO photodissociates slower than NO by that same factor. If HNO would be the parent molecule of NO, it would have to be at least twice as abundant to compensate for its faster photodissociation.

The upper limit on the N_2O column density is comparable to that of the detected NO emission in the south. Furthermore, the N_2O binding energy is ~ 2500 K (Congiu et al. 2012; Ioppolo et al. 2014), which is lower than that of methanol. Therefore, if N_2O ice is present on the grains, it will sublime and photodissociate in the gas into either $\text{NO} + \text{N}$ or $\text{N}_2 + \text{O}$ (van Dishoeck et al. 2006; Heays et al. 2017). As the photodissociation rate of N_2O is five times faster than that of NO, the formation of NO outpaces that of its destruction if N_2O photodissociation is the main pathway for NO. The additional atomic nitrogen slightly enhances the CN, but more importantly, the atomic nitrogen destroys part of the NO, lowering its column density compared to the $\text{NO} = 10^{-5}$ model by two orders of magnitude down to a peak value of $6.5 \times 10^{14} \text{ cm}^{-2}$. Therefore, N_2O could be the parent molecule of NO, but the high N abundance produced along with it would make this unlikely.

Overall, NO_2 is not detected with an upper limit that is an order of magnitude larger than that of NO. As it does photodissociate into NO, this could be the parent molecule of NO (van Dishoeck et al. 2006; Heays et al. 2017), but we cannot exclude the possibility that other molecules not considered here might be parents as well.

Another origin of the NO could be in OCN^- ice that has a typical abundance of 0.4% in low-mass young stellar objects and 0.6 – 1.53% with respect to H_2O in massive young stellar objects (van Broekhuizen et al. 2005; Öberg et al. 2011; Boogert et al. 2022). Additionally, OCN^- ice has recently been detected with an abundance of 0.3% with respect to H_2O in a cloud prior to star formation (McClure et al. 2023). It is likely that OCN^- quickly reacts with hydrogen to form HNCO or possibly another molecule upon desorption. Then, HNCO, as well as HCNO and HOCN, have been detected in the gas-phase in molecular clouds (Marcelino et al. 2010). The photodissociation of HNCO could also lead to the formation of NO, but quantifying its contribution requires knowledge of its photodissociation cross

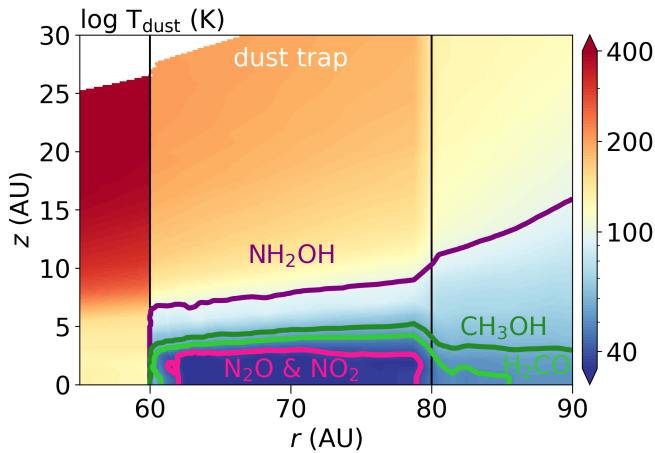


Figure 5.13: Snowlines of possible parent molecules of NO: N_2O and NO_2 (pink) and NH_2OH (purple). For comparison also the CH_3OH (dark green) and H_2CO (lighter green) are indicated. The colored background indicates the dust temperature.

section that has not been measured to date. In summary, multiple species that are frozen out on the grains in the IRS 48 dust trap could lead to the formation of NO in the gas-phase through photodissociation.

5.5.2 Comparison to other sources

In the disk of IRS 48, we find $\text{NO}/\text{N}_2\text{O} > 1$, assuming that N_2O would emit at 100 K, similarly to CH_3OH . This ratio is consistent with that of $\sim 8.8 - 10$ found in the giant molecular cloud Sgr B2(M) and (N) (Ziurys et al. 1994; Halfen et al. 2001), but it is inconsistent with the value of ≤ 0.5 in the young protosolar analog IRAS 16293–2422B (Ligterink et al. 2018a). This is interesting because both in IRAS 16293–2422B and in the IRS 48 disk, the emission of many molecules is explained by sublimating ices. The difference in the $\text{NO}/\text{N}_2\text{O}$ ratio could be due to chemical differences between the two sources.

In comet 67P, most of the volatile nitrogen is locked up in NH_3 (Rubin et al. 2019), although its abundance is very low at only 0.67% compared to H_2O . Other nitrogen carriers in this comet include N_2 (13% all w.r.t. NH_3), HCN (21%), HNCO (4%), some minor contributions ($< 1\%$) of NH_2CHO , CH_3CN , and HC_3N . Furthermore, refractory ammonia salts (NH_4^+X^-) or CHON particles in the dust grains on 67P may carry a large part of the total nitrogen budget (Rubin et al. 2019; Altwegg et al. 2020, 2022). Therefore, the NO emission in the IRS 48 disk could be enhanced by the sublimation of NH_3 ; but as we have shown with the models, this pathway alone is not sufficient to match the NO detection and the upper limit on the CN column density.

Another chemical difference between the IRS 48 disk and other sources arises from the H_2O to CH_3OH ratio, which is typically found to be 10 – 100 in the ice

on comets and on the dust around young stellar objects (Bottinelli et al. 2010; Boogert et al. 2015). In contrast, this ratio is only $\lesssim 0.2$ in the gas in the IRS 48 disk. This suggests that this ratio is very low in the ices in the IRS 48 dust trap or that the gas seen in the IRS 48 disk does not directly trace the ice abundances. The gas-phase H_2O to CH_3OH ratio could be modified compared to that in the ices due to photodissociation and (a lack of) subsequent formation. H_2O photodissociates twice as slowly as CH_3OH (Heays et al. 2017), increasing the expected H_2O to CH_3OH ratio in the gas compared to that in the ice. Furthermore, H_2O is formed in the gas-phase through OH if the gas temperature exceeds 300 K, whereas CH_3OH does not have an efficient gas-phase formation route (Garrod et al. 2006; Geppert et al. 2006). This further increases the expected H_2O to CH_3OH ratio in the gas compared to that in the ice.

Additionally, this ratio is found to be equal to 6 in the gas disk around the young outbursting source V883 Ori, using an H_2^{18}O column density of $(5.52 \pm 1.2) \times 10^{15} \text{ cm}^{-2}$ and an $^{13}\text{CH}_3\text{OH}$ column density of $6.9_{-0.72}^{+0.70} \times 10^{15} \text{ cm}^{-2}$ – both scaled to their main isotopologues using $^{12}\text{C}/^{13}\text{C} = 70$ and $^{16}\text{O}/^{18}\text{O} = 560$, but uncorrected for the dust that may hide part of the line emission (Wilson & Rood 1994; Milam et al. 2005; Lee et al. 2019; Tobin et al. 2023). The difference between the V883 Ori and IRS 48 disks could be due to a difference in the continuum optical depth. Then, H_2O and CH_3OH are both observed at sub-mm wavelengths in the V883 Ori disk but in the IRS 48 disk H_2O observed at 51 – 220 μm and the CH_3OH observed at sub-mm wavelengths. Yet, the $\tau = 1$ surface of the continuum at 100 μm is located only ~ 0.5 AU higher than that of the sub-mm. Therefore, the H_2O and CH_3OH observations probe up to very similar depths in the disk, suggesting that the optical depth of the 100 μm continuum is underestimated or that there is a chemical difference between the IRS 48 dust trap and V883 Ori.

In the IRS 48 disk, our upper limit on the warm gaseous H_2O column density of $\lesssim 10^{14} \text{ cm}^{-2}$ inside its snowline at 60 AU results in an upper limit on the abundance of $\lesssim 6 \times 10^{-9}$ with respect to hydrogen, using the hydrogen column density of $1.6 \times 10^{22} \text{ cm}^{-2}$ at 60 AU in the DALI model based on the $J = 6 - 5$ transition of C^{17}O (Bruderer et al. 2014; van der Marel et al. 2016). This upper limit is consistent with the gas-phase H_2O abundance in the cold, photodesorbed reservoir located outside the water snowline in the HD 100546 and HD 163293 disks that is low due to radial drift. It is not consistent with the abundance of warm gas-phase water in the inner disk (inside the water snowline) of HD 163296 (Pirovano et al. 2022).

The lack of CN emission in this disk constrains its C/O ratio to be $\lesssim 0.6$ both inside and outside the dust trap. In the south, this is in line with the C/O ratio that is expected for gas dominated by sublimating ices (Öberg et al. 2011). However, in the north side of the disk where no direct evidence of sublimating ices is seen, a low C/O of $\lesssim 0.6$ is more surprising as gas depleted in volatiles has a high C/O ratio of ~ 1 . Therefore, the low C/O ratio suggests that also the gas in the north side of the disk could be affected by ices that sublimated and then photodissociated. If this is the case, the dust trap must be relatively old such that the gas in the disk has either mixed or the dust trap has at least made one more full orbit than the sub-Keplerian gas.

5.6 Conclusions

In this work, we investigated the chemical origin of the first detection of NO in a disk. The special case of the IRS 48 dust trap allows us to investigate its origin, as this disk is a unique laboratory for sublimating ices. The NO column density and emission were modeled using the thermochemical code DALI with a nitrogen chemistry network. The effects of sublimating H₂O and NH₃ ices were investigated as well as the effect of sublimation of larger molecules that carry an NO bond. In summary, we conclude:

- NO in the observations is co-located with the IRS 48 dust trap in the south, and it is not detected in the north.
- Models indicate that the dust temperature in the dust trap midplane is up to ~ 30 K colder than the non-dust trap side of the disk.
- The fiducial model for the north side of the disk is consistent with the observations, but the fiducial model for the south side (dust trap location) underpredicts the NO column density by one order of magnitude.
- Sublimating water and/or NH₃ enhance the NO column density up to a factor of 10, but the observed NO emission is still not reproduced. These models overproduce the upper limits on H₂O, OH column densities. The upper limit on the CN emission constrains the NH₃ abundance to be $\lesssim 2.6 \times 10^{-4}$. Therefore, the high NO column density cannot be explained by sublimation of these molecules.
- An additional source of NO is needed to explain the observations. This is likely a molecule that carries an NO bond and freezes out in the dust trap midplane but sublimates in the higher layers of the disk. Possible candidates could be N₂O and HNCO.
- The C/O ratio in this disk is $\lesssim 0.6$ both in the dust trap side and in the non-dust trap side due to the lack of CN emission, if not all nitrogen is initially in N₂. If all nitrogen is initially in N₂, the C/O ratio is ≤ 1 .

The observed line emission from NO and COMs are co-spatial with the asymmetric dust trap in the IRS 48 disk. This coincidence strongly suggests a direct relation between the detected gas-phase molecules and mm dust grains which are expected host an ice reservoir. The first detection of NO in a protoplanetary disk opens a new opportunity for studying the C/O ratio in disks using NO and CN. Future observations aimed at targeting other nitrogen-bearing molecules are needed to further constrain the parent molecule that forms NO in these environments and characterize the partitioning of volatile nitrogen in this disk.

5.7 Acknowledgements

We thank the referee for the constructive comments. Furthermore, we would like to thank A. D. Bosman for the useful discussions. We acknowledge assistance from

Allegro, the European ALMA Regional Centre node in the Netherlands. Astrochemistry in Leiden is supported by the Netherlands Research School for Astronomy (NOVA), by funding from the European Research Council (ERC) under the European Union's Horizon 2020 research and innovation programme (grant agreement No. 101019751 MOLDISK), and by the Dutch Research Council (NWO) grant 618.000.001. BT acknowledges support from the Dutch Astrochemistry Network II, grant 648.000.022 from the Dutch Research Council (NWO). N.F.W.L. acknowledges funding by the Swiss National Science Foundation Ambizione grant 193453. This paper makes use of the following ALMA data: ADS/JAO.ALMA #2013.1.00100.S and #2017.1.00834.S. ALMA is a partnership of ESO (representing its member states), NSF (USA) and NINS (Japan), together with NRC (Canada), MOST and ASIAA (Taiwan), and KASI (Republic of Korea), in cooperation with the Republic of Chile. The Joint ALMA Observatory is operated by ESO, AUI/NRAO and NAOJ.

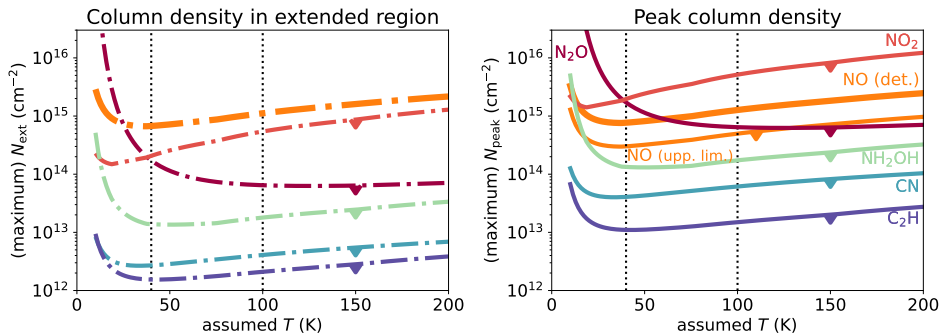


Figure 5.A.1: Derived (upper limits on the) column densities in the IRS 48 disk as a function of assumed temperature. The left panel presents column densities computed in an extended region (N_{ext} ; dash-dotted lines) and the right panel those in a single beam (N_{peak} ; solid lines). The NO column density is indicated with the thick orange line. The upper limit on the N_2O , NO_2 , NH_2OH , CN, and C_2H are indicated with the dark red, red, green, blue, and purple lines respectively. The upper limit on the NO column density in the north is indicated with the thin orange line in the right panel. The dotted vertical black lines indicate the two assumed temperatures for which the (upper limits on the) column densities are listed in Table 5.2.

Appendix

5.A Observations

The NO column density together with the upper limits on the column densities of NO in the north, N_2O , NO_2 , NH_2OH , CN, and C_2H for a range of temperatures is presented in Fig. 5.A.1. The details of this calculation are discussed in Sect. 5.2.3. The NO column density in this Figure is a factor of five larger than that found in Paper II due to an incorrect conversion to K in Paper II as explained in Sect. 5.3.2 (see Fig. 5.A.2 for the corrected spectrum). Finally, we present the channel maps of the $^{13}\text{CO } J = 3 - 2$ transition in Fig. 5.A.3 (before continuum subtraction) and Fig. 5.A.4 (after continuum subtraction).

The azimuthal profile of NO, CH_3OH , and ^{13}CO , along with the 0.89 mm continuum emission are presented in Fig. 5.A.5. These profiles are extracted by averaging the intensity from a 60 AU wide ring located at a radius of 62 AU (i.e., averaging between 32 AU and 92 AU) to compare the emission profiles at the radial location of the dust trap. Similar to the radial profiles presented in Fig. 5.3 the NO and methanol peak at the location of the dust trap. The ^{13}CO emission drops at the continuum peak due to optical depth effects.

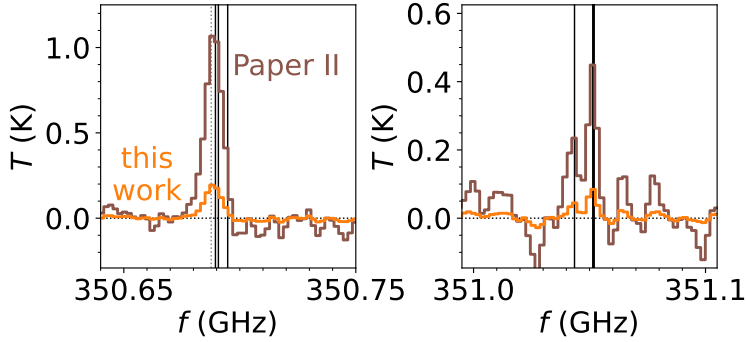


Figure 5.A.2: Observed and stacked spectrum of the NO lines detected inside 115 AU in units of K. The brown line indicates the spectrum presented in Paper II and the orange line presents the corrected spectrum with a 5 times lower flux presented in this work. The detected NO lines are indicated with the vertical black lines. The thick line at 351.052 GHz indicates that there are two NO lines at the same frequency. The methanol line is indicated with the dotted grey line. For details see Sect. 5.3.2. Note: there is a difference in the vertical scale between the panels.

5.B DALI

The setup of the DALI models used in this work is described in detail in the following subsection. Additionally, the model results for different the CN column density for different C/O ratios are presented in Appendix 5.B.2.2, the effect of the initial distribution of nitrogen are presented in Appendix 5.B.2.1, and the time evolution is presented in Appendix 5.B.2.4.

5.B.1 Model setup

5.B.1.1 Gas and dust density structure

The IRS 48 DALI disk model is based on the previously published gas and dust surface density model that was used to reproduce the spatially resolved CO isotopologue emission. The model for the south side reproduces the $^{13}\text{CO } J = 3 - 2$, $^{13}\text{CO } J = 6 - 5$, $\text{C}^{18}\text{O } J = 6 - 5$, and $\text{C}^{17}\text{O } J = 6 - 5$ emission and the total dust continuum flux at 0.44 mm and 0.89 mm within a factor of < 2 (Bruderer et al. 2014; van der Marel et al. 2016, Paper I). The CO $J = 6 - 5$ intensity is reproduced within a factor of ~ 3 by this model. The model for the north side dominates the $18.7 \mu\text{m}$ continuum flux and reproduces the observations within a factor of < 2 (van der Marel et al. 2013).

In the radial direction, the gas surface density profile is that of the self-similar solution of a viscously evolving disk Lynden-Bell & Pringle (1974); Hartmann et al.

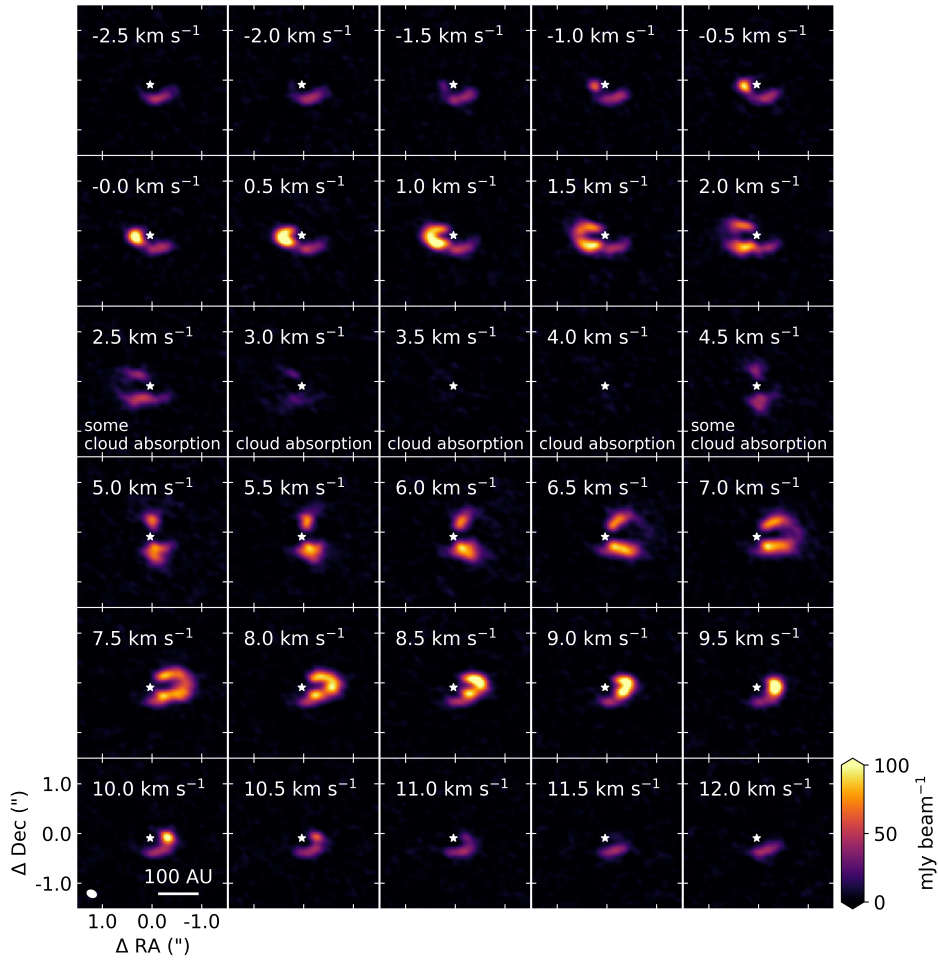


Figure 5.A.3: Channel maps of the $^{13}\text{CO } J=3-2$ transition before continuum subtraction. Channels between 2.5 and 4.5 km s^{-1} are affected by (some) cloud absorption. The beam and a 100 AU scale bar are indicated in the bottom-left panel. Additionally, the position of the star is indicated with the white star in each panel.

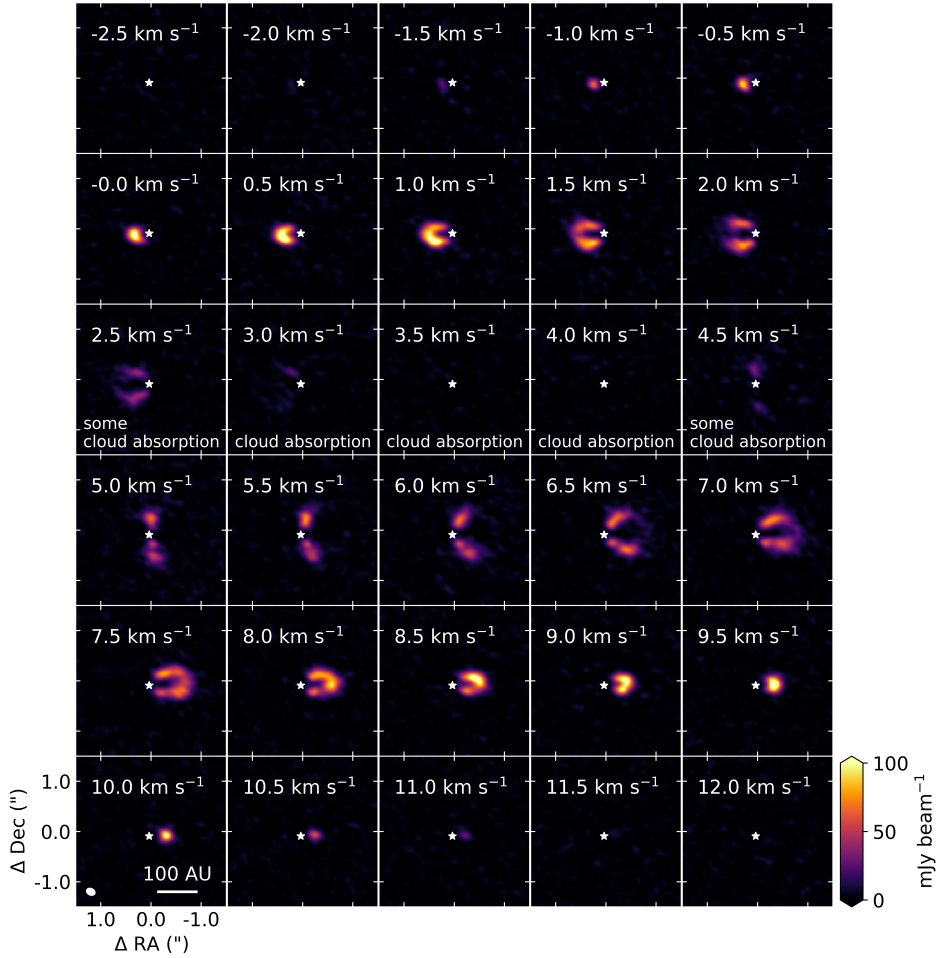


Figure 5.A.4: Channel maps of the $^{13}\text{CO } J = 3 - 2$ transition after continuum subtraction. Channels between 2.5 and 4.5 km s^{-1} are affected by (some) cloud absorption. The beam and a 100 AU scale bar are indicated in the bottom-left panel. Additionally, the position of the star is indicated with the white star in each panel.

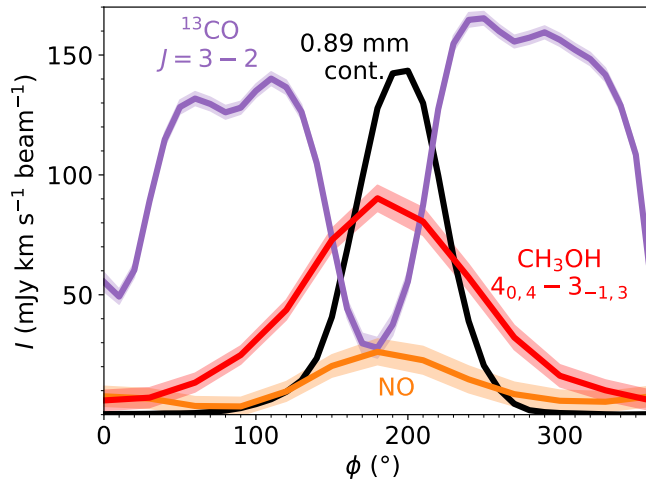


Figure 5.A.5: Azimuthal profile of the 0.89 mm continuum (black), NO (orange), ^{13}CO $J = 3 - 2$ (purple), and CH_3OH $4_{0,4} - 3_{-1,3}$ (red) emission. For each bin in ϕ , the emission at that position angle is averaged inside an 60 AU wide ring at a radius of 62 AU, consistent with the radial location of the dust trap.

(1998):

$$\Sigma_{\text{gas}}(R) = \Sigma_c \left(\frac{R}{R_c} \right)^{-\gamma} e^{-(R/R_c)^{2-\gamma}}, \quad (5.12)$$

with $\Sigma_{\text{gas}}(R)$ as the gas-surface density as a function of radius, R , then Σ_c as the surface density at the characteristic radius, R_c , and γ the power-law exponent. This relation is used outside the dust sublimation radius that is located at 0.4 AU. Inside the dust sublimation radius, the gas number density is set to the ISM value of $n_{\text{gas}} = 7.1 \times 10^2 \text{ cm}^{-3}$. The deep gas cavity that is seen in the IRS 48 disk is modeled by reducing the gas surface density between the sublimation radius and the cavity radius $R_{\text{cav out, gas}} = 25 \text{ AU}$ by a factor of 10^{-3} (see Fig. 5.B.1). In the vertical direction, the gas follows a Gaussian distribution with a scale height defined as:

$$h = h_c \left(\frac{R}{R_c} \right)^\psi, \quad (5.13)$$

with h_c as the scale height at R_c and ψ as the flaring index.

The deep 60 AU dust cavity that is seen in the observations is modeled by reducing the total (small + large) dust density by a factor of 10^{-20} between 1 and 60 AU. A small dusty inner disk is created by reducing the total dust density by a factor of 9×10^{-4} with respect to that of a full disk between 0.4 and 1 AU.

The dust consists of two dust populations (D'Alessio et al. 2006) following an MRN distribution (Mathis et al. 1977). The small dust ($0.005 - 1 \mu\text{m}$) follows the

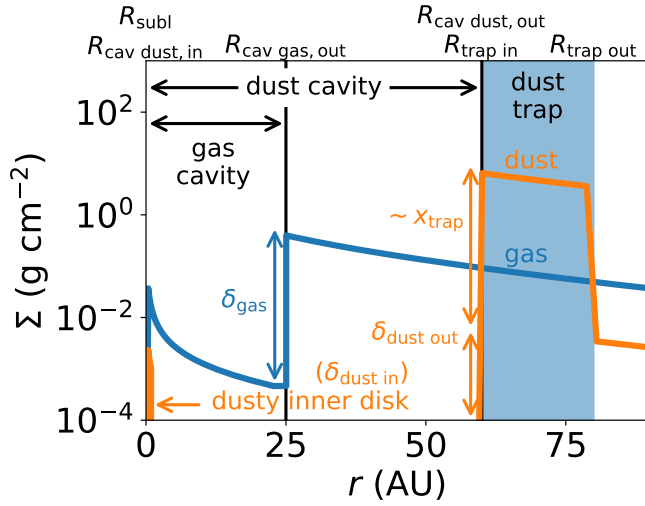


Figure 5.B.1: Gas (blue) and dust (orange) surface density in the DALI models of the dust trap (south) side of the IRS 48 disk. The dust trap is indicated with the shaded blue region.

number density of the gas scaled with the gas-to-dust mass ratio $\Delta_{\text{gas/dust}} = 20$. On the other hand, the large dust ($0.005 \mu\text{m} - 1 \text{ mm}$) is settled to the midplane by reducing its scale height with a factor of χ compared to the gas and small dust. This results in the following mass densities outside the dust trap (following Bruderer 2013):

$$\rho_{\text{small}} = \frac{(1 - f_{\text{ls}})\Sigma_{\text{gas}}}{\Delta_{g/d}\sqrt{2\pi}rh} \exp\left[-0.5\left(\frac{0.5\pi - \theta}{h}\right)^2\right], \quad (5.14)$$

$$\rho_{\text{large}} = \frac{f_{\text{ls}}\Sigma_{\text{gas}}}{\Delta_{g/d}\sqrt{2\pi}r h \chi} \exp\left[-0.5\left(\frac{0.5\pi - \theta}{h\chi}\right)^2\right], \quad (5.15)$$

where $f_{\text{ls}} = 0.85$ sets the mass fraction of the large grains and θ indicates the latitude coordinate (pole: $\theta = 0$; midplane: $\theta = \pi/2$).

The dust trap itself is modeled by modifying the dust density between 60 and 80 AU, as observations indicate a high surface density of large dust grains (van der Marel et al. 2013; Ohashi et al. 2020). As DALI is 2D and thus unable to produce azimuthal asymmetries, the IRS48 dust trap is simulated by producing models with and without a high-density dust ring. The density of large grains is increased by a factor of x_{trap} , whereas the small grains are decreased by that same

factor following Paper I:

$$\rho_{\text{small}} = \frac{\Sigma_{\text{gas}}}{x_{\text{trap}} \Delta_{g/d} \sqrt{2\pi r h}} \exp \left[-0.5 \left(\frac{0.5\pi - \theta}{h} \right)^2 \right] \text{ and} \quad (5.16)$$

$$\rho_{\text{large}} = \frac{x_{\text{trap}} \Sigma_{\text{gas}}}{\Delta_{g/d} \sqrt{2\pi r h} \chi} \exp \left[-0.5 \left(\frac{0.5\pi - \theta}{h\chi} \right)^2 \right]. \quad (5.17)$$

The fraction of large grains, f_{ls} , that is used outside the dust trap is not included here as the small grains likely grew to larger sizes which is taken into account by x_{trap} . A value of 1000 results in a dust surface density of 6 g cm^{-2} at 60 AU, consistent with the dust surface density of $2\text{-}8 \text{ g cm}^{-2}$ derived from polarization observations (Ohashi et al. 2020). In summary, two models are used: one for the non-dust trap (north) side of the disk and one for the dust trap (south) side, see also the right and left side of Fig. 5.5, respectively.

5.B.1.2 Stellar spectrum

The stellar spectrum is modeled as a $14.3 L_{\odot}$ star with an effective temperature of $9 \times 10^3 \text{ K}$, following Paper I. The stellar accretion rate of $4 \times 10^{-9} M_{\odot} \text{ yr}^{-1}$ (Salyk et al. 2013) is modeled by adding a 10^4 K black body. We have updated the X-ray luminosity of IRS 48 as no X-rays have been detected with Chandra, resulting in an upper limit on the X-ray luminosity (not corrected for extinction) of $< 10^{28} \text{ erg s}^{-1}$ (Imanishi et al. 2001).

5.B.1.3 Chemical network

The gas and dust temperature are calculated using the default chemical network in DALI that is based on the UMIST06 chemical network (Woodall et al. 2007; Bruderer 2013) and starts with the atomic initial conditions. This network is relatively small and does not include the necessary reactions to model nitrogen-bearing molecules such as NO and CN, and small hydrocarbons such as C_2H . Therefore, an updated version of the nitrogen chemistry network is used to calculate the molecular abundances using the temperature and density structure obtained in the previous step. This network was first presented in Visser et al. (2018); Cazzoneletti et al. (2018); Long et al. (2021). For this updated version, we have added the $\text{HNC} + \text{H} \rightarrow \text{HCN} + \text{H}$ and $\text{HNC} + \text{O} \rightarrow \text{NH} + \text{CO}$ reactions with the energy barriers derived in Hacar et al. (2020). Furthermore, we have set the binding energy of C_2H_3 ice to 10^4 K as this is the largest carbon chain in the network that acts as a sink to model the effect of the formation of larger hydrocarbons that remain frozen out on the grains. Finally, this network was initiated with molecular initial conditions (see Table 5.B.1). For computational reasons, the first network is run in steady state and the second network is run to 100 yr, 1 kyr (inside the dust trap), or 1 Myrs (outside the dust trap), appropriate for the dust trap around IRS 48. The effect of the initial distribution of nitrogen is further discussed in Appendix 5.B.2.1.

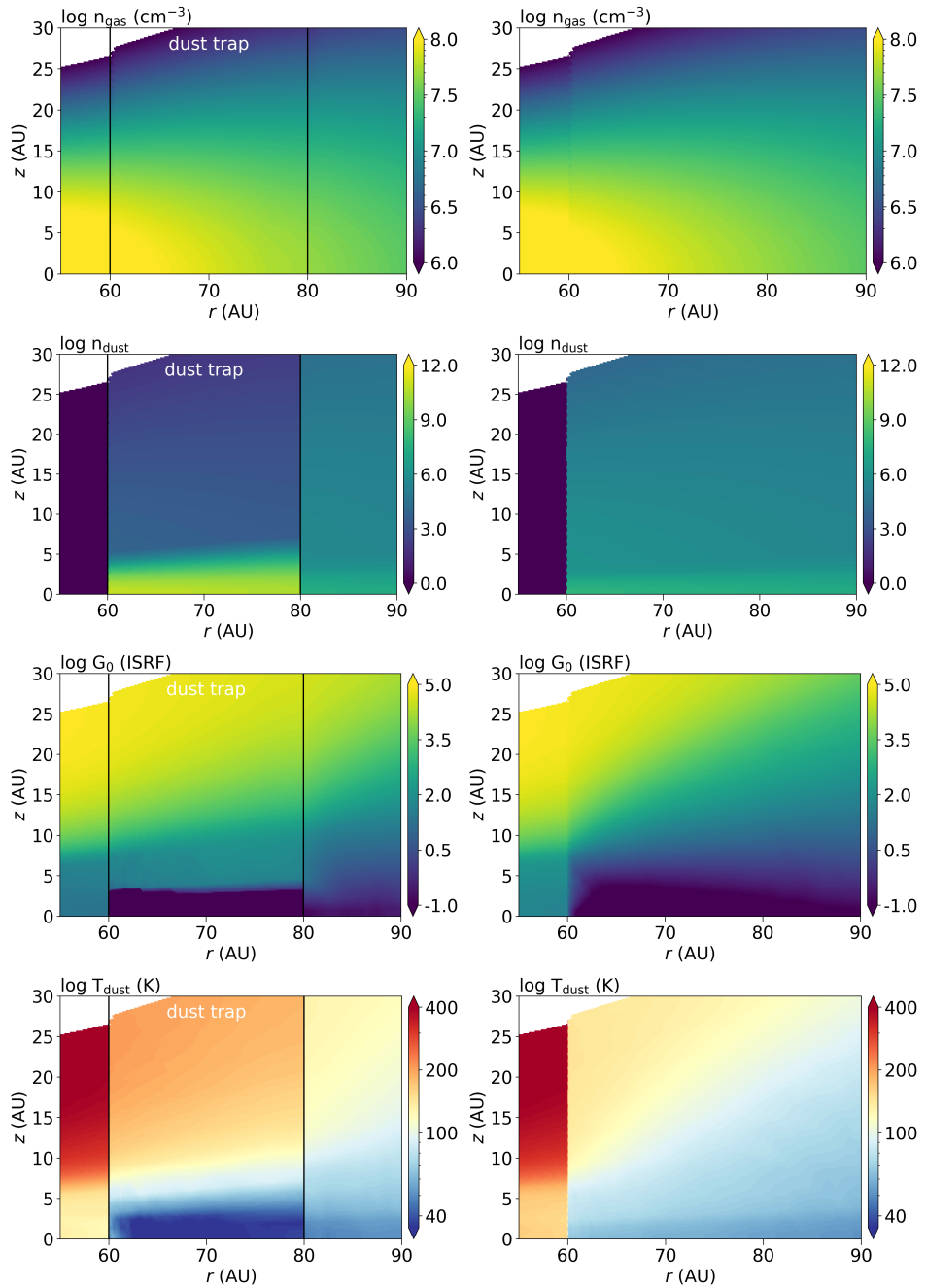


Figure 5.B.2: Density, UV field, and dust temperature structure of the DALI model for the dust trap side (south, left) and non-dust trap side (north, right). Top row presents the gas density structure (identical in both models), the second row the dust density structure, the third row the resulting UV field, and the fourth row the dust temperature.

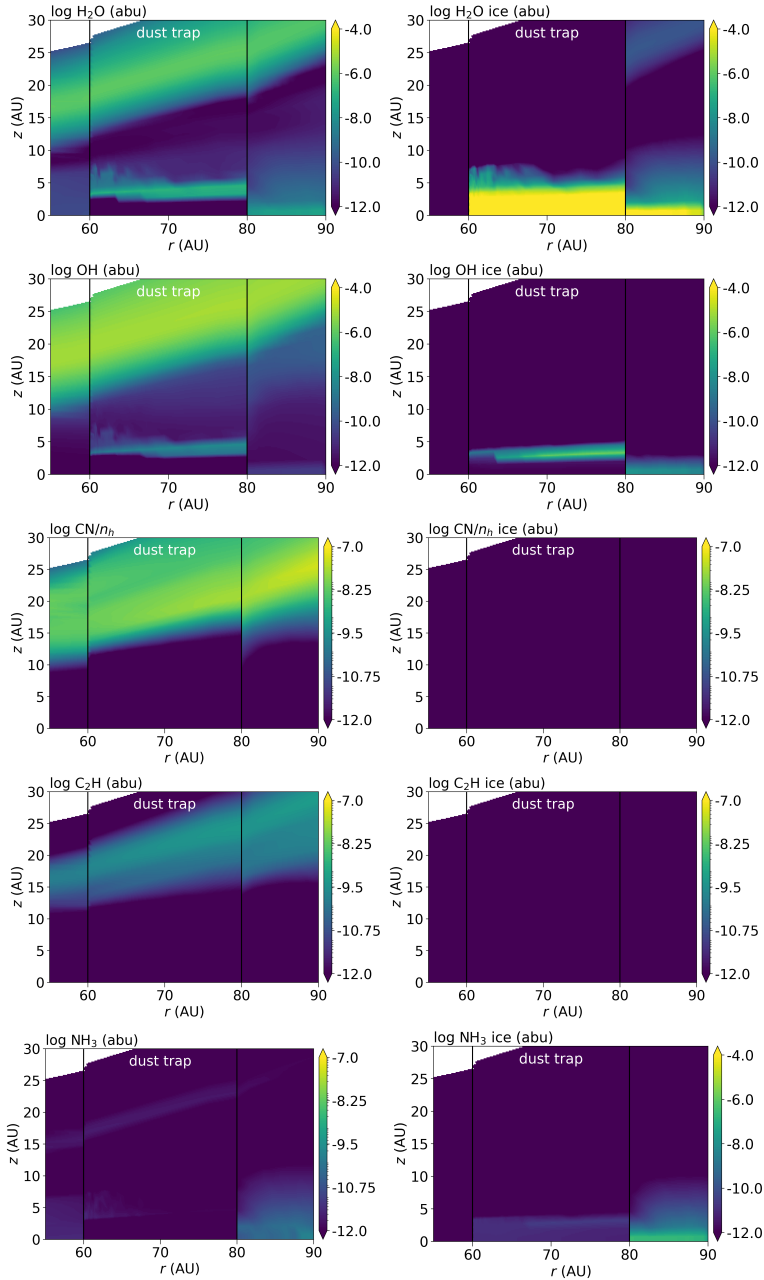


Figure 5.B.3: Abundance of gas (left) and ice (right) phase species in the dust trap side model of the IRS 48 disk. Top row presents the H₂O abundance, the second row that of OH, the third row that of CN, the fourth row shows C₂H, and the final row shows NH₃, the largest carbon chain in our network that acts as a sink for larger hydrocarbons.

Table 5.B.1: DALI model parameters

Model parameter	dust trap side (south)	non-dust trap side (north)	Description
<i>Physical structure</i>			
R_{subl}		0.4 AU	Sublimation radius
$R_{\text{cav in, dust}}$		1 AU	Inner radius of the dust cavity
$R_{\text{cav out, gas}}$		25 AU	Outer radius of the gas cavity
$R_{\text{cav out, dust}}$		60 AU	Outer radius of the dust cavity
$R_{\text{trap in}}$	60 AU	-	Inner radius of the dust trap
$R_{\text{trap out}}$	80 AU	-	Outer radius of the dust trap
R_c	60 AU		Characteristic radius of the surface density profile
R_{out}	120 AU		Outer radius of the disk
Σ_c	0.25 g cm ⁻²		Sets the gas surface density at the characteristic radius R_c
M_{disk}	$3.3 \times 10^{-4} M_{\odot}$		Mass of the disk
γ	1		Power law index of the surface density profile
h_c	0.14		Scale height angle at the characteristic radius R_c
ψ	0.22		Flaring index of the disk surface density
PAH abundance	0.1		Gas-phase abundance of PAHs w.r.t. to ISM value
δ_{gas}	10^{-3}		Relative drop in gas density inside the gas cavity ($R_{\text{subl}} < R < R_{\text{cav out, gas}}$)
$\delta_{\text{dust, in}}$	9×10^{-4}		Relative drop in dust density in the dusty inner disk w.r.t. the outer disk ($R_{\text{subl}} < R < R_{\text{cav in, dust}}$)

Table 5.B.1: Continued.

Model parameter	dust trap side (south)	non-dust trap side (north)	Description
$\delta_{\text{dust, out}}$		10^{-20}	Relative drop in dust density inside the dust cavity ($R_{\text{cav in, dust}} < R < R_{\text{cav out, dust}}$)
<i>Dust properties</i>			
χ		0.1	Settling of large grains
f_{ls}		0.85	Mass fraction of grains that is large
x_{trap}	1000	-	Increase of large dust grains inside the dust trap
$\Delta_{\text{gas/dust}}$		20	Gas-to-dust mass ratio
<i>Stellar properties</i>			
M_{\star}		$2 M_{\odot}$	Mass of the central star
$\dot{M}_{\star}^{(2)}$		$4 \times 10^{-9} M_{\odot} \text{ yr}^{-1}$	Mass accretion rate of the central star
<i>Stellar spectrum</i>			
L_{\star}		$14.3 L_{\odot}$	Luminosity of the central star
L_{X}		$1 \times 10^{27} \text{ erg s}^{-1}$	X-ray luminosity of the central star
T_{eff}		$9 \times 10^3 \text{ K}$	Effective temperature of the central star
T_{X}		$7 \times 10^7 \text{ K}$	Effective temperature of the X-ray radiation
$\zeta_{\text{c.r.}}$		$1 \times 10^{-18} \text{ s}^{-1}$	Cosmic ray ionization rate
<i>Observational geometry</i>			
i		50°	Disk inclination (0° is face-on)

Table 5.B.1: Continued.

Model parameter	dust trap side (south)	non-dust trap side (north)	Description
d		135 pc	Distance to the star
<i>Chemistry</i> ⁽³⁾			
H		5.2×10^{-5}	
He		1.4×10^{-1}	
H ₂		5.0×10^{-1}	
H ₂ O		1.9×10^{-4}	
CO		1.3×10^{-4}	
N ₂		3.1×10^{-5}	
Mg ⁺		1.0×10^{-11}	
Si ⁺		1.0×10^{-11}	
S ⁺		1.0×10^{-11}	
Fe ⁺		1.0×10^{-11}	

Notes. ⁽²⁾ The stellar accretion rate is converted to a 10^4 K black body and then added to the stellar spectrum. An accretion rate of $4 \times 10^{-9} M_{\odot} \text{ yr}^{-1}$ corresponds to a UV luminosity of $0.2 L_{\odot}$. ⁽³⁾ Abundance w.r.t. the total number of hydrogen atoms. All molecules start as gas-phase species.

5.B.2 Model results

5.B.2.1 Initial distribution of nitrogen

The fiducial model discussed in the main text is initialized with all nitrogen in N_2 . However, the initial distribution of nitrogen over the main nitrogen carriers such as N , N_2 , NH_3 is unknown. Therefore, we run all models with initially all nitrogen in N_2 (fiducial models), all nitrogen initially in N following Fogel et al. (2011), all nitrogen in NH_3 following Maret et al. (2006) and Daranlot et al. (2012), and a mixture of these three. The mixture is based on the dark cloud model in Walsh et al. (2015) and consists of an initial atomic nitrogen abundance of 3.3×10^{-5} , N_2 initially 2×10^{-5} , and NH_3 initially 8.8×10^{-6} with respect to hydrogen. All molecules start in the gas phase as the model is evolved for a short time.

An overview of the model results for different initial distributions of nitrogen and the effect of sublimating ices is presented in Fig. 5.B.4. The initial distribution of nitrogen has the most profound effect when NO gas is added to the initial conditions. Only when atomic nitrogen is initially absent, NO can survive. The reason for this is that NO is destroyed by atomic nitrogen to form N_2 . The models that start with atomic nitrogen, NH_3 or a mixture of N , NH_3 , and N_2 predict a higher NO column density when no sublimating ices are added to the initial conditions. Still, these models underpredict the NO column density. Furthermore, this difference is diminished when the effect of sublimating NH_3 , NH_3 & H_2O , and NO is modeled. Only in the case of sublimating water, the NO column density in the N_2 model is slightly lower than that in the other models. In summary, varying the initial distribution of nitrogen shows that the initial abundance of atomic nitrogen must be low to explain the observed NO emission.

5.B.2.2 Effect of evaporating ices on CN and C_2H

The dust trap in the IRS 48 disk is an ice trap. Sublimating H_2O and NH_3 cannot boost the NO column density to match the observations. In this section, their effect on the upper limits on CN and C_2H is investigated. The CN column density presented in Fig. 5.B.5 and is consistent with the upper limit derived from the observations for all models except those with an initial water abundance of $\gtrsim 3.8 \times 10^{-5}$ or an initial NH_3 abundance $\gtrsim 2.6 \times 10^{-4}$. Furthermore, the CN column density is slightly lower for the models that start with all nitrogen initially in N_2 . The reason for this is that the N_2 bond needs to be broken before CN can be formed in these models.

The results for the C_2H column density are presented in Fig. 5.B.6. The C_2H column density is sensitive to the C/O ratio in this disk as it decreases with an increasing abundance of water (first two rows of Fig. 5.B.6). The highest C/O ratio in the models explored here is 0.99, so just below a C/O ratio of 1 when C_2H is expected to become very bright (Bergin et al. 2016; Bergner et al. 2019; Miotello et al. 2019; Bosman et al. 2021a). In summary, the CN emission places the strongest constraint on the C/O ratio in this disk. Deeper observations of both CN and C_2H are needed to pinpoint the C/O ratio to an accuracy better than $\lesssim 0.6$.

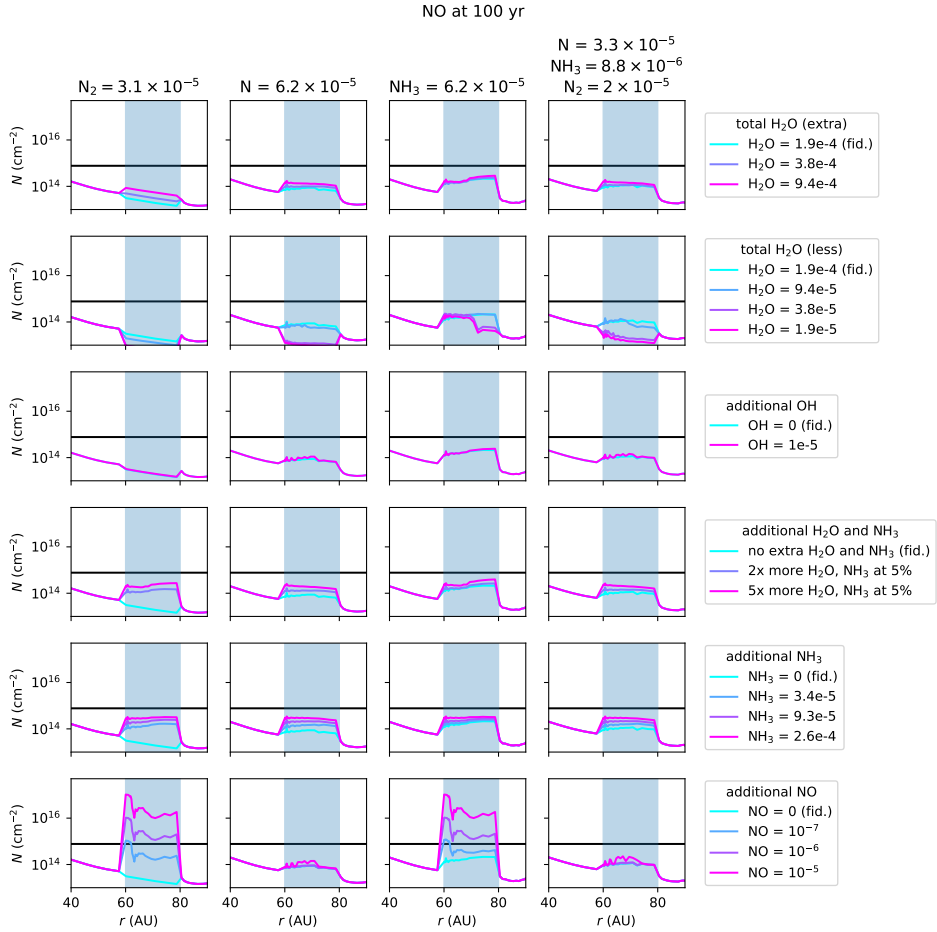


Figure 5.B.4: Predicted NO column density for different distributions of nitrogen and sublimating ices. Nitrogen initially starts all in N₂ (left column), N (second column), NH₃ (third column), and a mixture (fourth column). The effect of sublimating ices is presented in the different rows: sublimating water (top row), water depletion (second row), extra OH (third row), sublimating water and NH₃ simultaneously (fourth row), sublimating NH₃ (fifth row), and sublimating NO (final row). The horizontal black line indicates the NO column density derived from the observations. Only the models with a high initial NO abundance and all nitrogen initially in N₂ or NH₃ match the observed NO column density.

Finally, the warm H_2O and OH column densities are presented in Fig. 5.B.7 and 5.B.8. Only the H_2O and OH in the regions with $T_{\text{gas}} \geq 150$ K are taken into account as this is the temperature range probed by the *Herschel* PACS observations. Even at these high OH columns, formation of NO through OH are not efficient enough to explain the observations further strengthening the hypothesis that the NO is the photodissociation product of a larger molecule.

5.B.2.3 Chemical composition of the non-dust trap side

The chemical composition of the non-dust trap side is modeled by varying the initial abundance of gas-phase water. The resulting NO, CN, and C_2H column densities are presented in Figs. 5.B.9, 5.B.10, and 5.B.11. Similarly to the results in the dust trap, the NO and C_2H emission do not tightly constrain the disk C/O ratio. The CN indicates that the initial abundance of gas-phase water must be $\lesssim 9.4 \times 10^{-5}$, setting the C/O ratio to be $\lesssim 0.6$.

5.B.2.4 Time evolution

The NO column density after 10^3 yr is presented in 5.B.12. The NO column density is relatively stable over a 10^3 yr time period in the dust trap, except for the models where the initial NH_3 abundance is non-zero. In such cases, the NO column density in the outer parts of the dust trap decreases by a factor of a few up to an order of magnitude in the models where NH_3 is abundant.

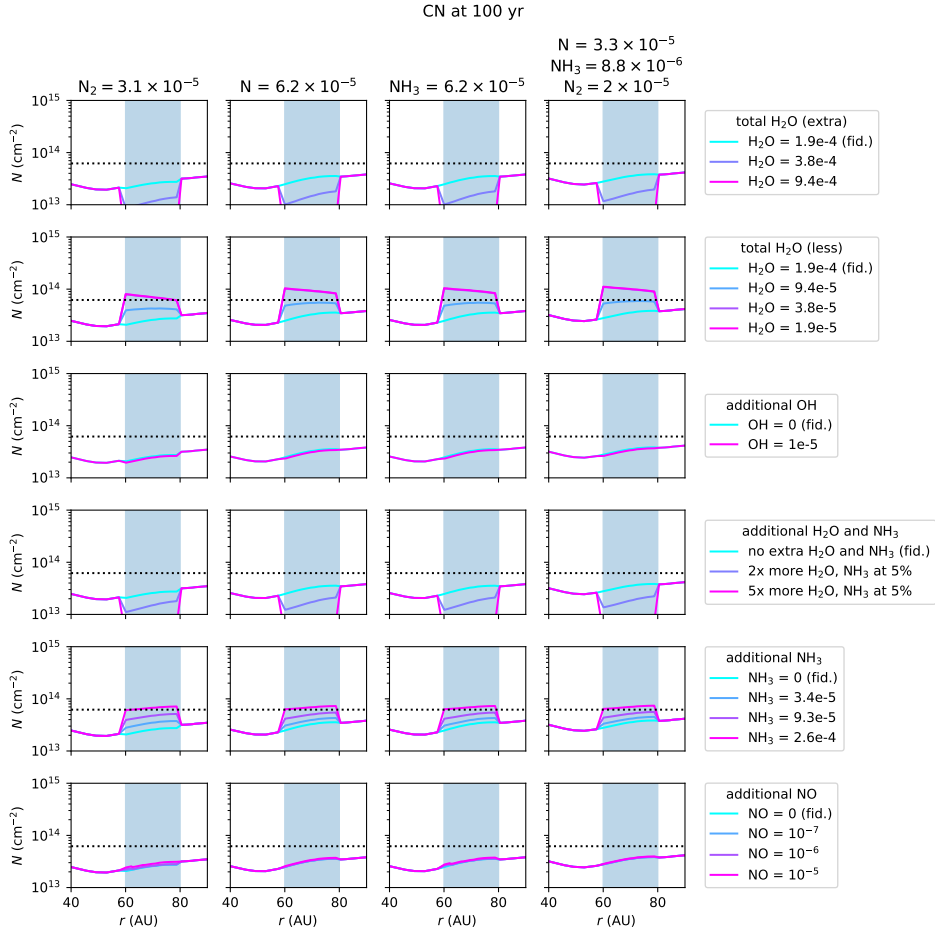


Figure 5.B.5: Predicted CN column density for different initial distributions of nitrogen (columns) and sublimating ices (rows). Horizontal black dotted line indicates the upper limit on the CN column density derived from the observations. The initial H₂O abundance needs to be at least 1.9×10^{-5} (if all nitrogen starts as N₂) or 3.8×10^{-5} (if nitrogen starts as NH₃, N, or a mix of NH₃, N and N₂). Similarly, the initial (additional) abundance of NH₃ is $\lesssim 2.6 \times 10^{-4}$ to match the CN upper limit.

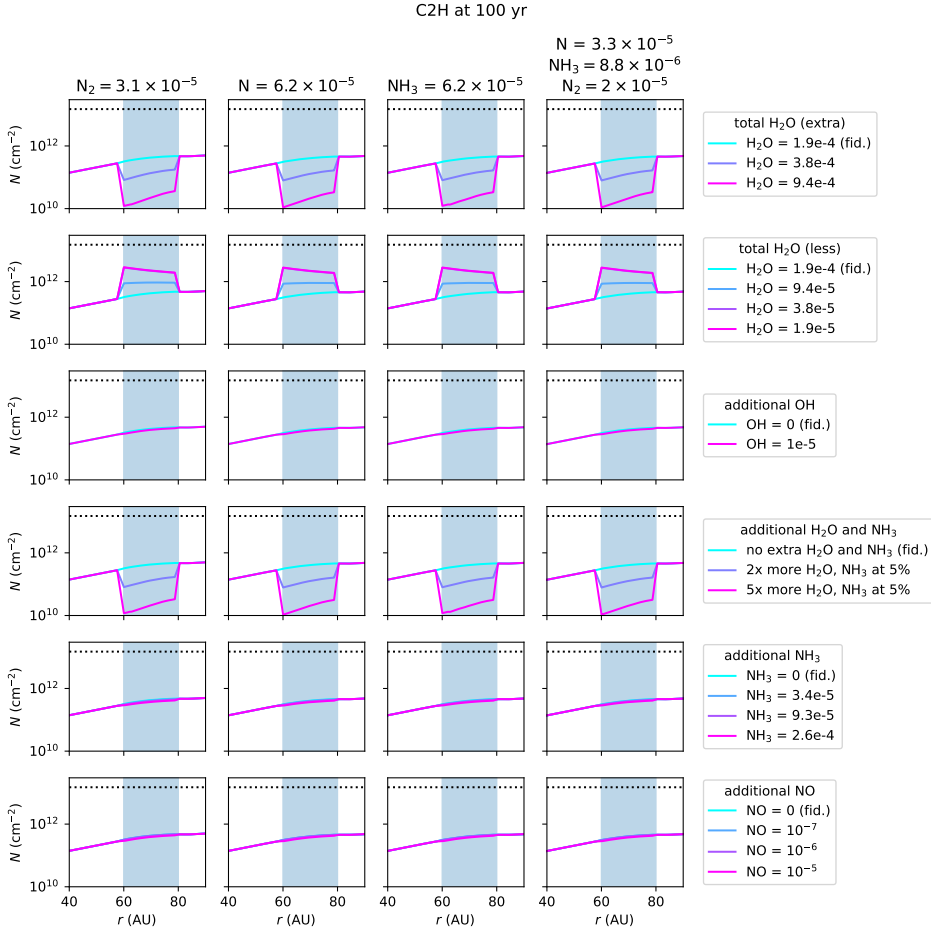


Figure 5.B.6: Predicted C₂H column density for different initial distributions of nitrogen (columns) and sublimating ices (rows). Horizontal black dotted line indicates the upper limit on the C₂H column density derived from the observations. All models are compatible with the upper limit on the C₂H from the observations.

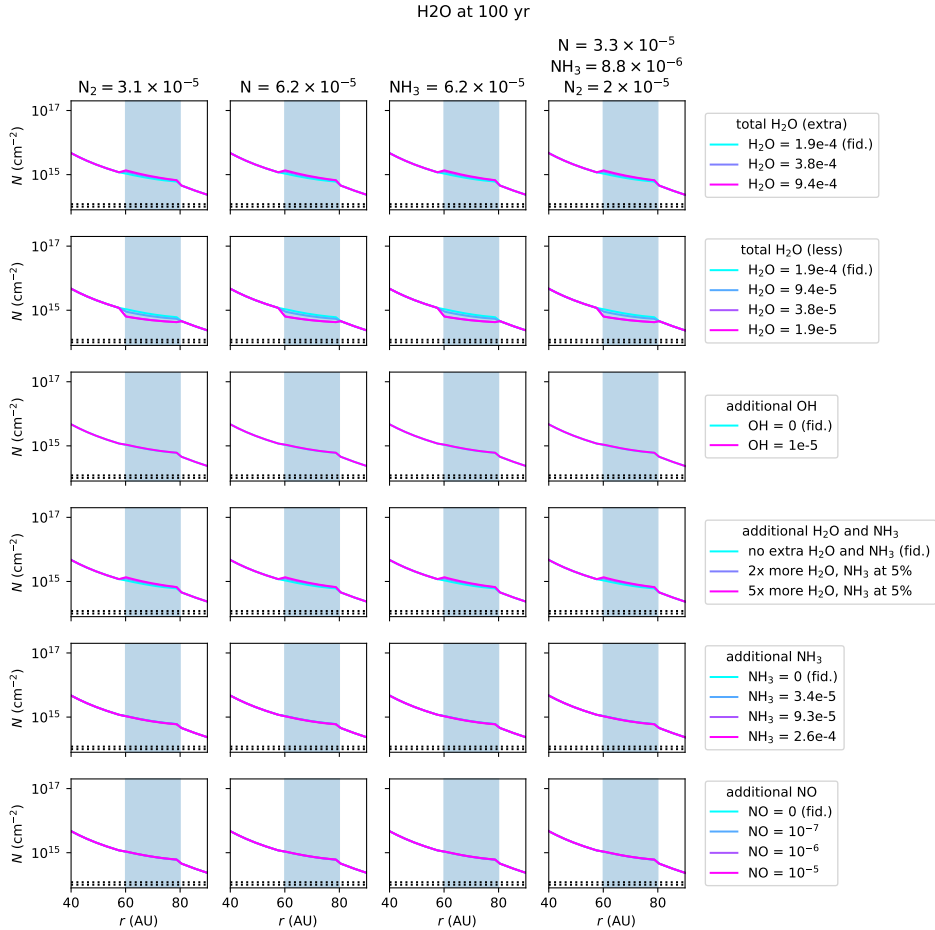


Figure 5.B.7: Predicted H₂O column density in the region where $T_{\text{gas}} \geq 150$ K, for different initial distributions of nitrogen (columns) and sublimating ices (rows). $T_{\text{gas}} \geq 150$ K is the temperature range probed by the *Herschel* PACS observations. Horizontal black dotted lines indicate the upper limit on the H₂O column density derived from the observations at 150 and 200 K. All models overpredict the upper limit on the H₂O column density. This could be due to optically thick dust at 51 – 220 μm hiding part of the H₂O column in the IRS 48 disk.

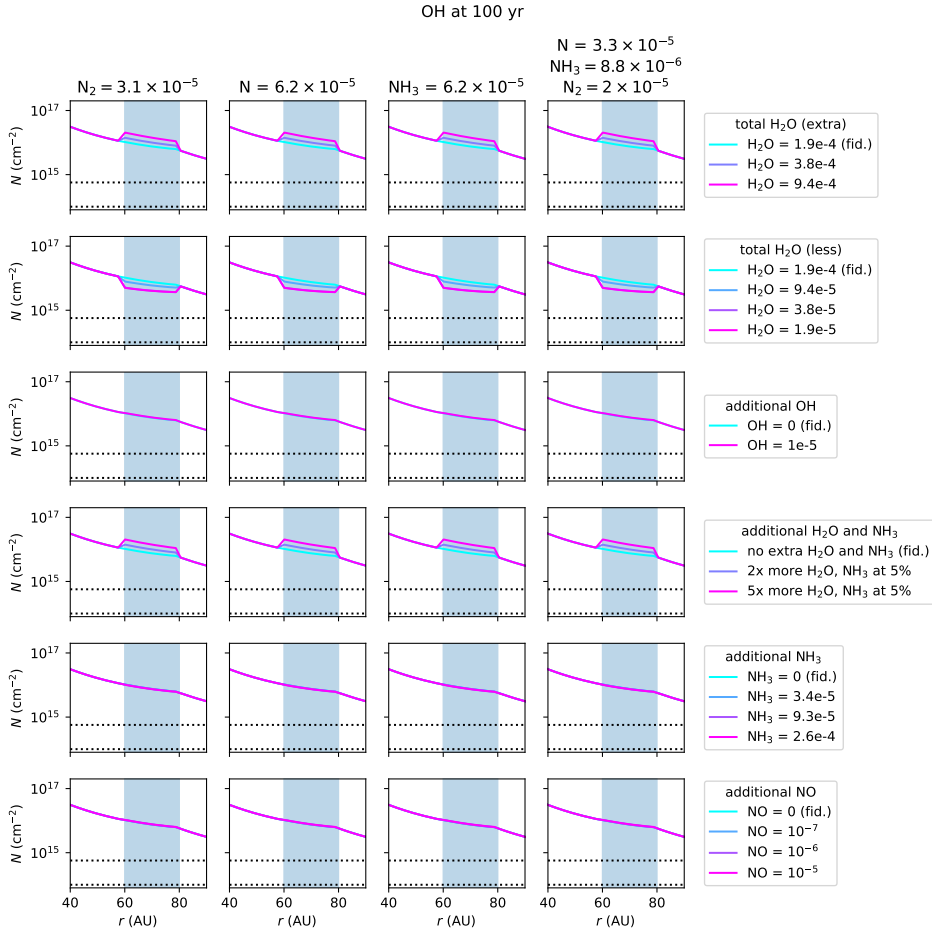


Figure 5.B.8: Predicted OH column density in the region where $T_{\text{gas}} \geq 150$ K for different initial distributions of nitrogen (columns) and sublimating ices (rows). $T_{\text{gas}} \geq 150$ K is the temperature range probed by the *Herschel* PACS observations. The horizontal black dotted lines indicate the upper limit on the OH column density derived from the observations 150 and 200 K. Similarly to H₂O, all models overpredict the upper limit on the OH column density. This could be due to optically thick dust at 51 – 220 μm hiding part of the OH column in the IRS 48 disk.

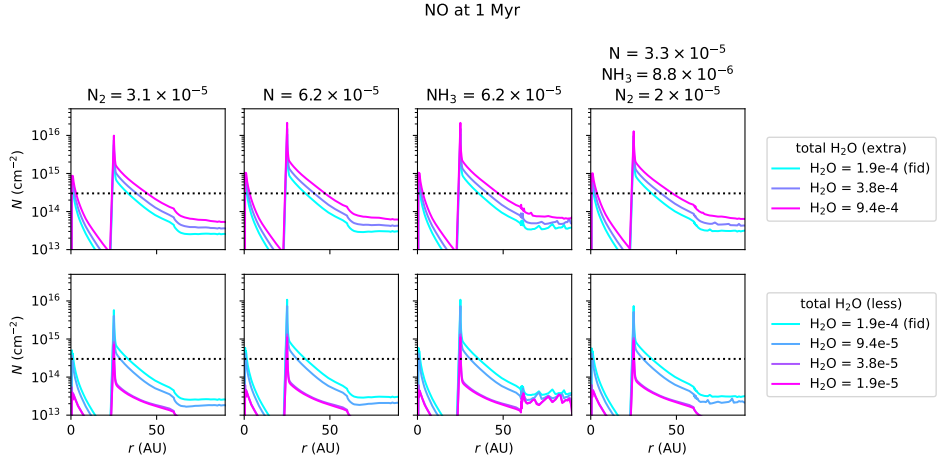


Figure 5.B.9: NO column density in the non-dust trap (north) side of the disk after 1 Myr. Black horizontal dotted line indicates the upper limit on the NO column density derived from the observations. Despite the narrow peak at 25 AU, the models are consistent with the derived upper limit on the NO column density in the north side of the IRS 48 disk.

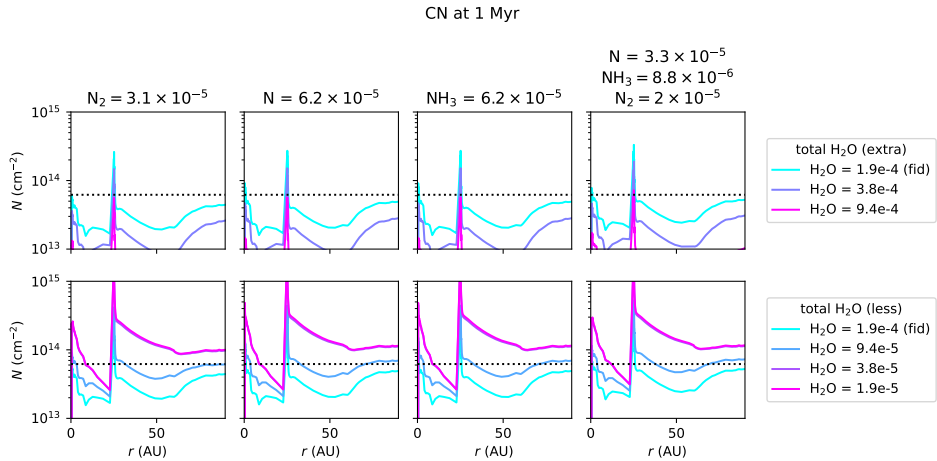
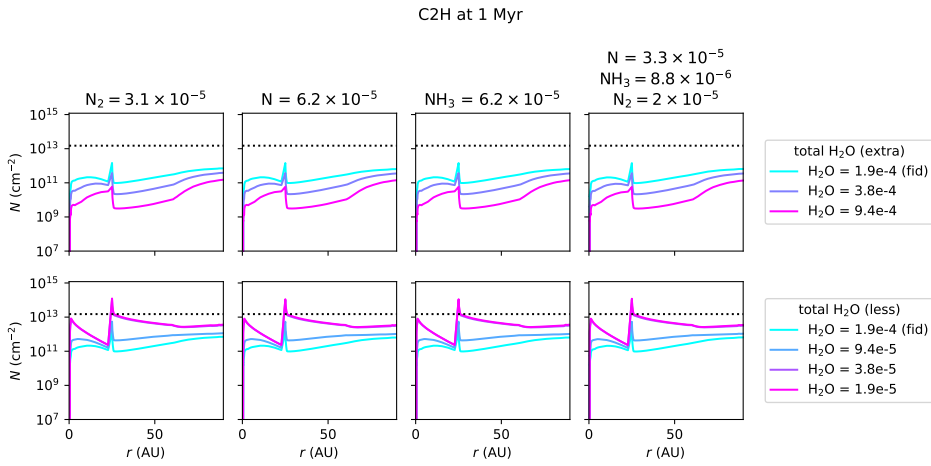


Figure 5.B.10: CN column density in the non-dust trap (north) side of the disk after 1 Myr. Models with an initial H₂O abundance of $(3.8 - 1.9) \times 10^{-5}$ overpredict the upper limit on the CN column density.



The models are consistent with the upper limit on the C₂H column density derived from observations except for a narrow peak at 25 AU for the models with the lowest initial H₂O abundance.

Figure 5.B.11: C₂H column density in the non-dust trap (north) side of the disk after 1 Myr.

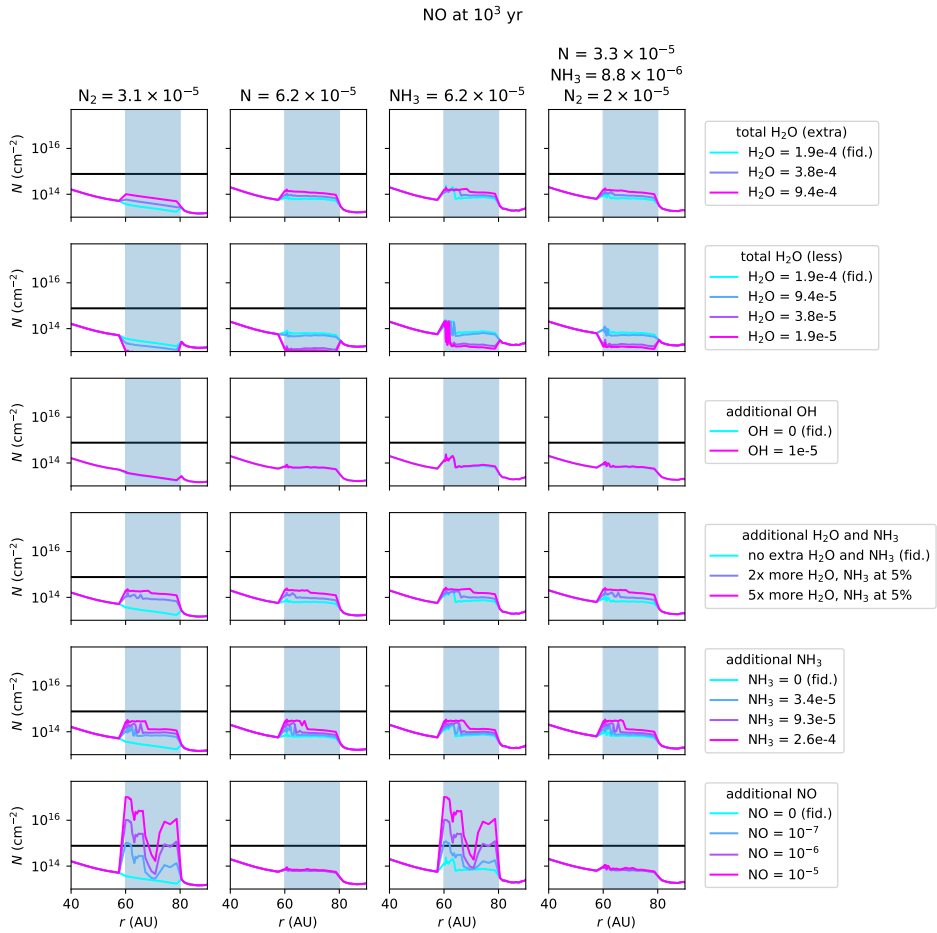


Figure 5.B.12: Predicted NO column density after 10^3 yr inside the dust trap for different initial distributions of nitrogen (columns) and sublimating ices (rows).

Chapter 6

Chemistry across dust and gas gaps in protoplanetary disks: modelling the co-spatial molecular rings in the HD 100546 disk

M. Leemker, A. S. Booth, E. F. van Dishoeck, L. Wölfer, B. Dent

Submitted to A&A

Abstract

Context. Large and nearby protoplanetary disks are commonly marked by prominent rings in the continuum emission, possibly carved by forming planets. High-resolution ALMA observations show that both the dust and the gas is structured. These molecular structures in the gas can be due to physical rings in the gas and dust density structure and/ or chemical rings. The aim of this work is to identify the expected location and intensity of rings seen in molecular line emission in gapped disks for a range of physical conditions across the gap. The molecular ring locations are compared to the location of the dust rings. In particular, we aim to model the molecular rings that are co-spatial with the dust in the HD 100546 disk using the thermochemical code DALI.

Aims. We analyze ALMA observations of CO isotopologues, [C I], HCN, CN, C₂H, NO, and HCO⁺ in the HD 100546 disk. A thermochemical model reproducing the CO isotopologue observations and the double ring seen in continuum emission is used to make predictions for various emission lines. The effect of the amount of gas in the dust gap, the C/O ratio, an attenuated background UV radiation field, and the flaring index of the disk on the distributions are investigated.

Results. The fiducial model of a gapped disk that provides a good fit to the continuum and the CO isotopologues, does not reproduce the morphology or the intensity of the [C I], CN, C₂H, and NO observations. The HCN and HCO⁺ intensities on the other hand, are reproduced within a factor of a few in most disk regions. The CO and HCO⁺ column densities are directly related to the gas gap depth and the CO isotopologue emission is consistent with a shallow gas gap of a factor of ten less gas. In contrast, a much deeper gap of at least four orders of magnitude less gas is needed to create a ring in the CN, C₂H, and NO column densities due to the increasing stellar UV field in the gap. The interstellar UV field creates an outer ring in C₂H and NO at $\sim 250 - 400$ au. Additionally, models predict that the HCN, CN, C₂H, NO, and HCO⁺ are abundant at a high disk layer of $z/r = 0.2 - 0.35$, in contrast to the observations in the same disk indicating $z/r \leq 0.1$. The models underpredict the [C I] and C₂H emission by a factor of at least ten and 50, respectively, in most disk regions, whereas the CN intensity is reproduced within a factor of a few. Increasing the C/O ratio from 0.99 to 1.01 increases the column density and intensity of CN, and C₂H by one and two orders of magnitude, respectively, whereas that of C increases by less than a factor of two.

Conclusions. The molecular rings predicted by thermochemical models do not naturally coincide with those seen in the dust. The rings seen in the HD 100546 disk can be best produced with a gas gap deeper than expected from the CO isotopologue emission, a C/O ratio of ~ 1 , and an attenuated background UV field.

6.1 Introduction

The gas, dust, and ice surrounding a young star are the building blocks of new planets. Many of the bright and large protoplanetary disks have been observed to not be smooth but have gaps, rings, and arcs in the continuum that are possibly carved by massive forming planets (e.g., Andrews et al. 2018; Huang et al. 2018; Long et al. 2018; Andrews 2020; Francis & van der Marel 2020). Recently, young planets with clear accretion signatures have been directly detected in the PDS 70 disk (Keppler et al. 2018; Haffert et al. 2019; Benisty et al. 2021), point-like sources possibly due to young planets are seen in the HD 169142 disk (Hammond et al. 2023)) and are debated in the AB Aur disk Currie et al. 2022; Zhou et al. 2023), and promising signs of planets through indirect methods such as CO gas kinematics are seen in many other disks (e.g., Pinte et al. 2018b; Teague et al. 2018a; Pinte et al. 2019; Izquierdo et al. 2022, 2023). The chemical composition of the solid core and gaseous atmosphere of these planets depends on the chemical composition of the ice on the dust grains and the gas in their protoplanetary disk. Comparing the composition in a protoplanetary disk to that measured in exoplanet atmospheres provides insights into where and when these planets have formed (Öberg et al. 2011; Öberg & Bergin 2016; Cridland et al. 2016; Mordasini et al. 2016; Cridland et al. 2017, 2023; Eistrup 2023).

The chemical composition of the gas and ice across a disk is not constant. Signs of chemical substructures have been found in simple gas-phase molecules such as the commonly observed HCO^+ , N_2H^+ , CN, HCN, and the recently detected NO (e.g., Cazzoletti et al. 2018; Bergner et al. 2019; Qi et al. 2019; Aikawa et al. 2021; Bergner et al. 2021; Law et al. 2021a; Zhang et al. 2021; Leemker et al. 2023; Temmink et al. 2023). These structures are seen both at the location of dust structures such as rings, gaps, and arcs, as well as in smooth regions of the disk. These ringed structures can thus be due to chemical rings, locally enhancing the abundance of a chemical species, or a physical ring in the underlying gas density structure.

Young planets that are embedded in their native protoplanetary disk can carve a deep gap in the dust, and if they are sufficiently massive, also a gap in the gas as traced by CO emission (Bruderer et al. 2014; Zhu et al. 2014; Dong et al. 2015b; Rosotti et al. 2016; Andrews et al. 2018; Long et al. 2018; Binkert et al. 2021; Öberg et al. 2021). These gaps and cavities seen in CO gas are typically shallower than those in the dust (e.g., van der Marel et al. 2016; Fedele et al. 2017; Zhang et al. 2021; Leemker et al. 2022). Moreover, some disks with gaps seen in the dust do not show a gap in the CO gas at the same location, for example the IM Lup and GM Aur disks outside 50 au (Zhang et al. 2021). A gas gap in a planet forming disk not only reduces the amount of gas and dust at that location, it also increases the intensity of the UV radiation as there is less dust to shield the UV (Cleeves et al. 2011; Facchini et al. 2018; Alarcón et al. 2020; Rab et al. 2020). This in turn leads to an increase of the dust temperature. The resulting gas temperature in the dust gap is a balance of the heating and cooling processes and can be either warmer or colder than the region just outside the gap. This change in temperature and UV field across the gap could lead to rings in other molecules as the chemistry

in disks is sensitive to both of these.

With the increasing number of high-resolution ALMA observations resolving the gaps and cavities not only in the dust, but also in the gas across multiple disks we can now test predictions of the models (e.g., Öberg et al. 2021). Modelling of CO, the most abundant molecule in disks after H₂, across gaps and cavities has shown that it remains abundant down to very low gas column densities where photodissociation becomes important (Woitke et al. 2009; Bruderer 2013). As the abundance of CO and its isotopologues does not change drastically across the gap, the optically thin isotopologues can be used to measure the depth of the gap whereas the optically thick ones can be used to measure the temperature (e.g., Fedele et al. 2017; Facchini et al. 2018; Alarcón et al. 2020; Calahan et al. 2021; Leemker et al. 2022). Additionally, modelling of HCO⁺ isotopologues across a gap shows that the ratio of DCO⁺ to HCO⁺ or H¹³CO⁺ is sensitive to the amount of gas in the gap (Smirnov-Pinchukov et al. 2020).

Chemical rings can be caused by snowlines of the major volatiles: H₂O, NH₃, CO₂, CO, and N₂. These snowlines are the midplane locations where 50% of a molecule is in the gas-phase and 50% is frozen out onto the dust grains. This is exceptionally clear in the structure of HCO⁺ and N₂H⁺. These molecules respond very strongly to the desorption of H₂O, CO, and N₂, resulting in ring-shaped emission outside, at, or inside the snowline (Qi et al. 2013; van 't Hoff et al. 2017; Leemker et al. 2021). On top of that, the abundance of HCO⁺, DCO⁺, and N₂H⁺ is set by the ionisation rate in the disk which may radially change due to substructures (e.g., Aikawa & Herbst 2001; Cleaves et al. 2014a; Aikawa et al. 2021).

In addition to snowlines, the stellar UV field is important for setting the chemistry in disks by photodissociating molecules in the surface layers of the disk. This not only destroys molecules, but it also enables formation paths to new ones. For example, the photodissociation of water can lead to the formation of NO and the photodissociation of CO leads to the presence of atomic carbon in disks (Thi et al. 2010; Bruderer et al. 2012; Schwarz & Bergin 2014; Leemker et al. 2023). Moreover, UV radiation can vibrationally excite molecular hydrogen (H₂^{*}) at intermediate disk radii. The extra energy stored in H₂^{*} can then be used to overcome the energy barrier to form CN and NO. Both models and observations show that CN is present in the surface layers of disks which is consistent with CN tracing the UV in the disk atmosphere (Visser et al. 2018; Cazzoletti et al. 2018; Paneque-Carreño et al. 2022). Apart from the innermost regions in the midplane, HCN follows the same trend as it is closely related to CN in the disk surface layers. Therefore, ring-shaped CN and HCN emission is expected even if the underlying gas and dust surface density profiles are smooth (Long et al. 2021).

In summary, molecular emission is not necessarily expected to follow the underlying physical structure of the disk such as rings, gaps, and cavities. This is clearly found in the observations of the five disks of the MAPS (Molecules with ALMA at Planet-forming Scales) program, where the structures seen in molecular line emission do not correlate with those in the dust apart from the MWC 480 disk and the inner 150 au (Law et al. 2021a; Jiang et al. 2022). Three other disks are a notable exception to this: the PDS 70, IRS 48, and the HD 100546 disks, where

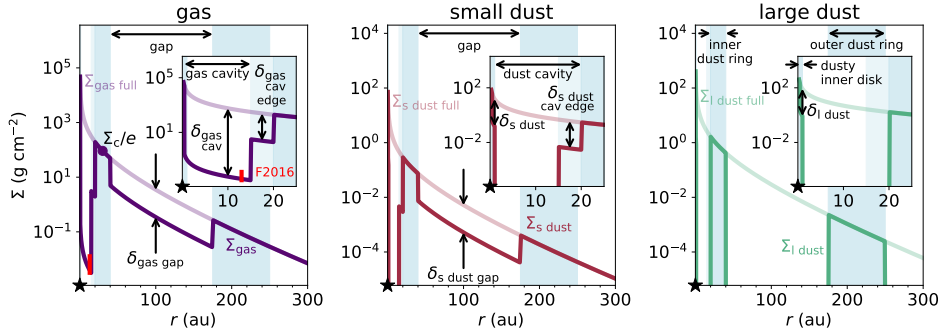


Figure 6.1: Surface density of the gas (purple), small dust (red), and large dust (green) in the fiducial model for the HD 100546 disk. The light purple, red, and green lines indicate the respective surface densities in a full disk without any gaps, cavities and rings. The blue shaded regions indicate the dusty inner disk and the two dust rings at 20-40 au and 175-250 au respectively. The surface density Σ_c/e at r_c is indicated with a scatter point in the left panel. Additionally, the DALI parameters that control drops and increases in the surface densities are indicated with arrows (see Table 6.B.1 for their values). The red bar in the inset in the left panel indicates the gas surface density based on CO by Fedele et al. (2016). The small insets in each panel focus on the inner 25 au of the disk.

small molecules such as HCO^+ , C_2H , NO, CS, SO, or SO_2 and complex organic molecules such as CH_3OH or CH_3OCH_3 are detected (Facchini et al. 2021; van der Marel et al. 2021b; Booth et al. 2021b,c; Brunken et al. 2022; Leemker et al. 2023; Booth et al. 2023a). These disks are all transition disks with a large cavity seen in the dust and in case of e.g., the PDS 70 IRS 48, HD 169142, and HD 135344B disks also in the gas also in the gas. For the PDS 70 and IRS 48 disks, the molecular line emission is seen at the dust ring/ trap that is just outside a deep cavity in both the gas and dust, which could reduce the molecular line emission due to a lack of gas inside the cavities. In contrast, besides from a small central cavity ($r \lesssim 15$ au), the HD 100546 disk does not show signs of a deep gap in the gas in the outer disk, yet the molecular rings are found to be coincident with the dust rings (Walsh et al. 2014a; Pinilla et al. 2015; Fedele et al. 2021, Booth et al. in prep.).

In this paper we aim to investigate the conditions that lead to molecular rings coinciding with the dust rings. In Sect. 6.2 we present the [C I] data in the HD 100546 disk and describe the setup of our thermochemical models that include a gas and dust cavity as well as a gap between the two rings seen in the HD 100546 continuum and CO isotopologues. In addition, we present a fiducial model that fits these data. Section 6.3 presents the predictions for [C I], HCN, CN, C_2H , NO, and HCO^+ in this disk under different physical conditions, varying parameters such as a deep gas gap, an elevated C/O ratio, an attenuated background UV field, and disk flaring. The results are discussed in Sect. 6.4 in the specific context of the HD 100546 observations and our conclusions are summarized in Sect. 6.5.

6.2 Methods

6.2.1 Source: HD 100546

HD 100546 is a $\sim 2 M_{\odot}$, 5 Myr old Herbig Ae/Be star with a luminosity of $\sim 36 L_{\odot}$ (Kama et al. 2016; Arun et al. 2019; Pineda et al. 2019). This star is located in a relatively isolated region at a distance of 108.1 ± 0.4 pc (Gaia Collaboration et al. 2016, 2023). The star is surrounded by a massive and gas-rich disk of $0.03\text{--}0.1 M_{\odot}$ based on CO isotopologue emission and an upper limit on the HD flux (Kama et al. 2016; Stapper et al. 2023). Both the CO gas and the dust in this disk are highly structured with small scale gas and dust spirals (a few $0''.1$), a large scale ($\sim 1''$) dusty spiral and a large scale spiral in the gas kinematics (Garufi et al. 2016; Follette et al. 2017; Sissa et al. 2018; Norfolk et al. 2022; Wölfer et al. 2023a). Additionally, the continuum emission in this disk is seen in three locations: an unresolved dusty inner disk, a bright inner ring from ~ 20 au to 40 au, and a weak outer ring at $< 1\%$ of the peak continuum intensity from ~ 150 au to 250 au (Bruderer et al. 2012; Walsh et al. 2014a; Pineda et al. 2019; Fedele et al. 2021).

The central cavity and gap between the two dust rings have been hypothesized to be carved by massive planets. The inner planet has been inferred from CO ro-vibrational emission and a feature seen in scattered light (e.g., Brittain et al. 2013, 2014; Currie et al. 2015). In addition, co-rotating SO is seen at the location of the proposed planet (Booth et al. 2023b). A second planet has been hypothesized between the two dust rings as a point source is seen at 50 – 60 au in scattered light observations (Quanz et al. 2013a; Currie et al. 2014). However, the nature of these potential planets is debated as no accretion signatures have been found at this location and different results have been found depending on the data quality and imaging techniques (Currie et al. 2017; Follette et al. 2017; Rameau et al. 2017). Therefore, more research is needed to firmly conclude if these planets are present.

ALMA observations of molecular lines have revealed a number of different molecules in this disk. The detection of formaldehyde and the complex organic molecule methanol in this warm disk indicates that the molecular inventory is likely inherited from the native dark cloud as the bulk of the disk is too warm for CO freeze-out (Booth et al. 2021c). The CS and SO emission are somewhat asymmetric to opposite sites of the disk, hinting at an overdensity of material close to the star shadowing the outer disk and causing an azimuthally varying C/O ratio (Keyte et al. 2023). Finally, many of the molecular lines except the CO isotopologues are close to co-spatial with the rings seen in the dust (Booth et al. 2023a, see also Fig. 6.5). In this work, we use high resolution ALMA observations of the dust and CO isotopologues (Pineda et al. 2019; Pérez et al. 2020; Wölfer et al. 2023b,a), intermediate resolution data of the dust, CO, $C^{17}O$, HCN, CN, C_2H , NO, and HCO^+ (Booth et al. 2023a), and [C I] observations.

6.2.2 ALMA data covering [C I]

The $^{12}\text{CO } J = 7 - 6$ and [C I] line emission data used in his paper were taken in Cycle 6 with ALMA in Band 10 (2018.1.00141.S; PI: B. Dent), using 43 antennas with baselines of 15-783 m. Starting from the archival pipeline-calibrated data we performed further data reduction using CASA (McMullin et al. 2007). Due to a low signal-to-noise ratio, no self-calibration was applied. We first subtracted the continuum using the `uvcontsub` task, flagging channels containing line emission, and then imaged the lines with `tcLEAN` for both the continuum-subtracted and non-subtracted data sets. In this process, we imaged the data at the highest spectral resolution possible and adopted a Briggs robust weighting of 0.5, which gave the best trade off between spatial resolution and sensitivity. We also applied a Keplerian mask ¹ using an inclination of 42° , position angle of 320° , distance of 110 pc, stellar mass of $2.13 M_\odot$, and systemic velocity of 5.7 km s^{-1} . We further used the multi-scale deconvolver (scales 0,5,10,20) and a slight `uv-taper` ($0''.05 \times 0''.05, 0^\circ$) to improve the signal-to-noise ratio in the images. The integrated intensity map and the spectrum are presented in Fig. 6.A.1.

6.2.3 DALI

To investigate the relative importance of physical versus chemical rings, we model the dust rings and rings seen in molecular line emission using the thermochemical code Dust And LInes (DALI; Bruderer et al. 2009, 2012; Bruderer 2013). The model presented in this work is based on those presented in Pirovano et al. (2022) and Keyte et al. (2023). We improve on the dust structure from the latter model by including a dust gap in the outer disk to match the double ringed structure of the continuum observations (Fedele et al. 2021; Booth et al. 2023a). Additionally, the gas density structure is improved by including a gas gap between the two dust rings and by including an inner gas cavity just inside the inner dust ring at 20 au to match the observed CO emission in those regions (Pérez et al. 2020; Booth et al. 2023a; Wölfer et al. 2023a). The general setup of the model is described below.

6.2.3.1 Gas density structure

The radial and vertical density structure of the disk follow the standard DALI setup for a flared disk with an exponentially tapered power law in the radial direction and a Gaussian distribution of the gas in the vertical direction (see Bruderer 2013, and Appendix 6.B.1.1 for details). To include the gas cavity and a gas gap in this disk, the gas surface density of the full disk is lowered as follows:

$$\Sigma_{\text{gas}} = \begin{cases} \Sigma_{\text{gas full}} \times 10^{-5} & (0.4 \text{ au} < r < 15 \text{ au}) \\ \Sigma_{\text{gas full}} \times 10^{-2} & (15 \text{ au} < r < 20 \text{ au}) \\ \Sigma_{\text{gas full}} & (20 \text{ au} < r < 40 \text{ au}) \\ \Sigma_{\text{gas full}} \times \delta_{\text{gas gap}} & (40 \text{ au} < r < 175 \text{ au}) \\ \Sigma_{\text{gas full}} & (175 \text{ au} < r < 1000 \text{ au}), \end{cases} \quad (6.1)$$

¹https://github.com/richteague/keplerian_mask

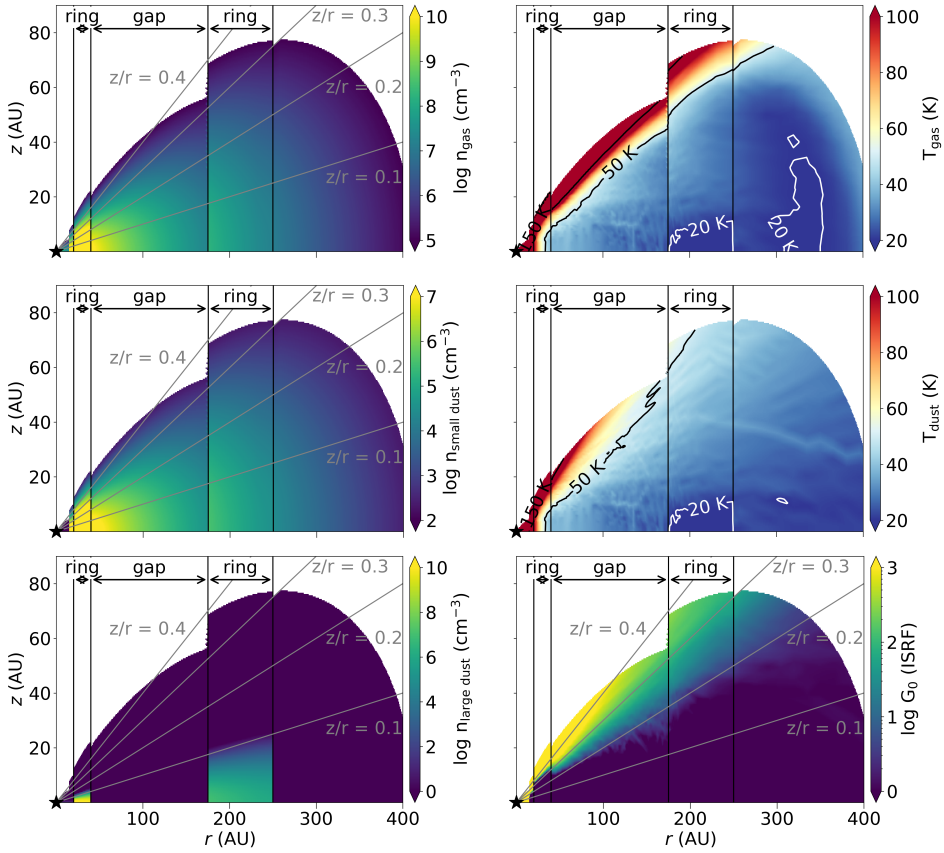


Figure 6.2: Structure of the fiducial DALI model. From left to right and top to bottom: gas, small dust, and large dust density, gas and dust temperature, and UV field. Only the regions with a gas number density above 10^5 cm^{-3} are shown. Outside 250 au, the midplane gas density is too low for the gas and dust temperature to be coupled.

with $\delta_{\text{gas gap}}$ lowering the gas density in the gap, see the left panel of Fig. 6.1 and the top left panel of Fig. 6.2.

6.2.3.2 Dust density structure

The small grains follow the gas outside the inner gas cavity as they are expected to be well mixed with the gas. Outside the gas cavity but inside the dust cavity the small grains also follow the gas. Inside the gas cavity down to the dusty inner disk that is observed in continuum emission up to $< 2 \text{ au}$ (Benisty et al. 2010; Pineda et al. 2019; Pérez et al. 2020), the small grains are depleted by a factor of 10^{-10} to mimic a cavity devoid of any dust. The dusty inner disk inside 1 au is depleted in small (5 nm–1 μm) and large (5 nm–1 mm) grains by a factor of 10^{-2} (see also the middle and right panels in Fig. 6.1 and the middle left and bottom

left panels Fig. 6.2):

$$\Sigma_{\text{s dust}} = \begin{cases} \Sigma_{\text{s dust full}} \times 10^{-2} & (0.4 \text{ au} < r < 1 \text{ au}) \\ \Sigma_{\text{s dust full}} \times 10^{-10} & (1 \text{ au} < r < 15 \text{ au}) \\ (1 - f_{\text{ls}}) \times \Sigma_{\text{gas}} / \Delta_{\text{gd}} & (15 \text{ au} < r < 1000 \text{ au}). \end{cases} \quad (6.2)$$

In the vertical direction the small dust follows the gas.

Observations show that the large dust in the HD 100546 disk is mainly present at three different locations: a dusty inner disk, an inner ring at 20 – 40 au and an outer ring at 175 – 250 au (Walsh et al. 2014a; Pineda et al. 2019; Fedele et al. 2021). The cavity in the large dust in our model is 5 au larger than that in the small dust and the gas, similar to what is observed in other transition disks (Perez et al. 2015; van der Marel et al. 2016; Leemker et al. 2022; Wölfer et al. 2023b). This is parametrized as:

$$\Sigma_{\text{l dust}} = \begin{cases} \Sigma_{\text{l dust full}} \times 10^{-2} & (0.4 \text{ au} < r < 1 \text{ au}) \\ \Sigma_{\text{l dust full}} \times 10^{-10} & (1 \text{ au} < r < 20 \text{ au}) \\ \Sigma_{\text{l dust full}} & (20 \text{ au} < r < 40 \text{ au}) \\ \Sigma_{\text{l dust full}} \times 10^{-10} & (40 \text{ au} < r < 175 \text{ au}) \\ \Sigma_{\text{l dust full}} & (175 \text{ au} < r < 250 \text{ au}) \\ \Sigma_{\text{l dust full}} \times 10^{-10} & (250 \text{ au} < r < 1000 \text{ au}). \end{cases} \quad (6.3)$$

The outer ring extends to 250 au, see also the right panel of Fig. 6.1. Additionally, the large grains are settled to the disk midplane (bottom left panel in Fig. 6.2). The dust in the midplane of the outer dust ring is sufficiently cold for some CO freeze-out as the dust temperature drops below 20 K (middle row, right panel in Fig. 6.2).

6.2.4 Stellar spectrum

The stellar spectrum of HD 100546 observed by the Far Ultraviolet Spectroscopic Explorer (FUSE) and the the International Ultraviolet Explorer (IUE) and presented in Bruderer et al. (2012) is used. These observations have been dereddened and extended to longer wavelengths using a B9V template (Pickles 1998). Additionally, an X-ray luminosity of $7.9 \times 10^{28} \text{ erg s}^{-1}$ (Stelzer et al. 2006) with a temperature of $7 \times 10^7 \text{ K}$ is included to account for more energetic radiation.

6.2.5 Chemistry

The chemistry is modelled using a chemical network suited for modelling small nitrogen bearing molecules such as CN, HCN, and NO, and small hydrocarbons such as C₂H. This network was first presented in Visser et al. (2018); Cazzoletti et al. (2018); and Long et al. (2021). Similar to Leemker et al. (2023), the binding energy of C₂H₃ (ethylenyl) is set to 10^4 K to mimic the conversion of C₂H₃ to larger COMs on the grain surfaces. This network includes the main gas-phase formation and destruction routes of the molecules of interest, the freeze-out and thermal-,

and non-desorption of the major volatiles. The non-thermal desorption rates of H_2O and CO are updated from 1.3×10^{-3} and 2.7×10^{-3} molecules desorbed per grain per incident UV photon to 5×10^{-4} and 1.4×10^{-3} molecules desorbed per grain per incident UV photon respectively (Öberg et al. 2007, 2009; Paardekooper et al. 2016; González Díaz et al. 2019; Fillion et al. 2022). Additionally, some grain surface reactions are included such as the formation of H_2 on grains and PAHs. Moreover, the hydrogenation of O, C, N, and CN on grains to form H_2O , CH_4 , NH_3 , and HCN ices are included, but no detailed ice chemistry such as the conversion of CO to H_2CO or CH_3OH is modelled as the HD 10546 disk is warm and no large-scale CO freeze-out is expected.

The abundance of the CO isotopologues is predicted with the CO isotopologue network presented in Miotello et al. (2016). This network includes the ^{12}C , ^{13}C , ^{16}O , ^{17}O , and ^{18}O isotopes, with their ratios taken as $^{12}\text{C}/^{13}\text{C} = 77$, $^{16}\text{O}/^{18}\text{O} = 560$, and $^{16}\text{O}/^{17}\text{O} = 1792$ (Wilson & Rood 1994). Both chemical networks are started with molecular initial conditions and a fiducial C/O ratio of 0.4 (see Table 6.B.1 and 6.B.1.2).

For the HCO^+ abundance, the chemical network presented in Leemker et al. (2021) is used. This is a small chemical network centred around HCO^+ . This network does include the freeze-out and thermal desorption of H_2O , but not that of CO . As the only carbon-bearing molecules in this network are CO and HCO^+ , this network is only run for the models with $\text{C}/\text{O} < 1$. This network is evolved using the density and temperature structure of the DALI model together with initial CO and H_2O abundances to match the C/O ratio.

6.2.6 Raytracing

The synthetic ALMA observations are produced using the raytracer in DALI. The level populations without assuming local thermodynamical equilibrium (LTE) are calculated using the collisional rate coefficients for ^{12}CO , ^{13}CO , C^{18}O , C^{17}O , C, HCN , CN , C_2H , NO , and HCO^+ in the LAMDA database² (Launay & Roueff 1977; Johnson et al. 1987; Roueff & Le Boulrot 1990; Schroder et al. 1991; Staemmler & Flower 1991; Schöier et al. 2005; Dumouchel et al. 2010; Lique et al. 2010; Yang et al. 2010; Spielfiedel et al. 2012; Denis-Alpizar et al. 2020; Ben Khalifa & Loreau 2021). An overview of the investigated transitions is presented in Table 6.A.1. The observed C_2H and NO data cover two respectively three lines that are blended with themselves. Therefore, these two and three transitions were raytraced and added assuming the emission is optically thin. Finally, all synthetic image cubes are convolved to a beam matching that of the observations.

6.2.7 The fiducial model

Thermo-chemical models are not expected to reproduce the observed line emission within the uncertainty of the data as the predicted molecular line emission depends both on the abundance of a certain molecule as well as the temperature of the emitting layer. The parameter studies of the DALI thermo-chemical code show a

²<https://home.strw.leidenuniv.nl/~moldata/>

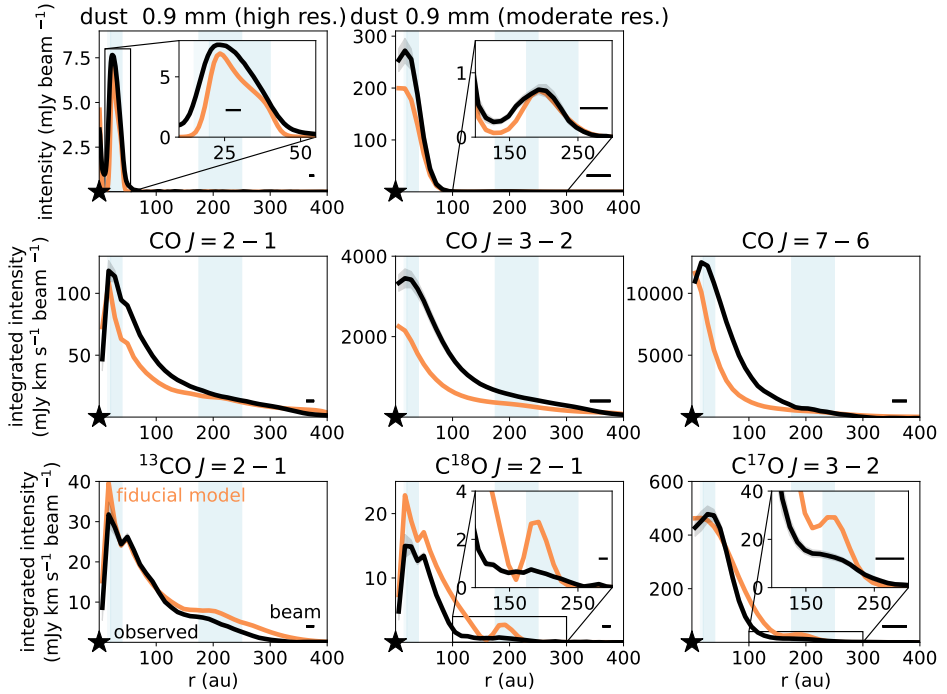


Figure 6.3: Azimuthally averaged radial profiles of the dust and CO isotopologue emission observed in the HD 100546 disk (black) together with the fiducial model (orange). The beam is indicated with the horizontal bar in the bottom right corner of each panel. The continuum observations are taken from Pineda et al. (2019) (high resolution 0.9 mm continuum), Booth et al. (2023a) (moderate resolution 0.9 mm continuum), the CO, ^{13}CO , and C^{18}O $J = 2 - 1$ transitions are first presented in Pérez et al. (2020) and Wölfer et al. (2023a), the CO $J = 7 - 6$ transition is presented in Wölfer et al. (2023a), and the CO $J = 3 - 2$ and C^{17}O $J = 3 - 2$ transitions are presented in Booth et al. (2023a).

factor of ~ 2 difference in line flux due e.g. uncertainties in reaction rates in the chemical networks (Bruderer et al. 2012; Bruderer 2013). Therefore, a model is expected to reproduce the data within a factor of 2–3 in general (Kama et al. 2016; Sturm et al. 2023a). Instead of matching the observed line intensities within the uncertainty of the data, we look for trends in the abundances and line intensities for a range of key parameters such as gap depth and chemical composition.

The key feature of the emission in the HD 100546 disk is that all molecular rings are co-spatial with the dust rings, whereas the CO isotopologue emission appears smooth. The only structure seen in the CO isotopologue emission is a central gas cavity and a weak shelf of C^{18}O and C^{17}O emission extending from 150 au to 250 au (see insert in the bottom middle and right corner of Fig. 6.3). Therefore, the aim of the fiducial model is not to fit the CO isotopologues perfectly. Instead, the aim of the fiducial model is to provide a basis that roughly fits the continuum

and the CO isotopologues and explore under what conditions the molecular rings coincide with those seen in the continuum emission. The observations of the outer molecular rings are all consistent with emission originating from close to the midplane (Booth et al. 2023a). Therefore, the fiducial model has a low flaring index of $\psi = 0$ and a low scale height of $h_c = 0.1$ at the characteristic radius. A comparison of our fiducial model with those presented in Pirovano et al. (2022) and Keyte et al. (2023) is shown in Fig. 6.B.1, where the main differences are that the model presented in this work is significantly less flared than those presented in Pirovano et al. (2022) and Keyte et al. (2023), and has a gas cavity at < 15 au that is not present in Keyte et al. (2023). An overview of the parameters of the fiducial model is presented in Table 6.B.1.

The gas and dust density, temperature, and UV field in this model are presented in Fig. 6.2. The midplane gas density inside the gap drops down to a low value of 10^7 cm^{-3} at 250 au, which is too low for the gas and dust to be thermally coupled in the midplane. Therefore, the gas temperature at these locations is colder than that of the dust. The small dust follow the gas outside the gas cavity at 15 au. The large dust is only seen in the two dust rings at 20–40 au and 175–200 au. A steep drop in the UV field is seen at $z/r = 0.2$. This layer also roughly separates the warm surface layer of the disk from the layers below 50 K closer to the midplane. This flat model intercepts less UV radiation from the central star than more flared models, which causes a small amount of CO freeze-out in the outer dust ring.

The resulting emission of the mm-dust and the CO isotopologues is presented in Fig. 6.3. The top row presents the fits of the fiducial model to the dusty inner disk and the dust ring from 20–40 au seen in the high resolution continuum (left panel) as well as the much weaker dust ring at 175–250 au seen at moderate spatial resolution (middle panel; Pineda et al. 2019; Booth et al. 2023a). The weak outer continuum ring is not seen in the left panel due to the high spatial resolution and small maximum recoverable scale (26 au in radius) of that dataset.

The gas density structure is improved by including a 15 au gas cavity that is seen in the high spatial resolution $J = 2 - 1$ transition of ^{12}CO , ^{13}CO , and C^{18}O presented in the middle and bottom left panels in Fig. 6.3 (Pérez et al. 2020; Wölfer et al. 2023a). To match these data, the gas density inside the gas cavity is lowered by a factor of 10^{-5} and between the gas (15 au) and dust cavity (20 au) by a factor of 10^{-2} . Outside the gas cavity, the ^{13}CO , C^{18}O , and C^{17}O emission matches that of the observations (Pérez et al. 2020; Booth et al. 2023a; Wölfer et al. 2023a), with an especially close match being achieved for the ^{13}CO and C^{17}O emission. The ^{12}CO $J = 3 - 2$ and $J = 7 - 6$ emission presented in Booth et al. (2023a) and Wölfer et al. (2023a) is underproduced by at most a factor of ~ 2 likely due to the gas temperature that is slightly too low in this flat model. However, the main focus of the fiducial model is on the rarest CO isotopologues (C^{18}O and C^{17}O), the dust rings and the molecular line emission.

The lack of mm-dust between the two dust rings in the HD 100546 disk may be due to a massive planet carving a gap in the disk (Pinilla et al. 2015; Fedele et al. 2021; Pyerin et al. 2021). Therefore, the gas density in this region may be lower than in a full disk model. This is explored in Fig. 6.B.2 and we find that CO isotopologue emission is consistent with a shallow gas gap where the gas is

depleted by at most one order of magnitude, assuming that the gas and dust gap have the same widths.

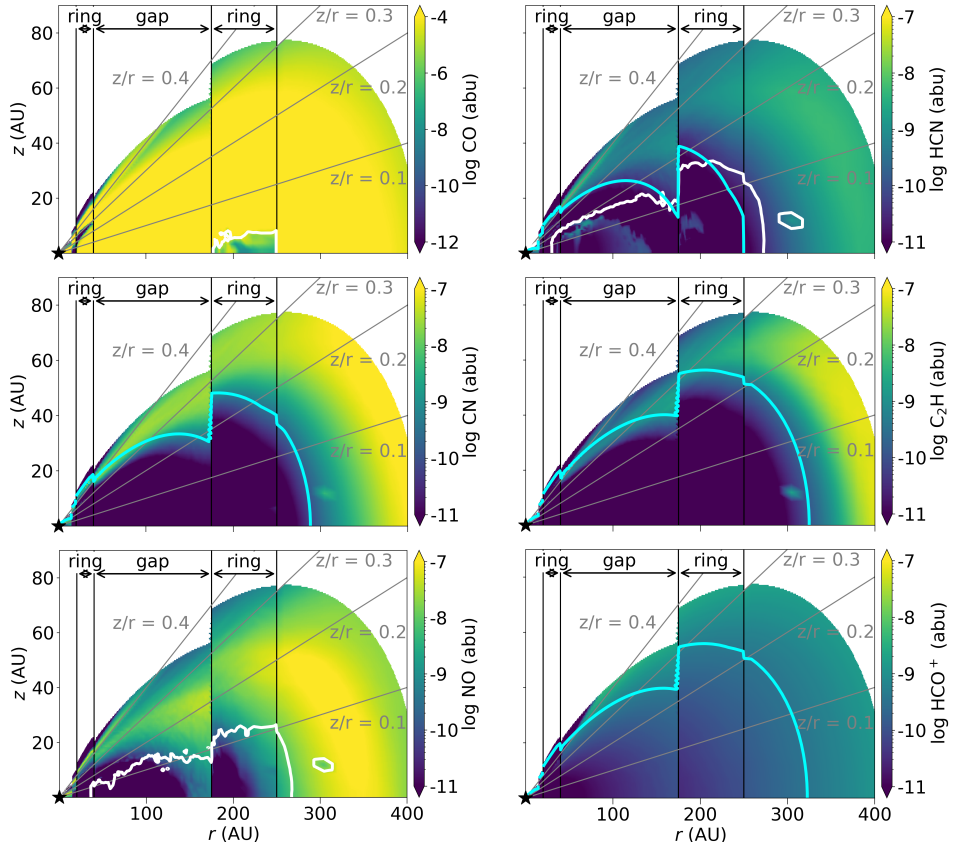


Figure 6.4: 2D abundance maps of CO, HCN, CN, C₂H, NO, and HCO⁺. Note that the CO abundance is shown on a different colorscale. The white contour indicates the snowline of CO, HCN, and NO in their respective channels. The blue contour shows the critical density assuming a temperature of 50 K. Only the regions with a gas number density above 10⁵ cm⁻³ are shown. As the CO and NO critical densities are lower than this, those contours are not shown in the respective panels.

6.3 Results

The HD 100546 disk is one of the few objects where the observed HCN, CN, C₂H, and HCO⁺ emission lines are seen in two concentric rings that are co-spatial with the continuum emission (see Booth et al. 2023a, or Fig. 6.5 in this work). In contrast to the IRS 48 and PDS 70 disks, however, this disk does not have a deep gap between the two dust rings (see Sect. 6.2.7). The abundance structure and emission of HCN, CN, C₂H, NO, and HCO⁺ are presented in this section, where

we explore their sensitivity to the model parameters to better understand what shapes their emission.

6.3.1 2D abundance maps

The 2D abundance structures of the molecules of interest, HCN, CN, C₂H, NO, and HCO⁺, are presented in Fig. 6.4 together with the CO abundance for reference. The abundances are calculated with respect to the total hydrogen density: $n_h = n(\text{H}) + 2 \times n(\text{H}_2)$. All of these molecules except CO follow the same global morphology: a surface layer with a high abundance that extends from the inner dust ring or the gap out to the outer disk at 400 au where the layer moves down to the midplane. Additionally, HCN and CO are abundant at lower disk layers and the NO and HCO⁺ layers extend to the disk midplane from ~ 150 au outward. The CO is abundant throughout the entire disk except in the surface layers where CO is photodissociated and in the midplane in the outer dust ring where CO is frozen out onto the dust grains.

HCN, CN, C₂H, and NO are sensitive to the UV field. The UV radiation in the surface layer forms vibrationally excited molecular hydrogen, H₂*. This molecule then reacts with N to form NH that then reacts with C⁺ to form CN⁺ that is converted to CN and HCN. Additionally, a pathway through CH and N to form CN is also seen in this region. As the UV field only penetrates the surface layers of the disk, the HCN, CN, and C₂H are also constrained to this layer and thus reside in a layer where the number density of molecular hydrogen is below the respective critical densities (cyan contours in Fig. 6.4). The HCN molecule is not only abundant in a surface layer at $z/r > 0.2$; a secondary layer formed through different chemical reactions exists around a scale height of 0.1. Here, the HCN is mainly formed through a reaction of atomic carbon with H₂ to form CH₂ through radiative association which then reacts with O and N to form CO and HCN. As this layer is below the HCN snow surface (white contour in Fig. 6.2), this HCN quickly freezes-out.

Somewhat deeper in the disk at $z/r = 0.2$ NO is abundant. The NO is mainly formed through the reaction of NH with O with a minor contribution of the reactions of OH and N (< 10%). The NO layer lies somewhat deeper in the disk than that of HCN, CN, and C₂H due to the destruction of NO by atomic carbon and nitrogen that (re)forms CO, CN, and N₂. At lower layers below $z/r = 0.1$, NO quickly freezes-out onto the dust grains as the NO snowline is located at a scale height of 0.1 in the dust gap and the outer dust ring. The thin NO layer at $z/r = 0.4$ is due to the photodissociation of water forming OH (see also Leemker et al. 2023).

Finally, the HCO⁺ abundance is high at $\sim 10^{-9}$ in the highest layers of the disk above $z/r = 0.3$ due to the high ionisation enhancing the H₃⁺ abundance in this region. In addition to ionisation, the HCO⁺ ion traces the water snowline: a high HCO⁺ abundance is only seen outside the water snowline where water cannot destroy HCO⁺ (Phillips et al. 1992; Bergin et al. 1998). The water snowline in this model is located at the outer edge of the gas cavity at 15 au. Therefore, the HCO⁺ abundance at larger radii scales as $\sqrt{\zeta_{\text{c.r.}}/n_{\text{H}_2}}$ with a weak dependence on

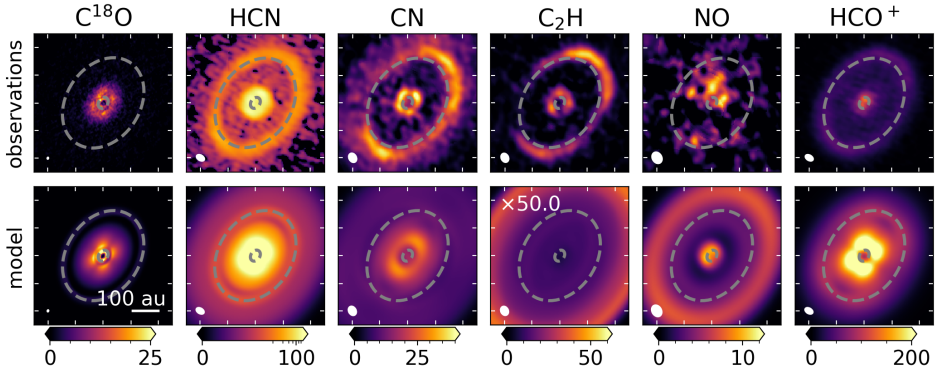


Figure 6.5: Integrated intensity (moment 0) maps of C^{18}O , HCN, CN, C_2H , NO, and HCO^+ emission in the HD 100546 disk. The top row presents the observations (Booth et al. 2023a) and the bottom row the predictions of the fiducial model. All intensities are in $\text{mJy km s}^{-1} \text{beam}^{-1}$. The dotted grey ellipses indicate the dust rings seen in the high spatial resolution (inner ring) and in the moderate spatial resolution (outer ring) 0.9 mm continuum. The tickmarks on the panels are spaced by $1''$, the horizontal bar in the bottom left panel indicates a 100 au scale. The HCN is shown on a logarithmic scale to highlight the weak outer ring and the modelled C_2H emission has been multiplied by a factor of 50. The beam of each of the observations is indicated with the white ellipse in the bottom left corner.

temperature (Leemker et al. 2021). This may overpredict the HCO^+ abundance outside the inner dust ring in this disk as cold, gas-phase water seen outside ~ 40 au in this disk and water photodesorption is not included in the small chemical network (van Dishoeck et al. 2021; Pirovano et al. 2022).

Altogether, the 2D abundance structures of HCN, CN, C_2H , NO, and HCO^+ are dominated by a layer with a high abundance centred at $z/r \sim 0.2 - 0.3$. This layer is located at or above the critical density of HCN, CN, and C_2H , therefore, these molecules may not be in LTE. This is similar to the observed emitting layer of CO and higher than the layer of $z/r \leq 0.1$ that the HCN, CN, C_2H , and HCO^+ observations suggest (Booth et al. 2023a). The high abundance layer moves down slightly inside the gas gap due to the lower gas density, but apart from this, no clear jump in the abundance at the location of the outer dust ring is seen.

6.3.2 Integrated intensity maps

The integrated intensity (moment 0) maps of the data and the fiducial model are presented in Fig. 6.5. The modelled C^{18}O emission reproduces the observations within a factor of two for most disk regions with the outer ring in C^{18}O being more prominent in the model than in the data (see also Fig. 6.3, bottom row). For the other molecules on the other hand, the observed intensities or the double ringed profile are not reproduced. Only the modelled HCN and HCO^+ emission do show a hint of an outer ring at the location of the second dust ring and the C_2H and NO show a (weak) ring outside the outer dust ring.

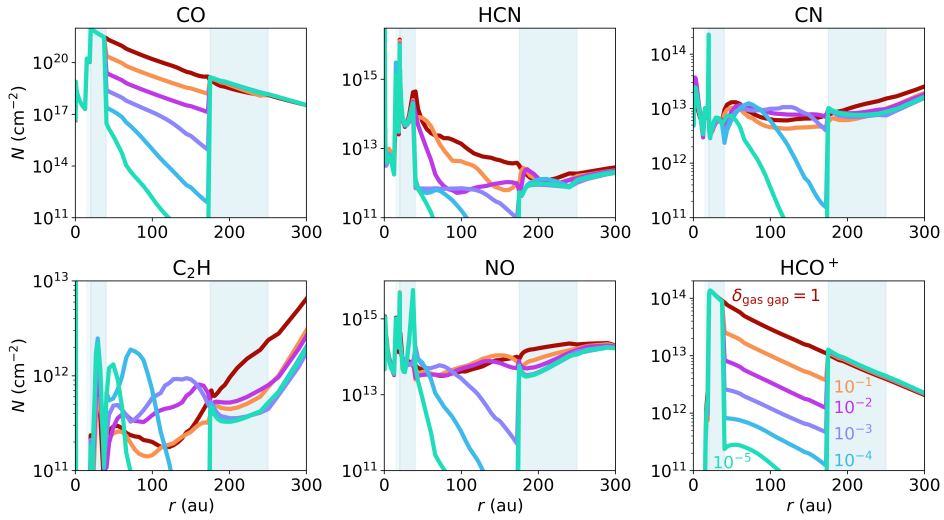


Figure 6.6: Column densities of CO, HCN, CN, C₂H, NO, and HCO⁺ in the fiducial model with a C/O ratio and a gas gap depth of 1 (no gap; dark red), 10⁻¹ (fiducial model; orange), 10⁻² (pink), 10⁻³ (purple), 10⁻⁴ (blue), and 10⁻⁵ (very deep gap; light blue). The small dust density is dropped by the same factor in the gap as in the gas.

The inner ring that is observed in HCN and CN is reproduced by the model within a factor of ~ 2 but the observed C₂H ring at 40 au is not seen in the model. The modelled HCO⁺ emission is ring-shaped in the inner disk with a ring at 60 au, whereas the data are centrally peaked at the spatial resolution of the observations. The intensity in the modelled ring is two times higher than what is observed at the central location.

The model predicts outer rings in HCN and HCO⁺ that are only a factor of ~ 3 weaker and a factor of two brighter than what is observed, respectively. However, the model does not reproduce the outer ring in C₂H as the modelled ring is two orders of magnitude weaker and 170 au further out than seen in the data. Similarly, the observed outer ring in CN is not recovered by the model and the modelled NO emission is mostly seen just outside the inner dust ring and outside the outer dust ring whereas the observations show some emission between the two dust rings and possibly at the location of the outer dust ring. In summary, Fig. 6.5 shows that despite a good fit to the continuum and CO isotopologue emission, the model does not reproduce the observations of molecules other than CO isotopologues, especially for CN, C₂H, and NO. The chemical network used to calculate these abundances reproduces the CN, HCN, HNC, and C₂H emission in other protoplanetary disks within a factor of a few in general (e.g., Cazzoletti et al. 2018; Visser et al. 2018; Miotello et al. 2019; Long et al. 2021). Therefore, the difference between the model predictions and the observations in the HD 100546 disk are likely due to the physical structure of the disk rather than uncertainties in the chemical network.

6.3.3 A deeper gas gap

A possible solution to create double rings in the molecular line emission is to induce a deep gas gap between the two dust rings. The ^{12}CO emission does not show any evidence of a gas gap deeper than the fiducial depth of a factor of 10, neither does the C^{17}O where only a shoulder of emission extending out to 200 – 300 au is observed (see Fig. 6.B.2). Still, a depletion of gas could affect the molecular line emission. Therefore, the effect of a deeper gas gap is investigated in this subsection. The small dust is assumed to follow the drop in the gas density.

6.3.3.1 Column densities

The effect of the depth of the gap between 40 and 175 au on the column density is presented in Fig. 6.6 where the column densities inside 250 au are smoothed in log space with a savgol filter in `scipy` over 10 points and a 3rd order polynomial to remove any artificial spikes due to low photon statistics in the model. The CO column density directly traces the drop in the gas density for gaps up to three orders of magnitude in gas density. For deeper gaps, CO photodissociation becomes important and the CO column density drops even faster than the gas density.

The HCO^+ column density directly follows that of the gas where a drop of two orders of magnitude in gas column density results in a one order of magnitude drop in the HCO^+ column density. The reason for this is that the HCO^+ number density outside the water snowline follows $n(\text{HCO}^+) \propto \sqrt{\zeta_{\text{c.r.}} \times n(\text{H}_2)}$, with $\zeta_{\text{c.r.}}$ the cosmic ray ionisation rate and $n(\text{H}_2)$ the density of molecular hydrogen (see eq. B.6 in Leemker et al. 2021). Therefore, the HCO^+ column density in the gap is directly related to that of the gas.

The CN, C_2H , and NO show a different pattern than CO, but a similar pattern to each other, in their column densities when the gap depth is increased. For shallow to somewhat deep gas gaps ($\delta_{\text{gas gap}} \sim 1 - 10^{-2}$) their column densities are independent of the gap depth within a factor of a few. For very deep gas gaps ($\delta_{\text{gas gap}} \sim 10^{-4} - 10^{-5}$) a steep decrease in the column density is seen in the outer parts of the gap. The sharp peaks in the HCN, CN, C_2H , and NO column densities at the inner ring and cavity (15, 20, and 40 au) may be sensitive to the precise conditions in this region.

This behaviour can be understood from the 2D UV field and CN abundance which are presented in Fig. 6.7. Shown are the results for a shallow gap (10^{-1}) and two deep gaps (10^{-3} and 10^{-5}). In left column, a shallow gas gap is present, but the CN is only abundant in a layer high above the midplane at $z/r = 0.3$ in the gap. Changing the amount of gas in this region only shifts this layer up or down, but it does not affect the column density greatly as the midplane abundance of CN is low. For a deep gas gap (middle and right columns), the UV field is more intense in the gap than in the model with a shallow gas gap. As CN is sensitive to the UV field, its abundance increases in the gap. The resulting CN column density is an interplay of an increase in the abundance that is most prominent at small radii, and a decrease in the gas column density that is most effective at large radii. This causes a peak in the CN column density that moves to smaller

radii of 75 and 50 au with deeper gaps of 10^{-4} and 10^{-5} , respectively. As C_2H and NO are also sensitive to the UV field, their abundances and column densities show the same qualitative behaviour. Especially for C_2H , the inward travelling peak in the column density is clearly visible at 160 au, 140 au, 70 au, and 50 au for $\delta_{\text{gas gap}} = 10^{-2}, 10^{-3}, 10^{-4}, 10^{-5}$, respectively.

The HCN column density always decreases or stays constant with deeper gaps due to the moderate HCN abundance in the midplane together with the high abundance in the surface layer. The component in the midplane slowly decreases up to a gap depth of 10^{-2} , lowering the HCN column density simultaneously. For deeper gaps, the midplane component of the HCN vanishes and the HCN column density steeply drops with gas density, similar to the pattern seen for CN , C_2H , and NO .

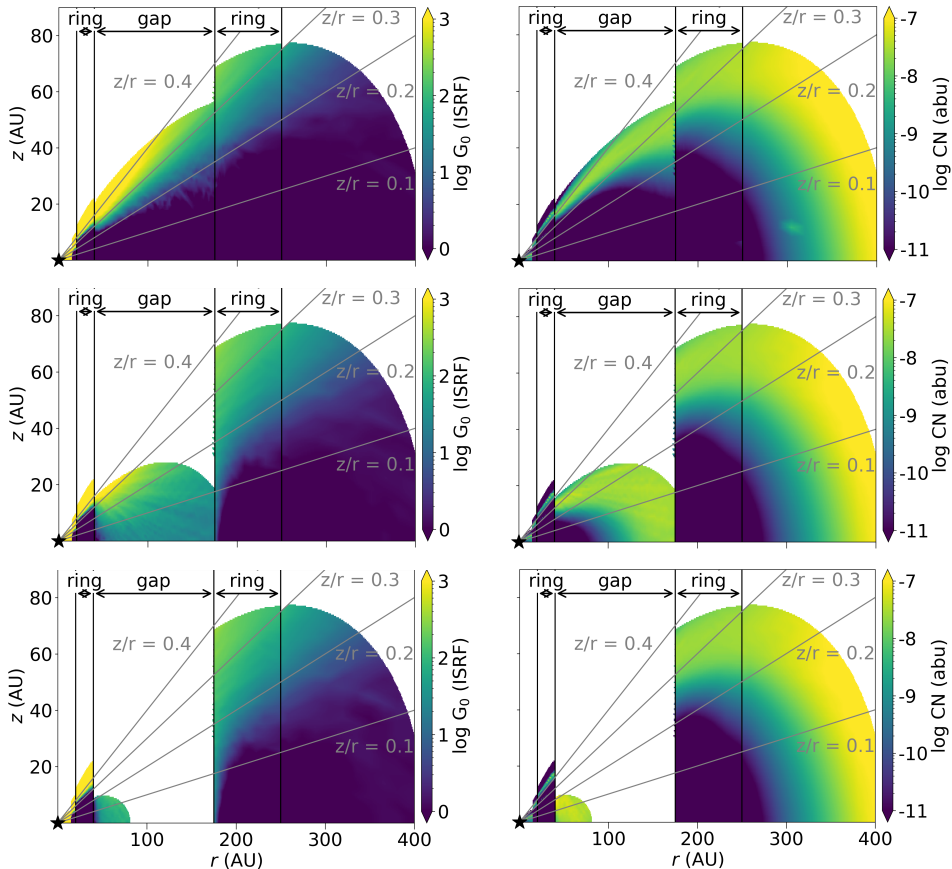


Figure 6.7: The UV field and CN abundance for different gas gap depth. From left to right: $\delta_{\text{gas gap}} = 10^{-1}, 10^{-3},$ and 10^{-5} . The top row shows the UV field in units of G_0 and the bottom row the CN abundance. Only the regions with a gas number density above 10^5 cm^{-3} are shown.

6.3.3.2 Emission maps

The integrated intensity (moment 0) maps for different gas gap depths are presented in Fig. 6.8 and Fig. 6.B.4. The fiducial model is presented on the second row and the moment maps are identical to those presented in Fig. 6.5 but on a different colorscale. In general, the molecular line emission shows ringed emission for all models that have some degree of gas depletion between the dust rings ($\delta_{\text{gas gap}} = 10^{-1} - 10^{-5}$). However, double rings are only seen for the models with a very deep gas gap ($\delta_{\text{gas gap}} = 10^{-4} - 10^{-5}$). These rings are typically located outside the dust rings instead of at the dust as seen in the observations. For example, the NO emission shows a very clear double ring for these models, but the outer ring is located at 300 au where no NO is seen in the data. The C₂H emission shows a ring of emission inside the gas gap that moves inwards with increasing gap depths following the corresponding C₂H column density. This effect is also seen in the CN and NO emission, although it is less pronounced. The NO emission just outside the inner ring is sensitive to a sharp peak in the column density and may be very sensitive to the conditions in this region. The remaining three molecules, C¹⁸O, HCN and HCO⁺ all show double ringed profile for all models with some gas depletion.

The model with a deep gas gap of 10^{-4} times less gas best reproduces the double ringed nature of the HCN, CN, and C₂H observations, whereas the model with a factor of ten more gas ($\delta_{\text{gas gap}} = 10^{-3}$) reproduces the diffuse HCO⁺ emission between the dust rings better. The first model reproduces the morphology of the molecular line emission just outside the inner dust ring for CN and C₂H while also predicting a reasonable intensity for HCN. Additionally, this model reproduces the presence of an outer ring seen in HCN, CN, and HCO⁺. The CO isotopologue emission on the other hand is best reproduced by a disk with a shallow gap of only 10^{-1} times less gas as the C¹⁸O emission in the gap is directly related to the drop in gas density.

6.3.3.3 Molecular column densities and line ratios

Ratios of column densities can give additional insights into the underlying processes as they are less sensitive to the absolute model results. The column density ratios of HCO⁺/CO, C₂H/CO, CN/HCN, and CN/NO are presented in Fig. 6.9 for a model without a gas gap and models with gap depths up to 10^{-5} . The first three ratios increase with radius outside the outer gas cavity in the full gas disk model, whereas the CN/NO ratio first increases inside the dust gap, then slowly decreases up to the outer dust ring and then somewhat increases again. This is caused by the different radii where the CN and NO column densities peak in the disk. The HCO⁺/CO and C₂H/CO ratios increase due to the increasing column density in HCO⁺ and C₂H as that of CO smoothly decreases with radius. Finally, the increase in the CN/HCN ratio is driven by the decreasing column density of HCN.

When a gas gap is introduced, the ratios presented in Fig. 6.9 all increase compared to the model without a gas gap except for a disk with a gap of 10^{-1} and 10^{-2} times less gas where the CN/NO ratio stays roughly constant in the gap.

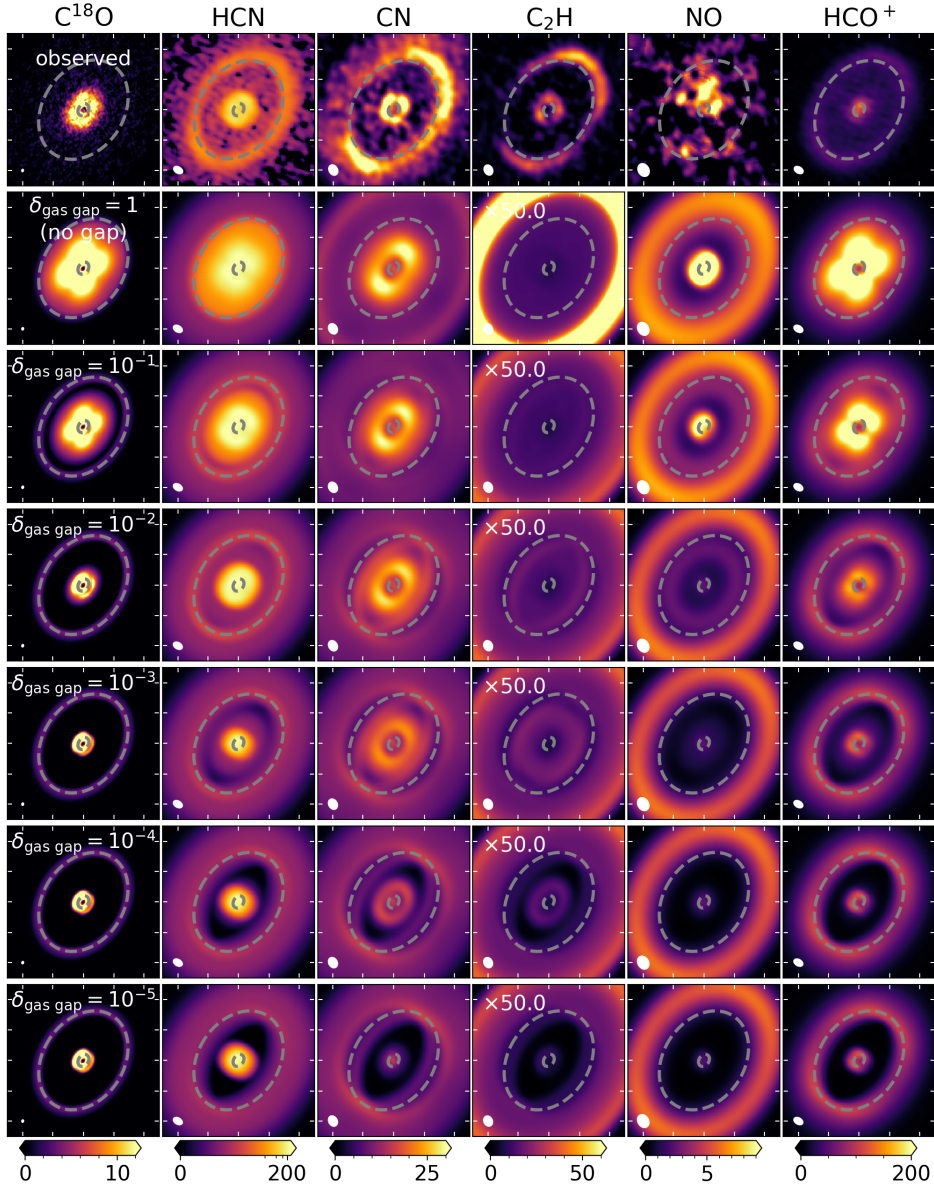


Figure 6.8: Integrated intensity (moment 0) maps in $\text{mJy km s}^{-1} \text{beam}^{-1}$ for C^{18}O , HCN, CN, C_2H , NO, and HCO^+ from left to right. The different rows present the results for different depth of the gas gap with the gap depth ($\delta_{\text{gas gap}}$) indicated in the top of the left column. The HCN emission is shown on a logarithmic scale to highlight the weak outer ring. The beam is indicated in the bottom left corner of each panel and the tickmarks on the axes are spaced $1''$ apart.

The same trend is seen in the ratios for models with $\delta_{\text{gas gap}} = 1 - 10^{-2}$ of the corresponding molecular lines presented in Fig. 6.B.7. For deeper gas gaps, the line ratios become insensitive to the gas gap depths due to the finite resolution of the observations. This is because part of the bright emission in the rings leaks into the gap regions, causing these regions to be dominated by the rings for deep gas gaps. Altogether, the column density ratios of HCO^+/CO , $\text{C}_2\text{H}/\text{CO}$, and CN/HCN show a strong dependence on the gas gap depth that is much weaker in the ratios of the emission lines.

6.3.4 Different C/O ratios

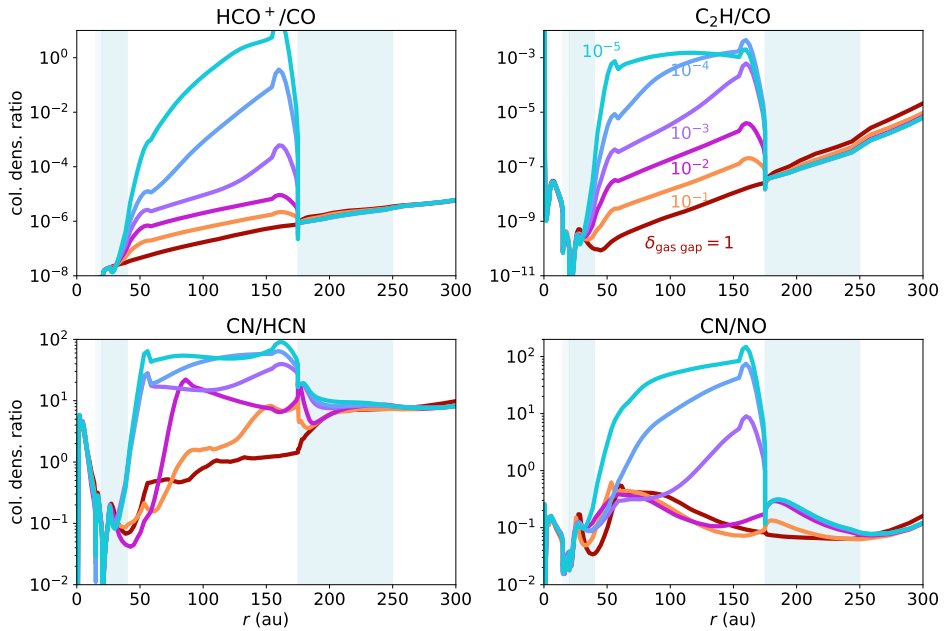


Figure 6.9: Column density ratios of HCO^+/CO (top left), $\text{C}_2\text{H}/\text{CO}$ (top right), CN/HCN (bottom left), and CN/NO (bottom right) for different gas gap depths.

6.3.4.1 Column densities and emission profiles

The observed C_2H emission is two orders of magnitude brighter than predicted by the fiducial model. Observations in other disks show that the C_2H emission becomes significantly brighter when the C/O ratio of the gas exceeds 1 (e.g., Bergin et al. 2016; Miotello et al. 2019; Bosman et al. 2021b). In this section, the effect of an increased C/O ratio is explored in the fiducial model with a gas gap of $\delta_{\text{gas gap}} = 10^{-1}$. The 2D abundance maps for C_2H and NO are presented in Fig. 6.10. The 2D abundance maps in the top row are the maps for the fiducial model and are the same as those presented in Fig. 6.4. The middle and bottom

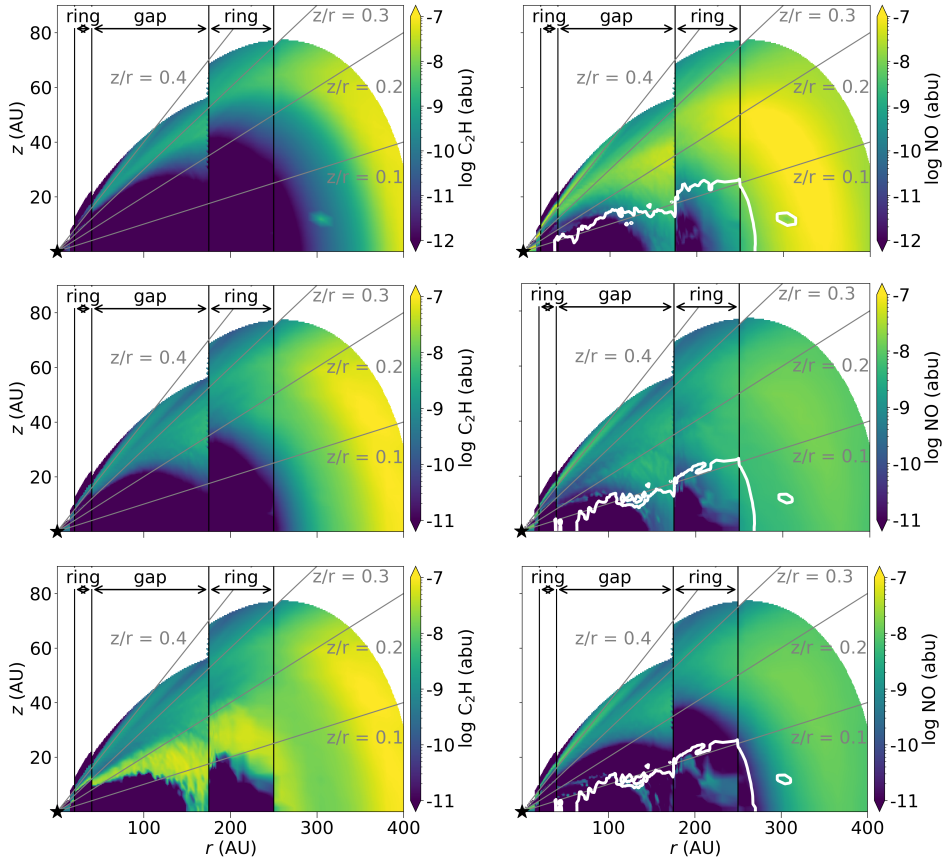


Figure 6.10: The C_2H (left column row) and NO (right column row) abundance for different C/O ratios. From left to right: $\text{C}/\text{O} = 0.4$ (fiducial value), 0.99, and 1.01. Only the regions with a gas number density above 10^5 cm^{-3} are shown. The white contour indicates the NO snowline.

row show these maps for a C/O ratio just below one at 0.99 and just above one at 1.01. As the C/O ratio increases, the layer where C₂H is abundant moves down from $z/r = 0.3$ for C/O = 0.4 to $z/r = 0.2$ for C/O = 0.99 and then it jumps down to $z/r = 0.15$ for a C/O ratio that is only 0.02 higher at 1.01. The peak C₂H abundance in this layer also jumps from $\sim 2 \times 10^{-9}$ to 4×10^{-9} and to 7×10^{-8} for C/O = 0.4, 0.99, and 1.01, respectively. A similar trend is seen for HCN, CN, and C.

The NO abundance shows the opposite behaviour as NO is expected to become less abundant when the C/O ratio is high. This is also seen in the 2D abundance maps as the NO abundance quickly decreases if the C/O is increased from 0.4 to 0.99 by removing water. As the C/O ratio further increases the NO layer splits into two regions around $z/r = 0.05$ below its snow surface and one at $z/r = 0.2 - 0.3$. HCO⁺ and CO both carry one oxygen atom and one carbon atom and are therefore not as sensitive to the C/O ratio. The column densities for these molecules for C/O ratios between 0.4 and 1.2 are presented in Fig. 6.B.6 in Appendix 6.B.3.3.

The step-like behaviour of the CN and C₂H abundance is also seen in the azimuthally averaged integrated intensity profiles presented in Fig. 6.11. If the C/O ratio increases from 0.99 to 1.01, the CN and C₂H integrated intensities increase by a factor of a few to one order of magnitude and by two orders of magnitude in the gap, respectively. The C/O ratio does change the integrated intensity across the disk, but the locations of the CN and C₂H peaks remain around those seen in the data except for a large peak at 300 – 400 au seen in C₂H. Interestingly, the observed C₂H emission falls between that predicted by models with C/O = 0.99 and 1.01, possibly indicating a C/O ratio in the rings that is very close to 1.00.

The HCN emission only shows a double peak profile for the models with C/O = 0.4 and 0.8 as the column density inside the gap increases faster with increasing C/O than that just outside the gap. The model with a C/O of 0.8 matches the intensity in the outer dust ring particularly well whereas in the model with C/O = 0.4 matches the inner ring within a factor of ~ 2 .

The top left panel in Fig. 6.11 presents the azimuthally averaged radial profile of the observed [C I] emission in the HD 100546 disk. Unlike the HCN, CN, C₂H, and HCO⁺ emission, the [C I] does not show a double peaked profile at the dust rings. This could partially be due to the small maximum recoverable scale of 2" (~ 108 au in radius), filtering the emission at larger distances. Therefore, the model may overpredict the observed line intensity outside this radius. Inside ~ 108 au, the fiducial model underpredicts the emission of atomic carbon by an order of magnitude. The only model that recovers the observed [C I] intensity up to 150 au is the model with a C/O of 1.2.

The effect of the C/O ratio on the NO emission is that the NO peak moves inwards from 300 au to ~ 40 au. The high intensity at small radii is due to some additional NO at $z/r = 0.1 - 0.2$ in the models with C/O > 1. The intensity in the outer disk decreases with increasing C/O ratio due to the lower abundance.

In summary, increasing the C/O ratio increases the predicted intensity for [C I], HCN, CN, C₂H, and NO inside 100 au and for NO it decreases the intensity outside 100 au. The observed emission lines are reproduced by different C/O ratios for

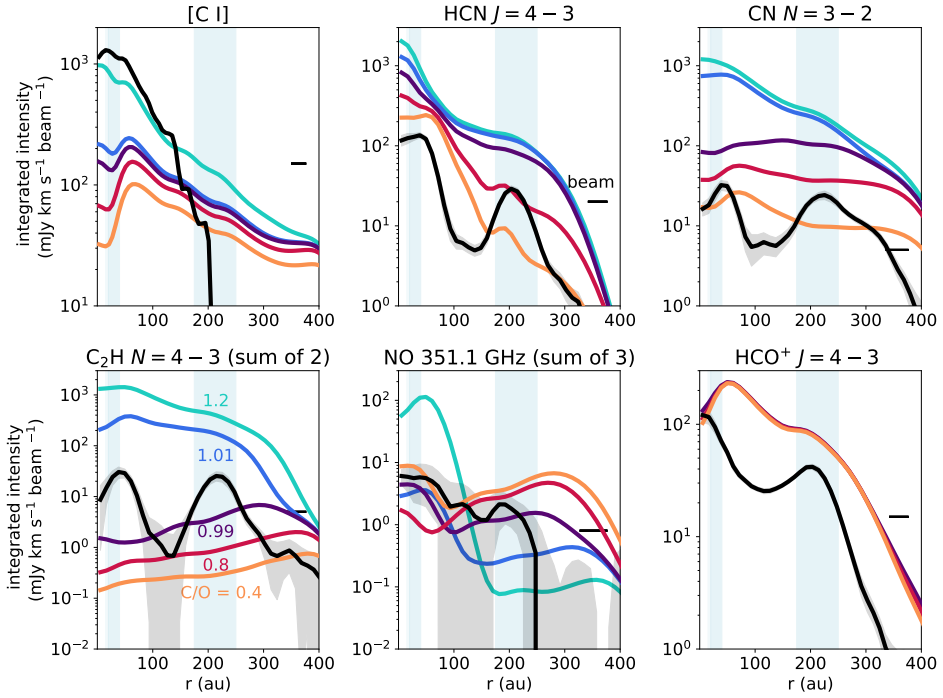


Figure 6.11: Azimuthally averaged integrated intensity of the molecular line emission for different C/O ratios in a model with a gas gap depth of 10^{-1} . The black line indicated the observed intensities.

each molecule. For example, the region inside 150 au is best reproduced by $C/O = 1.2$ for [C I], but this overpredicts the CN and C_2H emission by more than an order of magnitude. At the location of the outer dust ring, the cyanides (HCN and CN) and NO are compatible with a C/O ratio of 0.8, but the C_2H requires a C/O ratio very close to 1 ($0.99 < C/O < 1.01$).

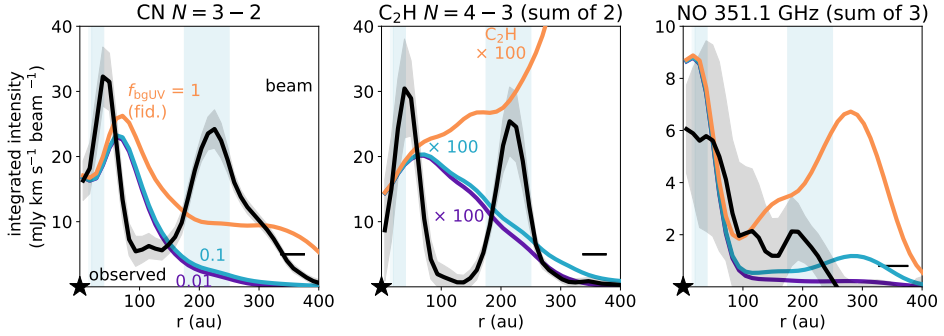


Figure 6.12: Azimuthally averaged integrated intensity of the CN, C_2H , and NO for different background UV radiation fields. The modeled C_2H emission is increased by a factor of 100 to show it on the same scale as the observations.

6.3.4.2 Column density and emission line ratios

To eliminate some of the uncertainties of comparing absolute modelled intensities to the observed ones, the column density and line ratios of $HCO^+/C^{17}O$, $C_2H/C^{17}O$, CN/HCN, and CN/NO are presented in Appendix 6.B.3.3. The latter three column density ratios all increase in most disk regions with increasing C/O due to the enhancement of C_2H and CN, and the decrease of NO. In particular, the CN/NO ratio outside 100 au and the $C_2H/C^{17}O$ in the entire disk are sensitive to small changes in the C/O . Comparing the observed emission line ratios to the modelled ones shows that the C/O needs to be very close to 1.00 as the $C_2H/C^{17}O$ ratio for $C/O = 0.99$ underpredicts the observed value and that of $C/O = 1.01$ overpredicts the observations. The CN/NO line ratio only traces the C/O ratio for $r > 175$ au, and is therefore not a good tracer of the C/O in the disk.

6.3.5 Background UV

One striking feature that most of the models presented here show is that the CN, C_2H , and NO emission are too bright outside the outermost dust ring. This raises the question if the modelled external UV field is too strong as all of these molecules at least partially trace the UV field. The models assume that the external UV field is $1 G_0$, the mean UV field in the interstellar medium. However, HD 100546 is an isolated star with a tenuous envelope may result in a lower external UV field (Grady et al. 2001).

The effect of a lower UV field on the CN, C₂H, and NO column density is presented in Fig. 6.B.11. Lowering the background UV field by a factor of ten decreases the CN and C₂H column densities by that same factor outside the outer dust ring. The NO decreases by a factor of 5 in that same region. This is also reflected in the azimuthally averaged radial intensity profiles presented in Fig. 6.12. The shelf of CN and the peak of C₂H at 375 au are not visible for the lowered background radiation fields, creating a ring of emission at the location of the outer dust ring. The effect of a lower background UV field on the [C I], HCN, and HCO⁺ emission is small.

In particular, a lower background UV radiation field more closely reproduces the double peak profile of the C₂H emission, with both peaks having a similar intensity. The C₂H intensities in these models is a factor of 200 lower than what is observed for C/O = 0.4. Additionally, the NO emission in the outer disk is not overpredicted if the background radiation field is lowered. Overall, a lower background UV field seems to improve the comparison with observations outside the outer dust ring.

6.3.6 Flaring

The observations of HCN, CN, C₂H, and HCO⁺ show two emission rings that are concentric around the position of the star. This indicates that these molecules emit from a layer close to the disk midplane ($z/r \leq 0.1$, Booth et al. 2023a) as an elevated layer would shift these rings w.r.t. the position of the star. Such an offset is indeed seen in the models for CN. Figure 6.13 presents this with the light and dark blue ellipses for different flaring indices of the disk. The ellipses indicate the projected location of the peak CN number density at the inner rim of the outer dust ring. For the two flattest models ($\psi = -0.1$ and 0) the CN at $r = 175$ au peaks at $z = 55 - 53$ au whereas for the two more flared models ($\psi = 0.1$ and 0.2), the CN peaks at a height of $66 - 68$ au at $r = 176$ au. These ellipses trace two rings in the CN emission in the moment 0 maps. These two rings increase and move slightly further apart with increasing flaring index, tracing the height where the CN is abundant. As this height only changes by ~ 10 au between a very flared and a close to flat disk, flaring alone cannot explain the observed emitting heights. However, the emission in the moment 0 map is not only depends on the vertical structure but also on the density and temperature. Observations of C¹⁸O in the Elias 2-27 disk show a ring that is close to being centered at the position of the star. Yet the C¹⁸O channel maps show that the emitting surface is flared, with $z/r \sim 0.2$ (Paneque-Carreño et al. 2021). Therefore, deriving the emitting height from integrated intensity maps may hide part of the true vertical structure of the disk. The column density and radial emission profiles for other molecules are presented in Appendix 6.B.5.

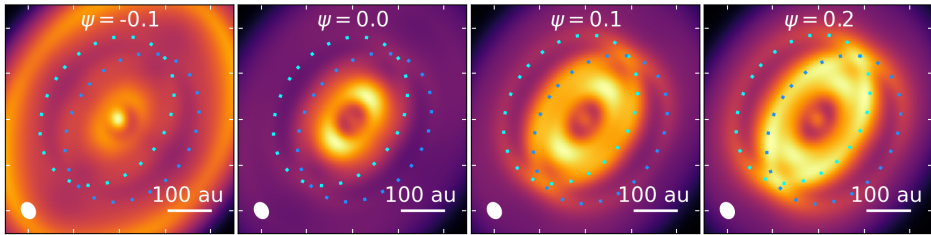


Figure 6.13: Moment 0 maps of the CN emission for models with different flaring indices $\psi = -0.1$ to $+0.2$. The light and dark blue ellipses indicate the projected location at which the modelled CN number density peaks at the inner rim of the outer dust ring, which corresponds to $z = 53 - 68$ au. The panels are shown on an individual colorbar for clarity.

6.4 Discussion

Correlations between the radial structures in the dust and gas could point to a common origin such as massive planets that are carving gaps in disks or to the sublimation of ices as seen in the IRS 48 disk (van der Marel et al. 2021b; Booth et al. 2021b; Brunken et al. 2022; Leemker et al. 2023). The observations in the HD 100546 disk show a clear correlation between the dust rings and the HCN, CN, C₂H, and HCO⁺ emission suggesting a direct relation between the structures in the gas and the dust. However, the rare CO isotopologue emission, tracing the CO column density, does not show the same double ringed structure. In this work, we used thermochemical models to investigate under what conditions molecular rings are co-spatial with the dust rings.

6.4.1 Radial structures

6.4.1.1 CO isotopologues, HCO⁺, and HCN

The thermochemical models spanning a range of gas gap depth ($\delta_{\text{gas gap}} = 1-10^{-5}$) show that three molecules directly respond to a the depletion of gas in the gap: CO isotopologues, HCO⁺, and HCN. Comparing the modelled CO isotopologues to the observations shows that a shallow gas gap ($\delta_{\text{gas gap}} = 10^{-1}$) is needed as a deeper gas gap creates a gap in the emission that is not seen in the observations. A double ring is seen in HCN and HCO⁺ if the modelled gas gap is at least two orders of magnitude deep (or one order of magnitude if the disk is viewed face-on due to projection effects, see Fig. 6.B.5 in Appendix 6.B.2.2). Interestingly, despite the correlations seen in the models, no general correlation is observed in the MAPS sources between the HCN and HCO⁺ rings and the dust and only a weak ($\sim 3\sigma$) correlation is seen between the CO isotopologue emission and the dust.

The trend in the HCO⁺ and CO isotopologues across the gas gap is also seen in other modelling works. Modelling of HCO⁺ across a gas gap outside the CO snowline predicts that the ratio of the HCO⁺ to the total gas column density

increases when a gas gap is introduced (Alarcón et al. 2020; Smirnov-Pinchukov et al. 2020). A difference in the model predictions is seen for the model with only a dust gap and no gas gap ($\delta_{\text{gas gap}} = 1$). This model presented in Smirnov-Pinchukov et al. (2020) shows an increased HCO^+/CO column density ratio in the dust gap whereas this is not seen in the models presented in this work (Fig. 6.9). A possible cause for this is that the gap in Smirnov-Pinchukov et al. (2020) is located outside the CO snowline. Part of the CO ice desorbs and reacts to form HCO^+ , boosting the HCO^+ column density in their model. This is not seen in our models as CO is abundant throughout the disk instead of just in the dust gap.

6.4.1.2 CN, C₂H, and NO

The other modelled molecules follow a more intricate relation with the gas gap depth. Modelling of the HD 100546 disk shows that the locations of the rings seen in CN, C₂H, and NO are set by an interplay of gas column density between the two dust rings, and the resulting UV field. A deeper gas gap results in a lower gas column density and a higher UV field, which moves the peak CN, C₂H, and NO column density to smaller radii with increasing gap depths. Yet, the column density of these molecules is mostly insensitive to the gas gap depths for gaps shallower than $\delta_{\text{gas gap}} \sim 10^{-4}$. Only for the deepest gaps of $\delta_{\text{gas gap}} = 10^{-4} - 10^{-5}$, the rings in CN, C₂H, and NO are close in radius to those seen in the dust.

For shallower gaps, the CN, C₂H, and NO rings peak at various radii both inside (CN, C₂H) and outside (NO) the dust rings and do in general not coincide with the dust rings or each other. Additionally, the inner and outer rings of a particular molecule are predicted to have very different intensities. This is similar to the results of the MAPS program which observed CN and C₂H and found no general and significant correlation between structures in the dust and in the molecular line emission in four out of five disks, despite some overlapping features (Law et al. 2021a; Jiang et al. 2022). For the models with a gap of $10^{-1} - 10^{-3}$, the C₂H is predicted to peak inside the dust gap, similar to what is seen in the MWC 480 disk, the only MAPS disk where gas structures other than CO isotopologue emission do correlate with the dust and in the AS 209 disk (Alarcón et al. 2021). The location of the inner CN ring is only sensitive to gas gap depth if the gap is depleted by five orders of magnitude in gas. Therefore, chemistry is the main driver of the ring locations for shallow gas gaps.

In summary, the radial locations of the rings seen in the HD 100546 disk cannot be explained by a single gas gap depth as the CO isotopologue emission, HCN, and HCO^+ are best reproduced by a shallow gap ($\delta_{\text{gas gap}} = 10^{-1} - 10^{-2}$), whereas the double ring in CN and C₂H is only reproduced for a deep gas gap of $\delta_{\text{gas gap}} = 10^{-4} - 10^{-5}$, partially due vertical structure of the disk. Unlike HD 100546, the PDS 70 and IRS 48 disk both have a deep gas cavity just inside the molecular rings, forcing the line emission to be co-spatial with that of the dust. Therefore, if a physical gap is present in a disk, for example due to a massive planet, the molecular rings are likely also physical rather than chemical rings.

6.4.2 Chemistry in the rings and gap

In addition to physical rings in the disk density structure, chemical rings can also affect the observed emission. The chemistry across the gap may vary due to e.g., thermal and non-thermal sublimation of the ice mantles on the dust and UV shielding by small dust grains.

Water ice is likely present on the dust grains in the gap between the two dust rings in the HD 100546 disk (Honda et al. 2016). Photodesorption of this water ice could explain the gas-phase water seen from just outside the inner dust ring (starting from 35 – 40 au) to $\sim 300 - 400$ au (Du et al. 2017; van Dishoeck et al. 2021). The outer radius is not well constrained as the line profile that is used to constrain the emitting location is most sensitive to the inner radius rather than the outer radius (priv. comm. with M. R. Hogerheijde). Additionally, the line profile does not show evidence for a jump in the H_2O abundance at the location of the outer dust ring. Modelling of the cold water lines shows that gas-phase water has an abundance of 3×10^{-9} in the outer disk ($\sim 40 - 300$ au, Pirovano et al. 2022). Photodesorption of water ice is not included in the network used to predict the HCO^+ abundance in this work. As HCO^+ is destroyed by gas-phase water, the predicted HCO^+ abundance and emission are thus overestimated in the gas gap and also at larger radii out to 300 au. The difference between the modelled HCO^+ emission in the gap and the observed intensity could thus be due to this effect. As the gas gap does not contain large grains, water ice must be present on small grains.

Another mechanism that could lead to the rings seen in HCN, CN, C_2H , and HCO^+ and the detection of NO is grain surface chemistry. The temperature structure of the fiducial model suggests that the outer dust ring is sufficiently cold to have some HCN, CN, C_2H , NO, and CO freeze-out (see Fig. 6.4). Chemical networks including grain surface chemistry predict that the CO ice can be hydrogenated to H_2CO and CH_3OH , two molecules that are detected at this location in the disk (Walsh et al. 2014b; Booth et al. 2021c, 2023a). As the outer dust ring is too cold for thermal desorption of methanol, a non-thermal desorption processes could lead to a higher abundance. This process could also somewhat enhance the gas-phase abundance of HCN and NO by $10^{-3} - 10^{-4}$ times their ice abundance as both of these molecules have significant ice abundance ($> 10^{-7}$) in that region. The high NO abundance in the IRS 48 disk may have an origin in the ice (Leemker et al. 2023). C_2H and CN on the other hand do not have a high abundance in the ice and these emission rings thus require a different origin such as gas-phase formation or sublimation of larger molecules that form CN and C_2H after sublimation.

The sublimation of ices could also be reflected in the gas-phase C/O ratio as most ices are oxygen rich. The $\text{C}_2\text{H}/\text{C}^{17}\text{O}$ ratio is the most sensitive to the C/O ratio of the ratios investigated in this work. The CN/NO ratio has been suggested as a tracer of the gas-phase C/O ratio (Hily-Blant et al. 2010b; Daranlot et al. 2012; Le Gal et al. 2014). However, the models presented in this work show that the relation between CN/NO and C/O is more complicated than this. The reason for that is that a secondary layer of NO appears for C/O ratios larger than 1.

Our models suggest that the C/O ratio in the dust rings needs to be elevated from 0.4 to 0.8-1 to reproduce the HCN, CN, and C₂H emission in the dust rings, while the C/O in the gas gap is roughly consistent with the fiducial value of 0.4. The C/O in the rings is somewhat higher than the C/O of 0.5 derived from CS and SO by Keyte et al. (2023). In particular, the C₂H emission is very sensitive to the C/O ratio, consistent with what is found in earlier works (e.g., Bergin et al. 2016; Miotello et al. 2019; Bosman et al. 2021b). Additionally, the bright C₂H emission without having a deep gas gap points to an elevated C/O as also suggested in the AS 209 disk (Alarcón et al. 2021). The C₂H emission at the outer dust ring in HD 100546 could be due to freeze-out of CO and other oxygen bearing molecules in this region leading to a high C/O ratio (Öberg et al. 2011; van der Marel et al. 2021c, and Fig. 6.4). Two other mechanisms that could lead to an elevated C/O ratio are photoablation of carbonaceous grains and destruction of CO by He⁺ (e.g., Bergin et al. 2014; Anderson et al. 2017; Klarmann et al. 2018; Bosman et al. 2021b). The latter process is included in the chemical network. The low C₂H emission could indicate that the cosmic ray ionisation rate or the X-ray flux are higher than modelled in this disk. The spatial overlap between the dust rings and the C₂H emission suggests that destruction of carbon grains could contribute to the elevated C/O ratio. Instead of an enhancement in the C/H ratio, the O/H ratio could also be suppressed by, for example the freeze-out of oxygen bearing molecules such as CO and methanol. As the C/H and O/H ratios in the HD 100546 photosphere are consistent with the Solar values, the increase in the C/O ratio in the disk is likely local (Kama et al. 2016).

HCO⁺ not only traces the desorption of water, it is also sensitive to the ionization in the disk (e.g., Aikawa & Herbst 2001; Cleaves et al. 2015b). The observed column density ratios of HCO⁺/CO in the MAPS disks increases with radius or stays roughly constant at $\sim 10^{-6} - 10^{-4}$ (Aikawa et al. 2021). The general trend of an increasing ratio with radius is recovered by our models, but the observed values require a gas gap depth of $\sim 10^{-2} - 10^{-4}$. Comparing this to the HD 100546 disk shows that either the gas gap is shallow ($\delta_{\text{gas gap}} = 1 - 10^{-1}$) for the outer half of the gap, or that the ionisation rate in the modelled gap is too high.

The ratio of CN/HCN, tracing the UV indicates that the gap in HD 100546 needs to be $10^{-1} - 10^{-2}$ deep (see Fig. 6.B.7). Radial variations in the CN/HCN column density ratio likely trace radial variations in the UV field due to changes in the dust density structure due to enhanced HCN photodissociation compared to CN photodissociation (Bergner et al. 2021). The models presented in this work show a similar trend where the CN/HCN column density ratio peaks inside the gas gap and decreases in the outer dust ring (see Fig. 6.9). Similarly, this ratio has a low value of a few 10^{-2} in the inner dust ring where the small dust surface density is two orders of magnitude higher than that in the outer dust ring (see Fig. 6.1). The model without a gap in the gas and small dust grains but with a gap in the large dust grains does not show a peak in the CN/HCN column density ratio in the gap, indicating that this ratio is primarily sensitive to the small dust grains that have a larger opacity in the UV than the large dust grains.

In summary, the rings seen in the HD 100546 disk likely have a chemical origin as the gas density structure alone cannot explain the observed molecule rings.

The C/O ratio in the rings needs to be elevated above the fiducial value of 0.4 to reproduce the observed intensity in the C₂H, CN, [C I], and NO.

6.5 Conclusions

In this work we have modeled the HD 100546 disk to explore the radial location and intensity of molecular rings seen in HCN, CN, C₂H, NO, and HCO⁺ (Booth et al. 2023a). In particular, we investigated under which conditions these molecular rings overlap with those seen in the continuum. The fiducial model provides a good fit to the continuum emission and the emission of CO isotopologues with a deep dust and gas cavity inside 20 au and 15 au respectively, and a deep dust gap and a shallow gas gap from 40 – 175 au. The abundance of the other molecules of interest, HCN, CN, C₂H, and NO are predicted with a dedicated nitrogen network and that of HCO⁺ is predicted with the network presented in Leemker et al. (2021). In summary we find that:

1. The dust and CO isotopologue gas emission in the HD 100546 disk is reproduced by a model with a deep gas ($r < 15$ au) and dust cavity ($r < 20$ au), a deep dust gap and a shallow gas gap with a factor of ten less gas from 40 – 175 au. A gas gap deeper than one order of magnitude is excluded by the CO isotopologue data.
2. Thermochemical models predict that the molecular rings in HCN, CN, C₂H, NO, and HCO⁺ do not follow the dust rings in general, in contrast to the HD 100546 disk observations.
3. Introducing a gas gap in the models increases the UV field, and thus the HCN, CN, C₂H, and NO abundance within the gap. For gas gaps of one to approx. four orders of magnitude deep, the column density of CN, C₂H, and NO increases to above that in the model without a gas gap ($\delta_{\text{gas gap}} = 1$) in certain gap regions. For very deep gas gaps ($\delta_{\text{gas gap}} \sim 10^{-4} - 10^{-5}$) the molecular rings emit at a similar location as the dust rings.
4. An elevated C/O ratio mainly affects the total modelled intensity of [C I], HCN, CN, C₂H, and NO but not the radial location of the emission rings. The modelled CN and C₂H column density and emission increase by roughly one to two orders of magnitude, respectively, when the bulk model C/O ratio is increased from 0.99 to 1.01.
5. A lower background UV radiation field in the models reduces the column density of CN, C₂H, and NO and it increases that of HCN in the outer disk ($r > 100$ au).
6. The flaring index of the disk only has a minor effect on the height of the layer where a high CN abundance is seen, despite models with lower flaring indices being more flat.

7. To reconcile the observed ring locations with those predicted by models, a deep gas gap (factor $\leq 10^{-4}$) is needed to reproduce the double rings seen in CN and C₂H, while the diffuse HCN and HCO⁺ emission between the dust rings is best reproduced by a model with $10^{-2} - 10^{-3}$ times less gas.
8. The model predicts ring-shaped NO emission that is not seen in the observations. A lower background UV field by a factor of ten reduces the outer NO ring and creates a double ring seen in C₂H close to the dust rings.
9. The observed intensities of the [C I], CN, and C₂H are only reproduced by the models with an elevated C/O of $\sim 0.8 - 1.2$. Especially, the C₂H emission requires C/O = 1.00.

This work shows that thermochemical models do not predict molecular rings to be co-spatial with those seen in the dust in general. The constraints from modelling multiple molecules across a gas gap provides a first step towards a full picture of the chemical makeup of the planet-forming material. Multi-line observations of multiple molecules at high spatial and spectral resolution and sensitivity are needed to better constrain the layer from which these molecules emit. These observations can then be used to test thermochemical models and derive the chemical composition of the planet-forming material.

6.6 Acknowledgements

The authors would like to thank Luke Keyte and Dylan T. Natoewal for the useful discussions on the DALI modelling. In addition, Michiel Hogerheijde is thanked for the discussion on water in the HD 100546 disk. This work is supported by grant 618.000.001 from the Dutch Research Council (NWO). Astrochemistry in Leiden is supported by funding from the European Research Council (ERC) under the European Union's Horizon 2020 research and innovation programme (grant agreement No. 101019751 MOLDISK) and by the Netherlands Research School for Astronomy (NOVA).

This paper makes use of the following ALMA projects: 2011.0.00863.S, 2015.1.00806.S, 2016.1.00344.S, 2018.1.00141.S, 2021.1.00738.S. ALMA is a partnership of ESO (representing its member states), NSF (USA) and NINS (Japan), together with NRC (Canada), MOST and ASIAA (Taiwan), and KASI (Republic of Korea), in cooperation with the Republic of Chile. The Joint ALMA Observatory is operated by ESO, AUI/NRAO and NAOJ. The National Radio Astronomy Observatory is a facility of the National Science Foundation operated under cooperative agreement by Associated Universities, Inc.

Table 6.A.1: Continuum wavelengths and molecular transitions.

Molecule	Transition	beam	$n_{\text{crit}}(50 \text{ K})$	ref.
continuum	0.9 mm (high res.)	$0''.05 \times 0''.03$ (34°)		1
continuum	0.9 mm (moderate res.)	$0''.38 \times 0''.30$ (31°)		2
^{12}CO	$J = 2 - 1$	$0''.097 \times 0''.077$ (-16°)	2.7×10^3	3
^{12}CO	$J = 3 - 2$	$0''.35 \times 0''.23$ (60°)	9.2×10^3	2
^{12}CO	$J = 7 - 6$	$0''.23 \times 0''.17$ (30°)	1.2×10^5	4
^{13}CO	$J = 2 - 1$	$0''.098 \times 0''.077$ (-15°)	2.3×10^3	3
C^{18}O	$J = 2 - 1$	$0''.097 \times 0''.076$ (-13°)	2.3×10^3	3
C^{17}O	$J = 3 - 2$	$0''.39 \times 0''.31$ (29°)	8.5×10^3	2
[C I]	$^3P_2 - ^3P_1$	$0''.21 \times 0''.16$ (28°)	1.4×10^3	5
HCN	$J = 4 - 3$	$0''.34 \times 0''.23$ (60°)	1.4×10^7	2
CN	$3_{0,7/2,7/2} - 2_{0,5/2,5/2}$	$0''.38 \times 0''.30$ (29°)	3.8×10^6	2
CN	$3_{0,7/2,9/2} - 2_{0,5/2,7/2}$	$0''.38 \times 0''.30$ (29°)	3.8×10^6	2
CN	$3_{0,7/2,5/2} - 2_{0,5/2,3/2}$	$0''.38 \times 0''.30$ (29°)	3.8×10^6	2
$\text{C}_2\text{H}^{(a)}$	$4_{9/2,5} - 3_{7/2,4}$	$0''.37 \times 0''.30$ (27°)	1.3×10^6	2
$\text{C}_2\text{H}^{(a)}$	$4_{9/2,4} - 3_{7/2,3}$	$0''.37 \times 0''.30$ (27°)	1.2×10^6	2
$\text{NO}^{(a)}$	$4_{1,7/2,9/2} - 3_{-1,5/2,7/2}$	$0''.47 \times 0''.37$ (31°)	2.7×10^4	2
$\text{NO}^{(a)}$	$4_{1,7/2,7/2} - 3_{-1,5/2,5/2}$	$0''.47 \times 0''.37$ (31°)	2.4×10^4	2
$\text{NO}^{(a)}$	$4_{1,7/2,5/2} - 3_{-1,5/2,3/2}$	$0''.47 \times 0''.37$ (31°)	2.4×10^4	2
HCO^+	$J = 4 - 3$	$0''.34 \times 0''.23$ (60°)	2.6×10^6	2

Notes. ^(a) All components of a single molecule are added together assuming the emission is optically thin. The critical densities are calculated assuming that the main collision partner is H_2 . References: 1. Pineda et al. (2019), 2. Booth et al. (2023a), 3. Pérez et al. (2020) and Wölfer et al. (2023a), 4. Wölfer et al. (2023a), 5. This work.

Appendix

6.A Observed lines

The integrated intensity map and the spectrum of the [C I] emission in the HD 100546 disk is presented in Fig. 6.A.1. An overview of the observations used in this work is presented in Table 6.A.1. In addition to the observations, the critical density for each line is listed as some molecules are found to emit from elevated disk layers below the critical density.

6.B DALI

6.B.1 Model setup

6.B.1.1 Radial and vertical structure

Radially, the gas density follows the solution for a viscously evolving disk model (Lynden-Bell & Pringle 1974; Hartmann et al. 1998; Andrews et al. 2011):

$$\Sigma_{\text{gas full}} = \Sigma_c \left(\frac{r}{r_c} \right)^{-\gamma} e^{-(r/r_c)^{2-\gamma}}, \quad (6.4)$$

with $\Sigma_{\text{gas full}}$ the gas surface density of a full disk, Σ_c/e the gas surface density at the characteristic radius r_c , r the radius, and γ the power law index of the surface density profile. The surface density is defined from the sublimation radius r_{subl} to the outer radius of the disk $r_{\text{out, disk}}$. Assuming a typical dust sublimation temperature of 1500 K, the sublimation radius is located at $\sim 0.07 \text{ au} \times \sqrt{L/L_\odot}$, with L the luminosity of the central star (Dullemond et al. 2001). For the $36 L_\odot$ HD 100546, this corresponds to 0.4 au.

Vertically, we assume that the gas follows a Gaussian distribution with the scale height h given by

$$h = h_c \left(\frac{r}{r_c} \right)^\psi, \quad (6.5)$$

with h_c the scale height at r_c and ψ the flaring index.

The dust in DALI is modeled using a small dust population and a large dust population. Both populations have a minimum grain size of 5 nm but the small grains have a maximum size of 1 μm , whereas the large grains go up to 1 mm. An MRN distribution with an index of -3.5 is used to set the grain sizes a within

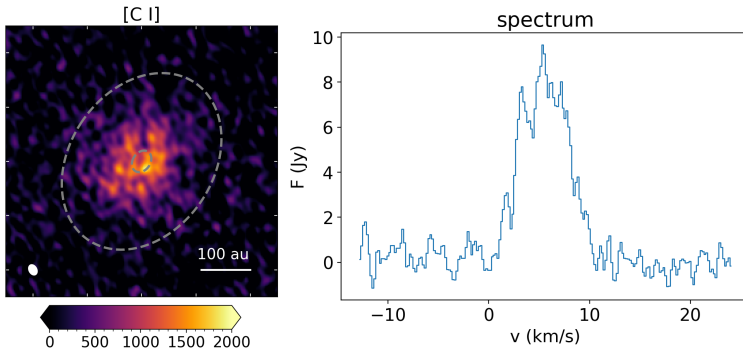


Figure 6.A.1: Observations of [C I] in the HD 100546 disk. Left: integrated intensity map. The grey dashed lines indicate the dust rings in the HD 100546 disk. The beam is indicated in the bottom left corner and a 100 au scale bar is shown in the bottom right corner. Right: spectrum.

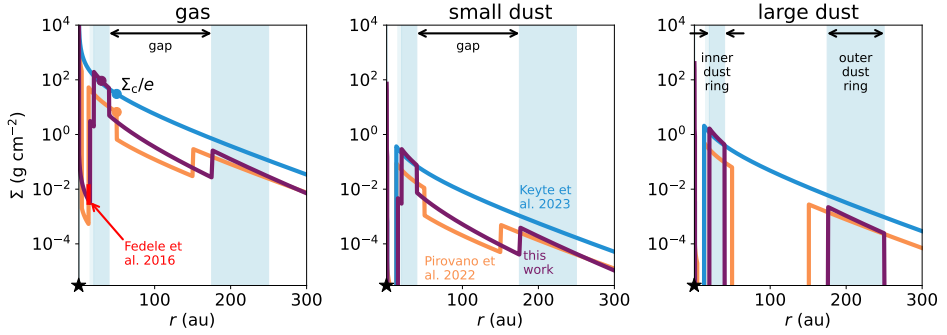


Figure 6.B.1: Surface density of the gas (left), small dust (middle), and large dust (right) in three models for the HD 100546 disk. The blue lines show the full gas disk model presented in Keyte et al. (2023), the orange lines show the model presented in Pirovano et al. (2022), and the purple lines show the model presented in this work. The shaded blue background indicates the dusty inner disk and the dust rings modelled in this work. The surface density Σ_c/e at r_c is indicated with a scatter point in the left panel.

these populations (Mathis et al. 1977). Furthermore, the mass ratio of the large grain population compared to that of the small grains is set by f_{ls} such that the small and large dust in a full disk follow:

$$\Sigma_{s \text{ dust full}} = \frac{(1 - f_{ls})\Sigma_{\text{gas full}}}{\Delta_{gd}} \quad (6.6)$$

$$\Sigma_{l \text{ dust full}} = \frac{f_{ls}\Sigma_{\text{gas full}}}{\Delta_{gd}}, \quad (6.7)$$

with Δ_{gd} the global gas-to-dust mass ratio. A comparison of the radial structure used in this work to those used by Pirovano et al. (2022) and Keyte et al. (2023) is presented in Fig. 6.B.1.

Edge-on disks show that the large dust is settled to the disk midplane (Villenave et al. 2020). Therefore, the vertical scale height of the large dust is reduced by a settling parameter χ . Thus, the small and large dust are not following the same radial and vertical distributions and the average grain size is calculated per cell, which is used for further calculations.

6.B.1.2 Initial conditions of the chemical networks

The chemical networks are started using mostly molecular initial conditions. Initially, all volatile carbon is locked up in CO and all remaining oxygen is locked up in H₂O such that the C/O ratio is 0.4. In the case of a C/O ratio larger than 1, all oxygen is initialized in the form of CO and the remaining carbon is put in as CH₄. The precise initial partition of nitrogen over N, N₂, and NH₃ in protoplanetary disks is unknown, therefore we rescale the predictions of dark cloud models at 0.3 Myr (N: N₂: NH₃: total number of N atoms = 0.48 : 0.19 : 0.13 : 1;

Walsh et al. 2015). Finally, hydrogen is mainly in H_2 when the model is initialised. An overview of the initial conditions is presented in Table 6.B.1. The chemistry is evolved to the age of the HD 100546 disk of 5 Myr (Arun et al. 2019) and a cosmic ray ionisation rate consistent with that found in other protoplanetary disks of 10^{-18} s^{-1} is adopted (Aikawa et al. 2021).

Table 6.B.1: DALI model parameters

Model parameter	value	Description
<i>Physical structure</i>		
$r_{\text{subl}} - r_{\text{dust cav in}}$	0.4 – 1 au	dusty inner disk
$\delta_{\text{gas cav}}, \delta_{\text{s dust}}, \text{in}, \delta_1^{\text{dust}}, \text{in}$	$10^{-5}, 10^{-2}, 10^{-2}$	surface density drop for $r_{\text{subl}} < r < r_{\text{cav in}}, \text{dust}$
$r_{\text{dust cav in}} - r_{\text{gas cav out}}$	1 – 15 au	gas cavity
$\delta_{\text{gas cav}}, \delta_{\text{s dust cav}}, \delta_1^{\text{dust cav}}$	$10^{-5}, 10^{-10}, 10^{-10}$	surface density drop for $r_{\text{dust cav in}} < r < r_{\text{gas cav out}}$
$r_{\text{gas cav out}} - r_{\text{dust cav out}}$	15 – 20 au	region outside gas cavity but inside dust cavity
$\delta_{\text{gas cav edge}}, \delta_{\text{s dust cav edge}}, \delta_1^{\text{dust cav edge}}$	$10^{-2}, 10^{-2}, 10^{-10}$	surface density drop for $r_{\text{gas cav out}} < r < r_{\text{dust cav out}}$
$r_{\text{gap in}} - r_{\text{gap out}}$	40 – 175 au	gap
$\delta_{\text{gas gap}}, \delta_{\text{s dust gap}}, \delta_1^{\text{dust gap}}$	$10^{-1}, 10^{-1}, 10^{-10}$	surface density drop for $r_{\text{gap in}} < r < r_{\text{gap out}}$
$r_1 \text{ dust out} - r_{\text{out}}$	250 – 1000 au	disk region outside the second ring
$\delta_{\text{gas out}}, \delta_{\text{s dust out}}, \delta_1^{\text{dust out}}$	1, 1, 10^{-10}	surface density drop for $r_1 \text{ dust out} < r < r_{\text{out}}$
r_{c}	30 au	Characteristic radius of the surface density profile
Σ_{c}	250 g cm^{-2}	Sets the gas surface density at the characteristic radius r_{c}
M_{disk}	$5 \times 10^{-2} M_{\odot}$	Mass of the disk
γ	1.1	Power law index of the surface density profile
h_{c}	0.1	Scale height angle at the characteristic radius r_{c}
ψ	0	Flaring index of the disk surface density
PAH abundance	0.1	Gas-phase abundance of PAHs w.r.t. to ISM value
<i>Dust properties</i>		
χ	0.2	Settling of large grains
f_{ls}	0.85	Mass-fraction of grains that is large

Table 6.B.1: Continued.

Model parameter	value	Description
$\Delta_{\text{gas/dust}}$	100	Gas-to-dust mass ratio
<i>Stellar properties</i>		
M_{\star}	$2.5 M_{\odot}$	Mass of the central star
L_{\star}	$36 L_{\odot}$	Luminosity of the central star
L_X	$7.9 \times 10^{28} \text{ erg s}^{-1}$	X-ray luminosity of the central star
T_X	$7 \times 10^7 \text{ K}$	Effective temperature of the X-ray radiation
$\zeta_{\text{c.r.}}$	$1 \times 10^{-18} \text{ s}^{-1}$	Cosmic ray ionization rate
<i>Observational geometry</i>		
i	41°	Disk inclination (0° is face-on)
d	108.1 pc	Distance to the star
<i>Chemistry</i> ⁽¹⁾		
H	5.2×10^{-5}	
He	1.4×10^{-1}	
N	3.0×10^{-5}	
H ₂	5.0×10^{-1}	
H ₂ O	1.9×10^{-4}	
CO	1.3×10^{-4}	
N ₂	1.2×10^{-5}	
NH ₃	8.1×10^{-6}	

Table 6.B.1: Continued.

Model parameter	value	Description
Mg ⁺	1.0×10^{-11}	
Si ⁺	1.0×10^{-11}	
S ⁺	1.0×10^{-11}	
Fe ⁺	1.0×10^{-11}	
t_{end}	5 Myr	

Notes. ⁽¹⁾ Abundance w.r.t. the total number of hydrogen atoms. All molecules start as gas-phase species.

6.B.2 Model predictions

6.B.2.1 Emission profiles and emitting heights of CO isotopologues

The azimuthally averaged radial profiles of the CO isotopologue emission are presented in Fig. 6.B.2. The models with a drop in gas density and small dust density of 1 (no drop) up to 10^{-5} are shown in the same figure with the colored lines. The model without a drop in the gas and small dust density overpredicts the $C^{18}O$ and $C^{17}O$ emission that are the most optically thin and thus the most sensitive to the gas column density. On the other hand, the models with a deeper gap (10^{-2} , 10^{-3}) than the fiducial model (10^{-1}), underpredict the $C^{18}O$ and $C^{17}O$ emission in the gap. Additionally, these models show a clear gap in the brighter ^{12}CO and ^{13}CO lines that is not seen in the observations. This cannot be due to the limited spatial resolution of the observations as the gas gap is fully resolved with 4 beams across the gas gap for $C^{17}O$, the lowest spatial resolution line in this work, and 14 for $C^{18}O$ which has the highest spatial resolution. Outside the gas gap, at the outer dust ring, the $C^{18}O$ emission is overpredicted. However, a lower gas and thus CO isotopologue column density lowers the $C^{17}O$ column density in the gas gap to a value below its minimum value to self-shield. Therefore, a model that fits the $C^{18}O$ in that region will not reproduce the shelf in $C^{17}O$. Therefore, the CO isotopologue observations show that the gas density is depleted by at most a factor of 10^{-1} between the two dust rings under the assumption that the gas and dust gap have the same widths.

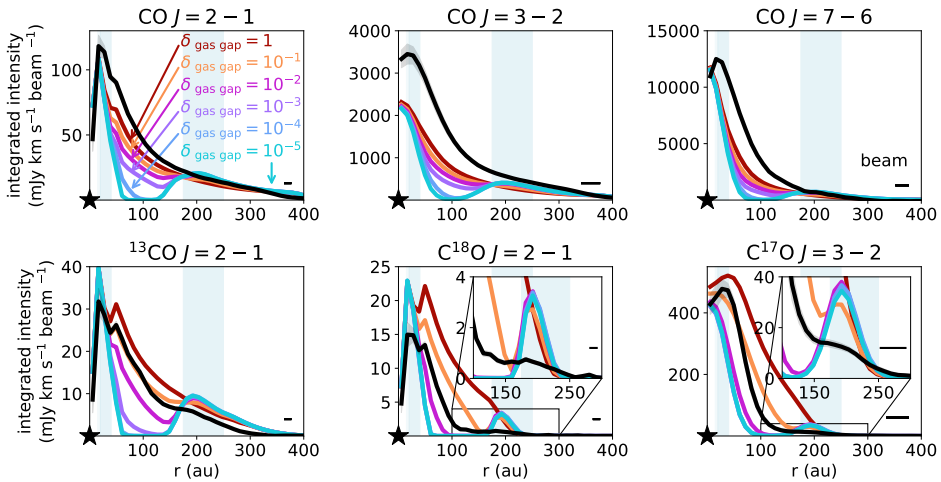


Figure 6.B.2: Azimuthally averaged radial profiles of the dust and CO isotopologue emission observed in the HD 100546 disk (black) together with model predictions for different gaps. In the models, the gas density in the gap (40 – 175 au) is reduced by a factor of 1 (no gap; dark red), 10^{-1} (orange), 10^{-2} (pink), 10^{-3} (purple), 10^{-4} (blue), and 10^{-5} (very deep gap; light blue). For all these models, the drop in the small dust density follows that of the gas. The beam is indicated with the horizontal bar in the bottom right corner of each panel.

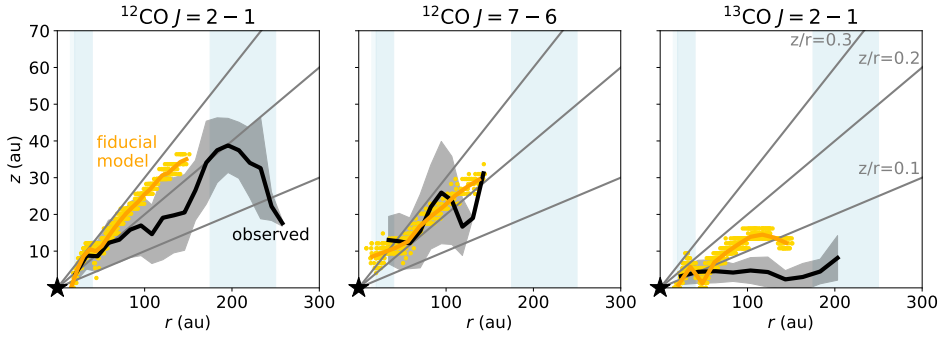


Figure 6.B.3: Emitting heights of the $^{12}\text{CO } J = 2 - 1$, and $J = 7 - 6$, and the $^{13}\text{CO } J = 2 - 1$ transition. The observed emitting heights are presented in black and those of the fiducial model in orange.

The emitting heights of the $^{12}\text{CO } J = 2 - 1$ and $J = 7 - 6$ transitions together with that of the $^{13}\text{CO } J = 2 - 1$ transition are presented in Fig. 6.B.3. These emitting heights are derived using the ALFAHOR package by masking the individual channels after visually inspecting the data (Paneque-Carreño et al. 2023). Wölfer et al. (2023a) found evidence for an asymmetry in the vertical structure between the blue and red shifted sides of this disk. As the DALI models used in this work are azimuthally symmetric, the observed emitting heights are presented as an average of both disk sides.

The fiducial model reproduces the observed emitting height of the $^{12}\text{CO } J = 2 - 1$ and $J = 7 - 6$ transitions within 1.5σ for a radius up to 150 au. The lack of vertical segregation between different transitions of one molecule is seen in other DALI models as well (Paneque-Carreño in prep.). Finally, the ^{13}CO emission is seen very close to the disk midplane at a height of only a few au in the observations. The model reproduces the trend that the ^{13}CO emission comes from deeper disk layers than the ^{12}CO , and is consistent within $\sim 2\sigma$ from the observations up to 150 au.

6.B.2.2 Emission profiles and column densities of [C I], HCN, CN, C_2H , NO, and HCO^+ for different gas gaps

The azimuthally averaged radial profiles for the HCN, CN, C_2H , NO, and HCO^+ moment 0 maps presented in Fig. 6.5 are presented in Fig. 6.B.4. Instead of the C^{18}O emission, the profile for the atomic carbon line is presented in the top left corner. The colored lines indicate the models for different gas gap depths between the two dust rings, identical to those in e.g. Fig. 6.B.2. The rings seen in the observations (black) do not coincide with those seen in the models in general. Additionally, the modelled [C I] emission inside 200 au is up to an order of magnitude weaker than what is observed. At larger radii, the model slightly overpredicts the observations, but emission at these scales may be missing due to the small maximum recoverable scale ($2''$ diameter, 108 au radius) of the observation. As the models predict that the molecules are abundant in an elevated layer at

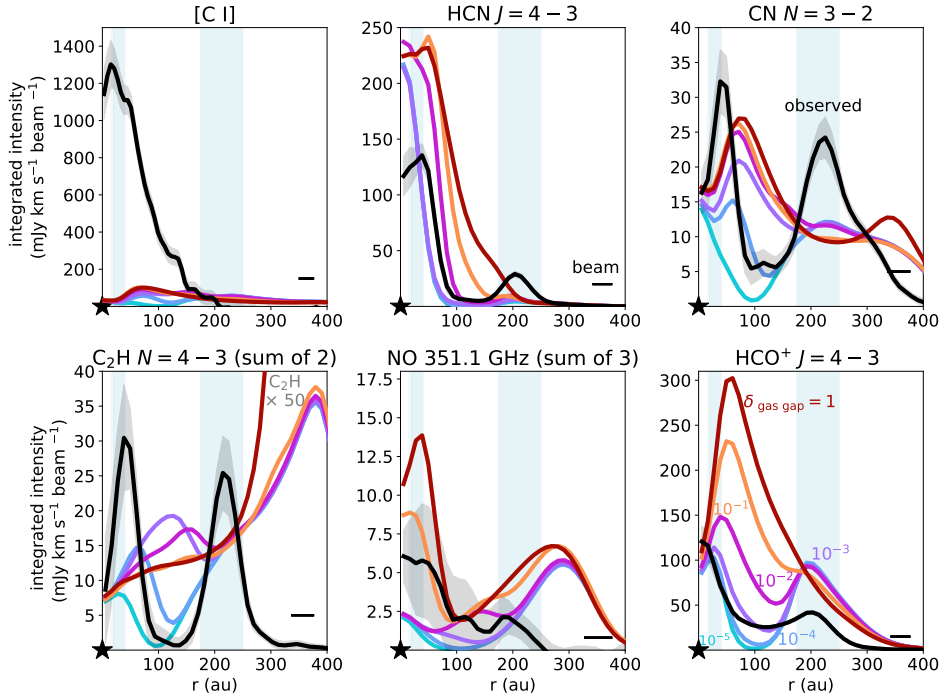


Figure 6.B.4: Azimuthally averaged radial profiles of the [C I], HCN, CN, C₂H, NO, and HCO⁺ emission predicted by models with a gas gap depth of 1 (no gap; dark red), 10⁻¹ (orange), 10⁻² (pink), 10⁻³ (purple), 10⁻⁴ (blue), and 10⁻⁵ (very deep gap; light blue). The C₂H emission is increased by a factor of 50 for all models to show it on the same scale as the observations. The peak C₂H intensity of the full disk model is 2 mJy km s⁻¹ beam⁻¹. The small dust density is dropped by the same factor in the gap. The observed intensities are indicated with the black lines.

$z/r \sim 0.2 - 0.3$, the disk inclination of 41° causes deprojection effects that wash out some of the rings in the CN and move those in C₂H to the location of the outer dust ring. Therefore, the azimuthally averaged radial profiles predicted by a face-on disk model are presented in Fig. 6.B.5.

Similar to the trend seen for the HCO⁺ column density, the HCO⁺ emission in the gap decreases for deeper gap depths. Even for the shallowest gas gap ($\delta_{\text{gas gap}} = 10^{-1}$), a shallow gap and a ring are seen in the HCO⁺ emission. For deeper gas gaps, the double ring nature of the HCO⁺ emission becomes more pronounced (see Fig. 6.B.4 for a more quantitative figure). The modelled intensity in the outer ring lays within a factor of 2.5 of the data for all models. To reproduce the diffuse emission observed in the gas gap, a model with a moderately deep gap of $10^{-2} - 10^{-3}$ is needed. These models as well as those, with even deeper gap of $10^{-4} - 10^{-5}$ match the intensity of the HCO⁺ in the gas cavity within 2.5σ , though the models predict a ring at 30 – 40 au instead of centrally peaked emission.

The CN emission shows a bright inner ring just outside the inner dust ring

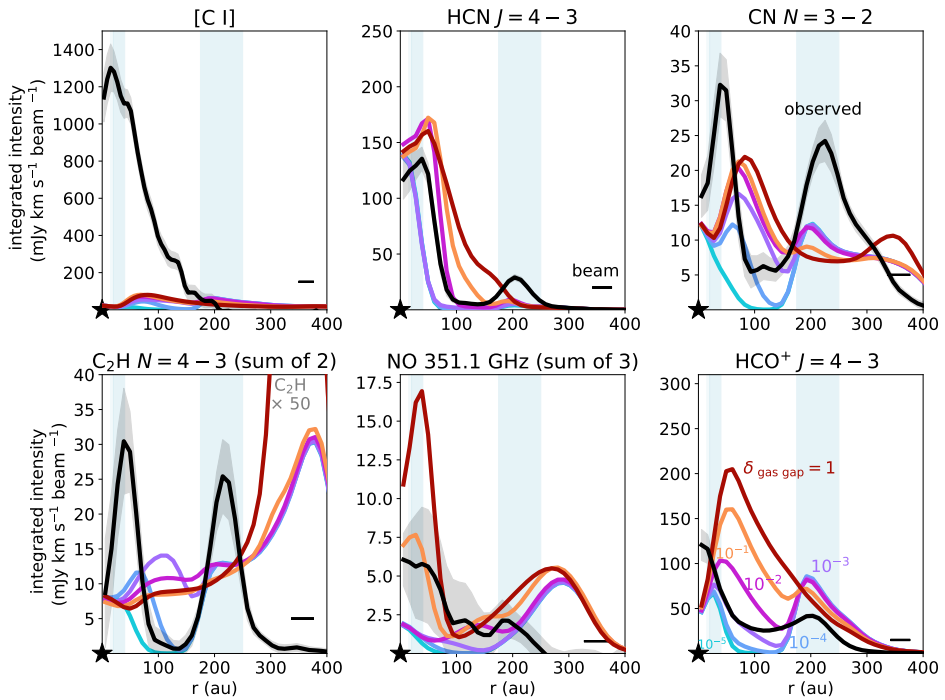


Figure 6.B.5: Same as Fig. 6.B.4 but then for face-on disk. The modelled C_2H emission is increased by a factor of 50 to show it on the same scale as the observations.

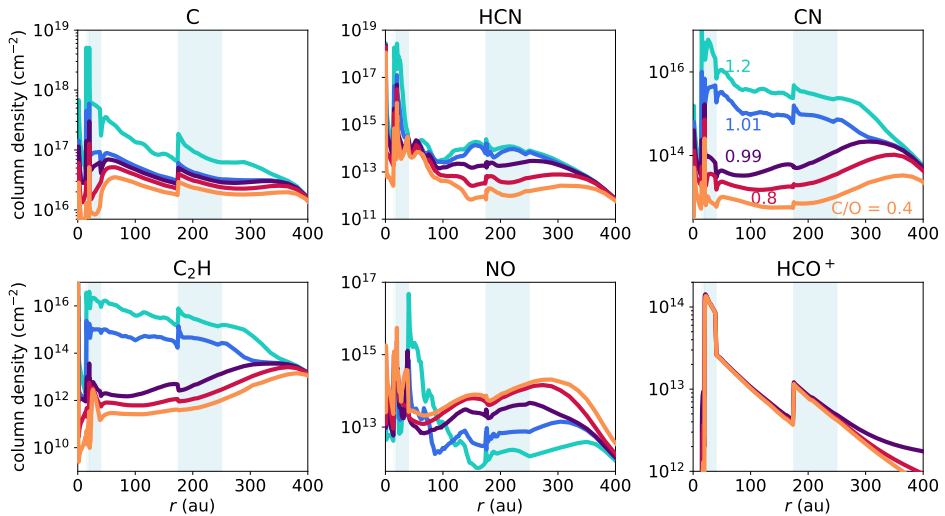


Figure 6.B.6: Column densities of the molecular lines studied in this work for different C/O ratios.

and diffuse emission outwards. For gaps up to $\delta_{\text{gas gap}} = 10^{-3}$, the CN intensity stays more or less constant. For deeper gaps, the CN intensity follows the trends seen in the column density and the inner ring becomes weaker. The models with gaps deeper than 10^{-2} all show emission from an elevated layer as the outer ring consists of two ellipses that are offset along the disk minor axis. This is not seen in the data where the outer CN ring is centred at the position of the star. Apart from this, the model with a deep gap of 4 orders of magnitude less gas resembles the observations quite closely as two distinct rings with an intensity within a factor of ~ 3 of the observations are seen.

C_2H emits as a bright outer ring seen at 375 au due to the high column density in this region. This is much further out than the second ring seen in the data and not affected by the depth of the gas gap. Inside the gap, a ring at low intensity is seen. This ring follows the trend seen in the column density, moves inwards, and brightens as the gas gap becomes deeper. The bright ring seen in the model with a 10^{-4} deep gas gap is only peaks one beam further out than the ring seen in the observations but the modelled intensity is a factor of 40 too low. The inward travelling ring is also seen in the NO emission causing a very bright inner ring for the two models with the deepest gas gaps. The outer ring seen just outside the outer dust ring in the models is not detected in the observations.

Finally, the HCN shows a bright inner ring with an intensity within a factor of two of the observations for the models with a shallow gas gap. For the models with a gap deeper than 10^{-2} a gap and then a very weak ($\lesssim 5\%$) ring at the location of the outer dust ring are seen as highlighted by the white contours in Fig. 6.8. This ring has an intensity of only 3 – 5 times weaker than what is observed.

6.B.2.3 Column densities of [C I], HCN, CN, C_2H , NO, and HCO^+ for different C/O ratios

The column densities of C, HCN, CN, C_2H , NO, and HCO^+ for different C/O ratios are presented in Fig. 6.B.6. The column densities of the molecules that contain a carbon atom but no oxygen, C, HCN, CN, and C_2H , all increase with increasing C/O. In particular, the CN and C_2H are sensitive to a C/O ratio increasing from 0.99 to 1.01 as their column densities increase by one and two orders of magnitude, respectively. The NO molecule, that only carries an oxygen atom and no carbon, shows the opposite trend in general. The only exception to this is the high NO column density just outside the inner dust ring in the models with $\text{C/O} > 1$. Finally, the HCO^+ is not sensitive to the C/O ratio in most disk regions as it carries both oxygen and carbon atoms.

6.B.3 Molecular ratios

6.B.3.1 Column density ratios for different gap depths

The HCO^+/CO ratio for gaps up to two orders of magnitude deep is mainly driven by the CO density that is directly proportional to the gas density and the HCO^+ density that goes with the square root of the gas density (see Figs. 6.6 and 6.9). For deeper gaps, CO photodissociation drives the HCO^+/CO ratio up.

Even though no HCO^+ photodissociation is included in the small network, its photodissociation rate is 44 times lower than that of CO (Heays et al. 2017). Therefore, the HCO^+/CO ratio is most sensitive to the gas density.

The $\text{C}_2\text{H}/\text{CO}$ ratio is primarily driven by the drop in the CO column density for gaps up to 10^{-3} as the C_2H column density only starts to drop steeply for gaps deeper than that. This causes the $\text{C}_2\text{H}/\text{CO}$ ratio to saturate at a few 10^{-3} in the outer regions of the 10^{-5} deep gas gap. The CN/HCN ratio rapidly increases when the gap depth is lowered from 10^{-1} to 10^{-2} as the midplane HCN component is removed inside of ~ 80 au. For deeper gaps, the ratio settles between a value of 10 – 100 inside the gap. Outside the gap, CN is a factor of ten more abundant than HCN.

In contrast to the former ratios, the CN/NO ratio is almost independent of gap depths for a disk with no gas gaps and gaps with up to two orders of magnitude less gas. This is due to the CN and NO column density that are both insensitive to the gap depths for these models. For deeper gaps, both the CN and the NO column density decrease as the gas gap becomes deeper but the CN column density does so at a slower rate than that of NO. Therefore, the CN/NO column density ratio is higher inside the gap than outside.

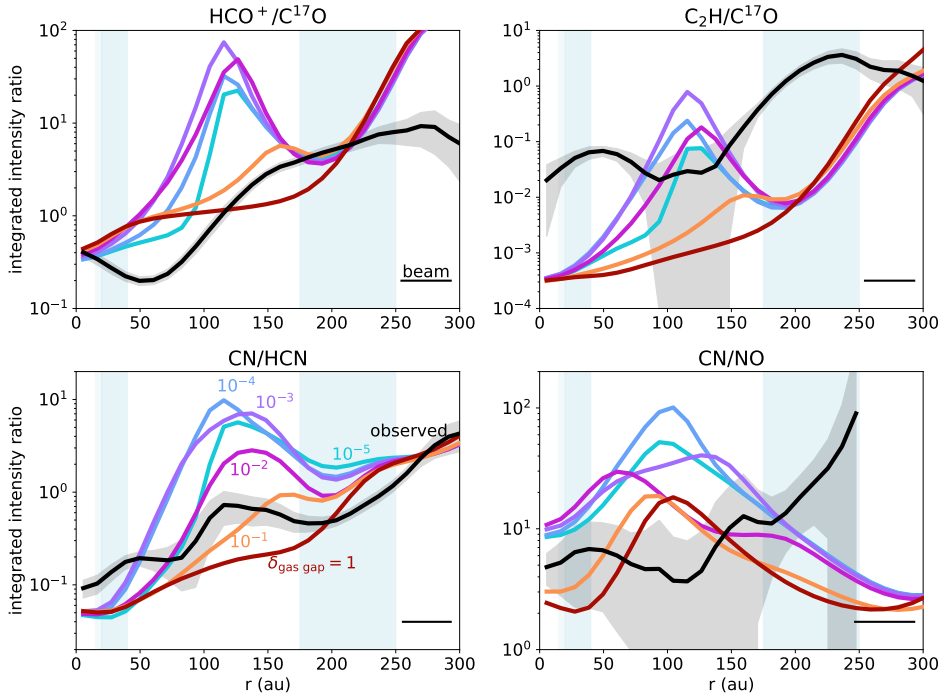


Figure 6.B.7: Emission line ratios of HCO^+/CO (top left), $\text{C}_2\text{H}/\text{CO}$ (top right), CN/HCN (bottom left), and CN/NO (bottom right) for different gas gap depths.

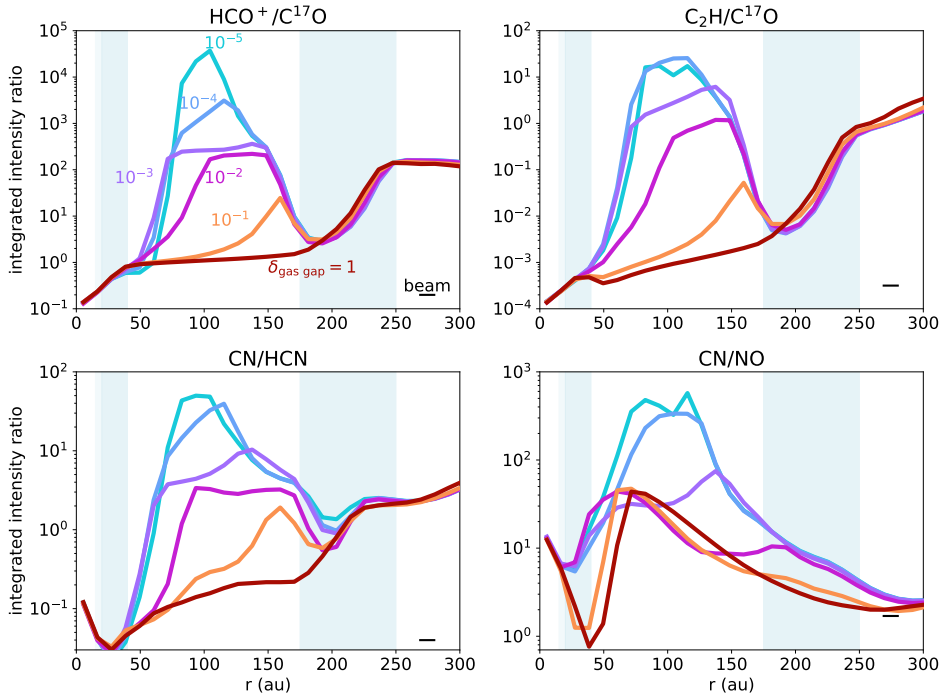


Figure 6.B.8: Same as Fig. 6.B.7 but then for a small beam of $0''.1$.

6.B.3.2 Emission line ratios for different gap depths

The corresponding figure for the emission lines is presented in Fig. 6.B.7. For each ratio, the profile of the molecule at the highest spatial resolution is smoothed to the resolution of the image at lower resolution. The modelled ratios of HCO^+/CO , $\text{C}_2\text{H}/\text{CO}$, CN/HCN , and CN/NO all peak inside the gas gap if the gas gap is at least 10^{-1} deep. The column density ratio increases with gap depth for most regions inside the gas gap, however, the ratio of the integrated intensity does not. This is due to the beam size of the observations. The size and orientation of the beam is such that the dust gap is sampled by only ~ 2 beams across the disk minor axis. Therefore, the line ratio in the gap is dominated by the bright emission at the gap edges. If the models are convolved with a 3–4 times smaller beam of $0''.1$, the gap depth can be traced up to a very deep gas gap of 10^{-4} times less gas, see Fig. 6.B.8.

All models reproduce the $\text{HCO}^+/\text{C}^{17}\text{O}$ ratio seen inside the inner dust ring ($r < 20$ au) and at 200 au where the outer dust ring is located. The observations show that this ratio first decreases in the gap and then increases, whereas the models with a gas gap show a peak at 125 au ($\delta_{\text{gas gap}} = 10^{-2} - 10^{-5}$) or 150 au ($\delta_{\text{gas gap}} = 10^{-1}$). The fiducial model with a gap of only one order of magnitude best reproduces the observed ratio outside 100 au. The other models show a ratio of $\text{HCO}^+/\text{C}^{17}\text{O}$ that is too high, indicating that the ionisation is too high or the

abundance of gas-phase water as traced by HCO^+ is too low in the gap. The latter is consistent with the detection of cold, gas-phase water lines originating from $\sim 40 - 300$ au in this disk (van Dishoeck et al. 2021; Pirovano et al. 2022). This is because the modelled HCO^+ abundance does not account for photodesorbed water.

The observed $\text{C}_2\text{H}/\text{C}^{17}\text{O}$ ratio peaks just outside the inner dust ring and at the outer edge of the outer dust ring. The models with a gas gap show the opposite behaviour where a peak at ~ 100 au in the $\text{C}_2\text{H}/\text{C}^{17}\text{O}$ ratio is predicted. Only the model without a drop in the gas density reproduces the overall trend of the observations with an offset of two orders of magnitude. This offset is driven by the modelled C_2H emission being too weak by that same factor.

The ratio of CN/HCN increases with radius, with a peak seen inside the gas gap and a decrease in the outer dust ring. The models with a gas gap predict the same trend across the disk, with the ratio agreeing within a factor of ~ 4 for the models with gaps up to 10^{-2} . The observations are most consistent with a gap depth of one to two orders of magnitude. The UV field in the models with deeper gas gaps is too intense to reproduce the CN/HCN ratio.

Finally, the CN/NO ratio is presented in the bottom right panel of 6.B.7. The CN/NO ratio of ~ 5 at the inner dust ring is reproduced by the models that do not have a very deep gas gap of $10^{-4} - 10^{-5}$. For the latter models, the NO intensity is much higher, lowering the CN/NO ratio. In the outer dust ring the observed ratio is ~ 10 , whereas the models underpredict this by an order of magnitude.

In summary, the line ratios of HCO^+/CO , $\text{C}_2\text{H}/\text{CO}$, and CN/HCN at the spatial resolution of the observations are only sensitive to the gas gap depths up to a gap with two orders of magnitude less gas. The latter ratio is well reproduced by the models, whereas the $\text{C}_2\text{H}/\text{C}^{17}\text{O}$ is not due to the weak C_2H emission. The $\text{HCO}^+/\text{C}^{17}\text{O}$ ratio can be used to trace gas gaps that are up to two orders of magnitude depleted in gas.

6.B.3.3 Column density and line ratios for different C/O ratios

The column density ratios for various molecules as function of the C/O ratio are presented in Fig. 6.B.9. The corresponding emission line ratios are presented in Fig. 6.B.10. The $\text{HCO}^+/\text{C}^{17}\text{O}$ ratio presented in the top left corner does not depend on the C/O ratio of the gas for most disk regions. Only outside the outermost dust ring, the $\text{HCO}^+/\text{C}^{17}\text{O}$ ratio decreases by one order of magnitude down to the observed value for a C/O of 0.99 instead of 0.4.

The $\text{C}_2\text{H}/\text{C}^{17}\text{O}$ ratio is driven by the C_2H emission that increases steeply with an increasing C/O ratio. Between the two dust rings, the observed $\text{C}_2\text{H}/\text{C}^{17}\text{O}$ is best explained by a model with a C/O just below 1 at 0.99, whereas in the outer dust ring the model with a C/O of 1.01 is close to the observed ratio. The C/O ratio greatly affects the value of the $\text{C}_2\text{H}/\text{C}^{17}\text{O}$ ratio, but it does not change the location of the peaks and dips in the profile. Therefore, a global change in the C/O ratio alone cannot explain the observations.

Increasing the C/O ratio increases the CN intensity more than it does so for the HCN . Therefore, the CN/HCN ratio increases with increasing C/O ratio. The

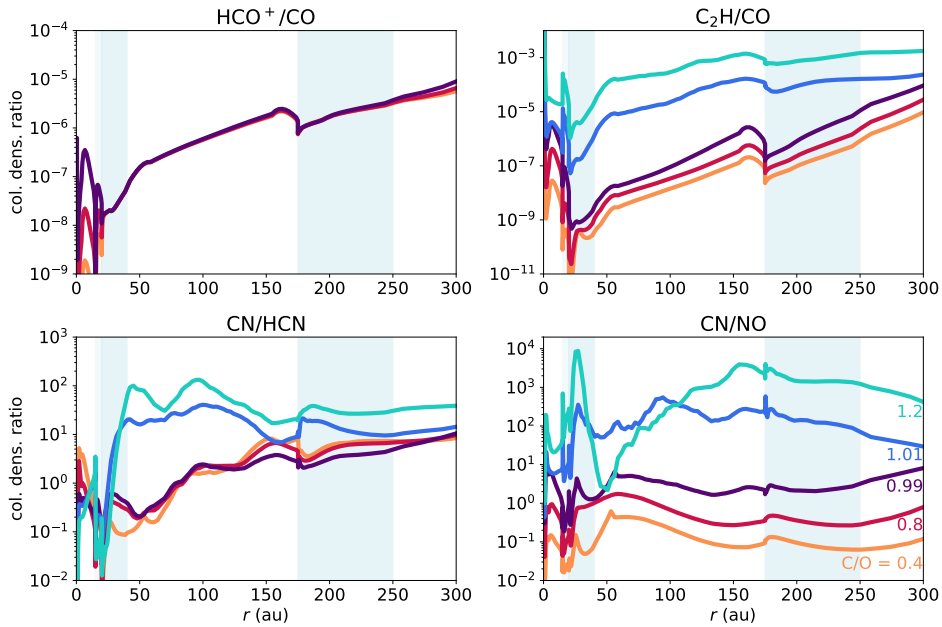


Figure 6.B.9: Column density ratios for different molecules and different C/O ratios.

morphology of the observed ratio is best reproduced by a C/O of 0.4–0.8, whereas the value inside the gap is reproduced within $\sim 1\sigma$ for C/O = 0.99. The CN/NO ratio on the other hand is best reproduced by a low C/O of 0.4. In the outer disk, the CN/NO ratio increases by one order of magnitude for a C/O of 0.4, 0.8, 0.99, 1.01, and 1.2. Even though the S/N on the CN/NO ratio is low, the value in the outer dust ring is indicative of a slightly elevated C/O ratio of 0.8.

6.B.4 Background UV

In Fig. 6.B.11, the column densities for models with a lower background UV radiation field are presented. This parameter mainly affects the column densities in the outer disk where a lower UV field lowers the column density of C, CN, C₂H, and NO, whereas it increases that of HCN somewhat due to less efficient photodissociation.

6.B.5 Flaring

The column density and azimuthally averaged radial profiles of CO, HCN, CN, C₂H, NO, and HCO⁺ are presented in Fig. 6.B.12 and 6.B.13, respectively. Flaring alone has a minor to no effect on the CO and HCO⁺ column densities, whereas those of HCN, CN, C₂H, and NO do generally increase with decreasing flaring indices. These differences in the column densities are partially countered by the changing temperature structure as less flared disks intercept less UV.

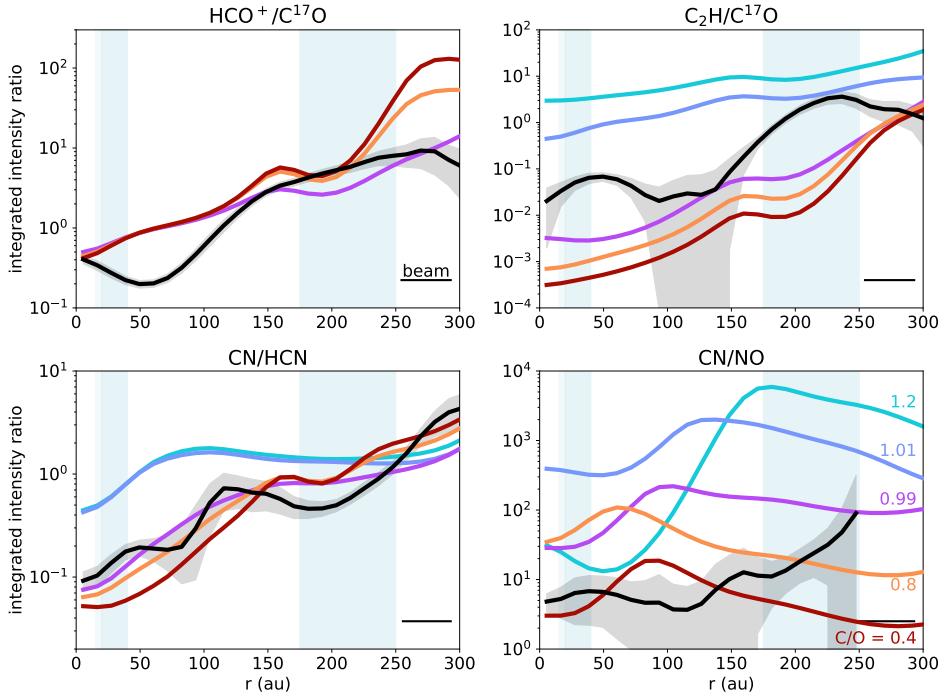


Figure 6.B.10: Emission line ratios of HCO^+/CO (top left), $\text{C}_2\text{H}/\text{CO}$ (top right), CN/HCN (bottom left), and CN/NO (bottom right) for different gas gap depths. The black line indicated the observed emission line ratio for each pair.

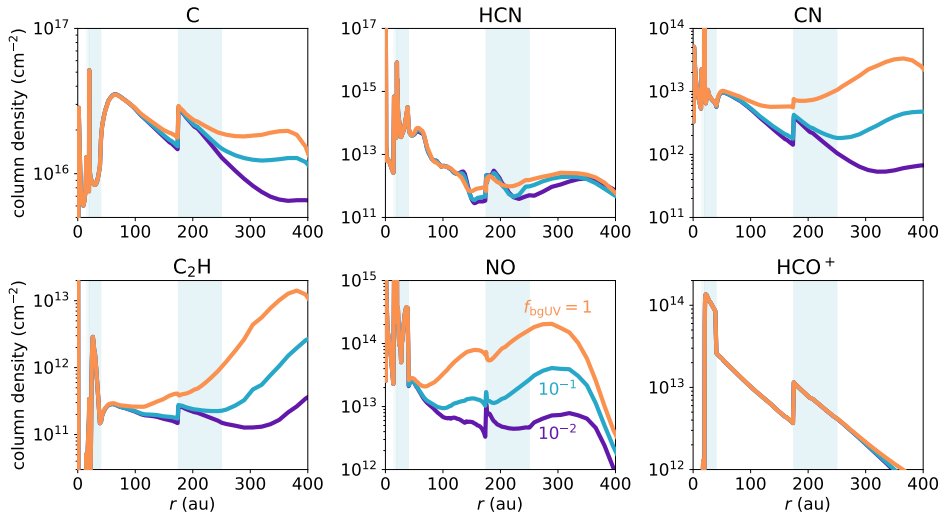


Figure 6.B.11: Column densities of different molecules studied in this work for different background UV radiation fields.

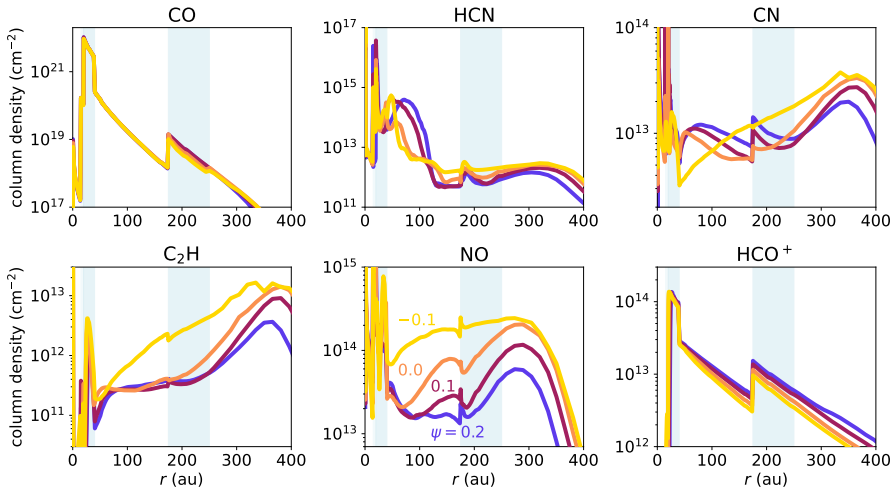


Figure 6.B.12: Column densities of different molecules studied in this work for different flaring indices.

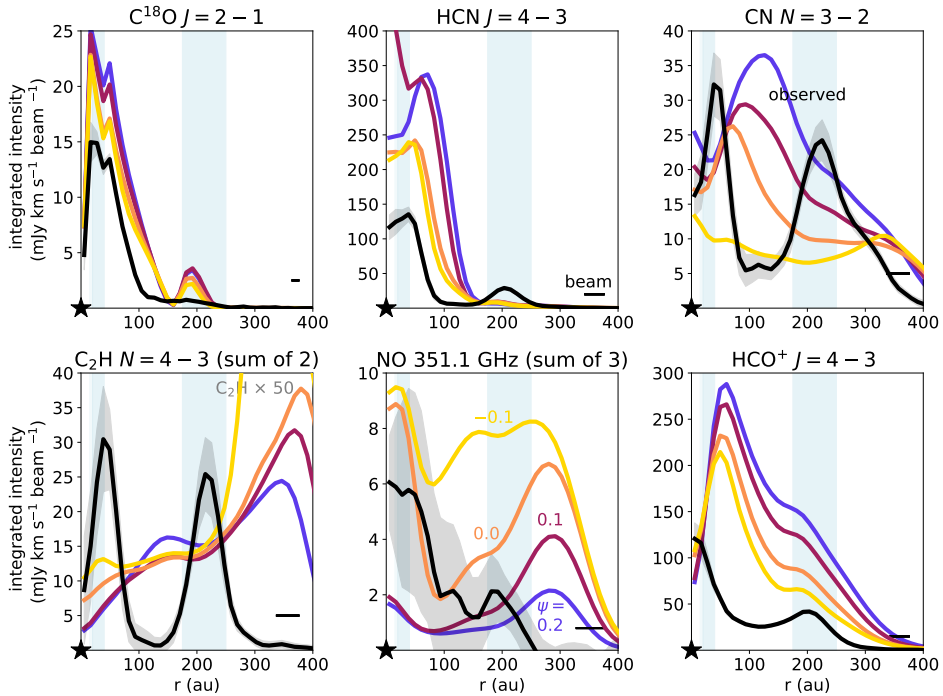


Figure 6.B.13: Molecular line emission of different molecules studied in this work for different flaring indices.

Bibliography

- Adams, N. G., Smith, D., & Grief, D. 1978, *International Journal of Mass Spectrometry and Ion Processes*, 26, 405
- Agúndez, M., Roueff, E., Le Petit, F., & Le Bourlot, J. 2018, *A&A*, 616, A19
- Aikawa, Y., Cataldi, G., Yamato, Y., et al. 2021, *ApJS*, 257, 13
- Aikawa, Y., Furuya, K., Nomura, H., & Qi, C. 2015, *ApJ*, 807, 120
- Aikawa, Y. & Herbst, E. 1999, *A&A*, 351, 233
- Aikawa, Y. & Herbst, E. 2001, *A&A*, 371, 1107
- Alarcón, F., Bosman, A. D., Bergin, E. A., et al. 2021, *ApJS*, 257, 8
- Alarcón, F., Teague, R., Zhang, K., Bergin, E. A., & Barraza-Alfaro, M. 2020, *ApJ*, 905, 68
- Alexander, R., Pascucci, I., Andrews, S., Armitage, P., & Cieza, L. 2014, in *Protostars and Planets VI*, ed. H. Beuther, R. S. Klessen, C. P. Dullemond, & T. Henning, 475
- Altwegg, K., Balsiger, H., Bar-Nun, A., et al. 2015, *Science*, 347, 1261952
- Altwegg, K., Balsiger, H., & Fuselier, S. A. 2019, *ARA&A*, 57, 113
- Altwegg, K., Balsiger, H., Hänni, N., et al. 2020, *Nature Astronomy*, 4, 533
- Altwegg, K., Combi, M., Fuselier, S. A., et al. 2022, *MNRAS*, 516, 3900
- Anderson, D. E., Bergin, E. A., Blake, G. A., et al. 2017, *ApJ*, 845, 13
- Anderson, D. E., Cleeves, L. I., Blake, G. A., et al. 2022, *ApJ*, 927, 229
- André, P., Men'shchikov, A., Bontemps, S., et al. 2010, *A&A*, 518, L102
- André, P., Ward-Thompson, D., & Barsony, M. 1993, *ApJ*, 406, 122
- Andrews, S. M. 2020, *ARA&A*, 58, 483

- Andrews, S. M., Huang, J., Pérez, L. M., et al. 2018, *ApJ*, 869, L41
- Andrews, S. M., Rosenfeld, K. A., Kraus, A. L., & Wilner, D. J. 2013, *ApJ*, 771, 129
- Andrews, S. M., Wilner, D. J., Espaillat, C., et al. 2011, *ApJ*, 732, 42
- Andrews, S. M., Wilner, D. J., Hughes, A. M., Qi, C., & Dullemond, C. P. 2010, *ApJ*, 723, 1241
- Andrews, S. M., Wilner, D. J., Zhu, Z., et al. 2016, *ApJ*, 820, L40
- Anicich, V. G., Futrell, J. H., Huntress, Wesley T., J., & Kim, J. K. 1975, *International Journal of Mass Spectrometry and Ion Processes*, 18, 63
- Ansdell, M., Williams, J. P., Trapman, L., et al. 2018, *ApJ*, 859, 21
- Ansdell, M., Williams, J. P., van der Marel, N., et al. 2016, *ApJ*, 828, 46
- Armitage, P. J. 2019, *Saas-Fee Advanced Course*, 45, 1
- Arun, R., Mathew, B., Manoj, P., et al. 2019, *AJ*, 157, 159
- Audard, M., Ábrahám, P., Dunham, M. M., et al. 2014, in *Protostars and Planets VI*, ed. H. Beuther, R. S. Klessen, C. P. Dullemond, & T. Henning, 387–410
- Bae, J., Isella, A., Zhu, Z., et al. 2023, in *Astronomical Society of the Pacific Conference Series*, Vol. 534, *Astronomical Society of the Pacific Conference Series*, ed. S. Inutsuka, Y. Aikawa, T. Muto, K. Tomida, & M. Tamura, 423
- Bae, J. & Zhu, Z. 2018, *ApJ*, 859, 118
- Bai, X.-N. 2016, *ApJ*, 821, 80
- Bakes, E. L. O. & Tielens, A. G. G. M. 1994, *ApJ*, 427, 822
- Balbus, S. A. & Hawley, J. F. 1991, *ApJ*, 376, 214
- Banzatti, A., Pinilla, P., Ricci, L., et al. 2015, *ApJ*, 815, L15
- Banzatti, A., Pontoppidan, K. M., Salyk, C., et al. 2017, *ApJ*, 834, 152
- Barenfeld, S. A., Carpenter, J. M., Ricci, L., & Isella, A. 2016, *ApJ*, 827, 142
- Ben Khalifa, M. & Loreau, J. 2021, *MNRAS*, 508, 1908
- Benisty, M., Bae, J., Facchini, S., et al. 2021, *ApJ*, 916, L2
- Benisty, M., Tatulli, E., Ménard, F., & Swain, M. R. 2010, *A&A*, 511, A75
- Bergin, E. A., Alves, J., Huard, T., & Lada, C. J. 2002, *ApJ*, 570, L101
- Bergin, E. A., Cleeves, L. I., Crockett, N., & Blake, G. A. 2014, *Faraday Discussions*, 168, 61

- Bergin, E. A., Du, F., Cleeves, L. I., et al. 2016, *ApJ*, 831, 101
- Bergin, E. A., Hogerheijde, M. R., Brinch, C., et al. 2010, *A&A*, 521, L33
- Bergin, E. A., Melnick, G. J., & Neufeld, D. A. 1998, *ApJ*, 499, 777
- Bergin, E. A. & Tafalla, M. 2007, *ARA&A*, 45, 339
- Bergner, J. B., Öberg, K. I., Bergin, E. A., et al. 2019, *ApJ*, 876, 25
- Bergner, J. B., Öberg, K. I., Guzmán, V. V., et al. 2021, *ApJS*, 257, 11
- Béthune, W., Lesur, G., & Ferreira, J. 2017, *A&A*, 600, A75
- Betts, J. & Back, R. A. 1965, *Canadian Journal of Chemistry*, 43, 2678
- Binkert, F., Szulágyi, J., & Birnstiel, T. 2021, *MNRAS*, 506, 5969
- Birnstiel, T., Andrews, S. M., Pinilla, P., & Kama, M. 2015, *ApJ*, 813, L14
- Birnstiel, T., Dullemond, C. P., & Brauer, F. 2010, *A&A*, 513, A79
- Birnstiel, T., Klahr, H., & Ercolano, B. 2012, *A&A*, 539, A148
- Blevins, S. M., Pontoppidan, K. M., Banzatti, A., et al. 2016, *ApJ*, 818, 22
- Blondel, P. F. C. & Djie, H. R. E. T. A. 2006, *A&A*, 456, 1045
- Blum, J. & Wurm, G. 2008, *ARA&A*, 46, 21
- Bok, B. J. & Reilly, E. F. 1947, *ApJ*, 105, 255
- Boley, A. C. 2009, *ApJ*, 695, L53
- Boogert, A. C. A., Brewer, K., Brittain, A., & Emerson, K. S. 2022, arXiv e-prints, arXiv:2210.12639
- Boogert, A. C. A., Gerakines, P. A., & Whittet, D. C. B. 2015, *ARA&A*, 53, 541
- Booth, A. S., et al., & et al. 2023a, TBD, in prep, TBD
- Booth, A. S. & Ilee, J. D. 2020, *MNRAS*, 493, L108
- Booth, A. S., Ilee, J. D., Walsh, C., et al. 2023b, *A&A*, 669, A53
- Booth, A. S., Law, C. J., Temmink, M., Leemker, M., & Macías, E. 2023c, *A&A*, 678, A146
- Booth, A. S., Tabone, B., Ilee, J. D., et al. 2021a, *ApJS*, 257, 16
- Booth, A. S., van der Marel, N., Leemker, M., van Dishoeck, E. F., & Ohashi, S. 2021b, *A&A*, 651, L6
- Booth, A. S., Walsh, C., Ilee, J. D., et al. 2019, *ApJ*, 882, L31

- Booth, A. S., Walsh, C., Terwisscha van Scheltinga, J., et al. 2021c, *Nature Astronomy*, 5, 684
- Bosman, A. D., Alarcón, F., Bergin, E. A., et al. 2021a, *ApJS*, 257, 7
- Bosman, A. D., Alarcón, F., Zhang, K., & Bergin, E. A. 2021b, *ApJ*, 910, 3
- Bosman, A. D. & Bergin, E. A. 2021, *ApJ*, 918, L10
- Bosman, A. D., Bergin, E. A., Loomis, R. A., et al. 2021c, *ApJS*, 257, 15
- Bosman, A. D., Tielens, A. G. G. M., & van Dishoeck, E. F. 2018a, *A&A*, 611, A80
- Bosman, A. D., Walsh, C., & van Dishoeck, E. F. 2018b, *A&A*, 618, A182
- Boss, A. P. 1997, *Science*, 276, 1836
- Botschwina, P., Horn, M., Flügge, J., & Seeger, S. 1993, *J. Chem. Soc., Faraday Trans.*, 89, 2219
- Bottinelli, S., Boogert, A. C. A., Bouwman, J., et al. 2010, *ApJ*, 718, 1100
- Bowman, W. C. & de Lucia, F. C. 1982, *J. Chem. Phys.*, 77, 92
- Brauer, F., Dullemond, C. P., & Henning, T. 2008, *A&A*, 480, 859
- Brinch, C. & Hogerheijde, M. R. 2010, *A&A*, 523, A25
- Brittain, S. D., Carr, J. S., Najita, J. R., Quanz, S. P., & Meyer, M. R. 2014, *ApJ*, 791, 136
- Brittain, S. D., Najita, J. R., Carr, J. S., et al. 2013, *ApJ*, 767, 159
- Brown, J. M., Herczeg, G. J., Pontoppidan, K. M., & van Dishoeck, E. F. 2012, *ApJ*, 744, 116
- Brown, W. A. & Bolina, A. S. 2007, *MNRAS*, 374, 1006
- Bruderer, S. 2013, *A&A*, 559, A46
- Bruderer, S., Benz, A. O., van Dishoeck, E. F., et al. 2010, *A&A*, 521, L44
- Bruderer, S., Doty, S. D., & Benz, A. O. 2009, *ApJS*, 183, 179
- Bruderer, S., van der Marel, N., van Dishoeck, E. F., & van Kempen, T. A. 2014, *A&A*, 562, A26
- Bruderer, S., van Dishoeck, E. F., Doty, S. D., & Herczeg, G. J. 2012, *A&A*, 541, A91
- Brunken, N. G. C., Booth, A. S., Leemker, M., et al. 2022, *A&A*, 659, A29
- Bryden, G., Chen, X., Lin, D. N. C., Nelson, R. P., & Papaloizou, J. C. B. 1999, *ApJ*, 514, 344

- Burrus, C. A. & Gordy, W. 1956, *Physical Review*, 101, 599
- Calahan, J. K., Bergin, E., Zhang, K., et al. 2021, *ApJ*, 908, 8
- Carney, M. T., Fedele, D., Hogerheijde, M. R., et al. 2018, *A&A*, 614, A106
- Carpenter, J., Brogan, C., Iono, D., & Mroczkowski, T. 2023, in *Physics and Chemistry of Star Formation: The Dynamical ISM Across Time and Spatial Scales*, 304
- Carr, J. S. & Najita, J. R. 2008, *Science*, 319, 1504
- Carr, J. S., Najita, J. R., & Salyk, C. 2018, *Research Notes of the American Astronomical Society*, 2, 169
- Casassus, S., Hales, A., de Gregorio, I., et al. 2013, *A&A*, 553, A64
- Casassus, S. & Pérez, S. 2019, *ApJ*, 883, L41
- Caselli, P., Benson, P. J., Myers, P. C., & Tafalla, M. 2002, *ApJ*, 572, 238
- Caselli, P. & Ceccarelli, C. 2012, *A&A Rev.*, 20, 56
- Caselli, P., Walmsley, C. M., Terzieva, R., & Herbst, E. 1998, *ApJ*, 499, 234
- Cassen, P. & Moosman, A. 1981, *ICARUS*, 48, 353
- Cazzoletti, P., van Dishoeck, E. F., Visser, R., Facchini, S., & Bruderer, S. 2018, *A&A*, 609, A93
- Ceccarelli, C., Caselli, P., Bockelée-Morvan, D., et al. 2014, in *Protostars and Planets VI*, ed. H. Beuther, R. S. Klessen, C. P. Dullemond, & T. Henning, 859–882
- Cernicharo, J., Tercero, B., Marcelino, N., Agúndez, M., & de Vicente, P. 2023, *A&A*, 674, L4
- Chen, L., Moór, A., Kreplin, A., et al. 2019, *ApJ*, 887, L32
- Chuang, K. J., Fedoseev, G., Ioppolo, S., van Dishoeck, E. F., & Linnartz, H. 2016, *MNRAS*, 455, 1702
- Chuang, K. J., Fedoseev, G., Qasim, D., et al. 2020, *A&A*, 635, A199
- Cieza, L. A., Casassus, S., Tobin, J., et al. 2016, *Nature*, 535, 258
- Clarke, C. J., Gendrin, A., & Sotomayor, M. 2001, *MNRAS*, 328, 485
- Cleeves, L. I., Bergin, E. A., & Adams, F. C. 2014a, *ApJ*, 794, 123
- Cleeves, L. I., Bergin, E. A., Alexander, C. M. O. D., et al. 2014b, *Science*, 345, 1590
- Cleeves, L. I., Bergin, E. A., Bethell, T. J., et al. 2011, *ApJ*, 743, L2

- Cleeves, L. I., Bergin, E. A., & Harries, T. J. 2015a, *ApJ*, 807, 2
- Cleeves, L. I., Bergin, E. A., Qi, C., Adams, F. C., & Öberg, K. I. 2015b, *ApJ*, 799, 204
- Codella, C., Bianchi, E., Tabone, B., et al. 2018, *A&A*, 617, A10
- Collings, M. P., Anderson, M. A., Chen, R., et al. 2004, *MNRAS*, 354, 1133
- Congiu, E., Fedoseev, G., Ioppolo, S., et al. 2012, *ApJ*, 750, L12
- Cornwell, T. J. 2008, *IEEE Journal of Selected Topics in Signal Processing*, 2, 793
- Crapsi, A., van Dishoeck, E. F., Hogerheijde, M. R., Pontoppidan, K. M., & Dullemond, C. P. 2008, *A&A*, 486, 245
- Cridland, A. J., Facchini, S., van Dishoeck, E. F., & Benisty, M. 2023, *A&A*, 674, A211
- Cridland, A. J., Pudritz, R. E., & Alessi, M. 2016, *MNRAS*, 461, 3274
- Cridland, A. J., Pudritz, R. E., Birnstiel, T., Cleeves, L. I., & Bergin, E. A. 2017, *MNRAS*, 469, 3910
- Cuppen, H. M., van Dishoeck, E. F., Herbst, E., & Tielens, A. G. G. M. 2009, *A&A*, 508, 275
- Currie, T., Brittain, S., Grady, C. A., Kenyon, S. J., & Muto, T. 2017, *Research Notes of the American Astronomical Society*, 1, 40
- Currie, T., Cloutier, R., Brittain, S., et al. 2015, *ApJ*, 814, L27
- Currie, T., Lawson, K., Schneider, G., et al. 2022, *Nature Astronomy*, 6, 751
- Currie, T., Marois, C., Cieza, L., et al. 2019, *ApJ*, 877, L3
- Currie, T., Muto, T., Kudo, T., et al. 2014, *ApJ*, 796, L30
- Czekala, I., Loomis, R. A., Teague, R., et al. 2021, *ApJS*, 257, 2
- D'Alessio, P., Calvet, N., Hartmann, L., Franco-Hernández, R., & Servín, H. 2006, *ApJ*, 638, 314
- Daranlot, J., Hincelin, U., Bergeat, A., et al. 2012, *Proceedings of the National Academy of Science*, 109, 10233
- de Juan Ovelar, M., Min, M., Dominik, C., et al. 2013, *A&A*, 560, A111
- Denis-Alpizar, O., Stoecklin, T., Dutrey, A., & Guilloteau, S. 2020, *MNRAS*, 497, 4276
- Dent, W. R. F., Thi, W. F., Kamp, I., et al. 2013, *PASP*, 125, 477
- Dipierro, G., Price, D., Laibe, G., et al. 2015, *MNRAS*, 453, L73

- Dodson-Robinson, S. E. & Salyk, C. 2011, *ApJ*, 738, 131
- Donati, J. F., Bouvier, J., Alencar, S. H., et al. 2019, *MNRAS*, 483, L1
- Dong, R., Liu, S.-y., Eisner, J., et al. 2018, *ApJ*, 860, 124
- Dong, R., Zhu, Z., Rafikov, R. R., & Stone, J. M. 2015a, *ApJ*, 809, L5
- Dong, R., Zhu, Z., & Whitney, B. 2015b, *ApJ*, 809, 93
- Draine, B. T. 2003, *ARA&A*, 41, 241
- Draine, B. T. 2006, *ApJ*, 636, 1114
- Drażkowska, J. & Alibert, Y. 2017, *A&A*, 608, A92
- Drażkowska, J., Bitsch, B., Lambrechts, M., et al. 2023, in *Astronomical Society of the Pacific Conference Series*, Vol. 534, *Protostars and Planets VII*, ed. S. Inutsuka, Y. Aikawa, T. Muto, K. Tomida, & M. Tamura, 717
- Drozdovskaya, M. N., Walsh, C., van Dishoeck, E. F., et al. 2016, *MNRAS*, 462, 977
- Du, F. & Bergin, E. A. 2014, *ApJ*, 792, 2
- Du, F., Bergin, E. A., Hogerheijde, M., et al. 2017, *ApJ*, 842, 98
- Dubrulle, B., Morfill, G., & Sterzik, M. 1995, *ICARUS*, 114, 237
- Dullemond, C. P., Dominik, C., & Natta, A. 2001, *ApJ*, 560, 957
- Dullemond, C. P., Juhasz, A., Pohl, A., et al. 2012, *RADMC-3D: A multi-purpose radiative transfer tool*, *Astrophysics Source Code Library*, record ascl:1202.015
- Dumouchel, F., Faure, A., & Lique, F. 2010, *MNRAS*, 406, 2488
- Dutrey, A., Wakelam, V., Boehler, Y., et al. 2011, *A&A*, 535, A104
- Eistrup, C. 2023, *ACS Earth and Space Chemistry*, 7, 260
- Eistrup, C., Walsh, C., & van Dishoeck, E. F. 2016, *A&A*, 595, A83
- Eistrup, C., Walsh, C., & van Dishoeck, E. F. 2018, *A&A*, 613, A14
- Endres, C. P., Schlemmer, S., Schilke, P., Stutzki, J., & Müller, H. S. P. 2016, *Journal of Molecular Spectroscopy*, 327, 95
- Ercolano, B. & Pascucci, I. 2017, *Royal Society Open Science*, 4, 170114
- Ercolano, B., Picogna, G., Monsch, K., Drake, J. J., & Preibisch, T. 2021, *MNRAS*, 508, 1675
- Espaillet, C., Muzerolle, J., Najita, J., et al. 2014, in *Protostars and Planets VI*, ed. H. Beuther, R. S. Klessen, C. P. Dullemond, & T. Henning, 497

- Evans, Neal J., I., Dunham, M. M., Jørgensen, J. K., et al. 2009, *ApJS*, 181, 321
- Facchini, S., Benisty, M., Bae, J., et al. 2020, *A&A*, 639, A121
- Facchini, S., Birnstiel, T., Bruderer, S., & van Dishoeck, E. F. 2017, *A&A*, 605, A16
- Facchini, S., Pinilla, P., van Dishoeck, E. F., & de Juan Ovelar, M. 2018, *A&A*, 612, A104
- Facchini, S., Teague, R., Bae, J., et al. 2021, *AJ*, 162, 99
- Facchini, S., van Dishoeck, E. F., Manara, C. F., et al. 2019, *A&A*, 626, L2
- Favre, C., Bergin, E. A., Cleeves, L. I., et al. 2015, *ApJ*, 802, L23
- Favre, C., Cleeves, L. I., Bergin, E. A., Qi, C., & Blake, G. A. 2013, *ApJ*, 776, L38
- Favre, C., Fedele, D., Maud, L., et al. 2019, *ApJ*, 871, 107
- Fedele, D., Bruderer, S., van Dishoeck, E. F., et al. 2013a, *A&A*, 559, A77
- Fedele, D., Bruderer, S., van Dishoeck, E. F., et al. 2013b, *ApJ*, 776, L3
- Fedele, D., Carney, M., Hogerheijde, M. R., et al. 2017, *A&A*, 600, A72
- Fedele, D., Toci, C., Maud, L., & Lodato, G. 2021, *A&A*, 651, A90
- Fedele, D., van den Ancker, M. E., Henning, T., Jayawardhana, R., & Oliveira, J. M. 2010, *A&A*, 510, A72
- Fedele, D., van Dishoeck, E. F., Kama, M., Bruderer, S., & Hogerheijde, M. R. 2016, *A&A*, 591, A95
- Fedoseev, G., Chuang, K. J., van Dishoeck, E. F., Ioppolo, S., & Linnartz, H. 2016, *MNRAS*, 460, 4297
- Fedoseev, G., Ioppolo, S., Lamberts, T., et al. 2012, *J. Chem. Phys.*, 137, 054714
- Ferreira, J., Dougados, C., & Cabrit, S. 2006, *A&A*, 453, 785
- Fillion, J.-H., Dupuy, R., Féraud, G., et al. 2022, *ACS Earth and Space Chemistry*, 6, 100
- Fischer, W. J., Hillenbrand, L. A., Herczeg, G. J., et al. 2023, in *Astronomical Society of the Pacific Conference Series*, Vol. 534, *Astronomical Society of the Pacific Conference Series*, ed. S. Inutsuka, Y. Aikawa, T. Muto, K. Tomida, & M. Tamura, 355
- Flaherty, K. M., Hughes, A. M., Rose, S. C., et al. 2017, *ApJ*, 843, 150
- Flaherty, K. M., Hughes, A. M., Rosenfeld, K. A., et al. 2015, *ApJ*, 813, 99

- Flaherty, K. M., Hughes, A. M., Teague, R., et al. 2018, *ApJ*, 856, 117
- Flock, M., Ruge, J. P., Dzyurkevich, N., et al. 2015, *A&A*, 574, A68
- Flower, D. R. 1999, *MNRAS*, 305, 651
- Fogel, J. K. J., Bethell, T. J., Bergin, E. A., Calvet, N., & Semenov, D. 2011, *ApJ*, 726, 29
- Follette, K. B., Grady, C. A., Swearingen, J. R., et al. 2015, *ApJ*, 798, 132
- Follette, K. B., Rameau, J., Dong, R., et al. 2017, *AJ*, 153, 264
- Francis, L. & van der Marel, N. 2020, *ApJ*, 892, 111
- Franz, R., Picogna, G., Ercolano, B., & Birnstiel, T. 2020, *A&A*, 635, A53
- Fraser, H. J., Collings, M. P., McCoustra, M. R. S., & Williams, D. A. 2001, *MNRAS*, 327, 1165
- Frerking, M. A., Langer, W. D., & Wilson, R. W. 1982, *ApJ*, 262, 590
- Furlan, E., Fischer, W. J., Ali, B., et al. 2016, *ApJS*, 224, 5
- Furuya, K., Aikawa, Y., Nomura, H., Hersant, F., & Wakelam, V. 2013, *ApJ*, 779, 11
- Furuya, K., Drozdovskaya, M. N., Visser, R., et al. 2017, *A&A*, 599, A40
- Furuya, K., van Dishoeck, E. F., & Aikawa, Y. 2016, *A&A*, 586, A127
- Gaia Collaboration, Brown, A. G. A., Vallenari, A., et al. 2018, *A&A*, 616, A1
- Gaia Collaboration, Prusti, T., de Bruijne, J. H. J., et al. 2016, *A&A*, 595, A1
- Gaia Collaboration, Vallenari, A., Brown, A. G. A., et al. 2023, *A&A*, 674, A1
- Galli, D. & Shu, F. H. 1993, *ApJ*, 417, 220
- Garrod, R., Park, I. H., Caselli, P., & Herbst, E. 2006, *Faraday Discussions*, 133, 51
- Garrod, R. T. & Herbst, E. 2006, *A&A*, 457, 927
- Garufi, A., Quanz, S. P., Schmid, H. M., et al. 2016, *A&A*, 588, A8
- Geers, V. C., Pontoppidan, K. M., van Dishoeck, E. F., et al. 2007a, *A&A*, 469, L35
- Geers, V. C., van Dishoeck, E. F., Visser, R., et al. 2007b, *A&A*, 476, 279
- Geppert, W. D., Hamberg, M., Thomas, R. D., et al. 2006, *Faraday Discussions*, 133, 177

- Gericke, K. H., Lock, M., Schmidt, F., & Comes, F. J. 1994, *J. Chem. Phys.*, 101, 1988
- Goldsmith, P. F. & Langer, W. D. 1999, *ApJ*, 517, 209
- González Díaz, C., Carrascosa de Lucas, H., Aparicio, S., et al. 2019, *MNRAS*, 486, 5519
- Gorti, U. & Hollenbach, D. 2004, *ApJ*, 613, 424
- Grady, C. A., Polomski, E. F., Henning, T., et al. 2001, *AJ*, 122, 3396
- Grady, C. A., Schneider, G., Hamaguchi, K., et al. 2007, *ApJ*, 665, 1391
- Grant, S. L., van Dishoeck, E. F., Tabone, B., et al. 2023, *ApJ*, 947, L6
- Gray, R. O., Riggs, Q. S., Koen, C., et al. 2017, *AJ*, 154, 31
- Green, J. D., Evans, Neal J., I., Jørgensen, J. K., et al. 2013, *ApJ*, 770, 123
- Greene, T. P., Wilking, B. A., Andre, P., Young, E. T., & Lada, C. J. 1994, *ApJ*, 434, 614
- Güttler, C., Blum, J., Zsom, A., Ormel, C. W., & Dullemond, C. P. 2010, *A&A*, 513, A56
- Guzmán, V. V., Bergner, J. B., Law, C. J., et al. 2021, *ApJS*, 257, 6
- Guzmán-Díaz, J., Mendigutía, I., Montesinos, B., et al. 2021, *A&A*, 650, A182
- Habart, E., Natta, A., Testi, L., & Carbillet, M. 2006, *A&A*, 449, 1067
- Hacar, A., Bosman, A. D., & van Dishoeck, E. F. 2020, *A&A*, 635, A4
- Hacar, A., Tafalla, M., & Alves, J. 2017, *A&A*, 606, A123
- Hacar, A., Tafalla, M., Kauffmann, J., & Kovács, A. 2013, *A&A*, 554, A55
- Haffert, S. Y., Bohn, A. J., de Boer, J., et al. 2019, *Nat. Astron.*, 3, 749
- Haisch, Karl E., J., Lada, E. A., & Lada, C. J. 2001, *ApJ*, 553, L153
- Halfen, D. T., Apponi, A. J., & Ziurys, L. M. 2001, *ApJ*, 561, 244
- Hammond, I., Christiaens, V., Price, D. J., et al. 2023, *MNRAS*, 522, L51
- Harsono, D., Bjerkele, P., van der Wiel, M. H. D., et al. 2018, *Nature Astronomy*, 2, 646
- Harsono, D., Bruderer, S., & van Dishoeck, E. F. 2015, *A&A*, 582, A41
- Harsono, D., Persson, M. V., Ramos, A., et al. 2020, *A&A*, 636, A26
- Hartmann, L., Calvet, N., Gullbring, E., & D'Alessio, P. 1998, *ApJ*, 495, 385

- Hasegawa, T. I., Herbst, E., & Leung, C. M. 1992, *ApJS*, 82, 167
- He, J., Vidali, G., Lemaire, J.-L., & Garrod, R. T. 2015, *ApJ*, 799, 49
- Heays, A. N., Bosman, A. D., & van Dishoeck, E. F. 2017, *A&A*, 602, A105
- Herbst, E. & van Dishoeck, E. F. 2009, *ARA&A*, 47, 427
- Hildebrand, R. H. 1983, *QJRAS*, 24, 267
- Hily-Blant, P., Walmsley, M., Pineau Des Forêts, G., & Flower, D. 2010a, *A&A*, 513, A41
- Hily-Blant, P., Walmsley, M., Pineau Des Forêts, G., & Flower, D. 2010b, *A&A*, 513, A41
- Hogerheijde, M. R., Bergin, E. A., Brinch, C., et al. 2011, *Science*, 334, 338
- Honda, M., Kudo, T., Takatsuki, S., et al. 2016, *ApJ*, 821, 2
- Howard, C. D., Sandell, G., Vacca, W. D., et al. 2013, *ApJ*, 776, 21
- Hsieh, T.-H., Murillo, N. M., Belloche, A., et al. 2019, *ApJ*, 884, 149
- Huang, J., Andrews, S. M., Dullemond, C. P., et al. 2018, *ApJ*, 869, L42
- Hueso, R. & Guillot, T. 2005, *A&A*, 442, 703
- Hughes, A. M., Duchêne, G., & Matthews, B. C. 2018, *ARA&A*, 56, 541
- Ikoma, M., Nakazawa, K., & Emori, H. 2000, *ApJ*, 537, 1013
- Imanishi, K., Koyama, K., & Tsuboi, Y. 2001, *ApJ*, 557, 747
- Ioppolo, S., Fedoseev, G., Minissale, M., et al. 2014, *Physical Chemistry Chemical Physics (Incorporating Faraday Transactions)*, 16, 8270
- Isella, A., Benisty, M., Teague, R., et al. 2019, *ApJ*, 879, L25
- Isella, A., Guidi, G., Testi, L., et al. 2016, *Phys. Rev. Lett.*, 117, 251101
- Izquierdo, A. F., Facchini, S., Rosotti, G. P., van Dishoeck, E. F., & Testi, L. 2021, *arXiv e-prints*, arXiv:2111.06367
- Izquierdo, A. F., Facchini, S., Rosotti, G. P., van Dishoeck, E. F., & Testi, L. 2022, *ApJ*, 928, 2
- Izquierdo, A. F., Testi, L., Facchini, S., et al. 2023, *A&A*, 674, A113
- Jeans, J. H. 1928, *Astronomy and cosmogony*
- Jensen, S. S., Jørgensen, J. K., Furuya, K., Haugbølle, T., & Aikawa, Y. 2021, *A&A*, 649, A66
- Jensen, S. S., Jørgensen, J. K., Kristensen, L. E., et al. 2019, *A&A*, 631, A25

- Jiang, H., Zhu, W., & Ormel, C. W. 2022, *ApJ*, 924, L31
- Johansen, A. & Lambrechts, M. 2017, *Annual Review of Earth and Planetary Sciences*, 45, 359
- Johansen, A., Oishi, J. S., Mac Low, M.-M., et al. 2007, *Nature*, 448, 1022
- Johns, J. W. C. 1985, *Journal of the Optical Society of America B Optical Physics*, 2, 1340
- Johnson, C. T., Burke, P. G., & Kingston, A. E. 1987, *Journal of Physics B Atomic Molecular Physics*, 20, 2553
- Jonkheid, B., Kamp, I., Augereau, J. C., & van Dishoeck, E. F. 2006, *A&A*, 453, 163
- Jonusas, M. & Krim, L. 2016, *MNRAS*, 459, 1977
- Jørgensen, J. K., Müller, H. S. P., Calcutt, H., et al. 2018, *A&A*, 620, A170
- Jørgensen, J. K., Visser, R., Sakai, N., et al. 2013, *ApJ*, 779, L22
- Jorsater, S. & van Moorsel, G. A. 1995, *AJ*, 110, 2037
- Kama, M., Bruderer, S., van Dishoeck, E. F., et al. 2016, *A&A*, 592, A83
- Kama, M., Trapman, L., Fedele, D., et al. 2020, *A&A*, 634, A88
- Kamp, I., Tilling, I., Woitke, P., Thi, W. F., & Hogerheijde, M. 2010, *A&A*, 510, A18
- Kamp, I. & van Zadelhoff, G. J. 2001, *A&A*, 373, 641
- Kenyon, S. J. & Hartmann, L. 1987, *ApJ*, 323, 714
- Keppler, M., Benisty, M., Müller, A., et al. 2018, *A&A*, 617, A44
- Keyte, L., Kama, M., Booth, A. S., et al. 2023, *Nature Astronomy*, 7, 684
- Kim, J. K., Theard, L. P., & Huntress, W. T., J. 1974, *International Journal of Mass Spectrometry and Ion Processes*, 15, 223
- Kimura, H., Wada, K., Kobayashi, H., et al. 2020, *Monthly Notices of the Royal Astronomical Society*, staa2467
- Klapper, G., Lewen, F., Gendriesch, R., Belov, S. P., & Winnewisser, G. 2000, *Journal of Molecular Spectroscopy*, 201, 124
- Klarmann, L., Ormel, C. W., & Dominik, C. 2018, *A&A*, 618, L1
- Klippenstein, S. J., Georgievskii, Y., & McCall, B. J. 2010, *Journal of Physical Chemistry A*, 114, 278
- Kokubo, E. & Ida, S. 1996, *ICARUS*, 123, 180

- Kóspál, Á., Ábrahám, P., Diehl, L., et al. 2023, *ApJ*, 945, L7
- Kounkel, M., Hartmann, L., Loinard, L., et al. 2017, *ApJ*, 834, 142
- Kral, Q., Matrà, L., Wyatt, M. C., & Kennedy, G. M. 2017, *MNRAS*, 469, 521
- Kratter, K. & Lodato, G. 2016, *ARA&A*, 54, 271
- Kratter, K. M., Murray-Clay, R. A., & Youdin, A. N. 2010, *ApJ*, 710, 1375
- Kraus, A. L. & Ireland, M. J. 2012, *ApJ*, 745, 5
- Kristensen, L. E. & Dunham, M. M. 2018, *A&A*, 618, A158
- Krumholz, M. R., Bate, M. R., Arce, H. G., et al. 2014, in *Protostars and Planets VI*, ed. H. Beuther, R. S. Klessen, C. P. Dullemond, & T. Henning, 243–266
- Kwon, W., Looney, L. W., Mundy, L. G., Chiang, H.-F., & Kemball, A. J. 2009, *ApJ*, 696, 841
- Lacy, J. H., Knacke, R., Geballe, T. R., & Tokunaga, A. T. 1994, *ApJ*, 428, L69
- Lada, C. J. 1987, in *Star Forming Regions*, ed. M. Peimbert & J. Jugaku, Vol. 115, 1
- Lada, C. J. & Lada, E. A. 2003, *ARA&A*, 41, 57
- Lambrechts, M. & Johansen, A. 2012, *A&A*, 544, A32
- Launay, J. M. & Roueff, E. 1977, *A&A*, 56, 289
- Law, C. J., Booth, A. S., & Öberg, K. I. 2023a, *ApJ*, 952, L19
- Law, C. J., Loomis, R. A., Teague, R., et al. 2021a, *ApJS*, 257, 3
- Law, C. J., Teague, R., Loomis, R. A., et al. 2021b, *ApJS*, 257, 4
- Law, C. J., Teague, R., Öberg, K. I., et al. 2023b, *ApJ*, 948, 60
- Le Gal, R., Hily-Blant, P., Faure, A., et al. 2014, *A&A*, 562, A83
- Le Gal, R., Öberg, K. I., Teague, R., et al. 2021, *ApJS*, 257, 12
- Lee, C.-F., Codella, C., Ceccarelli, C., & López-Sepulcre, A. 2022, *ApJ*, 937, 10
- Lee, J.-E., Lee, S., Baek, G., et al. 2019, *Nature Astronomy*, 3, 314
- Leemker, M., Booth, A. S., van Dishoeck, E. F., et al. 2022, *A&A*, 663, A23
- Leemker, M., Booth, A. S., van Dishoeck, E. F., et al. 2023, *A&A*, 673, A7
- Leemker, M., van't Hoff, M. L. R., Trapman, L., et al. 2021, *A&A*, 646, A3
- Lepp, S., Dalgarno, A., & Sternberg, A. 1987, *ApJ*, 321, 383

- Lesur, G., Ferreira, J., & Ogilvie, G. I. 2013, *A&A*, 550, A61
- Li, H., Colgate, S. A., Wendroff, B., & Liska, R. 2001, *ApJ*, 551, 874
- Li, H., Finn, J. M., Lovelace, R. V. E., & Colgate, S. A. 2000, *ApJ*, 533, 1023
- Ligterink, N. F. W., Calcutt, H., Coutens, A., et al. 2018a, *A&A*, 619, A28
- Ligterink, N. F. W., Walsh, C., Bhuin, R. G., et al. 2018b, *A&A*, 612, A88
- Lin, D. N. C. & Pringle, J. E. 1987, *MNRAS*, 225, 607
- Lique, F., Spielfiedel, A., Feautrier, N., et al. 2010, *J. Chem. Phys.*, 132, 024303
- Lique, F., van der Tak, F. F. S., Klos, J., Bulthuis, J., & Alexander, M. H. 2009, *A&A*, 493, 557
- Long, F., Bosman, A. D., Cazzoletti, P., et al. 2021, *A&A*, 647, A118
- Long, F., Pinilla, P., Herczeg, G. J., et al. 2018, *ApJ*, 869, 17
- Loomis, R. A., Cleeves, L. I., Öberg, K. I., et al. 2018, *ApJ*, 859, 131
- Louvet, F., Dougados, C., Cabrit, S., et al. 2018, *A&A*, 618, A120
- Lovelace, R. V. E., Li, H., Colgate, S. A., & Nelson, A. F. 1999, *ApJ*, 513, 805
- Lynden-Bell, D. & Pringle, J. E. 1974, *MNRAS*, 168, 603
- Lyra, W., Turner, N. J., & McNally, C. P. 2015, *A&A*, 574, A10
- Malfait, K., Bogaert, E., & Waelkens, C. 1998, *A&A*, 331, 211
- Manara, C. F., Ansdell, M., Rosotti, G. P., et al. 2023, in *Astronomical Society of the Pacific Conference Series*, Vol. 534, *Protostars and Planets VII*, ed. S. Inutsuka, Y. Aikawa, T. Muto, K. Tomida, & M. Tamura, 539
- Manara, C. F., Morbidelli, A., & Guillot, T. 2018, *A&A*, 618, L3
- Manara, C. F., Natta, A., Rosotti, G. P., et al. 2020, *A&A*, 639, A58
- Mandell, A. M., Bast, J., van Dishoeck, E. F., et al. 2012, *ApJ*, 747, 92
- Marcelino, N., Brünken, S., Cernicharo, J., et al. 2010, *A&A*, 516, A105
- Maret, S., Bergin, E. A., & Lada, C. J. 2006, *Nature*, 442, 425
- Martín-Doménech, R., Muñoz Caro, G. M., Bueno, J., & Goesmann, F. 2014, *A&A*, 564, A8
- Mathews, G. S., Klaassen, P. D., Juhász, A., et al. 2013, *A&A*, 557, A132
- Mathis, J. S., Ruml, W., & Nordsieck, K. H. 1977, *ApJ*, 217, 425
- McCall, B. J., Huneycutt, A. J., Saykally, R. J., et al. 2004, *Phys. Rev.*, 70, 052716

- McClure, M. K., Dominik, C., & Kama, M. 2020, *A&A*, 642, L15
- McClure, M. K., Rocha, W. R. M., Pontoppidan, K. M., et al. 2023, *Nature Astronomy* [arXiv:2301.09140]
- McElroy, D., Walsh, C., Markwick, A. J., et al. 2013, *A&A*, 550, A36
- McGuire, B. A. 2022, *ApJS*, 259, 30
- McGuire, B. A., Burkhardt, A. M., Kalenskii, S., et al. 2018, *Science*, 359, 202
- McMullin, J. P., Waters, B., Schiebel, D., Young, W., & Golap, K. 2007, in *Astronomical Society of the Pacific Conference Series*, Vol. 376, *Astronomical Data Analysis Software and Systems XVI*, ed. R. A. Shaw, F. Hill, & D. J. Bell, 127
- Meeus, G., Montesinos, B., Mendigutía, I., et al. 2012, *A&A*, 544, A78
- Meeus, G., Salyk, C., Bruderer, S., et al. 2013, *A&A*, 559, A84
- Meheut, H., Lovelace, R. V. E., & Lai, D. 2013, *MNRAS*, 430, 1988
- Meijerink, R., Pontoppidan, K. M., Blake, G. A., Poelman, D. R., & Dullemond, C. P. 2009, *ApJ*, 704, 1471
- Merín, B., Brown, J. M., Oliveira, I., et al. 2010, *ApJ*, 718, 1200
- Milam, S. N., Savage, C., Brewster, M. A., Ziurys, L. M., & Wyckoff, S. 2005, *ApJ*, 634, 1126
- Millar, T. J., Bennett, A., Rawlings, J. M. C., Brown, P. D., & Charnley, S. B. 1991, *A&AS*, 87, 585
- Minissale, M., Aikawa, Y., Bergin, E., et al. 2022, *ACS Earth and Space Chemistry*, 6, 597
- Miotello, A., Bruderer, S., & van Dishoeck, E. F. 2014, *A&A*, 572, A96
- Miotello, A., Facchini, S., van Dishoeck, E. F., et al. 2019, *A&A*, 631, A69
- Miotello, A., Kamp, I., Birnstiel, T., Cleeves, L. C., & Kataoka, A. 2023, in *Astronomical Society of the Pacific Conference Series*, Vol. 534, *Protostars and Planets VII*, ed. S. Inutsuka, Y. Aikawa, T. Muto, K. Tomida, & M. Tamura, 501
- Miotello, A., van Dishoeck, E. F., Kama, M., & Bruderer, S. 2016, *A&A*, 594, A85
- Miotello, A., van Dishoeck, E. F., Williams, J. P., et al. 2017, *A&A*, 599, A113
- Mitchell, J. B. A. 1990, *Phys. Rep.*, 186, 215
- Mordasini, C., van Boekel, R., Mollière, P., Henning, T., & Benneke, B. 2016, *ApJ*, 832, 41

- Müller, H. S. P., Schlöder, F., Stutzki, J., & Winnewisser, G. 2005, *Journal of Molecular Structure*, 742, 215
- Müller, H. S. P., Thorwirth, S., Roth, D. A., & Winnewisser, G. 2001, *A&A*, 370, L49
- Murillo, N. M., Lai, S.-P., Bruderer, S., Harsono, D., & van Dishoeck, E. F. 2013, *A&A*, 560, A103
- Najita, J. R., Strom, S. E., & Muzerolle, J. 2007, *MNRAS*, 378, 369
- Nazari, P., Meijerhof, J. D., van Gelder, M. L., et al. 2022, *A&A*, 668, A109
- Nelson, R. P., Gressel, O., & Umurhan, O. M. 2013, *MNRAS*, 435, 2610
- Nomura, H., Tsukagoshi, T., Kawabe, R., et al. 2021, *ApJ*, 914, 113
- Norfolk, B. J., Pinte, C., Calcino, J., et al. 2022, *ApJ*, 936, L4
- Notsu, S., Akiyama, E., Booth, A., et al. 2019, *ApJ*, 875, 96
- Novotný, O., Buhr, H., Stützel, J., et al. 2010, *Journal of Physical Chemistry A*, 114, 4870
- Öberg, K. I. & Bergin, E. A. 2016, *ApJ*, 831, L19
- Öberg, K. I. & Bergin, E. A. 2021, *Phys. Rep.*, 893, 1
- Öberg, K. I., Fuchs, G. W., Awad, Z., et al. 2007, *ApJ*, 662, L23
- Öberg, K. I., Furuya, K., Loomis, R., et al. 2015, *ApJ*, 810, 112
- Öberg, K. I., Guzmán, V. V., Walsh, C., et al. 2021, *ApJS*, 257, 1
- Öberg, K. I., Linnartz, H., Visser, R., & van Dishoeck, E. F. 2009, *ApJ*, 693, 1209
- Öberg, K. I., Murray-Clay, R., & Bergin, E. A. 2011, *ApJ*, 743, L16
- Ogilvie, G. I. & Lubow, S. H. 2002, *MNRAS*, 330, 950
- Oh, D., Hashimoto, J., Tamura, M., et al. 2016, *PASJ*, 68, L3
- Ohashi, S., Kataoka, A., van der Marel, N., et al. 2020, *ApJ*, 900, 81
- Okuzumi, S., Momose, M., Sirono, S.-i., Kobayashi, H., & Tanaka, H. 2016, *ApJ*, 821, 82
- Ormel, C. W. & Klahr, H. H. 2010, *A&A*, 520, A43
- Osorio, M., Anglada, G., Carrasco-González, C., et al. 2014, *ApJ*, 791, L36
- Owen, J. E., Ercolano, B., & Clarke, C. J. 2011, *MNRAS*, 412, 13
- Paardekooper, D. M., Fedoseev, G., Riedo, A., & Linnartz, H. 2016, *A&A*, 596, A72

- Paardekooper, S. J. & Mellema, G. 2006, *A&A*, 453, 1129
- Pagani, L., Salez, M., & Wannier, P. G. 1992, *A&A*, 258, 479
- Paneque-Carreño, T., Miotello, A., van Dishoeck, E. F., et al. 2022, *A&A*, 666, A168
- Paneque-Carreño, T., Miotello, A., van Dishoeck, E. F., et al. 2023, *A&A*, 669, A126
- Paneque-Carreño, T., Pérez, L. M., Benisty, M., et al. 2021, *ApJ*, 914, 88
- Panić, O., Hogerheijde, M. R., Wilner, D., & Qi, C. 2008, *A&A*, 491, 219
- Pascucci, I., Cabrit, S., Edwards, S., et al. 2023, in *Astronomical Society of the Pacific Conference Series*, Vol. 534, *Protostars and Planets VII*, ed. S. Inutsuka, Y. Aikawa, T. Muto, K. Tomida, & M. Tamura, 567
- Payzant, J. D., Schiff, H. I., & Bohme, D. K. 1975, *J. Chem. Phys.*, 63, 149
- Pegues, J., Öberg, K. I., Bergner, J. B., et al. 2020, *ApJ*, 890, 142
- Penteado, E. M., Walsh, C., & Cuppen, H. M. 2017, *ApJ*, 844, 71
- Pérez, S., Casassus, S., Baruteau, C., et al. 2019, *AJ*, 158, 15
- Pérez, S., Casassus, S., Hales, A., et al. 2020, *ApJ*, 889, L24
- Perez, S., Casassus, S., Ménard, F., et al. 2015, *ApJ*, 798, 85
- Persson, M. V., Jørgensen, J. K., van Dishoeck, E. F., & Harsono, D. 2014, *A&A*, 563, A74
- Phillips, T. G., van Dishoeck, E. F., & Keene, J. 1992, *ApJ*, 399, 533
- Pickering, E. C. 1890, *Annals of Harvard College Observatory*, 18, 1
- Pickett, H. M., Poynter, R. L., Cohen, E. A., et al. 1998, *J. Quant. Spectr. Rad. Transf.*, 60, 883
- Pickles, A. J. 1998, *PASP*, 110, 863
- Picogna, G., Ercolano, B., Owen, J. E., & Weber, M. L. 2019, *MNRAS*, 487, 691
- Pineda, J. E., Szulágyi, J., Quanz, S. P., et al. 2019, *ApJ*, 871, 48
- Pinilla, P., Benisty, M., & Birnstiel, T. 2012a, *A&A*, 545, A81
- Pinilla, P., Birnstiel, T., Ricci, L., et al. 2012b, *A&A*, 538, A114
- Pinilla, P., Birnstiel, T., & Walsh, C. 2015, *A&A*, 580, A105
- Pinilla, P., Klarmann, L., Birnstiel, T., et al. 2016, *A&A*, 585, A35
- Pinilla, P., Pohl, A., Stammerl, S. M., & Birnstiel, T. 2017, *ApJ*, 845, 68

- Pinte, C., Ménard, F., Duchêne, G., et al. 2018a, *A&A*, 609, A47
- Pinte, C., Price, D. J., Ménard, F., et al. 2018b, *ApJ*, 860, L13
- Pinte, C., van der Plas, G., Ménard, F., et al. 2019, *Nat. Astron.*, 3, 1109
- Pirovano, L. M., Fedele, D., van Dishoeck, E. F., et al. 2022, *A&A*, 665, A45
- Podio, L., Garufi, A., Codella, C., et al. 2020, *A&A*, 642, L7
- Pollack, J. B., Hubickyj, O., Bodenheimer, P., et al. 1996, *ICARUS*, 124, 62
- Pontoppidan, K. M., Meijerink, R., Dullemond, C. P., & Blake, G. A. 2009, *ApJ*, 704, 1482
- Pringle, J. E. 1981, *ARA&A*, 19, 137
- Pyerin, M. A., Delage, T. N., Kurtovic, N. T., et al. 2021, *A&A*, 656, A150
- Qi, C., Öberg, K. I., Andrews, S. M., et al. 2015, *ApJ*, 813, 128
- Qi, C., Öberg, K. I., Espaillat, C. C., et al. 2019, *ApJ*, 882, 160
- Qi, C., Öberg, K. I., Wilner, D. J., et al. 2013, *Science*, 341, 630
- Quanz, S. P., Amara, A., Meyer, M. R., et al. 2013a, *ApJ*, 766, L1
- Quanz, S. P., Avenhaus, H., Buenzli, E., et al. 2013b, *ApJ*, 766, L2
- Rab, C., Kamp, I., Dominik, C., et al. 2020, *A&A*, 642, A165
- Rafikov, R. R. 2002, *ApJ*, 569, 997
- Rakshit, A. B. 1982, *International Journal of Mass Spectrometry and Ion Processes*, 41, 185
- Raman, A., Lisanti, M., Wilner, D. J., Qi, C., & Hogerheijde, M. 2006, *AJ*, 131, 2290
- Rameau, J., Follette, K. B., Pueyo, L., et al. 2017, *AJ*, 153, 244
- Redhead, P. A. 1962, *Vacuum*, 12, 203
- Regály, Z., Juhász, A., Sándor, Z., & Dullemond, C. P. 2012, *MNRAS*, 419, 1701
- Reggiani, M., Quanz, S. P., Meyer, M. R., et al. 2014, *ApJ*, 792, L23
- Rice, W. K. M., Armitage, P. J., Wood, K., & Lodato, G. 2006, *MNRAS*, 373, 1619
- Richard, D. & Zahn, J.-P. 1999, *A&A*, 347, 734
- Rivilla, V. M., Martín-Pintado, J., Jiménez-Serra, I., et al. 2020, *ApJ*, 899, L28
- Roberts, H., Herbst, E., & Millar, T. J. 2003, *ApJ*, 591, L41

- Robitaille, T. P. 2011, *A&A*, 536, A79
- Robitaille, T. P., Whitney, B. A., Indebetouw, R., Wood, K., & Denzmore, P. 2006, *ApJS*, 167, 256
- Rosotti, G. P., Juhasz, A., Booth, R. A., & Clarke, C. J. 2016, *MNRAS*, 459, 2790
- Roueff, E. & Le Bourlot, J. 1990, *A&A*, 236, 515
- Rubin, M., Altwegg, K., Balsiger, H., et al. 2019, *MNRAS*, 489, 594
- Ruíz-Rodríguez, D., Cieza, L. A., Williams, J. P., et al. 2017, *MNRAS*, 468, 3266
- Ruíz-Rodríguez, D. A., Williams, J. P., Kastner, J. H., et al. 2022, *MNRAS*, 515, 2646
- Salinas, V. N., Hogerheijde, M. R., Bergin, E. A., et al. 2016, *A&A*, 591, A122
- Sallum, S., Follette, K. B., Eisner, J. A., et al. 2015, *Nature*, 527, 342
- Salyk, C., Blake, G. A., Boogert, A. C. A., & Brown, J. M. 2009, *ApJ*, 699, 330
- Salyk, C., Herczeg, G. J., Brown, J. M., et al. 2013, *ApJ*, 769, 21
- Salyk, C., Lacy, J., Richter, M., et al. 2019, *ApJ*, 874, 24
- Salyk, C., Pontoppidan, K. M., Blake, G. A., et al. 2008, *ApJ*, 676, L49
- Sandell, G. & Weintraub, D. A. 2001, *ApJS*, 134, 115
- Sastry, K. V. L. N., Helminger, P., Charo, A., Herbst, E., & De Lucia, F. C. 1981, *ApJ*, 251, L119
- Schöier, F. L., van der Tak, F. F. S., van Dishoeck, E. F., & Black, J. H. 2005, *A&A*, 432, 369
- Schoonenberg, D. & Ormel, C. W. 2017, *A&A*, 602, A21
- Schroder, K., Staemmler, V., Smith, M. D., Flower, D. R., & Jaquet, R. 1991, *Journal of Physics B Atomic Molecular Physics*, 24, 2487
- Schwarz, K. R. & Bergin, E. A. 2014, *ApJ*, 797, 113
- Schwarz, K. R., Bergin, E. A., Cleeves, L. I., et al. 2016, *ApJ*, 823, 91
- Schwarz, K. R., Calahan, J. K., Zhang, K., et al. 2021, *ApJS*, 257, 20
- Schworer, G., Lacour, S., Huélamó, N., et al. 2017, *ApJ*, 842, 77
- Segura-Cox, D. M., Schmiedeke, A., Pineda, J. E., et al. 2020, *Nature*, 586, 228
- Semenov, D., Favre, C., Fedele, D., et al. 2018, *A&A*, 617, A28
- Semmoud-Monnanteuil, N., Colmont, J. M., Perrin, A., Flaud, J. M., & Camy-Peyret, C. 1989, *Journal of Molecular Spectroscopy*, 134, 176

- Shakura, N. I. & Sunyaev, R. A. 1973, *A&A*, 24, 337
- Shu, F. H. 1977, *ApJ*, 214, 488
- Shu, F. H., Adams, F. C., & Lizano, S. 1987, *ARA&A*, 25, 23
- Simon, M. N., Pascucci, I., Edwards, S., et al. 2016, *ApJ*, 831, 169
- Simons, M. A. J., Lamberts, T., & Cuppen, H. M. 2020, *A&A*, 634, A52
- Sissa, E., Gratton, R., Garufi, A., et al. 2018, *A&A*, 619, A160
- Skatrud, D. D., De Lucia, F. C., Blake, G. A., & Sastry, K. V. L. N. 1983, *Journal of Molecular Spectroscopy*, 99, 35
- Smirnov-Pinchukov, G. V., Semenov, D. A., Akimkin, V. V., & Henning, T. 2020, *A&A*, 644, A4
- Spielfiedel, A., Feautrier, N., Najjar, F., et al. 2012, *MNRAS*, 421, 1891
- Staemmler, V. & Flower, D. R. 1991, *Journal of Physics B Atomic Molecular Physics*, 24, 2343
- Stammler, S. M., Birnstiel, T., Panić, O., Dullemond, C. P., & Dominik, C. 2017, *A&A*, 600, A140
- Stapper, L. M., et al., & et al. 2023, TBD, in review, TBD
- Stapper, L. M., Hogerheijde, M. R., van Dishoeck, E. F., & Mentel, R. 2022, *A&A*, 658, A112
- Stelzer, B., Micela, G., Hamaguchi, K., & Schmitt, J. H. M. M. 2006, *A&A*, 457, 223
- Stevenson, D. J. & Lunine, J. I. 1988, *ICARUS*, 75, 146
- Stoll, M. H. R. & Kley, W. 2014, *A&A*, 572, A77
- Strom, K. M. & Strom, S. E. 1993, *ApJ*, 412, L63
- Sturm, B., Bouwman, J., Henning, T., et al. 2010, *A&A*, 518, L129
- Sturm, J. A., Booth, A. S., McClure, M. K., Leemker, M., & van Dishoeck, E. F. 2023a, *A&A*, 670, A12
- Sturm, J. A., McClure, M. K., Beck, T. L., et al. 2023b, arXiv e-prints, arXiv:2309.07817
- Sturm, J. A., McClure, M. K., Bergner, J. B., et al. 2023c, *A&A*, 677, A18
- Suzuki, T. K., Ogihara, M., Morbidelli, A., Crida, A., & Guillot, T. 2016, *A&A*, 596, A74
- Szulágyi, J., Plas, G. v. d., Meyer, M. R., et al. 2018, *MNRAS*, 473, 3573

- Tabone, B., Rosotti, G. P., Cridland, A. J., Armitage, P. J., & Lodato, G. 2022a, *MNRAS*, 512, 2290
- Tabone, B., Rosotti, G. P., Lodato, G., et al. 2022b, *MNRAS*, 512, L74
- Tanaka, H. & Ida, S. 1999, *ICARUS*, 139, 350
- Taquet, V., Ceccarelli, C., & Kahane, C. 2012, *A&A*, 538, A42
- Teague, R. 2020, *richteague/keplerian_mask*: Initial Release
- Teague, R., Bae, J., & Bergin, E. A. 2019, *Nature*, 574, 378
- Teague, R., Bae, J., Bergin, E. A., Birnstiel, T., & Foreman-Mackey, D. 2018a, *ApJ*, 860, L12
- Teague, R., Guilloteau, S., Semenov, D., et al. 2016, *A&A*, 592, A49
- Teague, R., Henning, T., Guilloteau, S., et al. 2018b, *ApJ*, 864, 133
- Teague, R., Semenov, D., Guilloteau, S., et al. 2015, *A&A*, 574, A137
- Temmink, M., Booth, A. S., van der Marel, N., & van Dishoeck, E. F. 2023, *A&A*, 675, A131
- Terebey, S., Shu, F. H., & Cassen, P. 1984, *ApJ*, 286, 529
- Terwisscha van Scheltinga, J., Hogerheijde, M. R., Cleeves, L. I., et al. 2021, *ApJ*, 906, 111
- Testi, L., Birnstiel, T., Ricci, L., et al. 2014, in *Protostars and Planets VI*, ed. H. Beuther, R. S. Klessen, C. P. Dullemond, & T. Henning, 339–361
- Thalmann, C., Janson, M., Garufi, A., et al. 2016, *ApJ*, 828, L17
- Thalmann, C., Mulders, G. D., Hodapp, K., et al. 2014, *A&A*, 566, A51
- Theard, L. P. & Huntress, W. T. 1974, *J. Chem. Phys.*, 60, 2840
- Thi, W. F., Mathews, G., Ménard, F., et al. 2010, *A&A*, 518, L125
- Thi, W. F., Woitke, P., & Kamp, I. 2011, *MNRAS*, 412, 711
- Thommes, E. W., Duncan, M. J., & Levison, H. F. 2003, *ICARUS*, 161, 431
- Tielens, A. G. G. M. 2003, *Science*, 300, 68
- Tielens, A. G. G. M. & Hagen, W. 1982, *A&A*, 114, 245
- Tobin, J. J., Hartmann, L., Chiang, H.-F., et al. 2012, *Nature*, 492, 83
- Tobin, J. J., Sheehan, P. D., Megeath, S. T., et al. 2020, *ApJ*, 890, 130
- Tobin, J. J., van't Hoff, M. L. R., Leemker, M., et al. 2023, *Nature*, 615, 227

- Toci, C., Lodato, G., Fedele, D., Testi, L., & Pinte, C. 2020, *ApJ*, 888, L4
- Trapman, L., Miotello, A., Kama, M., van Dishoeck, E. F., & Bruderer, S. 2017, *A&A*, 605, A69
- Trapman, L., Rosotti, G., Bosman, A. D., Hogerheijde, M. R., & van Dishoeck, E. F. 2020, *A&A*, 640, A5
- Trapman, L., Tabone, B., Rosotti, G., & Zhang, K. 2022, *ApJ*, 926, 61
- Tripathi, A., Andrews, S. M., Birnstiel, T., & Wilner, D. J. 2017, *ApJ*, 845, 44
- Tschudi, C. & Schmid, H. M. 2021, *A&A*, 655, A37
- Tsegaw, Y. A., Góbi, S., Förstel, M., et al. 2017, *Journal of Physical Chemistry A*, 121, 7477
- Tsunekawa, S. 1972, *Journal of the Physical Society of Japan*, 33, 167
- Tychoniec, Ł., Manara, C. F., Rosotti, G. P., et al. 2020, *A&A*, 640, A19
- Tychoniec, Ł., Tobin, J. J., Karska, A., et al. 2018, *ApJS*, 238, 19
- Uribe, A., Bans, A., & Königl, A. 2015, *ApJ*, 802, 54
- van Broekhuizen, F. A., Pontoppidan, K. M., Fraser, H. J., & van Dishoeck, E. F. 2005, *A&A*, 441, 249
- van der Marel, N., Birnstiel, T., Garufi, A., et al. 2021a, *AJ*, 161, 33
- van der Marel, N., Booth, A. S., Leemker, M., van Dishoeck, E. F., & Ohashi, S. 2021b, *A&A*, 651, L5
- van der Marel, N., Bosman, A. D., Krijt, S., Mulders, G. D., & Bergner, J. B. 2021c, *A&A*, 653, L9
- van der Marel, N., van Dishoeck, E. F., Bruderer, S., et al. 2016, *A&A*, 585, A58
- van der Marel, N., van Dishoeck, E. F., Bruderer, S., et al. 2013, *Science*, 340, 1199
- van der Marel, N., van Dishoeck, E. F., Bruderer, S., Pérez, L., & Isella, A. 2015, *A&A*, 579, A106
- van der Marel, N., Williams, J. P., Ansdell, M., et al. 2018, *ApJ*, 854, 177
- van Dishoeck, E. F. 2014, *Faraday Discussions*, 168, 9
- van Dishoeck, E. F., Herbst, E., & Neufeld, D. A. 2013, *Chemical Reviews*, 113, 9043
- van Dishoeck, E. F., Jonkheid, B., & van Hemert, M. C. 2006, *Faraday Discussions*, 133, 231

- van Dishoeck, E. F., Kristensen, L. E., Mottram, J. C., et al. 2021, *A&A*, 648, A24
- van Gelder, M. L., Tabone, B., Tychoniec, L., et al. 2020, *A&A*, 639, A87
- van Kempen, T. A., van Dishoeck, E. F., Salter, D. M., et al. 2009, *A&A*, 498, 167
- van 't Hoff, M. L. R., Persson, M. V., Harsono, D., et al. 2018a, *A&A*, 613, A29
- van 't Hoff, M. L. R., Tobin, J. J., Trapman, L., et al. 2018b, *ApJ*, 864, L23
- van 't Hoff, M. L. R., Walsh, C., Kama, M., Facchini, S., & van Dishoeck, E. F. 2017, *A&A*, 599, A101
- van Terwisga, S. E., Hacar, A., van Dishoeck, E. F., Oonk, R., & Portegies Zwart, S. 2022, *A&A*, 661, A53
- van Terwisga, S. E., van Dishoeck, E. F., Ansdell, M., et al. 2018, *A&A*, 616, A88
- van Terwisga, S. E., van Dishoeck, E. F., Cazzoletti, P., et al. 2019, *A&A*, 623, A150
- van Zadelhoff, G. J., Aikawa, Y., Hogerheijde, M. R., & van Dishoeck, E. F. 2003, *A&A*, 397, 789
- van Zadelhoff, G. J., van Dishoeck, E. F., Thi, W. F., & Blake, G. A. 2001, *A&A*, 377, 566
- van't Hoff, M. L. R., Harsono, D., Tobin, J. J., et al. 2020, *ApJ*, 901, 166
- Varberg, T. D., Stroh, F., & Evenson, K. M. 1999, *Journal of Molecular Spectroscopy*, 196, 5
- Villenave, M., Ménard, F., Dent, W. R. F., et al. 2020, *A&A*, 642, A164
- Visser, R. & Bergin, E. A. 2012, *ApJ*, 754, L18
- Visser, R., Bergin, E. A., & Jørgensen, J. K. 2015, *A&A*, 577, A102
- Visser, R., Bruderer, S., Cazzoletti, P., et al. 2018, *A&A*, 615, A75
- Visser, R., Geers, V. C., Dullemond, C. P., et al. 2007, *A&A*, 466, 229
- Visser, R., van Dishoeck, E. F., Doty, S. D., & Dullemond, C. P. 2009, *A&A*, 495, 881
- Vorobyov, E. I., Baraffe, I., Harries, T., & Chabrier, G. 2013, *A&A*, 557, A35
- Wada, K., Tanaka, H., Suyama, T., Kimura, H., & Yamamoto, T. 2008, *ApJ*, 677, 1296
- Wada, K., Tanaka, H., Suyama, T., Kimura, H., & Yamamoto, T. 2011, *ApJ*, 737, 36

- Wagner, K. R., Sitko, M. L., Grady, C. A., et al. 2015, *ApJ*, 798, 94
- Wakelam, V., Herbst, E., Loison, J.-C., et al. 2012, *ApJS*, 199, 21
- Wakelam, V., Loison, J. C., Mereau, R., & Ruaud, M. 2017, *Molecular Astrophysics*, 6, 22
- Walsh, C., Juhász, A., Pinilla, P., et al. 2014a, *ApJ*, 791, L6
- Walsh, C., Millar, T. J., & Nomura, H. 2013, *ApJ*, 766, L23
- Walsh, C., Millar, T. J., Nomura, H., et al. 2014b, *A&A*, 563, A33
- Walsh, C., Nomura, H., Millar, T. J., & Aikawa, Y. 2012, *ApJ*, 747, 114
- Walsh, C., Nomura, H., & van Dishoeck, E. 2015, *A&A*, 582, A88
- Watanabe, N. & Kouchi, A. 2002, *ApJ*, 571, L173
- Watson, W. D. 1976, *Reviews of Modern Physics*, 48, 513
- Weaver, E., Isella, A., & Boehler, Y. 2018, *ApJ*, 853, 113
- Wei, C.-E., Nomura, H., Lee, J.-E., et al. 2019, *ApJ*, 870, 129
- Weidenschilling, S. J. 1977, *MNRAS*, 180, 57
- Weingartner, J. C. & Draine, B. T. 2001, *ApJS*, 134, 263
- Whipple, F. L. 1972, in *From Plasma to Planet*, ed. A. Elvius, 211
- Williams, J. P., Bergin, E. A., Caselli, P., Myers, P. C., & Plume, R. 1998, *ApJ*, 503, 689
- Wilson, T. L. 1999, *Reports on Progress in Physics*, 62, 143
- Wilson, T. L. & Rood, R. 1994, *ARA&A*, 32, 191
- Woitke, P., Kamp, I., & Thi, W. F. 2009, *A&A*, 501, 383
- Woitke, P., Min, M., Pinte, C., et al. 2016, *A&A*, 586, A103
- Wölfer, L., et al., & et al. 2023a, TBD, in prep, TBD
- Wölfer, L., Facchini, S., Kurtovic, N. T., et al. 2021, *A&A*, 648, A19
- Wölfer, L., Facchini, S., van der Marel, N., et al. 2023b, *A&A*, 670, A154
- Wolk, S. J. & Walter, F. M. 1996, *AJ*, 111, 2066
- Woodall, J., Agúndez, M., Markwick-Kemper, A. J., & Millar, T. J. 2007, *A&A*, 466, 1197
- Xu, L.-H., Fisher, J., Lees, R. M., et al. 2008, *Journal of Molecular Spectroscopy*, 251, 305

- Xu, W. & Kunz, M. W. 2021a, MNRAS, 502, 4911
- Xu, W. & Kunz, M. W. 2021b, MNRAS, 508, 2142
- Yang, B., Stancil, P. C., Balakrishnan, N., & Forrey, R. C. 2010, ApJ, 718, 1062
- Yang, L., Ciesla, F. J., & Alexander, C. M. O. D. 2013, ICARUS, 226, 256
- Yang, Y.-L., Green, J. D., Pontoppidan, K. M., et al. 2022, ApJ, 941, L13
- Yen, H.-W., Koch, P. M., Liu, H. B., et al. 2016, ApJ, 832, 204
- Yen, H.-W., Koch, P. M., Manara, C. F., Miotello, A., & Testi, L. 2018, A&A, 616, A100
- Yıldız, U. A., Acharyya, K., Goldsmith, P. F., et al. 2013, A&A, 558, A58
- Yorke, H. W., Bodenheimer, P., & Laughlin, G. 1993, ApJ, 411, 274
- Youdin, A. N. & Goodman, J. 2005, ApJ, 620, 459
- Zhang, K., Bergin, E. A., Blake, G. A., Cleeves, L. I., & Schwarz, K. R. 2017, Nature Astronomy, 1, 0130
- Zhang, K., Blake, G. A., & Bergin, E. A. 2015, ApJ, 806, L7
- Zhang, K., Booth, A. S., Law, C. J., et al. 2021, ApJS, 257, 5
- Zhang, K., Pontoppidan, K. M., Salyk, C., & Blake, G. A. 2013, ApJ, 766, 82
- Zhang, S., Zhu, Z., Huang, J., et al. 2018, ApJ, 869, L47
- Zheng, W. & Kaiser, R. I. 2010, The Journal of Physical Chemistry A, 114, 5251, pMID: 20373797
- Zhou, Y., Bowler, B. P., Yang, H., et al. 2023, arXiv e-prints, arXiv:2308.16223
- Zhu, Z., Nelson, R. P., Dong, R., Espaillat, C., & Hartmann, L. 2012, ApJ, 755, 6
- Zhu, Z. & Stone, J. M. 2018, ApJ, 857, 34
- Zhu, Z., Stone, J. M., Rafikov, R. R., & Bai, X.-n. 2014, ApJ, 785, 122
- Zhu, Z., Zhang, S., Jiang, Y.-F., et al. 2019, ApJ, 877, L18
- Ziurys, L. M., Apponi, A. J., Hollis, J. M., & Snyder, L. E. 1994, ApJ, 436, L181

Nederlandse samenvatting

Naar de sterrenhemel boven ons kijken is iets wat mensen al eeuwen lang doen. Zo lang al dat er aanwijzingen zijn dat de gebouwen uit de prehistorie werden gebruikt om te zien wanneer een belangrijke en heldere ster opkwam of onderging. 's Nachts kijken naar de sterren heeft ons niet alleen een klok gebracht, maar ook ook de vraag: zijn wij alleen of is er ook ergens anders in leven in het heelal?

Op dit moment zijn er meer dan 5500 exoplaneten gevonden en de zoektocht naar nieuwe planeten gaat door. Genoeg plekken dus waar mogelijk leven zou kunnen zijn. Toch zijn de meeste van die planeten heel anders dan de Aarde. Sommigen zijn veel zwaarder, zoals Jupiter, en staan heel dicht bij de ster waardoor ze in minder dan één Aardse dag om hun ster draaien. Anderen staan juist heel ver weg en doen meer dan duizend Aardse jaren over één jaar in hun systeem. Van de meer dan 5500 ontdekte planeten zijn er maar zo'n 200 die lijken op de Aarde. Is de Aarde dan toch uniek? Of zijn er andere planeten die over alle ingrediënten beschikken om leven te laten ontstaan. En wat bepaalt welke ingrediënten aanwezig zijn op een planeet?

Om die vragen te kunnen beantwoorden hebben we krachtige telescopen nodig. Sommige van deze telescopen kunnen we richten op de exoplaneten die we al gevonden hebben om te bepalen of ze een atmosfeer hebben en of de gassen in die atmosfeer giftig zijn voor leven zoals we het kennen, of dat er misschien een kans is dat er leven op die planeet is of kan ontstaan. Andere telescopen kijken naar de plek waar jonge sterren en planeten geboren worden omdat het bestuderen van het gas en stof rond een jonge ster ons kan vertellen welke ingrediënten we kunnen verwachten op planeten. Waarnemingen laten zien dat sterren en planeten tegelijkertijd vormen en dat om zo'n jonge ster een schijf van gas en stof met een laagje ijs ronddraait. Een deel van het gas en stof in de schijf valt op de ster, en een ander deel vormt planeten of wordt weggeblazen.

Dit proefschrift richt zich op de vraag wat de chemische samenstelling is van het gas en ijs in protoplanetaire schijven. Een combinatie van waarnemingen en chemische modellen wordt gebruikt om deze vragen op te helderen. De waarnemingen laten zien dat bijna geen enkele schijf glad is, bijna elke schijf heeft ringen, gaten en bogen waar meer stof of een bepaald soort gas aanwezig is. Schijven met grote centrale gaten ("holtes") noemen we ook wel overgangsschijven. Deze structuren zouden veroorzaakt kunnen worden door planeten maar ook andere



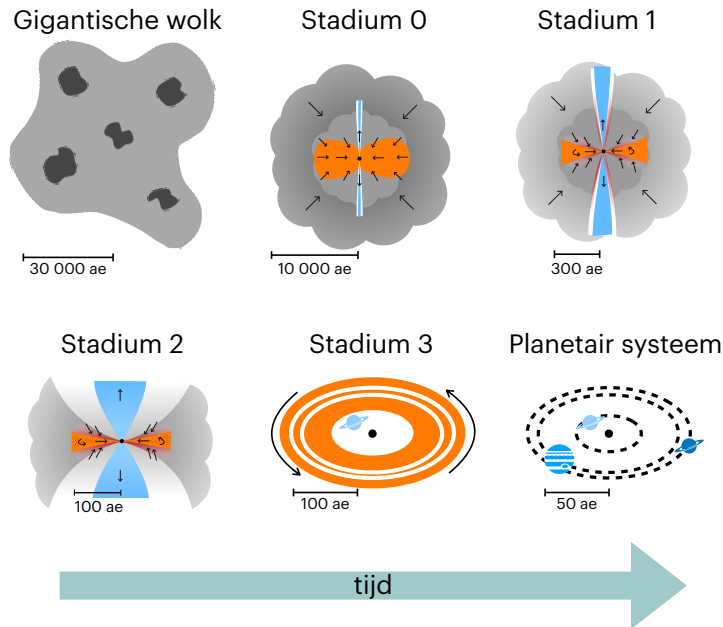
Figuur 1: Infrarood waarneming met JWST van de pilaren van creatie, een gigantische moleculaire wolk. In de donker bruine, compacte gebieden vormen jonge sterren. Afbeelding van: NASA, ESA, CSA, STScI.

processen kunnen een rol spelen. Dit proefschrift onderzoekt de oorzaak van deze structuren – planeten, een verandering in de dichtheid, of chemie – door te kijken naar verschillende moleculen in de gasfase en deze te vergelijken met het stof.

Jonge sterren

Jonge sterren worden geboren in hele grote moleculaire wolken, zie Fig. 1. Deze wolken bestaan uit koud gas en kleine stofdeeltjes met een laag ijs. Op sommige plekken is meer gas aanwezig dan op andere plekken. Onder bepaalde omstandigheden kunnen deze gebieden instorten waardoor deze niet alleen kleiner, maar ook warmer worden. In het centrum van de kern ontstaat een jonge protoster met daaromheen een protoplanetaire schijf. In deze schijf zit al het materiaal met een groot hoekmoment, omdat de wetten van de natuurkunde voorschrijven dat het hoekmoment behouden moet blijven.

De evolutie van een gigantische moleculaire wolk naar een planetair systeem wordt gepresenteerd in Fig. 2. De fase van de gigantische moleculaire wolk met vijf kernen is schematisch weergegeven in de linker bovenhoek. Stadium 0 laat zien hoe een ineengestorte kern eruit ziet. In het centrum is een jonge protoster aanwezig met daaromheen een schijf van gas en stof waar materiaal van de wolk op regent, maar die zelf ook uitregent op de protoster. Een deel van het materiaal van de schijf valt echter niet op de ster maar wordt via een straalstroom weggeblazen uit het systeem. Naar mate het systeem ouder wordt, wordt het materiaal dat de ster en de schijf omhult minder en wordt de straalstroom breder, zie Stadium 1.



Figuur 2: De evolutie van een gigantische moleculaire wolk naar een planetair systeem. Figuur aangepast van M. Persson.

In Stadium 2 wordt de protoplanetaire schijf goed zichtbaar. In deze schijf zijn planeten aan het vormen en tegelijkertijd wordt een deel van het gas weggeblazen door de ster. Wanneer bijna al het gas en stof van de schijf verwijderd is, wordt er gesproken van een systeem in Stadium 3. Uiteindelijk is al het gas en stof verdwenen en blijft de ster met één of meer planeten over.

Protoplanetaire schijven

Protoplanetaire schijven zijn geen statische objecten maar evolueren van een jonge schijf met veel gas en stof naar een schijf die voornamelijk bestaat uit overgebleven puin over een tijdschaal van een paar miljoen jaar. Wat het mechanisme is achter de evolutie van de schijf is nog niet bekend maar er zijn twee theoriën die mogelijk allebei belangrijk zijn. Wat de theoriën gemeen hebben is dat ze een manier hebben gevonden om het hoekmoment van het materiaal in de schijf te veranderen, dit is cruciaal omdat de schijf anders altijd blijft draaien zoals die dat in het begin deed. De eerste theorie is de visceuse evolutie van de schijf. Het gas dichtbij de ster draait sneller rond dan het gas ver weg. Hierdoor ontstaat wrijving tussen twee gedeeltes van het gas die tegen elkaar aan schuren. Dit versnelt het gas verder weg van de ster en vertraagt het gas dichterbij. Hierdoor wordt het hoekmoment van de schijf effectief naar buiten getransporteerd en kan het materiaal in het binnenste



Figuur 3: Artistieke afbeelding van een warme protoplanetaire schijf. Dichtbij de ster in het oranje gebied is het warm waardoor bijna alle moleculen, inclusief water, in de gasfase zijn. Verder weg van de ster is de schijf kouder (witte gebied) en is water bevroren. De overgang tussen deze twee gebieden is de watersneeuwlijn. De ringen in deze schijf zouden veroorzaakt kunnen worden door onder andere planeten. Afbeelding van ESO/L. Calçada.

van de schijf op de ster vallen. Een andere manier om hoekmoment te verplaatsen is door een wind vanaf het oppervlak te laten waaien. Dit kan als een magnetisch veld aanwezig is en het gas in de bovenste lagen geïoniseerd is. De hoeveelheid gas die met de wind meegevoerd wordt is klein maar het hoekmoment hiervan is relatief groot. Hierdoor kan de rest van de schijf verder evolueren.

Tijdens deze evolutie van de schijf groeit het stof groter tot deeltjes van 1 cm, 1 m en waarschijnlijk nog groter tot de grootte van rotsachtige planeten. Hoe dit precies gebeurt wordt op dit moment actief onderzocht. Het is waarschijnlijk dat er speciale plekken zijn in de schijf waar het stof groter kan groeien en niet naar binnen drijft door de continue tegenwind van het gas dat net wat langzamer ronddraait dan het stof. Een van de plekken waar planeten mogelijk makkelijker kunnen vormen is net buiten de watersneeuwlijn, de plek in de schijf waar water bevroert. Voor sterren die lichter zijn dan onze zon ligt dit op ongeveer dezelfde afstand als de Aarde, een afstand die voor sterrenkundige begrippen extreem dichtbij is en dus moeilijk te zien is met telescopen. Daarom wordt vaak naar zwaardere sterren of zelfs uitbarstende sterren gekeken waar de sneeuwlijn verder weg ligt en ook andere moleculen beter waar te nemen zijn, een voorbeeld hiervan is te zien in Fig. 3 waar de sneeuwlijn ten minste even ver van de ster ligt als Pluto van onze zon staat.

Dit proefschrift

Dit proefschrift richt zich op de temperatuur structuur in protoplanetaire schijven en hoe deze zich verhoudt tot de structuren in de emissie van verschillende moleculen in de gasfase en het stof. Kennis van de temperatuur structuur in protoplanetaire schijven is cruciaal om de hoeveelheid gas en de chemische samenstelling daarvan te bepalen. De hoofdvragen die in dit proefschrift behandeld worden zijn:

- Waar bevriest water in een protoplanetaire schijf en hoe kunnen we deze locatie vinden?
- Worden de grote centrale holtes in overgangsschijven gevormd door planeten of door andere processen?
- Wat is de relatie tussen de structuren die te zien zijn in het stof en in verschillende moleculen?

Hoofdstuk 2 gaat in op de eerste vraag: hoe kan de watersneeuwlijn gelokaliseerd worden in een protoplanetaire schijf. Het waarnemen van water (H_2O) en water isotopologen (bv. H_2^{18}O) vanaf de Aarde is lastig omdat er veel water in onze atmosfeer zit dat de emissie van water in een protoplanetaire schijf blokkeert. Telescopen in de ruimte missen echter de spatiële resolutie om de watersneeuwlijn ruimtelijk op te kunnen lossen. Om deze redenen richt dit hoofdstuk zich op het chemisch modelleren van een molecuul dat vernietigd wordt door water in de gasfase: HCO^+ en de isotopoloog H^{13}CO^+ . Een thermo-chemisch model wordt gekoppeld aan een chemisch netwerk speciaal voor HCO^+ om synthetische waarnemingen te maken. Deze resultaten laten zien dat hoge resolutie waarnemingen van HCO^+ kunnen worden gebruikt om de water sneeuwlijn te vinden in protoplanetaire schijven waarbij de water sneeuwlijn op een plek ligt waar niet al te veel stof aanwezig is. De toepassing van deze methode op een hete schijf rond een uitbarstende ster waar twee conflicterende locaties voor de watersneeuwlijn zijn gevonden, één op basis van het stof en één op basis van methanol in de gasfase, laat zien dat waarnemingen van gasfase moleculen cruciaal zijn om de watersneeuwlijn te vinden.

Hoofdstuk 3 gaat dieper in op de precieze locatie van de watersneeuwlijn in deze schijf door de 2D verdeling van HDO, een isotopoloog van water, te bestuderen. Door in detail te kijken naar de structuur van de HDO emissie op elke gemeten snelheid, kan de plek waar HDO emissie vandaan komt in straal en hoogte boven het middenvlak van de schijf bepaald worden. Deze methode laat het verrassende resultaat zien dat het sneeuwoppervlak, de 2D equivalent van de sneeuwlijn, bijna verticaal is. Verder is de locatie van het gevonden oppervlak consistent met de resultaten uit Hoofdstuk 2. Een zelfde analyse voor methanol, een molecuul dat op een net iets lagere temperatuur sublimiert dan water, laat een vergelijkbaar resultaat zien: een bijna verticaal oppervlak. Het oppervlak van methanol ligt ongeveer 10 tot 20 ae verder van de ster dan dat van water. Dit laat direct zien dat elk molecuul op zijn eigen temperatuur sublimiert en dat het ijs op stofdeeltjes

mogelijk bestaat uit verschillende lagen in plaats van dat het ijs een mix is van alle moleculen samen.

Hoofdstuk 4 richt zich op de tweede vraag die in dit proefschrift behandeld wordt. Bijna alle heldere en zware protoplanetaire schijven die worden waargenomen met ALMA laten structuren zien zoals ringen, gaten, holtes en bogen. Deze structuren zouden gevormd kunnen worden door zware planeten, maar op dit moment is maar in één schijf overvloedig bewijs voor actief vormende planeten gevonden terwijl een handvol andere schijven veelbelovende signalen laten zien. Dit hoofdstuk meet de hoeveelheid gas in de holtes in twee overgangsschijven en daarmee de massa van de planeten als die er zijn. Om de hoeveelheid gas te bepalen is kennis van de temperatuur van dat gas cruciaal. Dit hoofdstuk laat zien dat het gas in de holtes van de twee bestudeerde schijven warm is. Toch zijn de schijven ook verschillend omdat de ene schijf waarschijnlijk een zware planeet heeft terwijl de andere meerdere lichte planeten heeft gevormd.

Hoofdstuk 5 richt zich op de derde en laatste vraag die in dit proefschrift centraal staat. Waarnemingen van de asymmetrische schijf Oph-IRS 48 laten zien dat het mm-stof extreem asymmetrisch is terwijl er geen indicaties zijn dat het gas dat ook is. De grote verscheidenheid aan moleculen die alleen worden gezien op de plek van het stof en niet in andere delen van de schijf laat zien dat de stofval een ijsval is. In dit hoofdstuk wordt de eerste detectie van NO gemodelleerd met behulp van een thermo-chemisch model. Deze modellen reproduceren de emissie van de andere bestudeerde moleculen, maar om de emissie van NO te verklaren moet extra NO toegevoegd worden aan de begincondities van het netwerk. Dit wordt verklaard door het sublimeren van stikstofdragende moleculen in het ijs. Het gebrek aan CN in deze schijf laat zien dat het planeet-vormende materiaal rijk is aan zuurstof en arm in koolstof, twee van de cruciale elementen voor leven op Aarde.

Het laatste hoofdstuk, Hoofdstuk 6, richt zich op de correlatie tussen structuren in het stof en in het gas gezien in verschillende moleculen. De schijf die bestudeerd wordt is een overgangsschijf met een stofring relatief dichtbij de ster (20 – 40 ae) en een tweede stofring op ongeveer 200 ae. Deze tweede ring is heel licht, met een massa < 1% van de massa van de binnenste ring. Toch laten ALMA waarnemingen zien dat de moleculen goed te zien zijn in *allebei* de ringen ondanks het grote verschil in massa en afstand tot de ster voor allebei de ringen. Met behulp van thermo-chemische modellen wordt de meest voor de hand liggende verklaring voor de dubbele ring structuur in de moleculen uitgesloten: de CO isotopologen laten geen bewijs zien voor een gebrek aan gas tussen de stofringen. Het variëren van andere parameters in de modellen laat zien dat de voorspelde locatie van moleculaire ringen over het algemeen niet overeen komt met de plek van stofringen tenzij er bijvoorbeeld geen gas is tussen de stofringen of de chemische samenstelling in de ringen anders is dan daarbuiten. Om de waarnemingen in de HD 100546 schijf te verklaren is een combinatie nodig van model parameters waaronder een bijna perfect gebalanceerde hoeveelheid koolstof en zuurstof atomen in de ringen.

Toekomstperspectief

ALMA heeft onze ogen geopend voor de fysische en chemische structuren in protoplanetaire schijven. Waarnemingen richtten zich tot nu toe vooral op de grootste en helderste schijven, maar nieuwe programma's om de chemie in een grotere groep schijven te bestuderen worden nu waargenomen zoals het DECO programma in navolging van MAPS. Toch blijven studies die één bron in detail bestuderen onmisbaar omdat hier nieuwe fenomenen zoals een ijssval ontdekt kunnen worden. Daarbij zijn diepe waarnemingen onmisbaar om zwakke emissielijnen die veel informatie bevatten te detecteren.

De kracht van ALMA is niet alleen de hoge spatiële resolutie om de emissie ruimtelijk op te lossen maar ook de resolutie langs de frequentie-as. Hierdoor kan de snelheid van het gas nauwkeurig gemeten worden waardoor verstoringen in de snelheid van het gas door planeten gemeten kunnen worden. Daarbij kunnen ook verstoringen op grote schaal gemeten worden, zo kan bepaald worden of bijvoorbeeld de gehele schijf instabiel is.

De waarnemingen met ALMA zijn vooral gevoelig voor het buitenste gedeelte van protoplanetaire schijven. De recent gelanceerde JWST ruimtetelescoop is gevoelig voor de binnenste, warme gedeeltes van de schijf. De combinatie van deze twee telescopen geeft de mogelijkheid om een veel completer beeld te krijgen van de chemische samenstelling van de schijven en of deze samenstelling anders is in de binnenste gedeeltes dan in de buitenste gedeeltes. Bovendien kan met de JWST de samenstelling van het ijs bepaald worden, iets wat cruciaal is om te bepalen welke ingrediënten op een vormende planeet terechtkomen. Verder zal de ELT de plek in schijven kunnen laten zien waar Aardachtige planeten waarschijnlijk vormen. Met al deze nieuwe mogelijkheden zal er de komende jaren een nieuwe wereld aan planeetvorming te ontdekken zijn.

Publications

Refereed publications as first author

1. *A major asymmetric ice trap in a planet-forming disk. IV. Nitric oxide gas and a lack of CN tracing sublimating ices and a C/O ratio < 1*
Leemker, M., Booth, A. S., van Dishoeck, E. F., van der Marel, N., Tabone, B., Ligterink, N. F. W., Brunken, N. G. C., and Hogerheijde, M. R., 2023, *Astronomy & Astrophysics*, 673, 7.
2. *Gas temperature structure across transition disk cavities*
Leemker, M., Booth, A. S., van Dishoeck, E. F., Pérez-Sánchez, A. F., Szulágyi, J., Bosman, A. D., Bruderer, S., Facchini, S., Hogerheijde, M. R., Paneque-Carreño, T., and Sturm, J. A., 2022, *Astronomy & Astrophysics*, 663, 23.
3. *Chemically tracing the water snowline in protoplanetary disks with HCO⁺*
Leemker, M., van 't Hoff, M. L. R., Trapman, L., van Gelder, M. L., Hogerheijde, M. R., Ruíz-Rodríguez, D. A., and van Dishoeck, E. F., 2021, *Astronomy & Astrophysics*, 646, 3.

Submitted publications as first author

1. *Chemistry across dust and gas gaps in protoplanetary disks: modelling the co-spatial molecular rings in the HD 100546 disk*
Leemker, M., Booth, A. S., van Dishoeck, E. F., Wölfer, L., and Dent, B., submitted to *Astronomy & Astrophysics*.

Refereed publications as co-author

1. *Constraining the gas mass of Herbig disks using CO isotopologues*
Stapper, L. M., Hogerheijde, M. R., van Dishoeck, E. F., Lin, L., Ahmadi, A.,

- Booth, A. S., Grant, S. L., Immer, K., **Leemker, M.**, and Pérez-Sánchez, A. F., accepted for publication in *Astronomy & Astrophysics*.
2. *Tracing snowlines and C/O ratio in a planet-hosting disk. ALMA molecular line observations towards the HD 169142 disk*
Booth, A. S., Law, C. J., Temmink, M., **Leemker, M.**, and Macías, E., 2023, *Astronomy & Astrophysics*, 678, 146.
 3. *Deuterium-enriched water ties planet-forming disks to comets and protostars*
Tobin, J. J., van 't Hoff, M. L. R., **Leemker, M.**, van Dishoeck, E. F., Paneque-Carreño, T., Furuya, K., Harsono, D. Persson, M. V., Cleeves, L. I., Sheehan, P. D., and Cieza, L., 2023, *Nature*, 615, 7951.
 4. *Disentangling the protoplanetary disk gas mass and carbon depletion through combined atomic and molecular tracers*
Sturm, J. A., Booth, A. S., McClure, M. K., **Leemker, M.**, and van Dishoeck, E. F., 2023, *Astronomy & Astrophysics*, 670, 12.
 5. *A chemical map of the outbursting V883 Ori system: vertical and radial structures*
Ruíz-Rodríguez, D. A., Williams, J. P., Kastner, J. H., Cieza, L., **Leemker, M.**, and Principe, D. A., 2022, *Monthly Notices of the Royal Astronomical Society*, 515, 2.
 6. *The young embedded disk L1527 IRS: Constraints on the water snowline and cosmic-ray ionization rate from HCO⁺ observations*
van 't Hoff, M. L. R., **Leemker, M.**, Tobin, J. J., Harsono, D., Jørgensen, J. K., and Bergin, E. A., 2022, *The Astrophysical Journal*, 932, 1.
 7. *A major asymmetric ice trap in a planet-forming disk. III. First detection of dimethyl ether*
Brunken, N. G. C., Booth, A. S., **Leemker, M.**, Nazari, P., van der Marel, N., and van Dishoeck, E. F., 2022, *Astronomy & Astrophysics*, 659, A29.
 8. *A major asymmetric ice trap in a planet-forming disk. II. Prominent SO and SO₂ pointing to C/O < 1*
Booth, A. S., van der Marel, N., **Leemker, M.**, van Dishoeck, E. F., and Ohashi, S., 2021, *Astronomy & Astrophysics*, 651, L6.
 9. *A major asymmetric ice trap in a planet-forming disk. I. Formaldehyde and methanol*
van der Marel, N., Booth, A. S., **Leemker, M.**, van Dishoeck, E. F., and Ohashi, S., 2021, *Astronomy & Astrophysics*, 651, L5.

Submitted publications as co-author

1. *An ALMA molecular inventory of warm Herbig Ae disks: I. Molecular rings, asymmetries and complexity in the HD 100546 disk*

Booth, A. S., **Leemker, M.**, van Dishoeck, E. F., Evans, L., Ilee, J. D., Kama, M., Keyte, L., Law, C. J., van der Marel, N., Temmink, M., Nomura, H., Notsu, S., Öberg, K. I., and Walsh., C., submitted to the *Astrophysical Journal*.

2. *An ALMA molecular inventory of warm Herbig Ae disks: II. Abundant complex organics and volatile sulphur in the IRS 48 disk*

Booth, A. S., Temmink, M., van Dishoeck, E. F., Evans, L., Ilee, J. D., Kama, M., Keyte, L., Law, C. J., **Leemker, M.**, van der Marel, N., Nomura, H., Notsu, S., Öberg, K. I., and Walsh., C., submitted to the *Astrophysical Journal*.

Curriculum Vitae

On April second 1996, a day with typical Dutch weather semi-cloudy and cold, I was born in Zwijndrecht in the Netherlands. Not too long after that I moved to Ridderkerk to spend half of my weekends with my dad and step-mom, and to The Hague to spend the rest of the time with my mom. During this time I got to enjoy a big city near the sea and a small and quiet town with a house and a garden. I also remember watching TV shows about the universe and science after school when I was not swimming, doing gymnastics, making jigsaw puzzles or postcards. I was always interested in the questions starting with 'why' and 'how' things work.

The choice of my favourite high school was not difficult after I spent hours making jewellery, seeing a shape memory alloy, i.e., a piece of metal that you could bend in a certain shape, but would return to its original form when heated, and other things at the open day of the 'Christelijk College De Populier' in The Hague, right till I had to leave the building because the open day had ended already some time ago. This also, unsurprisingly, turned out to be my favourite course during the first three years. In addition to this science course, I loved all the courses that used numbers in one way or another and were challenging me to think about the problem I was solving, like math, physics, and chemistry but also biology and natural sciences. In addition to my regular high school classes, I took two courses offered by the LAPTop program of Leiden University. In my fifth year I took physics and in my final year I took Astronomy, both of which I enjoyed a lot.

Choosing what I was going to study after graduating from high-school was a challenge. I knew I liked to apply mathematics to solve difficult problems, but many of my study tests just confirmed to me that I chose the right courses in high school and would not narrow down the choice of studies. Then I realised that Leiden offered a double bachelor in Physics and Astronomy, the perfect choice for me as I enjoyed these LAPTop courses as a high-school student. During my second year I got the opportunity to go to La Palma to take my first astronomical observations that got published by another student in 2021. During the second half of my studies I helped bachelor students with their first year course work and I always enjoyed it when their eyes lit up when they grasped a difficult assignment. It was also around this time that one of my hobbies was taken to the next level with the start of an 18000 piece jigsaw puzzle that I would finish a little less than

a decade later.

After my double bachelor, I decided to start with an Astronomy Cosmology master to combine Physics and Astronomy while continuing to help students with their courses. My first research project was fully theoretical with the goal to model tidal truncation of protoplanetary disks in a stellar cluster in the group of Prof. Dr. S. F. Portegies Zwart. One of the courses that I took was 'Star and Planet Formation' by Prof. Dr. E. F. van Dishoeck. I enjoyed this course so much that I decided to switch the specialisation of my masters to a research master so I could do my second research project in her group. This second project was a true joy with Merel van 't Hoff helping me on a daily basis, teaching me about chemistry and radiative transfer, and the regular discussions with Prof. Dr. E. F. van Dishoeck about the progress I had made. While I was doing this project I learned that I wanted to pursue a career in Astronomy and I applied for PhD positions. When I got offered a position in Leiden I accepted it immediately, even before Ewine could inform the rest of the group that she had made me an offer.

During my PhD I got the chance to look both at the hot cavities of transition disks and the somewhat colder region where water sublimates tracing its snowline. In addition, I enjoyed the fun of exploring all possible outcomes of thermo-chemical models to solve the puzzle of why the observations look like they are, why do we see the molecules that we detect? This continued during my work as a teaching assistant for the Astrochemistry, Radiative Transfer, and Observational and Molecular Astronomy courses, and during the co-supervision of two master students, Nashanty Brunken and Dylan Natoewal, with Dr. A. S. Booth. Despite COVID19 cancelling many conferences during my PhD, I still got the opportunity to travel and present my work in London, Leeds, Heidelberg, Ringberg, Garching, Berlin, Kyoto, and Milan. After writing many ALMA proposals I am now awaiting my first A-rated program that will be observed around Christmas, one of the best work-related presents ALMA could have given me. I will continue doing my research with Prof. Dr. Stefano Facchini as a postdoc at the University of Milan.

Acknowledgements

During my my eleven years in Leiden, nine of which full-time, I met many great people that showed me the beauty and privilege of doing Astronomy. Your support has helped me to complete this thesis in the form it is now. I would like to thank you all for making Leiden Observatory a nice and warm place.

First of all, I would like to thank Ewine for her guidance and support over the past five years during my Masters project and my PhD. I am very grateful that you always made time to talk about science in your busy schedule and I really appreciate it that you got me involved in projects with new collaborators like John and Nienke. Michiel, thank you for the nice discussions and taking the time to sit down with me when I had a difficult question. Alice, thank you for always checking in on me at the start of your day when you dropped by my office full of energy. You have taught me a lot about observations, paper writing, and doing research in general.

It was great to be embedded in a large research group with expertise on many different aspects of the field from young objects to the older ones and from line rich sources to studies of samples of disks. Lucas, it was always great to turn around in the office and chat about the results we found in our research and help each other. I am very happy that we got to share an office and so much more during our PhDs. Lisa, we first met during a DALI workshop that we would repeat many more times. Even though we spend most of our PhDs in different countries it was always great to chat with you over a (virtual) lunch about everything that happen in our lives. Martijn, it was great being your paranymph. Thank you for all your help with removing emitting lines from an observed spectrum of the V883 Ori disk or doing the opposite and help me to squeeze as many as we could into one ALMA proposal. Ardjan, I enjoyed our morning coffee breaks to start up our days. Andrés, the kinks and spirals in your disks always twisted and turned my view of protoplanetary disks. Merel, thank you for always having an answer to my questions. Andrew and Sierk, you learned me a lot about random things like country codes for cell phones. Alex, Arthur, and Daniel, it was great to have you as pre-pandemic office mates. Arthur and Leon, thank you for helping me with all my DALI questions.

Nashanty, it was great to co-supervise you as a master student with Alice and I am very proud that you are now analyzing JWST data as a PhD student in the

group. Sierra, Giulio, Paolo, and Nico, even though most of our meetings were through a big LG-telecon screen, I enjoyed our meetings and chats when we met in person. Tere, I'm impressed with how fast you can speak in Spanish. You were a great roommate for the Berlin conference. Marissa, Milou, and Logan, it was great to work with you during the final year of my PhD. Pooneh, your excitement was always contagious and Yuan it was fun to go to the summer school in Heidelberg together.

Danny and Ioannis, your presence always lit up the conversation. It was great to go for lunch with the group where we also accreted some PhD students of other groups, like Maite, Luna, and Sam. Maite, I would like to thank you for making sure I would stop working at 17:00 sharp on Wednesdays to go for a fun dinner at either of our places. Fedde, thank you for making me go running at least semi-regularly. I would also like to thank all the PhD students of my year, Andrés, Anniek, Dora, Erik, Evgenii, Fedde, Maite, Marta, Morgan, Pooneh, Roland, Shun-Sheng, Yapeng, Zhenlin, and Yu for the games and our trip to the Efteling.

Finally, mamma en pappa dankjewel dat jullie er altijd voor me zijn en me helpen, bijvoorbeeld door helemaal naar Milaan te rijden om mij met al mijn spullen te verhuizen en om me op te komen opzoeken. Sagar, dankjewel voor alle rants over dingen die veel minder omslachtig hadden kunnen zijn. Marlise, het is altijd heel gezellig om bij te kletsen met een kopje thee met een van de duizenden-eeen theesmaken die we hebben. Lucas, dankjewel dat je er altijd voor me bent en me steunt door dik en dun. Zonder jou was mijn tijd in Leiden nooit zo mooi geweest als die nu is geworden.